DISSERTATION / DOCTORAL THESIS

Titel der Dissertation /Title of the Doctoral Thesis

Long-baseline universal matter-wave interferometry

verfasst von / submitted by

Yaakov Y. Fein

angestrebter akademischer Grad / in partial fulfilment of the requirements for the degree of

Doktor der Naturwissenschaften (Dr. rer. nat.)

Wien, 2020 / Vienna 2020

Contents

Abstract

Matter-wave interference is evidence for a coherent splitting and recombination of a particle's wavefunction, and thus provides an excellent testbed for confirming quantum mechanics in new regimes. Matter-wave interferometers are also extremely sensitive measurement devices and have made impressive headway in measuring gravity, gravity gradients, and rotation, as well as fundamental constants.

This thesis describes the construction and initial results of a new matter-wave interferometer, the Long-baseline Universal Matter-wave Interferometer (LUMI). LUMI relies on the near-field Talbot-Lau effect, which has several advantages for molecule interference experiments, including good scalability to high-mass particles, low coherence requirements, and a high throughput. The interferometer contains two nano-fabricated material gratings and a central grating which can be interchanged in situ between another material grating or an optical phase grating. This modularity enables experiments with a wide range of particle species, from atoms to complex molecules to metal clusters. The separation between each grating is one meter, which enables interferometry in a higher mass regime than previous experiments. The long baseline required the development of experimental techniques to compensate the dephasing effects of the Coriolis force and grating vibrations.

Results shown in this thesis demonstrate high fidelity interference of macromolecules beyond 25,000 atomic mass units and composed of up to 2000 atoms. These experiments represent a new record in superposition macroscopicity and place bounds on the parameter space of proposed collapse models which aim to describe the transition from a quantum to classical regime.

The universality of the interferometer scheme, combined with its inherent high force sensitivity, makes LUMI well suited to probing a range of atomic and molecular properties. Information about the material properties is encoded in the response of the interference fringes to an external field. An improved measurement of the static polarizability of fullerenes is demonstrated, as well as a direct measurement of the ground state diamagnetic susceptibility of isolated barium and strontium atoms. Measurements of the electric susceptibility of functionalized tripeptides are also described, as well as the implementation of a magnetic gradient for studying atoms and molecules with permanent magnetic moments.

Finally, an outlook is provided for the planned upgrade to the LUMI experiment which will enable interferometry of masses beyond 100,000 atomic mass units.

Zusammenfassung

Materiewelleninterferenz ist ein Beweis für eine kohärente Aufspaltung und Rekombination der Wellenfunktion eines Teilchens und bietet somit ein hervorragendes Testfeld zur Bestätigung der Quantenmechanik in neuen Regimen. Materiewelleninterferometer sind zudem äußerst empfindliche Messgeräte und haben beeindruckende Fortschritte bei der Messung von Schwerkraft, Schwerkraftgradienten, und Rotation sowie von Naturkonstanten erzielt.

Diese Arbeit beschreibt den Aufbau und die ersten Ergebnisse eines neuen Materiewelleninterferometers, des Long-baseline Universal Matter-wave Interferometer (LUMI). LUMI basiert auf dem Nahfeld Talbot-Lau Effekt, der für Molekülinterferenzexperimente mehrere Vorteile bietet, darunter eine gute Skalierbarkeit für Teilchen mit hoher Masse, niedrige Kohärenzanforderungen und einen hohen Durchsatz. Das Interferometer enthält zwei nanofabrizierte materielle Gitter und ein zentrales Gitter, das in situ zwischen einem weiteren materiellen Gitter oder einem optischen Phasengitter ausgetauscht werden kann. Diese Modularität ermöglicht Experimente mit einer Vielzahl von Partikelspezies, von Atomen über komplexe Moleküle bis hin zu Metallclustern. Der Abstand zwischen jedem Gitter beträgt einen Meter, was Interferometrie in einem Regime höherer Masse als in früheren Experimenten ermöglicht. Die lange Basislinie erforderte die Entwicklung experimenteller Techniken, um die Dephasierungseffekte der Coriolis-Kraft und der Gittervibrationen zu kompensieren.

In dieser Arbeit zeigen wir Interferenz mit hohem Kontrast von Makromolekülen über 25.000 atomare Masseneinheiten, die aus bis zu 2000 Atomen bestehen. Diese Experimente stellen einen neuen Rekord in der Überlagerungsmakroskopizität dar und setzen Grenzen für den Parameterraum möglicher Kollapsmodelle, die den Übergang vom Quanten- zum klassischen Regime beschreiben sollen.

Die Universalität des Aufbaus, in Kombination mit seiner inhärent hohen Kraftempfindlichkeit macht LUMI zu einem hervorragend geeigneten Instrument zur Untersuchung zahlreicher atomarer und molekularer Eigenschaften. Informationen über die Materialeigenschaften werden in der Reaktion der Interferenzstreifen auf ein externes Feld codiert. Eine verbesserte Messung der statischen Polarisierbarkeit von Fullerenen sowie eine direkte Messung der diamagnetischen Suszeptibilität von isolierten Barium- und Strontiumatomen im Grundzustand werden demonstriert. Es werden auch Messungen der elektrischen Suszeptibilität von funktionalisierten Tripeptiden sowie die Implementierung eines magnetischen Gradienten zur Untersuchung von Atomen und Molekülen mit permanenten magnetischen Momenten beschrieben.

Schließlich wird ein Ausblick auf das geplante Upgrade des LUMI-Experiments gegeben, das die Interferometrie von Massen über 100.000 Atommasseneinheiten ermöglicht.

1 Introduction

This chapter motivates the construction of the Long-baseline Universal Matter-wave Interferometer (LUMI) and outlines the structure of this thesis. A brief historical overview of matter-wave interference experiments is also given.

1.1 Motivation

There persists a sense of discomfort among physicists, philosophers, and laymen alike when it comes to the implications of quantum theory on the nature of reality. This is despite the unquestioned experimental success of the theory, which has been tested with unparalleled precision and in a wide parameter regime. Concepts like determinism and locality, deep-rooted paradigms of the classical world, are brought into question in the realm of quantum mechanics.

The concept of matter-waves, and particularly the phenomenon of matter-wave interference, provides a clear demonstration of these "hard to swallow" aspects of quantum theory. The double slit experiment and diffraction from gratings, fundamental experiments in classical optics, have been demonstrated not only with photons but with massive particles as well. Observing an interference pattern of molecules building up in real-time forces one to confront the apparent nonlocality of the wave function and the probabilistic nature of measured observables. At the same time, the validity of the theory's framework is continually being verified by quantum experiments in new parameter regimes. Testing the validity of the framework in a new regime is one of the key goals of high-mass interferometry experiments.

Matter-wave interferometers have been used as probes for fundamental physics, in tests of the weak equivalence principle [1], precision measurements of fundamental constants [2-4], and confirmation of the superposition principle in new regimes [5,6]. There is another aspect of these devices that makes them of more practical interest as well. The high force sensitivity of matter-wave interferometers makes them excellent inertial sensors [7-10], and they can also be used to extract properties of the interfering particles themselves.

An early distinction should be made regarding the type of interferometry referred to in this thesis. All interferometers involve the coherent splitting, propagation, and coherent recombination of a quantum state [1]. The state can be an internal state of the particle addressed by microwaves, such an in Ramsey's separated oscillatory field technique [11], or it can involve momentum states in which the beam splitting mechanism acts on the center-of-mass-motion of the particle. It is the latter form of interference that this thesis is concerned with, due to both the practical challenge of coherently manipulating internal states of complex molecules, and for the fundamental interest in delocalizing the center-of-mass of massive particles.

It was to address both fundamental and applied research goals that LUMI was built and tested over the course of this thesis. On the fundamental side, the long baseline enables interference of the highest masses to date, thus confirming the quantum superposition principle in a previously untested parameter regime. On the applied side, the long flight time and the ability to track the interference fringes on the nanometer level enables the measurement of forces as

small as 10^{-26} N. We take advantage of this with a series of metrology experiments on both atoms and molecules.

1.2 Historical perspective

It is interesting to put the LUMI experiment into a historical perspective, both to give credit where it is due and to show the longer-term outlook of matter-wave interferometry. After de Broglie's matter-wave hypothesis was first published in 1923 [12] (and expounded in his thesis in 1924), it took only three years for the hypothesis to be experimentally confirmed by the demonstration of electron diffraction by Thomson [13] as well as Davisson and Germer [14]. This fundamental insight into the nature of matter and its experimental verification earned de Broglie the Nobel Prize in Physics in 1929 while Davisson and Thomson received the 1937 prize. Diffraction experiments with neutral atoms and small molecules soon followed, with diffraction of H_2 accomplished already in 1930 by Estermann and Stern [15]. The first neutron interferometer was demonstrated in 1962 [16], with the advent of the perfect crystal interferometer [17] opening the door to a number of fundamental results, such as the effect of gravity and rotation on quantum mechanical phase [18,19] and the 4π rotation symmetry of a fermion [20,21]. Nowadays, the concept of matter waves is well accepted, with many published examples of atom and molecule interferometry experiments in a variety of interferometer schemes, employing a range of beam-splitting mechanisms [1].

Matter-wave interferometers have also been developed as extremely precise tools for measuring inertial forces, particle properties, and fundamental constants. The first demonstration of a gravity measurement with a matter-wave interferometer was made with neutrons in 1975 [18], and the first atom interferometer measurement in 1992 [22]. The sensitivity of atom interferometer gravity measurements quickly reached the level of $10^{-8}\,g/\sqrt{Hz}$ [23], matching the sensitivity of commercial sensors. Atom interferometer gyroscopes followed a similar narrative, with an early demonstration in 1991 [24] followed by experiments with improved sensitivities reaching 10^{-8} (rad/s)$/\sqrt{Hz}$ [7] and rotational stabilities of 10^{-9} rad/s [25]. Atom interferometers have also probed Newton's constant G [2,4], while neutron interferometry led the way in measuring $\hbar/m$ [26] before improved measurements with atom interferometers [27] which yield some of the most precise experimental values for the fine structure constant α. A measurement of the static polarizability of sodium in 1995 [28] is an early example of matter-wave interferometry being used as a tool for the measurement of particle properties, which is one of the goals of the LUMI experiment as well.

In more recent years, various groups have focused on exploring how macroscopic such superposition states of matter can become. The concept of macroscopicity in this context requires a more precise definition, which is discussed further in Chapter 2. A candidate for the definition should consider factors such as the mass of the particle, the time it spends in a superposition state, and the spatial extent of the superposition. Superconducting quantum interference devices (SQUIDs) can create superpositions of large numbers of electrons circulating clockwise and counter-clockwise [29], while large momentum transfer beam-

splitters have enabled atom interferometers to create superpositions up to half a meter across [6]. In a different regime, diffraction of macromolecules, beginning with the diffraction of fullerenes in 1999 [5], demonstrates quantum superposition in a new mass and internal complexity scale. Interference with molecules as large as 10,000 u was demonstrated with the predecessor to the LUMI experiment in Vienna [30] using a near-field interferometry scheme called Talbot-Lau interferometry first demonstrated for atoms in 1994 [31]. A more detailed overview of Talbot and Talbot-Lau interferometers is given in the following chapter. Pursuing the avenue of macromolecule interference is one of the main goals of the LUMI experiment, with interference of molecules beyond 25,000 u already demonstrated [32], and ongoing work to extend this even further.

While only a small historical subset of matter-wave interferometry experiments has been presented here, it should be sufficient to recognize the long history of the field as well as the many pioneering groups and techniques without which the LUMI experiment could not have been built.

1.3 Thesis outline

The thesis is structured as follows:

Chapter 2 describes the basic theory underlying the LUMI experiment and aspects specific to long-baseline interferometry. Collapse models are briefly discussed, including the bounds that can be placed upon them by high-mass interference experiments. The framework underlying metrological applications with matter-wave interferometers is reviewed, with a focus on magnetism. This chapter aims to provide the general theoretical framework for most of the experiments described in this thesis, without providing details of any single experiment.

Chapter 3 describes the general experimental setup and protocols. As a rule, details of components or experimental protocols that were used for several experiments are described here, while those that were used only for a single experiment are delegated to the chapter describing that experiment.

Chapter 4 describes experiments exploring fundamental quantum mechanics, focusing on the interference experiments with high-mass oligoporphyrins. The bounds on collapse models from these experiments as well as the obtained value of macroscopicity are discussed. The universal nature of the LUMI experiment is described and a brief overview of dark matter searches with matter-wave interferometers is also given.

Chapter 5 describes metrology experiments conducted at LUMI, discussing electric and magnetic measurements of both atoms and molecules. Some ongoing work involving magnetic investigations of molecules is also described.

Chapter 6 looks ahead to the next phase of planned experiments.

2 Theory

This chapter outlines the theoretical framework behind the LUMI experiment, namely the Talbot-Lau and Kapitza-Dirac effects, and the challenges of long-baseline interferometry. A class of collapse models known as continuous spontaneous localization is briefly reviewed, together with the bounds that can be placed on this model's parameter space via matter-wave interference experiments and the concept of macroscopicity. Finally, the background behind the interferometric measurement of various molecular properties is discussed.

2.1 The Talbot-Lau and Kapitza-Dirac effects: a conceptual overview

The Talbot effect is a near-field diffraction phenomenon that occurs upon coherent illumination of a monochromatic plane wave on a grating structure. First discovered with light in 1836 [33], it has found a wide range of uses in both conventional and matter-wave optics [34]. The key feature of the phenomenon is the self-imaging of the grating structure at integer distances of the Talbot length

$$L_T = \frac{d^2}{\lambda},$$

(1)

where d is the grating period and λ is the wavelength of the light, or, in the case of matter waves, the de Broglie wavelength λ_{dB}. This is known as the integer Talbot effect, and produces modulations in the wave with the same period of the grating, shifted transversely by π for every odd order. Scaled images of the pattern also appear at non-integer orders in the fractional Talbot effect. Together, the integer and fractional Talbot effects form a Talbot carpet as shown in Figure 1.
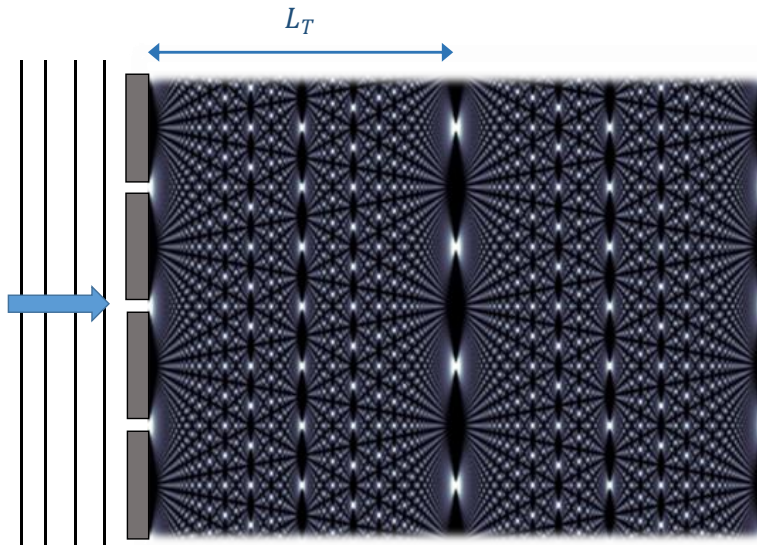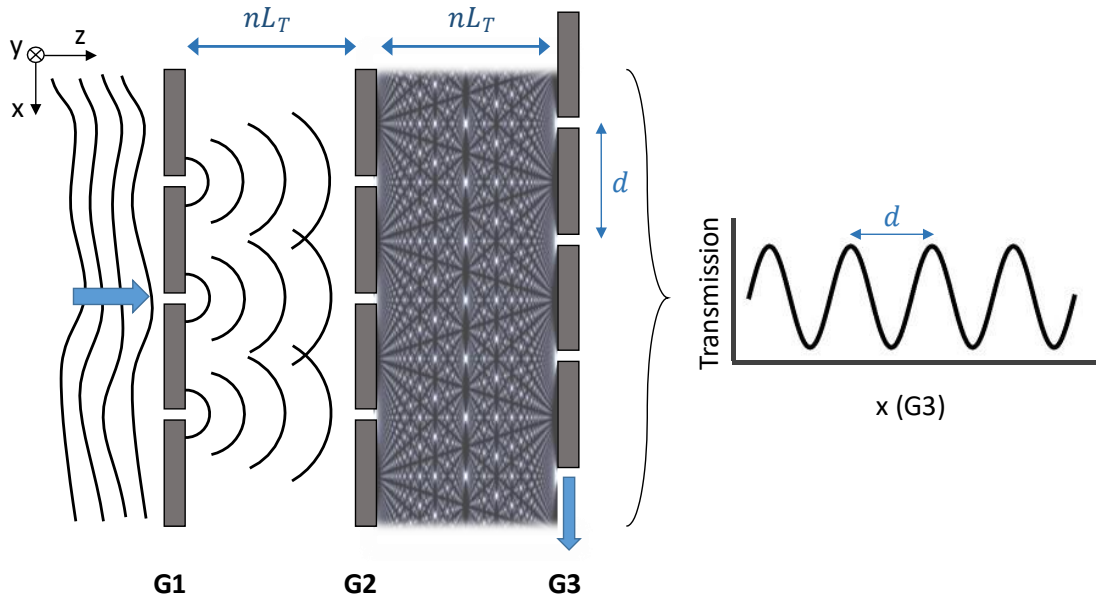

Figure 1: Illustration of the Talbot effect for a grating with a binary transmission function. A plane wave incident on a grating produces a Talbot carpet, with self-images of the grating

structure produced at regular intervals behind the grating. The integer effect is visible at the center (π-shifted) and at the right end of the pattern, while the fractional effect is visible as the fractal pattern of scaled periodicities in between. The grating in this simulation has an open fraction of 0.05 to exaggerate the fractional effect.

The related Lau effect [35] is the self-imaging of a grating when illuminated with a spherical wave. It was first demonstrated using white light focused onto a grating, passing a second grating a distance L_T downstream, and then imaged with a lens to observe interference fringes at infinity. The appearance of the same length scale L_T as in the Talbot effect can be understood by simple geometric arguments, since it is for this inter-grating separation that the path length difference from a slit in the first grating to neighboring slits in the second grating differs by integer multiples of λ. The Talbot and Lau effects can be thought of as reciprocal experiments, as discussed in Reference [36].

A similar setup as that used in Lau's experiment is employed in the so-called Talbot-Lau effect, as illustrated in Figure 2. In this case a Talbot carpet is produced even with a spatially incoherent beam incident on the first grating. In a simple physical picture, the first grating prepares coherence by providing the matter-wave a well-defined transverse position as it passes the grating slits, hence increasing its transverse momentum uncertainty by the Heisenberg uncertainty principle. This momentum uncertainty transforms into a position uncertainty some distance downstream from the grating sufficient to cover several periods of the second grating. Near-field diffraction then occurs at the second grating, producing an interference pattern behind the grating. Typically, a third grating is employed at the position of this expected pattern, which is transversely scanned to detect a flux modulation, thus eliminating the need for a spatially resolving detector.

Figure 2: *Illustration of the Talbot-Lau effect. The first grating (G1) serves to prepare sufficient transverse coherence in the beam such that the second grating (G2) produces a Talbot carpet. In Talbot-Lau interferometers, a third grating (G3) is often used as a detection mask. The transmitted flux through the interferometer as measured by an integrating detector varies periodically as the third grating is transversely scanned over the grating self-image. In the*

symmetric scheme with equal grating periods d and equal inter-grating separation near an integer multiple of L_T, the period of the transmitted flux is equal to the grating period. The coordinate system defined in the top left is used throughout unless otherwise stated.

For such a setup to yield high-visibility modulations in the beam density, a resonance criterion must be fulfilled which determines the allowed ratios of grating periods and grating separations. The condition for the grating periods of the first two gratings, $d_{1,2}$ and the distances between the grating $L_{1,2}$ is given by [37]

$$\frac{d_2}{d_1}\left(1 + \frac{L_2}{L_1}\right) = \frac{r}{s},\tag{2}$$

where r and s are mutually prime integers. The periodicity of the pattern d_3 sampled by the third grating is determined by

$$sd_3 = \frac{L_2}{L_1}d_1,\tag{3}$$

which can be used to create magnifying or de-magnifying interferometer schemes. In the simplest case, and the one dealt with throughout this thesis, $r:s = 2:1$ such that $d_1 = d_2 = d_3 = d$ and $L_1 = L_2 = L$.

There are several advantages over far-field diffraction in using the near-field Talbot-Lau effect to demonstrate spatial superpositions of high-mass particles. First, the interference fringes scale like $1/\sqrt{m}$, as compared to $1/m$ in far-field diffraction, with m the particle mass. This allows for detection of the interference pattern in such a scheme without the need for very long propagation distances behind the grating or demanding spatial resolution of the detector. Second, the coherence requirements of the beam source are reduced, which is a significant advantage when working with neutral beams of high-mass molecules where transverse cooling is technically challenging and narrow beam collimation is impractical. Finally, the use of gratings rather than single or double slits increases the throughput of the interferometer by orders of magnitude, which is particularly important when working with molecular beams of weak flux.

The three gratings used in the Talbot-Lau scheme have until now been assumed to be ideal physical transmission gratings, i.e. structures with periodic binary transmission functions and no phase component. The first and third gratings, which serve to create transverse coherence in the beam and act as a transmission mask respectively, must be transmission gratings. The second grating, however, can be implemented as a pure phase grating. There are thus various ways to realize gratings in Talbot and Talbot-Lau interferometers, using nano-fabricated material gratings, optical depletion gratings, optical phase gratings, or combinations thereof. The Talbot effect was demonstrated with nano-fabricated gratings for atoms [38] and for electrons [39], while pulsed optical phase gratings have also been employed for clouds of cold atoms [40,41]. A Talbot-Lau interferometer (TLI) was first demonstrated with potassium atoms in 1994 [31], with a similar design employed in References [42] and [43] for use with

molecules. Pulsed optical gratings have also been employed [44], and an interferometer combining material transmission gratings and an optical phase grating was first demonstrated in Reference [45].

Optical gratings have several advantages over nano-fabricated material gratings. First, they avoid the damage and clogging caused by a high flux of atoms or molecules through the gratings. Second, the Casimir-Polder interaction between the atoms or molecules and the second grating leads to strong dephasing for non-monochromatic beams. One approach which solves both of these issues is the use of three optical depletion gratings, while another is to use a mixed material-optical scheme in which material nano-gratings are used for the first and third gratings while the central grating is a pure phase grating formed by an off-resonant standing light wave. The phase shift is due to the dipole moment induced by the interaction of the standing light wave and the polarizable molecule. When the standing light wave is in the thin-grating Raman-Nath regime, this leads to diffraction via the Kapitza-Dirac effect [46], which was first conclusively demonstrated with atoms in 1983 [47]. The combined material-optical grating scheme is referred to as a Kapitza-Dirac Talbot-Lau interferometer (KDTLI). First demonstrated in Vienna in 2007 [45], this interferometer scheme has been used in a range of high-mass interference and molecular metrology experiments [30,48-52].

2.2 TLI vs. KDTLI

In this thesis, "TLI" is reserved for the all-material scheme with three nano-fabricated gratings, while "KDTLI" always refers to the mixed material-optical scheme with two nano-fabricated gratings and a central optical phase grating[1]. While the KDTLI is conceptually very similar to the TLI, the two schemes exhibit some different features. In a KDTLI, the inter-grating spacing L should be approximately a half-integer of L_T instead of an integer multiple as required for the TLI, as depicted in Figure 3. Conceptually, this difference arises because in the TLI coherence must be prepared over at least two slits, while in a KDTLI, coherence between a neighboring node and antinode, separated by half the period, is sufficient for interference. Practically, however, this difference is not easily visible when working with highly non-monochromatic beams, as illustrated in Figure 4.

The KDTLI scheme has several advantages over the all-material TLI for high-mass interference, especially with slow, polarizable particles. It avoids the strongly dispersive Casimir-Polder dephasing at the second grating, which is particularly beneficial for highly polarizable molecules with a broad velocity spread. It thus relaxes the longitudinal coherence requirements (alongside the inherently relaxed transverse coherence requirements offered by all TLI schemes), allowing high-visibility interference to be maintained even for highly non-

---

[1] These terms were previously also used to describe specific experiments rather than just the interferometer configurations. Since the LUMI experiment described in this thesis employs both the TLI and KDTLI configurations interchangeably, previous experiments are always clearly demarcated to avoid potential confusion. For example, when the interferometer introduced in 2007 by Gerlich et al. [45] is meant, it is referred to as the "previous KDTLI experiment."

monochromatic beams, as illustrated in Figure 4. The KDTLI scheme also has higher throughput than a TLI, since all molecules are transmitted through the phase grating.
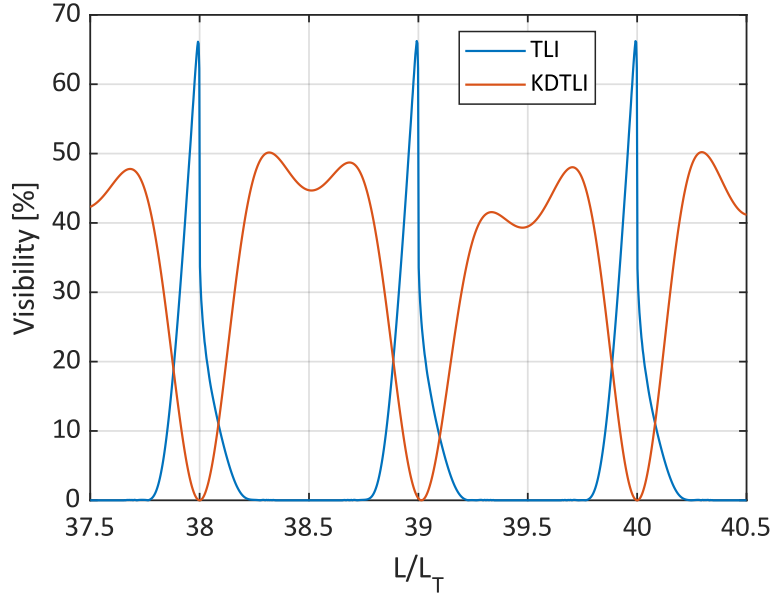
Figure 3: *Visibility of C_{60} in a TLI (blue) versus a KDTLI (red) as a function of L/L_T. The length L is kept fixed at 0.98 m while the velocity, and hence L/L_T , is varied. The narrower region of high visibility available in the TLI scheme is due to the Casimir-Polder interactions of the particle with the grating wall and limits the visibility in a non-monochromatic beam. A grating open fraction of 0.43 is used throughout and a laser power of 9 W for the KDTLI curve.*
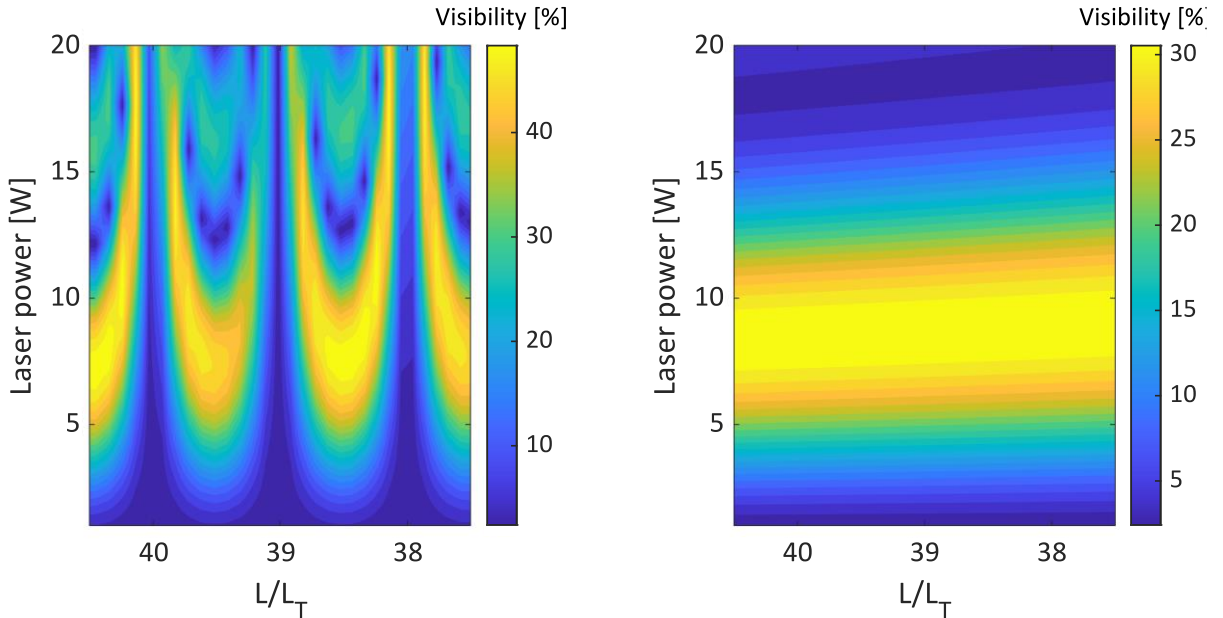
Figure 4: *Simulated visibility of C_{60} in a KDTLI as a function of inter-grating separation and laser power. As in Figure 3 L is left constant at 0.98 m while v is varied.* **Left:** *Calculated visibility map for monochromatic C_{60} beams with velocities ranging from 190 m/s to 205 m/s, showing maximum visibility near half integer Talbot lengths. The KDTLI curve in Figure 3 is a line-cut at 9 W.* **Right:** *Same as left, but for beams with a Gaussian velocity distribution centered at v_0*

and a spread of $\sigma = 0.1v_0$. The region of high contrast is maintained across several Talbot lengths, albeit with reduced visibility (note the rescaled color bar).

The KDTLI scheme is less advantageous, however, if one wants to investigate fast beams of less polarizable species, such as atomic beams or supersonic beams of small molecules. This is because the laser intensity required for sufficient phase modulation of the beam becomes difficult to achieve, and at the same time the high speed and low polarizability means that the particle-grating interactions which motivated the use of the phase grating in the first place are less critical.

For these reasons the LUMI experiment combines both the TLI and KDTLI schemes in the same device, by means of an interchangeable second grating. This enables experiments with slow beams of massive, highly polarizable molecules, atomic beams, and supersonic beams of small molecules. In this sense the LUMI experiment is a nearly universal interferometer.

2.3 Talbot-Lau interferometry: The mathematical framework

The key observable in our experiments is the flux as a function of transverse position of the third grating. While this quantity can be calculated in different ways, such as by direct application of the Fresnel-Kirchoff equation, a phase space Wigner function approach is employed here. This approach has several advantages, both in the intuitive way that the effect can be sequentially calculated as a series of grating and free-space propagation terms [53,54], and for the way in which decoherence can be included in the framework [55]. It also allows for a straightforward comparison of a purely classical phase space treatment and the quantum evolution, which we use to confirm that the effect we see is not due to classical shadow fringing.

The Wigner function is the quantum analog to the classical phase space probability distribution $f(x, p)$, and in one dimension is given by

$$w(x, p) = \frac{1}{2\pi\hbar} \int ds\, e^{ips/\hbar} \left\langle x - \frac{s}{2} \middle| \rho \middle| x + \frac{s}{2} \right\rangle, \tag{4}$$

where ρ is the density matrix operator. Treating only the transverse direction in the interferometer is valid because the longitudinal velocity is large compared to the transverse velocity and the gratings are extended in the vertical direction. The eikonal approximation, in which one neglects changes in the transverse component of the matter-wave during propagation through the grating, is used throughout [37].

Beginning with an incoherent state, the final transverse beam state can be determined by applying a sequence of free-space propagation transformations and grating transformations. The step-by-step details of the calculation relevant for both the all-material TLI and KDTLI are presented in several theses and publications [53,54,56], so only the key results are presented here. A symmetric setup as we have at LUMI is assumed throughout, in which all grating periods d are equal, and the inter-grating separations L are equidistant.

The flux S transmitted through the third grating as it is scanned transversely across x_s is given by

$$S(x_s) = \sum_m A_m^* B_{2m}\left(m\frac{L}{L_T}\right) C_m e^{2\pi i m x_s/d}. \tag{5}$$

Here, A_m and C_m are the Fourier components of the first and third gratings, which in LUMI are both material gratings of the same period, such that

$$A_m = f \operatorname{sinc}(\pi m f) = C_m, \tag{6}$$

where f is the open fraction of the grating period. The B term is known as the Talbot coefficient and describes the action of the second grating. This differs between the TLI and the KDTLI schemes, since they rely on different diffraction mechanisms.

Since the pattern is to a good approximation sinusoidal, the transmitted flux S can be Fourier expanded to first order and the visibility can be written as

$$V = \frac{S_{max} - S_{min}}{S_{max} + S_{min}} \approx 2 \operatorname{sinc}^2(\pi f) B_2\left(\frac{L}{L_T}\right), \tag{7}$$

which holds for both the TLI and KDTLI when the appropriate second order Talbot coefficient B is used. This equation is used throughout the thesis, both in confirming the expected visibility of the observed signal, and in metrology experiments where the velocity-dependent deflection must be weighted with the visibility function.

2.3.1 Talbot-Lau coefficient

The Talbot coefficient for the all-material TLI is discussed first, drawing on the results presented in Reference [37]. The interaction of a particle a distance r from the grating wall can be approximated by the long-range retarded potential $V(r) = -C_4/r^4$ where the C_4 coefficient can be calculated as shown in Reference [57]. The Talbot coefficient for a material grating can be expressed as

$$B_k(\xi) = \sum_{j=-\infty}^{\infty} b_j b_{j-k}^* e^{i\pi\xi(k-2j)}, \tag{8}$$

where

$$b_j = \frac{1}{d} \int_{-\frac{s'}{2}}^{\frac{s'}{2}} dx \exp\left[-\frac{ib}{\hbar v}\left(-\frac{C_4}{r_-^4} - \frac{C_4}{r_+^4}\right)\right], \tag{9}$$

with b the grating width and $r_\pm = fd/2 \pm x$. The integration is done over a velocity-dependent effective opening s' to avoid the divergence of the phase near the grating walls [37]. In practice this integral must be calculated numerically. Fixed integration limits at 5-10 nm from the grating walls (depending on the typical beam velocity) were able to reproduce results obtained

using a velocity-dependent cutoff and significantly reduced the computational time required for the numeric integrals.

2.3.2 Kapitza-Dirac Talbot-Lau coefficient

The Talbot coefficient for an optical phase grating can be calculated analytically, following the treatment in Reference [56]. In the standing light wave both the desired coherent diffraction via the Kapitza-Dirac effect and an absorptive contribution due to photon absorption must be considered. These are both described by the Talbot coefficient

$$B_k(\xi) = e^{-\beta_2(\xi)} \left(\frac{\beta_1(\xi) + \beta_2(\xi)}{\beta_1(\xi) - \beta_2(\xi)} \right)^{l/2} J_k \left[-\text{sgn}(\beta_1(\xi) \right. $$
$$\left. - \beta_2(\xi)) \sqrt{\beta_1^2(\xi) - \beta_2^2(\xi)} \right] \tag{10}$$

where J_k are Bessel functions of the first kind. The coherent phase modulation is contained in the term

$$\beta_1(\xi) = \phi_0 \sin\left(\frac{\pi \xi}{d} \right), \tag{11}$$

where

$$\phi_0 = 4\sqrt{2\pi} \frac{P\alpha_\lambda}{\epsilon_0 hcw_y v} \tag{12}$$

is the phase shift in an antinode of the standing light wave. Here, α_λ is the optical polarizability of the particle (in SI units) at the laser wavelength λ, P is the laser power, and w_y is the vertical $1/e^2$ laser beam waist.

The contribution of single-photon absorption can be modelled as a random walk of momentum kicks and is given by

$$\beta_2(\xi) = n_0 \sin^2\left(\frac{\pi \xi}{d} \right), \tag{13}$$

where

$$n_0 = \frac{8P\sigma_{abs}\lambda}{\sqrt{2\pi}hcw_y v} \tag{14}$$

is the mean number of absorbed photons in an antinode of the standing light wave and σ_{abs} is the absorption cross section at the laser wavelength. Note the sign difference in β_2 between Equation 10 and the corresponding equation in Reference [53], which is due to the difference between treating the momentum kicks from photon absorption appropriately as a coherent superposition versus as a classical mixture [56]. An additional incoherent term due to Rayleigh scattering of the particle in the optical grating is not relevant for the particle sizes considered in this thesis.

It is particularly important for the KDTLI scheme, which is the preferred setup for high-mass interference experiments, to be able to compare the observed pattern with expectations from the quantum model presented above and a classical model which can also predict a modulation in the flux due to moiré shadowing. The latter can be modeled analogously to the quantum treatment by using the classical phase space distribution in place of the Wigner function, with the key difference that the coherent term of the second grating interaction is treated as classical momentum kicks. The periodic phase modulation in Equation 11 is then replaced by

$$\phi_0 \sin\left(\frac{\pi\xi}{d}\right) \rightarrow \phi_0 \pi\xi, \tag{15}$$

and the classical result for the interferometer flux has the same form as Equation 5 with the substitution $B_k(\xi) \rightarrow B_k^{cl}(\xi)$, where

$$B_k^{cl}(\xi) = J_k\left(-\frac{\sqrt{8\pi}\alpha_\lambda P}{\epsilon_0 \hbar c w_y v}\xi\right). \tag{16}$$

2.4 Long-baseline interferometry

This section discusses the motivations and challenges of long-baseline Talbot-Lau interferometry. The effect of vibrations and the Coriolis force become critical for the LUMI experiment, and the required operational limits are discussed. The vibrational characterization of the interferometer and experimental implementation of the Coriolis compensation scheme are deferred to Chapter 3. The sensitivity to thermal and collisional decoherence as compared with previous, shorter, molecule interferometers is also estimated.

2.4.1 Long baseline: motivations

There are two main motivations for constructing a long-baseline Talbot-Lau interferometer. The first and primary reason is that it enables center-of-mass interference of high mass particles. For a monochromatic beam with given longitudinal beam velocity, the maximum mass particle that can be interfered in a Talbot-Lau type interferometer is proportional to the inter-grating spacing, which must be near a multiple of the Talbot length L_T. By increasing this distance by an order of magnitude from the previous KDTLI experiment [45], from 0.1 m to 1 m, particles with an order of magnitude larger mass become accessible. In a KDTLI the inter-grating separation should be equal to a half integer of L_T, although this is strongly relaxed with non-monochromatic beams, as shown in Figure 4. However, below the first Talbot order with $L < L_T/2$, the classical and quantum predictions for the fringes become difficult to distinguish. Thus, to observe interference of massive objects in such a scheme requires a sufficiently long baseline such that $L \geq L_T/2$, which sets a limit for the product $m \times v$.

The limits in the mass-velocity parameter space for KDTLI schemes with various parameters are shown in Figure 5, assuming $m = 2Lh/d^2 v$ for interference in the first Talbot order.

Producing beams of lower longitudinal velocity v is clearly necessary to achieve the highest mass available in a given setup, and that both the LUMI predecessor and LUMI itself have not reached their full potential in that regard. The reason lies in the experimental challenge of preparing slow, neutral, and, for the larger mass range, internally cold, beams of macromolecules. Details of beam preparation are discussed in several of the following chapters, with the ongoing work to achieve slow, internally cold, and massive beams of metal clusters in an upgraded interferometer scheme discussed in Chapter 6.
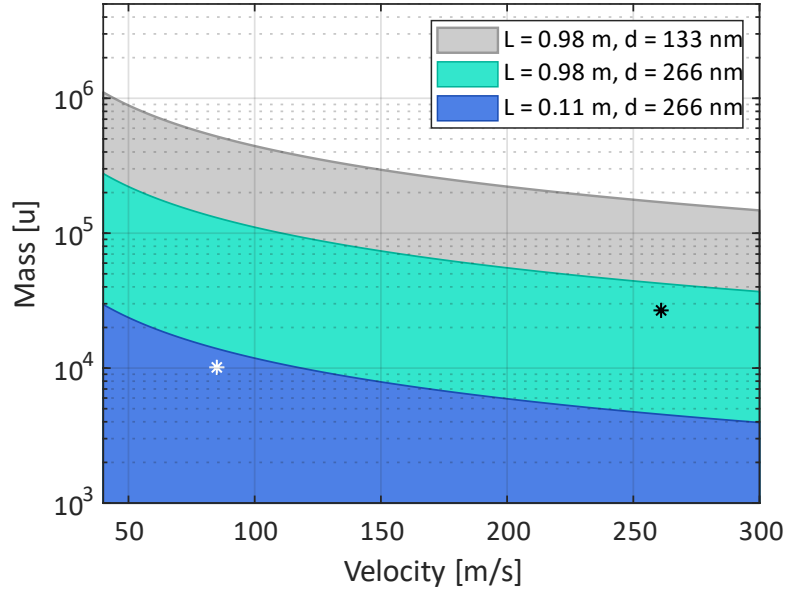
Figure 5: *The mass-velocity parameter space allowed for various KDTLI-type interferometers. The lower (blue) shaded region corresponds to the previous KDTLI experiment with L = 0.11 m, and the middle (green) shaded region corresponds to the current LUMI experiment with L = 0.98 m. The uppermost (grey) shaded region shows the extended parameter space available with a planned update to the LUMI experiment where three UV gratings (d = 133 nm) are employed. The white asterisk represents the highest mass interfered in the previous KDTLI experiment [30], while the black asterisk represents the highest mass interfered to date in the LUMI experiment [32].*

The second motivation for a long baseline Talbot Lau is the gain in sensitivity for metrology experiments. The information we want to extract when studying atomic or molecular properties is encoded in the phase and visibility of the interference fringes. Since the phase shift is proportional to the square of the time spent in the force field, there is a significant gain in sensitivity available by increasing the inter-grating distance, and thereby the interaction time.

Both of these aspects of long-baseline interferometry are explored in this thesis, with high-mass interference experiments described in Chapter 4 and metrology experiments in Chapter 5. However, the long baseline also introduces challenges, such as stringent vibration isolation requirements and sensitivity to the Earth's rotation. The magnitude of these effects is discussed below, with experimental details and results shown in Chapter 3. Finally, a more banal but equally challenging aspect of long-baseline interferometry is the need for an intense source and/or efficient detection scheme such that a sufficient flux can be observed to obtain meaningful statistics.

2.4.2 Long baseline: vibrations

Grating vibrations are a key concern for maintaining high visibility interference, and a long baseline tightens the requirements since lower frequency oscillations become more detrimental as the flight time is increased. Grating shifts yield a phase shift $\Delta\phi$ in a three-grating interferometer given by

$$\Delta\phi = \frac{2\pi}{d}(\Delta x_1 - 2\Delta x_2 + \Delta x_3), \tag{17}$$

where Δx_i is the transverse position of the ith grating as the particle passes it relative to an unshifted frame of reference [1]. This formula gives the phase of the interference pattern with respect to an inertial frame and is used to determine phase shifts due to forces which yield a shift of the wavefunction envelope, in complete analogy with a classical deflection.

In the following three main types of grating motions are considered: independent linear motion, common-mode linear motion, and torsional motion, as illustrated in Figure 6. Independent motion refers to motion with no fixed phase relation between the gratings, caused, for example, by exciting eigenfrequencies of the individual grating mounts. Common-mode motion refers to grating motion with a fixed phase relationship and can be linear or torsional. The main results of the first two classes of motion are given in Reference [58], but a different treatment of torsional motion is presented here.
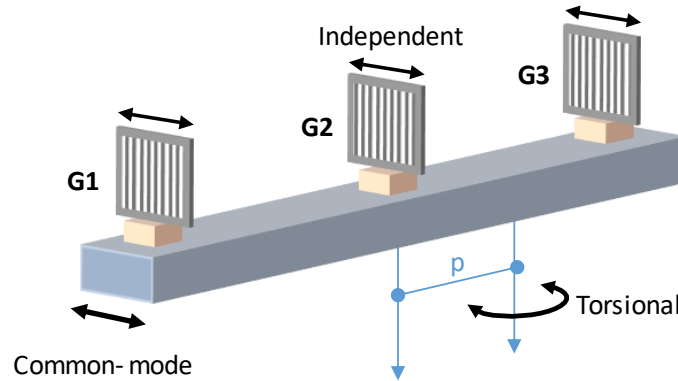
Figure 6: *Three types of motion affecting the three gratings are illustrated: independent motion (IM) of the gratings, common-mode linear motion (CM) of the entire interferometer, and torsional motion (TM) of the entire interferometer around a fixed pivot point a distance p from G2.*

For gratings moving periodically with respect to one another with angular frequency ω and amplitude A, the displacement of the ith grating as the atoms or molecules pass it can be written in the general form

$$\Delta x_i = A \sin\left(\frac{(i-1)\omega L}{v} + \phi_i\right), \tag{18}$$

where ϕ_i is the starting phase of the motion. These grating shifts contribute to a fringe phase shift as given in Equation 17, which leads to the visibility reduction for a given velocity class

$$\frac{V}{V_0} = \left| \left\langle \exp\left[i\frac{2\pi}{d}\left(\Delta x_1 - 2\Delta x_2 + \Delta x_3\right)\right]\right\rangle\right| \tag{19}$$

in which the average is performed over all independent ϕ_i, which entails three integrals for independent motion and one for common-mode motion. When the resulting quantity is velocity dependent, it must then also be averaged over the velocity distribution of the beam to obtain the observed visibility reduction.

For independent sinusoidal motion with amplitude A and angular frequency ω, the displacements of the three gratings with respect to the beam are

$$\begin{aligned}
\Delta x_1 &= A\sin(\phi_1), \\
\Delta x_2 &= A\sin\left(\frac{\omega L}{v} + \phi_2\right), \\
\Delta x_3 &= A\sin\left(\frac{2\omega L}{v} + \phi_3\right)
\end{aligned} \tag{20}$$

for an inter-grating spacing L and longitudinal velocity v. The reduced visibility is then given by the average over each random phase ϕ_i as in Equation 19, yielding the visibility reduction

$$\frac{V}{V_0} = \left|J_0\left(\frac{2\pi}{d}A\right)\right|^2\left|J_0\left(\frac{4\pi}{d}A\right)\right|, \tag{21}$$

where the frequency dependence drops out due to the phase averaging and J_0 is the 0th order Bessel function of the first kind.

Common-mode linear motion of the gratings can be described by

$$\begin{aligned}
\Delta x_1 &= A\sin(\phi_1), \\
\Delta x_2 &= A\sin\left(\frac{\omega L}{v} + \phi_1\right), \\
\Delta x_3 &= A\sin\left(\frac{2\omega L}{v} + \phi_1\right).
\end{aligned} \tag{22}$$

Averaging over all possible values of ϕ_1 leads to the visibility reduction

$$\frac{V}{V_0} = \left|J_0\left(\frac{8\pi A}{d}\sin^2\left(\frac{\omega L}{2v}\right)\right)\right|, \tag{23}$$

which must then be averaged over the velocity distribution to obtain the experimentally observed visibility reduction.

Figure 7 shows the visibility reduction for a Gaussian velocity distribution typical of a velocity-selected fullerene beam for both independent and common-mode linear grating motion with a range of amplitudes and frequencies. Although dependent on the empirical velocity distribution, independent vibrations of the gratings generally set the more stringent requirement across most frequencies. For the velocity distribution considered here they should be suppressed on the level of 10 nm to maintain more than 90% visibility.
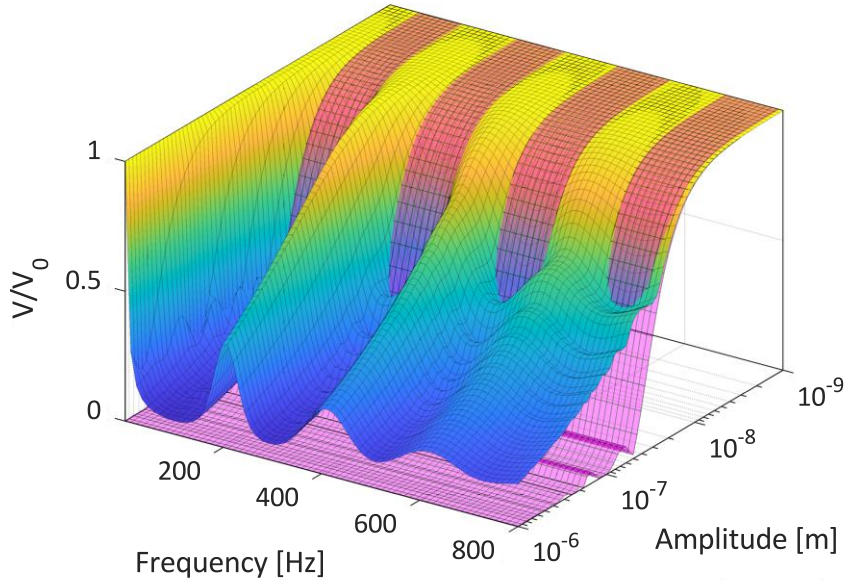
Figure 7: *Visibility reduction for independent (magenta surface in background) and common-mode (color-coded surface in foreground) vibrations for a 200 m/s beam with a 20 m/s spread and a one meter grating separation. The effect of independent motion is velocity independent, while the common-mode visibility reduction features revivals of the visibility as the gratings periodically rephrase, albeit washed out by the velocity spread. The velocity averaging for the common-mode vibrations is done numerically. Independent motion is typically the more stringent criterion, particularly at high frequencies.*

Torsional motion of the interferometer is a type of common-mode motion described by small angular displacements of amplitude θ_0 around a pivot point a distance p away from the second grating. Due to the symmetric pendulum suspension of the gratings it is expected that the dominant pivot point is located at the second grating, i.e. $p \approx 0$. The grating displacements in this case be written

$$
\begin{aligned}
\Delta x_1 &= \theta_0 \, (L - z)\sin(\phi_1), \\
\Delta x_2 &= -\theta_0 z \sin\left(\frac{\omega L}{v} + \phi_1\right), \\
\Delta x_3 &= -\theta_0 (L + z) \sin\left(\frac{2\omega L}{v} + \phi_1\right),
\end{aligned}
\tag{24}
$$

yielding the visibility reduction

$$
\frac{V}{V_0} = \left| J_0 \left(\frac{4\pi\theta_0 L}{d} \sqrt{\sin^2\left(\frac{\omega L}{v}\right) + \frac{p^2}{L^2}\left[1 - \cos\left(\frac{\omega L}{v}\right)\right]} \right) \right|.
\tag{25}
$$

The torsional visibility reduction is plotted in Figure 8 for the same velocity distribution as Figure 7 for a pivot point at the second grating. Torsional vibrations should be suppressed on the level of 10 nrad to maintain 95% visibility for the example considered here.
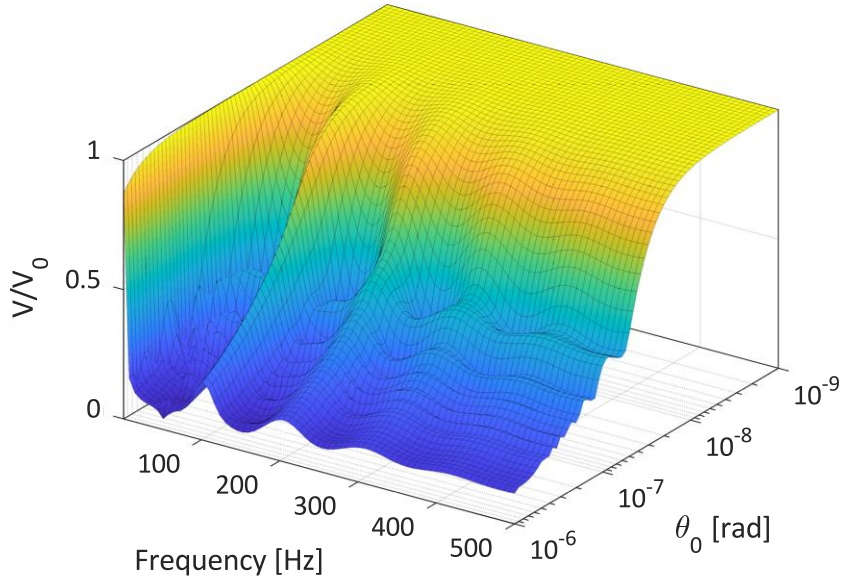
Figure 8: *Visibility reduction due to torsional motion for a pivot point located at the second grating, again for a 200 m/s beam with a spread of 20 m/s. As a subclass of common-mode motion the rephasing at certain frequencies is again apparent, and the overall constraints are weak compared to those set by independent grating vibrations.*

The expressions derived here determine the maximum vibrational noise permissible for high visibility interference, which was taken into consideration in the design of the interferometer and carefully characterized with a range of sensors after construction, as described in Chapter 3.

2.4.3 Long baseline: Coriolis

Besides an increased sensitivity to vibrations, the long baseline also makes the interferometer sensitive to the Sagnac phase caused by the Earth's rotation. This can be seen by considering the particle in a frame moving with a constant transverse acceleration a, in which case the phase shift of the interference fringes relative to a non-accelerating frame is found by applying Equation 17 to give

$$\Delta\phi = \frac{2\pi}{d} a \frac{L^2}{v^2}. \tag{26}$$

This formula can be used to determine the envelope phase shift of the interference fringes for any constant acceleration present for the entire duration of an interference measurement. Such a phase shift is generally detrimental when the beam contains a spread of velocities, since each velocity class will experience a different shift, yielding a final pattern with reduced visibility.

The Coriolis acceleration, $\boldsymbol{a}_{Cor} = -2\boldsymbol{\Omega} \times \boldsymbol{v}$, can be simplified assuming a beam velocity in the horizontal North-East plane with a negligible vertical component. The result is an in-plane perpendicular acceleration of $2\Omega_E v \sin\phi_{lat}$ and a vertical component of $2\Omega_E v_{east} \cos\phi_{lat}$, where $\Omega_E > 0$ is the Earth rotation frequency and ϕ_{lat} the latitude of the experiment.
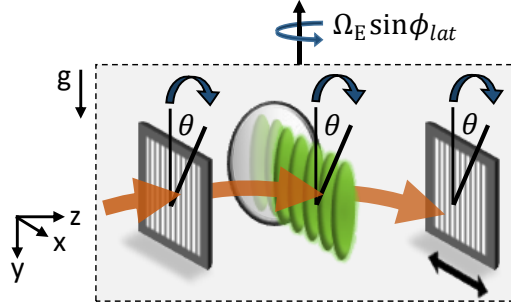
In the presence of both gravity and rotation, the net acceleration perpendicular to the gratings, which is the only one relevant for dephasing, is

$$a = 2\Omega_E[v \sin\phi_{lat} \cos\theta - v_{east} \cos\phi_{lat} \sin\theta] + g \sin\theta, \tag{27}$$

with $v = \sqrt{v_{east}^2 + v_{north}^2}$ and the roll angle θ defined relative to gravity and the coordinate system defined as in Figure 9. In the small angle limit $\theta \ll 1$ where we typically operate, this simplifies to

$$a \approx 2\Omega_E \sin\phi_{lat} v + g\theta \tag{28}$$

in which the term of order $\Omega_E\theta$ has been discarded. The similarly small effect of the centrifugal force has also been neglected in this treatment.

Figure 9: *Passive Coriolis compensation via gravity in a KDTLI. Both gravity and the Earth's rotation cause velocity-dependent phase shifts which are dephasing in the presence of non-monochromatic beams. This visibility reduction can be compensated by introducing a common roll offset θ to the three gratings such that overall phase is nearly velocity independent. The coordinate system defined here is the one used for interference scans unless stated otherwise. Figure adapted from Reference [59].*

When working with non-monochromatic beams in the absence of a significant Coriolis phase shift, it is preferential to align all gratings parallel to gravity to minimize the velocity-dependent phase shift due to gravity. This is the configuration employed by previous shorter-baseline molecule interferometers in Vienna with the exception of a time-domain experiment [44] which is insensitive to this issue. In the presence of a significant Coriolis term as in LUMI, this is no longer optimal, and aligning the gratings to gravity leads to a visibility reduction

$$\frac{V}{V_0} \approx \exp\left[-8\left(\frac{\pi\Omega_E \sin\phi_{lat} \sigma L^2}{d v_0^2}\right)^2\right] \tag{29}$$

for a Gaussian velocity distribution with spread σ and center velocity v_0.

To counteract this strong visibility reduction, a roll offset to gravity for all the three gratings is implemented, which introduces a gravitational phase shift that compensates the velocity dependence of the Coriolis phase shift. To determine the optimal roll offset one can Taylor expand Equation 28 around the velocity v_p, giving the total phase shift

$$\Delta\phi \approx \frac{2\pi}{d}\left[2\Omega_E \sin\phi_{lat}\left(\frac{1}{v_p} - \frac{v - v_p}{v_p^2}\right) + g\theta\left(\frac{1}{v_p^2} - 2\frac{v - v_p}{v_p^3}\right) + \cdots\right]. \tag{30}$$

The velocity dependence of the phase shift can be minimized to first order by setting the v-proportional term to zero by choosing a roll offset

$$\theta = -\frac{\Omega_E \sin\phi_{lat} v_p}{g}, \tag{31}$$

which yields an improved visibility reduction of

$$\frac{V}{V_0} \approx \left[1 + \left(\frac{4\pi\sigma^2 \Omega_E \sin\phi_{lat} L^2}{dv_0^3}\right)^2\right]^{-1/4}. \tag{32}$$

Both Equation 29 and Equation 32 assume that the velocity spread is small compared to the center velocity, and neglect the small effect of a velocity-dependent visibility amplitude. The degree of compensation is shown in Figure 10 for two choices of velocity spreads, as well as numeric results that do not make the approximations of the analytic expressions. Experimental data illustrating the compensation technique is shown in Chapter 3. Since the gravitational and Coriolis phases have different velocity dependences (v^{-2} vs. v^{-1}), the total phase cannot be made completely velocity independent, but the first order compensation is sufficient for the mean velocities and spreads considered thus far.
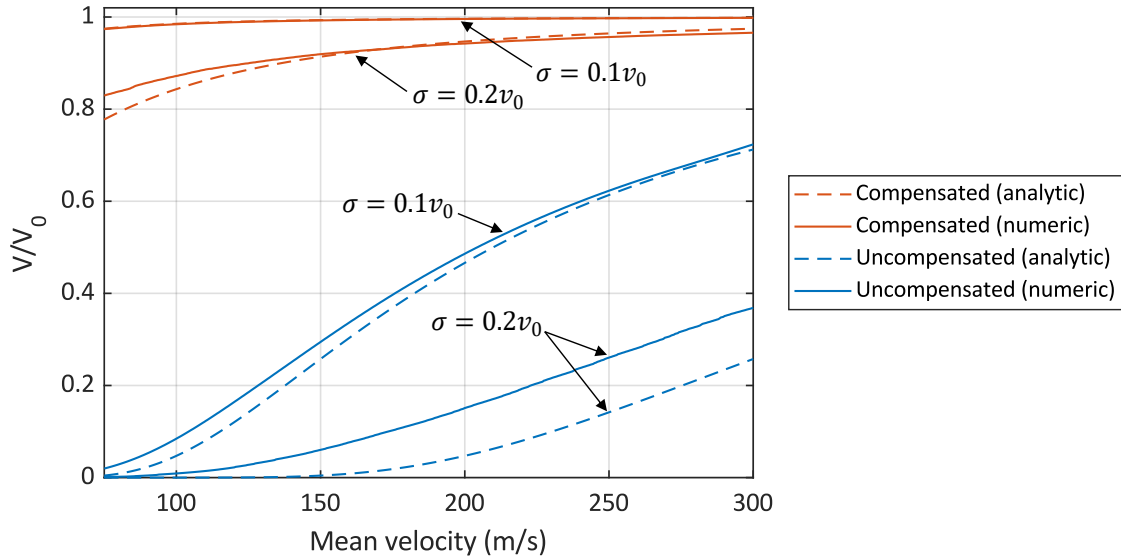
Figure 10: *Effectiveness of the passive Coriolis compensation scheme for two different velocity spreads. The analytic expressions are plotted with the dashed lines, and numeric results with solid lines. In the numeric results the roll angle is optimized for each velocity rather than determined by Equation 31, and the velocity dependence of the KDTLI visibility function is taken into account. Figure adapted from Reference [59].*

2.4.4 Long baseline: decoherence

The long flight time associated with the long baseline of LUMI also means that both thermal and collisional decoherence events become significantly more likely. Which-path information is revealed via the emission of thermal radiation and collisions with residual gas molecules, and the probability of these events increases with flight time. The influence of decoherence events on the interference visibility can be calculated in the Wigner representation, as described in Reference [55]. Experimental tests of thermal [60] and collisional [61] decoherence of C_{70} molecules in a Talbot-Lau interferometer show good agreement with the expected decoherence rates.

The effect of thermal decoherence can be estimated following the treatment of References [55] and [60], with the visibility reduction given by

$$\frac{V}{V_0} = \exp\left[-\int_0^{\frac{2L}{v}} dt \int_0^\infty d\lambda\, R_\lambda\big(\lambda, T(t)\big)\left\{1 - \mathrm{sinc}\left(\frac{2\pi d}{\lambda}\frac{L - |vt - L|}{L_T}\right)\right\}\right], \qquad (33)$$

where R_λ is the spectral photoemission rate of the molecule and T its temperature.
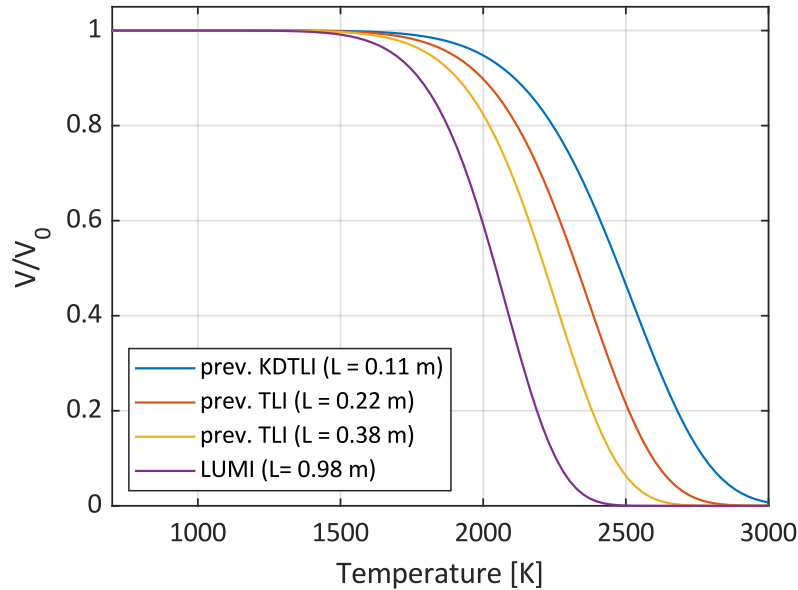
Figure 11: *Thermal decoherence of a 200 m/s C_{70} beam as a function of temperature for four different Talbot-Lau interferometer configurations. While thermal decoherence does not yet reduce interference visibility for C_{70} at typical thermal source temperatures used in LUMI (<1000 K), it may present a challenge for molecules with higher spectral photoemission rates and sources that produce significantly slower beams.*

Using C_{70} as a sample molecule one can compare the decoherence rates between the current experiment with $L = 0.98$ m and previous experiments with shorter baselines of $L = 0.22$ m (TLI with gold gratings [42]), $L = 0.38$ m (longer version of the TLI [60]), and $L = 0.11$ m (previous KDTLI [45]). The TLI experiments had $d = 991$ nm gratings, while the previous KDTLI had $d = 266$ nm gratings, as in the LUMI experiment. The grating period plays a role in the thermal decoherence since the amount of which-path information yielded by an emitted

photon depends on the ratio of the photon wavelength λ and the grating period d, as contained in the sinc term in Equation 33. Assuming a constant temperature of the molecule as it traverses the interferometer, the role of thermal decoherence in the various interferometers is shown in Figure 11.

The effect of collisional decoherence can be estimated following the treatment in Reference [61],

$$\frac{V}{V_0} = \left(\frac{C_6}{\hbar}\right)^{2/5} \frac{v_g^{3/5}}{v} \left(8.4946 + 1.6989 \frac{v^2}{v_g}\right) \tag{34}$$

with v_g the most probable velocity of the background gas and C_6 the van der Waals parameter for the interaction of the gas with the particle. The effect of collisional decoherence for various interferometers is plotted in Figure 12, assuming that N_2 comprises the majority of the residual gas in the vacuum chamber and using a van der Waals parameter of 2.1 meV nm^6 for C_{70} with N_2.
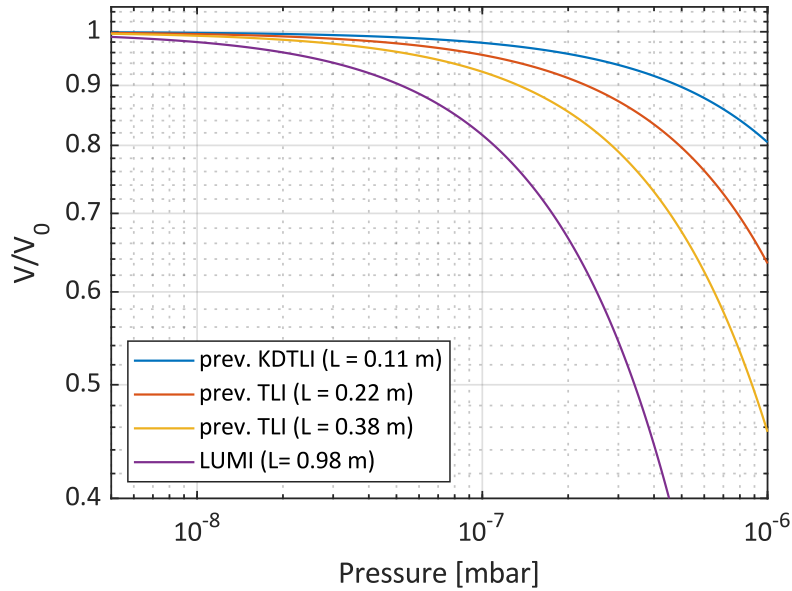
***Figure 12:** Collisional decoherence of a 200 m/s C_{70} beam with a background N_2 gas for four different Talbot-Lau configurations showing the strong dependence on inter-grating separation. The background gas is held at room temperature. Nearly 20% visibility loss occurs already at 10^{-7} mbar at LUMI, making low pressure a stringent criterion for successful interferometry experiments, particularly in the high mass regime where the collisional cross sections are larger.*

Both thermal and collisional decoherence will become more significant challenges for interference on the mass scale of 10^5 u. In the current LUMI configuration such particles would need to have a longitudinal beam velocity below 100 m/s, which represents a 2-3-fold increase in flight time over typical current values. Strategies for mitigating these decoherence effects in the next generation of LUMI are discussed in Chapter 6.

2.4.5 Long-baseline but near-field: a contradiction in terms?

The LUMI experiment operates in an unusual regime for a near-field interferometer. After all, with a two-meter baseline and nearly four meters from end to end, it is perhaps surprising that wavefront curvature continues to play a strong role in the diffraction. The transition to the far-field regime occurs when the propagation distance is large compared to a^2/λ_{dB}, with a the aperture size [62], and the Talbot-Lau effect in particular is visible as long as $L \ll NL_T$, where N is the number of illuminated slits [56]. Since $L \approx nL_T$ for high contrast interference in a TLI, where n is the integer-valued Talbot order, this condition requires that $n < N$. Most interference scans at LUMI are done with no horizontal delimiters in the beamline, such that the beam width is defined only by the source aperture, a 1 mm differential pumping slit located 0.5 m before the first grating, and the horizontal extent of the ionization region. Beam widths at the gratings of more than 1 mm are thus typical, such that over 4000 grating slits are illuminated, placing us safely in the near-field regime for even the highest Talbot orders investigated at LUMI.

When working with fast beams of light atoms or molecules, such as in the experiments with barium and strontium, we were operating near the 100th Talbot order. High visibility is maintained as long as the inter-grating separation is kept equal (and all other relevant alignment criteria satisfied). The velocity spread of the beam is actually beneficial, since it means that the Talbot condition does not need to be strictly adhered to in order to see interference fringes. This can be seen both from Figure 4 and the Talbot carpet simulations shown in Figure 13 in which Equation 5 is solved for a KDTLI configuration as the inter-grating spacing L is symmetrically changed.
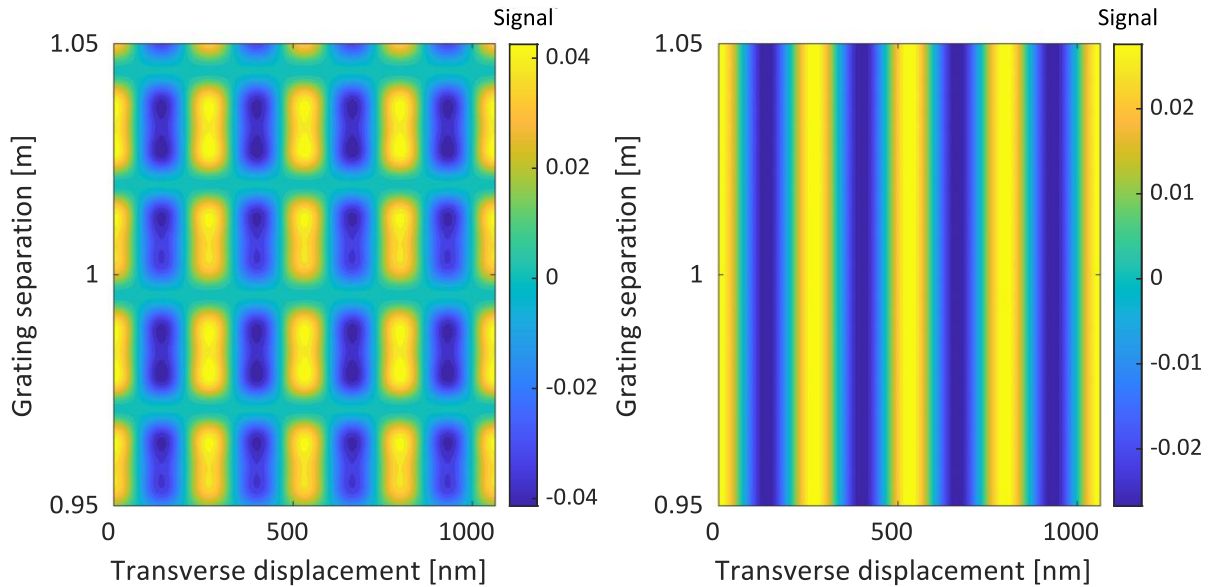
Figure 13: *Simulated longitudinal Talbot carpet for C_{60} as the inter-grating separation of a KDTLI is symmetrically increased.* ***Left:*** *The carpet produced by a monochromatic beam with a velocity of 190 m/s. The visibility of the pattern varies periodically with the Talbot length, which is 2.4 cm in this case.* ***Right:*** *The carpet produced by a beam with a Gaussian velocity distribution centered at 190 m/s with an 8% spread. The effect of velocity-dependent phase shifts such as Coriolis are neglected in these simulations.*

2.5 Collapse models and macroscopicity

The long baseline of LUMI enables interference of the highest mass particles to date, which allows one to directly validate quantum theory in a new regime and thereby restrict the parameter space of alternative models. In the following, a class of wavefunction collapse models and the concept of macroscopicity are introduced.

2.5.1 Continuous spontaneous localization

There exist several interpretations of quantum mechanics which claim to resolve the measurement problem in a self-consistent way, but collapse models are unique in providing a well-studied approach that can be directly tested in the laboratory. This branch of models is also different than other interpretations in that it directly modifies the mathematical framework of quantum mechanics. The first model of this type was proposed in 1986 by Ghiradi, Rimini, and Weber [63], and many variations and refinements have been proposed since then, as reviewed in Reference [64].

The best-studied modern approach is the continuous spontaneous localization (CSL) model [65-67]. The model is defined by a stochastic differential equation that adds two terms to standard quantum mechanics to cause the wavefunction collapse which depend on a coupling constant γ and the mass distribution of the particle [64]. The collapse is typically described by two constants, a rate λ_{CSL} and localization radius r_c, defined according to

$$\lambda_{CSL} = \frac{\gamma}{(4\pi r_c^2)^{3/2}}.$$
(35)

If we consider particles delocalized by more than the localization radius r_c, approximate forms of the effective collapse rate can be derived. For N molecules each composed of n atoms that are separated by less than r_c, the effective collapse rate scales quadratically with n,

$$\Gamma = \lambda_{\text{CSL}} N n^2,$$
(36)

while for particles separated by more than r_c the scaling is linear. The amplification mechanism described by Equation 36 is a key feature of CSL and is what motivates in particular high-mass interferometry experiments at LUMI, since any collapse is expected to scale quadratically with mass in the regime in which we work.

Bounds on the parameters λ and r_c can be placed by observing a superposition of a massive composite particle to persist for a certain time, since collapse to a certain radius is thereby directly excluded on this timescale. An approximate expression for bounds that can be placed on these parameters by Talbot-Lau matter-wave interferometry was derived in Reference [68], in which the visibility reduction due to CSL is written

$$\frac{V_{CSL}}{V} = \exp\left\{-2\lambda_{CSL}\tau \frac{m^2}{m_0^2}\left[1 - \frac{\sqrt{\pi}r_c}{N_T d}\text{erf}\left(\frac{N_T d}{2r_c}\right)\right]\right\},$$
(37)

where N_T is the Talbot order and τ the time spent in the interferometer. If 50% of the expected visibility V is observed in the experiment, then the combination of CSL parameters r_c and λ_{CSL} that would yield $V_{CSL}/V < 0.5$ are excluded. The bounds that are set by the high-mass interferometry experiments at LUMI are given in Chapter 4. An overview of bounds on collapse models due to matter-wave interference experiments can be found in Reference [69] and references therein. In the same work one can find references to bounds placed on CSL by non-interferometric experiments, which mainly look for anomalous heating due to the stochastic noise field or x-ray emission due to the collapse process. While such bounds are currently more restrictive than the best interferometric bounds, it is with the caveat that they are indirect tests that are less robust than interferometric bounds to features of the model such as the characteristics of the noise field [70].

2.5.2 Macroscopicity

A range of measures have been introduced in an attempt to quantify the macroscopicity of a given superposition state [71]. The measure introduced by Nimmrichter and Hornberger in 2013 [72] and further extended in 2019 [73] is used here since it provides a convenient means to directly compare the extent to which different interferometry experiments rule out modifications to quantum mechanics. If one considers a minimal modification to standard quantum mechanics which reproduces classical dynamics for "macroscopic" systems, the macroscopicity μ is defined as

$$\mu = \log_{10}\left(\frac{\tau_e}{1\,s}\right) \approx \log_{10}\left(\left|\frac{1}{\ln f}\right|\left(\frac{m}{m_e}\right)^2 \frac{t}{1\,s}\right). \tag{38}$$

Here, τ_e is the largest excluded time parameter of the modification, indicating that a macroscopicity of 1 is achieved if an electron is held in a superposition for 10 seconds. The approximate expression holds for interference experiments of particles whose spatial extent is smaller than their delocalization, where m is the mass of the interfering particle, m_e the electron mass, and f the fidelity of the interference measurement. The quadratic scaling with mass in the logarithm is a motivation for high-mass interference experiments, and the long-baseline employed by LUMI to perform such experiments yields a second advantage, since there is also a linear scaling with flight time t in the interferometer.

The LUMI experiment currently holds the highest demonstrated value of macroscopicity (see Chapter 4), but atom interference experiments with long interrogation times [74], fountains [6], and planned molecule and cluster interference experiments [75] may achieve even higher values in the future. As noted in the original paper [72], there are still many orders of magnitude which separate the highest macroscopicity values obtainable with such systems and systems which one might consider truly macroscopic, such as a cat. However, important statements about the validity of quantum mechanics can still be made with the experimental techniques currently available.

2.6 Interferometric-assisted metrology

In parallel to the experiments on pushing the mass scale of matter-wave interferometry, a significant effort was made in exploring the metrological capabilities of the LUMI experiment. One should first distinguish between two classes of measurements possible with a matter-wave interferometer. The first, and the one that atom interferometers have successfully employed in a range of precision experiments and applications, is to measure an inertial force like gravity or rotation. A second type of measurement applies a force to the beam in some interaction region, allowing one to extract an atomic or molecular property based on the response of the interference pattern. The following sections discuss the advantages of using matter-wave interferometers for these purposes, along with a brief review on relevant magnetic phenomena and the theoretical framework behind the three types of metrology experiments conducted at LUMI.

2.6.1 Interferometric inertial measurements

There is an inherent advantage in using matter-wave interferometers over light interferometers for inertial measurements due to the larger phase shift of matter-waves subject to a given acceleration. Two common applications are in sensing rotations or a constant acceleration like gravity, and the phase shifts of the fringes in a three-grating interferometer can be easily calculated using Equation 17 [1]. For rotations, the phase shift of a matter-wave interferometer ϕ_{MW} compared to that of a light interferometer, ϕ_L, is given by

$$\left(\frac{\phi_{MW}}{\phi_L}\right)_{Sagnac} = \frac{\lambda_L}{\lambda_{dB}}\left(\frac{c}{v}\right) \tag{39}$$

where it is assumed that the interferometers enclose equal areas, or, equivalently, that $d_L\lambda_{dB} = d_{MW}\lambda_L$ for grating periods $d_{L,MW}$. The ratio of phases can exceed 10 orders of magnitude, with a similarly impressive ratio for a constant acceleration rather than rotation. At first glance it seems that matter-wave interferometers should yield a massive improvement in sensitivity over light interferometers. However, the area enclosed by matter-wave interferometers is typically orders of magnitude less than for light interferometers, and the count rates much lower, so the gain in overall sensitivity is less dramatic.

While the use of atom interferometers for inertial sensing is well justified and has made significant advances in recent years [1], there has been little work on using molecule interferometers for similar measurements. Interferometers like LUMI are indeed sensitive to gravity and rotation, as demonstrated by the Coriolis compensation technique discussed in this chapter and demonstrated in Chapter 3. However, the sensitivity is not competitive with atom interferometers for technical reasons such as the flux and interferometer orientation, as discussed in Chapter 4 in the context of weak equivalence principle tests with molecule interferometers. Likewise, beam-splitting techniques such as large momentum transfer Bloch oscillation beam-splitters [76] which can dramatically increase the enclosed area of an atom interferometer, are not directly applicable to molecule interferometers like LUMI.

2.6.2 Interferometric property measurements

In interferometers with well separated diffracted beams, a constant potential can be applied to one beam to yield a measurable phase shift of the interference pattern, rendering it sensitive to potentials rather than just forces. This feature has been exploited in measurements of topological phases such as the scalar and vector Aharonov-Bohm effects [77,78] and the Aharonov-Casher effect [79]. A similar concept can be used to probe atomic properties, as illustrated by the early measurement of the electric polarizability of sodium atoms in a Mach-Zehnder interferometer [28]. In a TLI setting, where the beams are not well separated, a gradient field is typically employed and the corresponding envelope phase shift measured, in complete analogy to classical beam deflection. However, one gains an advantage in a TLI over classical beam deflection due to the orders-of-magnitude improved spatial resolution obtained by monitoring the phase shift of the interference fringes.

This thesis explores three types of metrology experiments: magnetic and electric deflection in uniform force fields, and contrast revivals in a magnetic field gradient. The various interaction zones within the interferometer for these three experiments are shown in Figure 14. These are used to measure induced magnetic and electric dipole moments as well as permanent magnetic moments. Other properties like optical polarizability α_ω [80] and permanent electric moment [81] can be also measured in similar schemes, the former by measuring the dependence on the optical grating power in a KDTLI and the latter by fitting interference visibility loss as a function of deflection voltage. This thesis focuses on measurements of the static polarizability and particularly on measurements of magnetic properties, since the latter are new in the context of interferometric-assisted deflection measurements. It is also particularly appealing and of practical utility to be able to investigate a broad range of species in the same device, as discussed in more detail in Chapter 5 along with more technical details and results of these metrology experiments.
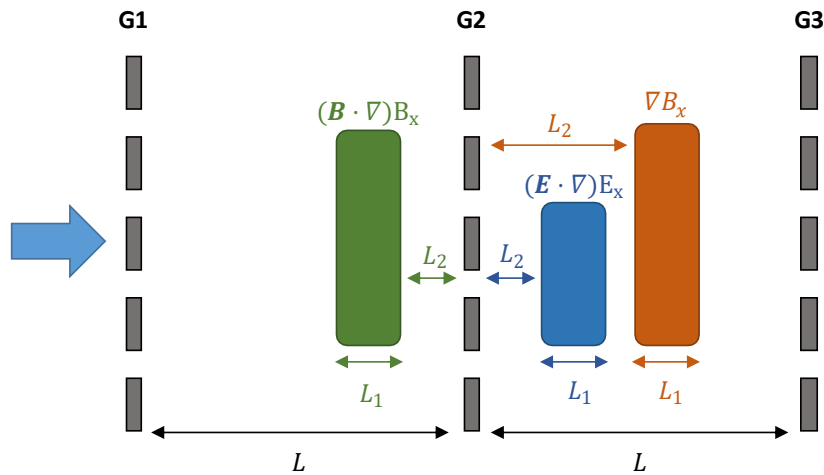
Figure 14: The geometry of the three different metrology experiments in LUMI. The beam enters from the left, with the magnetic deflector (green) positioned in front of the second grating, and the electric deflector (blue) and gradient magnetic field positioned after the second grating. The distances are defined in the same way for each metrology unit, and color-coded for clarity: L_1 is the length of the field region, L_2 is the distance of the nearest edge to

the second grating, and L is the inter-grating spacing. The experiments are discussed separately, so there is no ambiguity regarding the numerical value of a given length.

2.6.3 A few words on magnetism

Before describing the magnetic metrology experiments in LUMI, some theory underlying magnetism in atoms and molecules is briefly discussed, since results presented in this thesis touch on fundamental magnetic phenomena. One should first distinguish between bulk and isolated magnetic phenomena. Ferromagnetism, antiferromagnetism, ferrimagnetism, Pauli paramagnetism, and Landau diamagnetism, while responsible for most of our day-to-day contact with magnetism, are phenomena that are typically emergent in bulk materials. Since the atomic and molecular beams used in these experiments are dilute and the molecules and clusters considered thus far are not large enough to exhibit bulk properties, bulk magnetic phenomena are not observed, and we are left with two dominant forms of magnetism: atomic diamagnetism and atomic paramagnetism.

Diamagnetism, also known as Larmor or Langevin diamagnetism, is caused by the rearrangement of electrons to shield an external magnetic field, and is a fundamental effect present in all atoms and molecules. Paramagnetism is the attraction of a particle to regions of higher magnetic field, typically due to an inherent permanent magnetic moment of the atom or molecule. The permanent moment is due to the angular and spin momenta of the electrons and, to a much smaller extent, the nuclei. The paramagnetic contribution, if it is non-zero, tends to be several orders of magnitude larger than the diamagnetic contribution in typical magnetic fields strengths. However, there is another form of paramagnetism, known as temperature-independent paramagnetism or Van Vleck paramagnetism [82,83], which persists even in the absence of a permanent magnetic moment. Van Vleck paramagnetism is a second order effect which arises due to coupling to low-lying excited states and vanishes in systems such as closed-shell atoms. It is closer in magnitude to diamagnetism and they thus tend to compensate each other, which, for example, is responsible for the small net magnetic susceptibility of C_{60} [84].

To understand the origin of the different forms of magnetism in atoms and molecules, consider the effect of a constant magnetic field $\boldsymbol{B} = B\hat{\boldsymbol{z}}$ on an electron with potential energy U. Working in the Coulomb gauge such that $\nabla \cdot \boldsymbol{A} = 0$, with $\boldsymbol{A}$ the vector potential, gives the Hamiltonian [84]

$$\mathcal{H} = \frac{\boldsymbol{p}_i^2}{2m_e} + U_i + \mu_B B\big(L_{z,i} + g_s S_{z,i}\big) + \frac{e^2 B^2}{8m_e}(x_i^2 + y_i^2), \tag{40}$$

with the spin g-factor of the electron $g_s \approx 2$, and the Bohr magneton $\mu_B = e\hbar/2m_e$. In multi-electron atoms, a summation over the index i is implied. This equation can be divided into three terms, $\mathcal{H} = \mathcal{H}_0 + \mathcal{H}_1 + \mathcal{H}_2$, in which $\mathcal{H}_0$ is the non-magnetic Hamiltonian, $\mathcal{H}_1$ the paramagnetic term, and $\mathcal{H}_2$ the diamagnetic term.

Treating the magnetic terms in the Hamiltonian as a perturbation and applying time-independent perturbation theory (assuming a weak B for simplicity) yields the first and second order corrections to the ground-state energy E_0 as

$$\Delta E_0 = \mu_B B \langle 0|L_{z,i} + g_s S_{z,i}|0\rangle$$
$$+ \mu_B^2 B^2 \sum_{n \neq 0} \frac{|\langle 0|L_{z,i} + g_s S_{z,i}|n\rangle|^2}{E_0^{(0)} - E_n^{(0)}} + \frac{e^2 B^2}{8m_e}\langle 0|x_i^2 + y_i^2|0\rangle. \tag{41}$$

Here, the first term describes the first order paramagnetic contribution, the second term is the second order Van Vleck paramagnetism, and the third term is the diamagnetic contribution. The form of this equation elucidates the connection of Van Vleck paramagnetism to low-lying excited states $|n\rangle$ as well as the dependence of diamagnetism on the electron orbit radius.

One can derive the ground state atomic volume susceptibility $\chi^{(V)}$ in a volume V corresponding to the various terms in Equation 41 via

$$\chi^{(V)} = -\frac{1}{\mu_0 V}\frac{\partial^2 E_0}{\partial H^2}. \tag{42}$$

For an atom with spherical symmetry such that $\langle 0|x_i^2 + y_i^2|0\rangle = \bar{r}_i^2/3$, with $\bar{r}$ the mean squared atomic radius, the diamagnetic volume susceptibility can then be written [84]

$$\chi^{(V)} = -\frac{e^2 \mu_0}{6m_e V} Z\bar{r}^2 \tag{43}$$

with Z the number of electrons in the atom. The magnetization $\boldsymbol{M}$, the dipole moment per volume, is related to the susceptibility via

$$\boldsymbol{M} = \chi^{(V)}\boldsymbol{H}. \tag{44}$$

The volume magnetic susceptibility $\chi^{(V)}$ is unitless, but in this thesis the mass magnetic susceptibility χ (written with no superscript) is typically used. For an atom of mass m the mass susceptibility is defined via $\chi = \chi^{(V)}V/m$ and has units of m^3/kg (SI units used throughout). The use of mass susceptibility is convenient since it allows one to write the expression for the magnetic force without the volume appearing explicitly, as shown in the following section.

In paramagnetic materials the susceptibility, and hence magnetization, are strongly dependent on the temperature and applied magnetic field, while for diamagnetic materials the susceptibility is largely temperature independent. For paramagnetic atoms at finite temperatures the Zeeman split levels will be thermally populated, and the magnetization is given by

$$\boldsymbol{M} = n_m g_J \mu_B \mu_r J \, B_J\left(\frac{g_J \mu_B J\boldsymbol{B}}{k_B T}\right). \tag{45}$$

Here, J is the total electronic angular momentum, g_J the total angular momentum g-factor, n_m the density of the magnetic moments, μ_r the relative magnetic permeability, and $B_J(\xi)$ the Brillouin function

$$B_J(\xi) = \frac{2J+1}{2J} \coth\left(\frac{2J+1}{2J}\xi\right) - \frac{1}{2J}\coth\left(\frac{\xi}{2J}\right). \tag{46}$$

In the limit $\mu B \ll k_B T$ this reduces to Curie's law for the susceptibility

$$\chi^{(V)} = \frac{n_m \mu_r g_J^2 \mu_B^2 J(J+1)}{3k_B T} \equiv \frac{C_{Curie}}{T}. \tag{47}$$

The transition from atomic paramagnetism to a Brillouin function-like response has been observed in metal clusters as a function of temperature [85].

In molecules the picture becomes more complex than in atoms, since the magnetic field also couples to the molecules' rotational degrees of freedom. In molecules with no net nuclear or electronic spin there can still be a small rotational magnetic moment proportional to J [86]. While the magnitude of the rotational moment is typically smaller than a single nuclear magneton μ_N, it may still play a role in magnetic deflection of planar aromatic molecules in the LUMI experiment. More details on the origin of these rotational moments and the experimental implications are discussed in Chapter 5.

2.6.4 Magnetic deflection

A force on a magnetic dipole moment $\boldsymbol{\mu}$ can be written

$$\boldsymbol{F} = (\boldsymbol{\mu} \cdot \nabla)\boldsymbol{B}, \tag{48}$$

which holds equally for a constant permanent moment $\boldsymbol{\mu}_{perm}$ and an induced moment

$$\mu_{ind,j} = \sum_j \frac{m\chi_{ij}}{\mu_0} B_j, \tag{49}$$

with χ_{ij} the mass magnetic susceptibility tensor and m the mass of the particle. The isotropic scalar mass susceptibility is given by

$$\chi = \frac{1}{3}\sum_{ii} \chi_{ii}, \tag{50}$$

which is sufficient when considering magnetic deflection of atoms or symmetric molecules where the diagonalized susceptibility tensor has equal components $\chi_{11} = \chi_{22} = \chi_{33} = \chi$. However, an anisotropic susceptibility or permanent magnetic moment in a molecule may cause it to partially align in an external magnetic field, which, as discussed in Chapter 5, plays a role in molecular deflection experiments at LUMI.

To see that Equation 48 holds for both permanent and induced moments one can start with the expression $\boldsymbol{F} = -\nabla U$, with U the potential energy. A permanent moment in a magnetic field has a potential energy $U = -\boldsymbol{\mu}_{perm} \cdot \boldsymbol{B}$, while in the case of an induced moment the field must do work to induce the moment, giving $U = -(\boldsymbol{\mu}_{ind} \cdot \boldsymbol{B})/2$. Using the vector identity

$$\nabla(\boldsymbol{a} \cdot \boldsymbol{b}) = (\boldsymbol{a} \cdot \nabla)\boldsymbol{b} + (\boldsymbol{b} \cdot \nabla)\boldsymbol{a} + \boldsymbol{a} \times (\nabla \times \boldsymbol{b}) + \boldsymbol{b} \times (\nabla \times \boldsymbol{a}), \tag{51}$$

and noting that $\nabla \times \boldsymbol{B} = 0$ in the absence of currents, one arrives at the form of Equation 48 for both permanent and induced moments.

In our deflection experiments we are primarily concerned with induced magnetic moments, and in what follows it is assumed that the particles possess no permanent magnetic moment. For an isotropic susceptibility χ, the force in the transverse direction is given by

$$F_x = \frac{m(\boldsymbol{B} \cdot \nabla)B_x}{\mu_0}\chi. \tag{52}$$

To observe a deflection with minimal visibility reduction, F_x should be constant along x over the extent of the beam, which requires that $(\boldsymbol{B} \cdot \nabla)B_x$ is constant across the beam. In our setup this is achieved by a modified Halbach array of permanent magnets (see Figure 56) [87]. In general there is also a dependence on the longitudinal position z within the magnet array, i.e. $F_x = F_x(z)$, due to the finite slope of the $(\boldsymbol{B} \cdot \nabla)B_x$ as one approaches the center of the magnet array as well as fringe fields. Immediately after the interaction region the particles are deflected by

$$\Delta \mathrm{x}' = \int_0^{L_1} dz \int_0^z dz' \frac{F_x(z')}{mv^2} \tag{53}$$

and given a transverse velocity kick

$$\Delta v_x' = \int_0^{L_1} dz \frac{F_x(z)}{mv}, \tag{54}$$

where v without a subscript always refers to the longitudinal beam velocity. For the moment an interaction region before the second grating is assumed, but it is straightforward to extend it to the case of an interaction region after the second grating. From the reference frame of the particles, the second grating is shifted by

$$\Delta x_2 = -\Delta x' - \Delta v_x' \frac{L_2}{v} \tag{55}$$

and the third grating by

$$\Delta x_3 = -\Delta x' - \Delta v_x' \frac{(L + L_2)}{v}. \tag{56}$$

Inserting these grating shifts into Equation 17 gives for the deflection of the interference fringes

$$\Delta x = \Delta x' + \Delta v_x' \frac{(L_2 - L)}{v}. \tag{57}$$

In the case of an ideal force that is constant along L_1 and zero elsewhere, this reduces to

$$\Delta x = K \frac{F_x}{mv^2} = \frac{K(\boldsymbol{B} \cdot \nabla)B_x}{\mu_0 v^2} \chi \qquad (58)$$

with

$$K = \pm \left(\frac{L_1^2}{2} + L_1 L_2 - L_1 L \right) \qquad (59)$$

a constant geometry factor with the lengths as defined as in Figure 14. It is positive for an interaction region located before the second grating, as for the magnetic deflection region, and negative for one located after the second grating, as for the electric deflection region described below.

The experimentally observed fringe deflection is the result of an average over the empirical velocity distribution $\rho(v)$, with the averaged pattern given by

$$\bar{A} \cos\left(k(x + \overline{\Delta x})\right) = \int_0^\infty dv \rho(v)\, A \cos\left(k(x + \Delta x)\right) \qquad (60)$$

with $k = 2\pi/d$ and A the amplitude of fringes. This can then be solved for the mean deflection

$$\overline{\Delta x} = \arg\left[\int_0^\infty dv\, A(v)\rho(v)e^{ik\Delta x} \right], \qquad (61)$$

and the reduced sine amplitude

$$\bar{A} = \mathrm{abs}\left[\int_0^\infty dv\, A(v)\rho(v)e^{ik\Delta x} \right], \qquad (62)$$

which are the experimentally accessible parameters. Since phase shifts can typically be measured more precisely than visibilities, and since other features such as inhomogeneity in the $(\boldsymbol{B} \cdot \nabla)B_x$ can contribute to visibility reduction, we use the mean deflection to determine the susceptibility by fitting to Equation 61.

In general, one must also consider the velocity dependence of the amplitudes A. The form of A is determined by the visibility function in Equation 7 for the interferometer scheme used in the experiment. Assuming instead a constant A, as in some previous works [50,88], modifies the extracted atomic/molecular susceptibility on the level of a few percent for typical experimental parameters.

The presence of permanent magnetic moments will in general cause a reduction in interference visibility since if the moments are not aligned with the field they will be deflected in various directions, causing phase averaging of the interference curves. The magnitude of this effect can be estimated using the same formalism as for induced moments by assuming a constant ∇B_x and using the form of F_x for a permanent magnetic moment, $F_x = -\mu_{perm}\nabla B_x$. The various projections of the spin causing the permanent moment must then be averaged over, yielding a reduced visibility [89]. The reduction calculated in this way is a lower bound, since the gradient ∇B_x is not constant in a constant $(\boldsymbol{B} \cdot \nabla)B_x$ field, leading to further reduction due

to spatial averaging in the transverse direction. Permanent magnetic moments on the order of a nuclear magneton are already sufficient to completely dephase the interference fringes in our setup [89].

2.6.5 Electric deflection

Most of the discussion of magnetic deflection in a constant $(\boldsymbol{B} \cdot \nabla)B_x$ field carries over directly to deflection of a polarizable particle in a constant $(\boldsymbol{E} \cdot \nabla)E_x$ field. Interferometric-assisted electric deflection in a TLI/KDTLI setup has already been discussed in several theses [54,90] and publications [50,88,91], so it is treated only briefly here. The required field is provided by a tunable electrode designed for the previous KDTLI experiment [54], as described in Chapter 5 (see Figure 52).

In complete analogy to a magnetic dipole, an electric dipole subject to a constant $(\boldsymbol{E} \cdot \nabla)E_x$ experiences a force

$$F_x = \alpha_0 (\boldsymbol{E} \cdot \nabla)E_x = \alpha_0 K_E V^2, \tag{63}$$

where α_0 is the static polarizability of the particle, K_E a geometry factor for the electrode surface, and V the applied deflection voltage. The second equality follows from the geometry of the electrode [54,92] in which $E_z = (\partial E_i)/\partial z = 0$ and $E_x \approx 0$, and approximating the field as $E_y \approx -V/d_y(x)$ with $d_y(x)$ the vertical separation of the electrode surfaces at a given transverse position.

The deflection of the interference fringes then obeys Equation 57, which for an ideal force field with no fringe fields yields

$$\Delta x = \alpha_0 \frac{K K_E V^2}{m v^2}. \tag{64}$$

The polarizability can be extracted by fitting the observed deflections to Equation 61, with the only difference being the expression for the transverse force F_x. While the value of $(\boldsymbol{B} \cdot \nabla)B_x$ in the expression for magnetic force was directly measured with a Hall probe for the deflection magnet [87], the electrode was calibrated in situ using atomic cesium [91], as described in detail in Chapter 5. As for the magnetic deflection setup, the experiment is designed to probe induced rather than permanent moments, and the presence of a non-aligned permanent electric dipole moment in a constant $(\boldsymbol{E} \cdot \nabla)E_x$ field causes a reduction of interference visibility.

In some molecules considered in this thesis the quantity probed by such electric deflection is not merely the induced static polarizability α_0 but the electric susceptibility χ_{el}, which contains a contribution due to the "floppiness" of the molecule [82],

$$\chi_{el} = \alpha_0 + \frac{\langle d^2 \rangle_T}{3kT} \, , \tag{65}$$

where $\langle d^2 \rangle_T$ is the thermal average of the molecular dipole moment squared. The second term, sometimes called the Van Vleck term, is non-zero if molecular motion introduces a fluctuating

dynamic dipole moment, which can occur even in molecules that are non-polar in the ground state [51].

2.6.6 Interference revivals in a magnetic gradient

In contrast to permanent electric dipole moments, the permanent magnetic moments of atoms and molecules are quantized, as demonstrated by the seminal experiment of Stern and Gerlach [93]. This plays a role in our experiments at LUMI, as can be observed if we apply a constant magnetic gradient ∇B_x inside the interferometer. This is a Stern-Gerlach experiment, with the key difference that instead of directly observing a beam deflection we observe the resulting change in interference visibility. In weak magnetic fields, where the total angular momentum $\boldsymbol{F} = \boldsymbol{I} + \boldsymbol{J}$ is a good quantum number, the energy of each magnetic sublevel m_F is shifted by $\Delta E = \mu_B g_F m_F |\boldsymbol{B}|$, with g_F the hyperfine Landé g-factor and where the $\boldsymbol{B}$ direction defines the quantization axis. Each m_F sublevel will thus experience a constant force

$$\boldsymbol{F} = -\mu_B g_F m_F \nabla |\boldsymbol{B}|, \tag{66}$$

with the transverse component given by

$$F_x = -\mu_B g_F m_F \frac{(\boldsymbol{B} \cdot \nabla) B_x}{|\boldsymbol{B}|} \tag{67}$$

where we have again taken advantage of the property that $\nabla \times \boldsymbol{B} = 0$.

To determine the deflection of the interference fringes due to the gradient we apply Equation 57, where the force is due to a permanent rather than induced magnetic moment and the lengths L_1 and L_2 are as defined for the gradient interaction region as shown in Figure 14.

If a single m_F state is selected and maintained throughout the interferometer, the interference pattern in a constant ∇B_x will be deflected with no visibility loss. However, in an ensemble of spin states one will observe dephasing and periodic rephasing as a function of the applied field. As the gradient is increased, the deflection can equal multiples of the grating period, leading to revivals of the visibility rather than just a monotonic visibility loss as one would observe for a permanent electric dipole in an analogous experiment with an electric field gradient. The observed visibility dependence on the gradient depends on the level structure of the particle being studied, and the details are thus left to Chapter 5.

Unlike the permanent magnet used in the magnetic deflection experiments, anti-Helmholtz coils are used to create a tunable gradient field, which allows us to quantitatively measure permanent magnetic moments by measuring the interference visibility as a function of current. In combination with the good optical access through the center of the coils, this setup will also allow us to probe excited state dynamics.

3 Experimental setup

This chapter outlines the experimental setup and basic experimental protocol of the LUMI experiment. Since the system was designed to be modular and has undergone a series of modifications and additions over the course of this thesis work, focus is placed on the core components of the interferometer and the main experimental protocols for interference experiments. Modifications to the setup and experimental protocols for specific experiments are detailed in Chapter 4 and Chapter 5.

3.1 Overview of vacuum system and experimental setup

The long baseline of the interferometer presents some technical challenges, as outlined in the previous chapter. To avoid collisional decoherence in the interferometer, all experiments must be operated in ultra-high vacuum (UHV) conditions. The long interferometer baseline, and the wish to accommodate the various envisioned metrology experiments, necessitated a large vacuum system, both in length and diameter. The experimental setup is composed of three vacuum chambers separated by gate valves: a source chamber, an interferometer chamber, and a detection chamber, shown schematically in Figure 15.
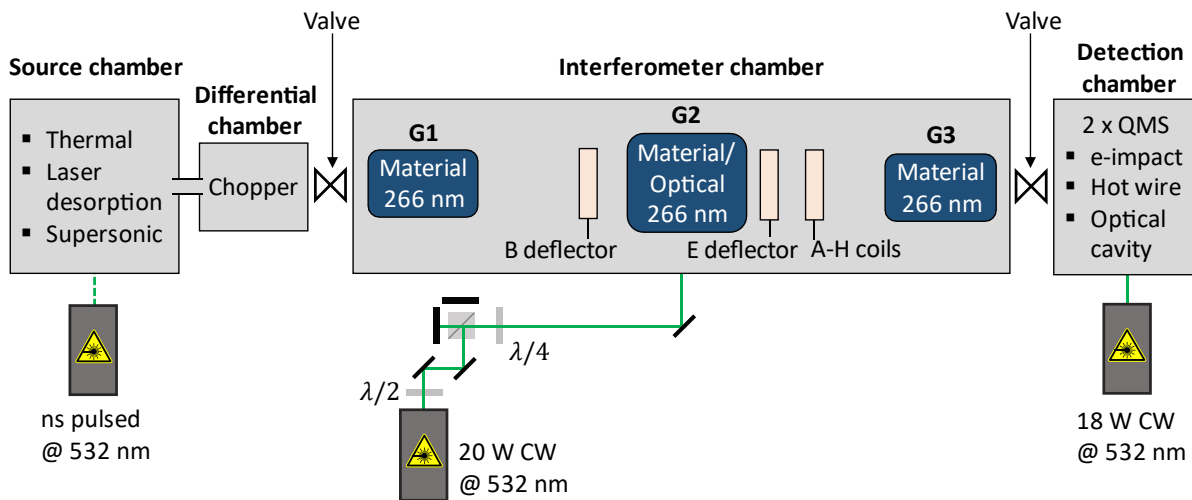
Figure 15: *Schematic of the key elements of the LUMI experiment. Light gray boxes indicate vacuum chambers, with the interferometer chamber separable from the source and detection region via gate valves. Some of the source and detection techniques used are listed to illustrate the modularity. The electric (E) deflector, magnetic (B) deflector, and anti-Helmholtz (A-H) coils are the metrology tools discussed further in Chapter 5. The three gratings (G1, G2, and G3) are discussed in detail below. Three laser systems are also shown: the rightmost provides the input for the thermal ionization cavity used for early fullerene measurements, the center provides the standing light wave which serves as the second grating in the KDTLI scheme, and the leftmost is a pulsed laser used to desorb molecules in the high-mass interference experiments.*

The interferometer chambers were custom designed[2] and are shown in more detail in Figure 16. A rack around the setup houses the miscellaneous electronics required for the experiment, with an integrated crane proving particularly useful for mounting or dismounting the large CF350 flanges or when installing new chambers. Three flow-boxes above the experiment and transparent curtains around the optical table ensure a dust-free environment for the optics and vacuum parts. The vacuum chambers and optics are mounted on a three-part "T"-shaped optical table (TMC Vibration Control/Ametek Ultra Precision Technologies) with cutouts for several of the pumps. The table can be floated for vibrational isolation, which is particularly beneficial in the low frequency range, as discussed later in this chapter.

Figure 16: *A scale drawing of the interferometer chamber with the interferometer suspended inside. The three largest sections house the gratings with various translation stages for inserting vertical and horizontal delimiters also shown. Two turbo pumps and two ion-getter titanium sublimation pumps are attached vertically below the chamber, housed inside cutouts of the optical table. CF350 flanges provide good access to the grating assemblies, and the various other flanges provide ample optical access and room for the various metrological devices, including the electrode, permanent deflection magnet, and anti-Helmholtz coils.*

---

[2] The vacuum chamber design as well as the design of the grating mounts were done primarily by Dr. Philipp Geyer. The chambers were manufactured by Hositrad Vacuum Technology.

Three independent pre-vacuum pumps are located in a neighboring room with their vacuum lines passing through a concrete block to provide vibrational isolation from the vacuum chambers. The interferometer chamber is pumped by two ion-getter titanium sublimation pumps in addition to two 700 l/s turbo-molecular (turbo) pumps. After delivery and assembly of the interferometer chambers, the system was baked out from within for several days via radiative heating from tungsten wire suspended inside the chamber provided with up to 8.5 A. A base pressure of about 2×10^{-9} mbar was achieved, although this varied regularly as various components were installed and removed from the interferometer chamber. Pressure during interference experiments was typically higher, especially when operating a beam source that required a seed gas.

The setup was designed to be modular in anticipation of the need to frequently exchange both sources and detection schemes depending on the atom or molecule being studied. The valves separating the source and detection chambers allow these modifications to be made without breaking the vacuum of the interferometer chamber.

3.2 The gratings

The three gratings are each mounted on a six-axis assembly of slip-stick piezo motors (SmarAct SLC/SR series) that provide control over nearly all translational and rotational degrees of freedom of the gratings. The coordinate system and angles referenced here are defined in Figure 17. The slip-stick mechanism is useful for this application since it allows for a large travel range at high speeds, combined with nanometer-level resolution and reproducibility. An integrated optical encoder gives absolute positional readout resolution of 1 nm for the linear stages and $15\mu°$ for the rotary stages, and a physical reference mark on each motor enables reliable repositioning to absolute positions. This enables rapid repositioning of the gratings to pre-aligned values and makes the system robust to power failure of the motor controllers. The high level of reproducibility is particularly useful during the alignment as well as for phase-sensitive measurements such as the magnetic deflection measurements described in Chapter 5. LabVIEW drivers allow for straightforward interfacing with the motors and encoders.
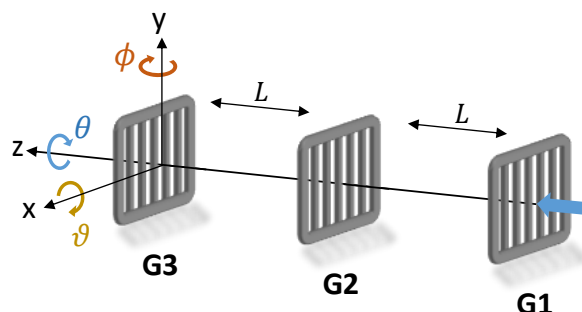
Figure 17: *Definition of the coordinate system and angles used in the context of grating alignment. A pitch ϑ is rotation around the transverse axis (yellow arrow), a yaw ϕ is a rotation around the vertical axis (orange arrow), and a roll θ is a rotation around the longitudinal axis (blue arrow). The longitudinal grating separation L is also shown, and the blue arrow before*

G1 indicates the direction of the beam. Three material gratings are illustrated here, but the same coordinate system is used for a center optical grating when employed.

The first and third grating motor assemblies are identical and are shown in Figure 18. The design includes a longitudinal positioner (123 mm travel range), two transverse positioners (large and small stages with ranges of 49 and 26 mm respectively), a vertical positioner (21 mm travel range), and yaw and roll rotary positioners. Only the pitch angle is not motorized, which does not present an issue since the alignment requirement for this degree of freedom is very lenient. The motors allow for the positioning of the grating in or out of the molecular beam, and precise relative alignment of the gratings to optimize interference contrast, as discussed later in this chapter.
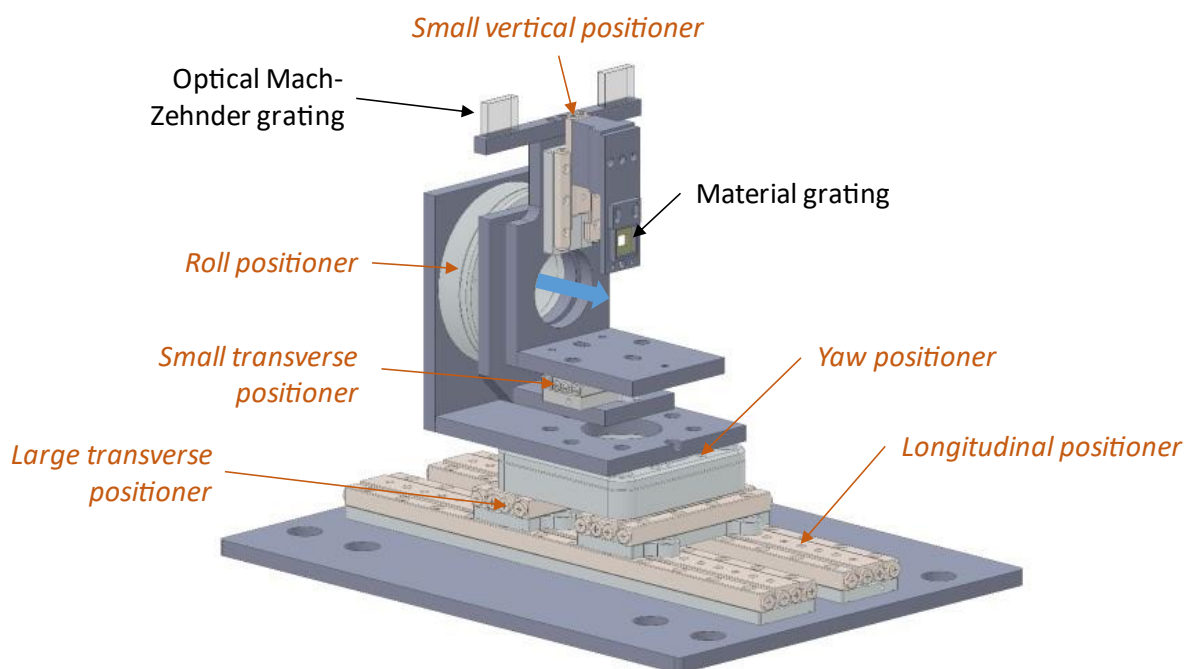

Figure 18: The motor assembly for the material gratings, identical for the first and third gratings. Positioners are shown in beige, and the material grating is mounted at the center of the small yellow square near the middle of the assembly. The assembly includes a long travel range longitudinal positioner, two transverse positioners, a vertical positioner, and yaw and roll rotary positioners. The top "T-piece" holds the gratings used for the optical Mach-Zehnder interferometer which were used for vibrational characterization of the setup. The blue arrow indicates the beamline, with the material grating shown vertically withdrawn from the beam.

The material gratings were fabricated at MIT by Dr. Tim Savas [94] and are from the same fabrication run as the gratings used in the previous KDTLI experiment [54]. A 266 nm grating structure was photolithographically etched into a 3×3 mm region at the center of a 10×10 mm section of a silicon nitride wafer. The grating is 160 ± 10 nm thick and is supported by another grating structure in the orthogonal direction with a period of about 1.5 µm. The periods of two material gratings that were etched from the same wafer as the gratings used in LUMI were independently measured by Ibsen Photonics as 266.209 and 266.203 nm respectively. The sub-Å equality of the period between gratings is an important condition for full interference

visibility, as described later in this chapter. The parameters for the gratings used in LUMI are given in Table 1.

All gratings can be raised completely out of the beamline with the nano-motors, which is a particularly useful feature for beam tests and to extend the lifetime of the first grating which sees the highest molecular flux. Contamination of the first grating is a serious issue, and during the initial alignment phase the grating became almost completely blocked in sections due to the consistent high flux of fullerenes, as shown in the scanning electron microscopy (SEM) images[3] in Figure 19. Interestingly, previously blocked sections of the grating which saw a high flux of cesium would increase in transmission, which the SEM images corroborated. Several tests were made to attempt to non-destructively clean blocked gratings, the most promising of which was plasma-cleaning. However, achieving the correct parameters in vacuum without dismounting the grating and losing the alignment proved challenging. Before the first interference signal was achieved, it was necessary to replace the first grating once; the replaced grating is the one shown in Figure 19. The current first grating also suffers from blockage in sections, but the installation of an additional beam delimiter before the grating and more careful monitoring of its transmission has helped extend its operational lifetime.
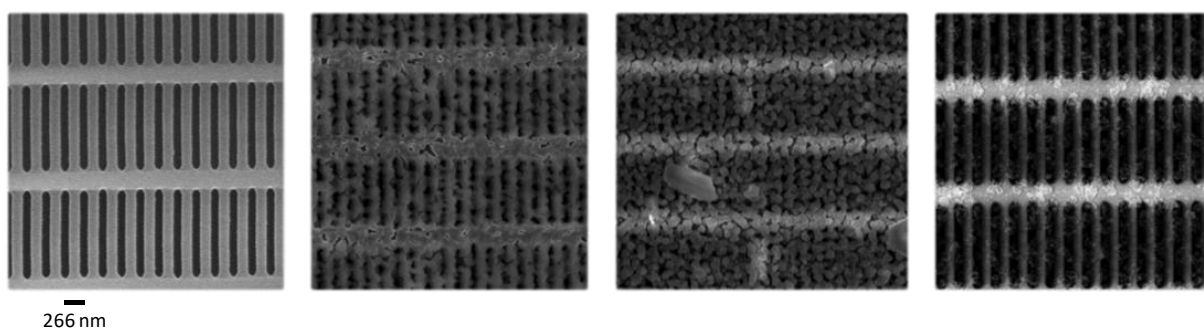
266 nm

Figure 19: *SEM images showing the various degrees of molecular coating of the first grating. **Left:** The grating structure immediately after fabrication. The 266 nm grating is visible along with a 1.5 μm period support structure (horizontal bars). **Middle left and right:** Partially and completely coated sections of the grating after intensive C_{60} flux, respectively. **Right:** Etching of the grating bars, likely a result of a chemical reaction in regions which were exposed to a high cesium flux.*

The optical phase grating is formed by back reflection of a Coherent Verdi V20 532 nm laser. The air-side optical setup is sketched in Figure 15. The beam is focused inside the vacuum chamber with an $f = 10$ cm cylindrical lens onto a 0° high-reflectivity mirror, such that the standing light wave is narrow in the direction of the molecular beam propagation. The focused beam waist of 25 μm is a compromise between reducing the yaw alignment requirement to avoid phase averaging over the standing light wave and maximizing the Rayleigh length. A

---

[3] The left image in Figure 19 was taken by Dr. Lucia Hackermüller at the MIT Nanostructures Laboratory and the others by Stefan Puchegger at the Faculty Center for Nano Structure Research at the University of Vienna.

Rayleigh length of 3.7 mm allows us to work with particle beams greater than 1 mm in width without losing quality of the standing light wave.

The motor assembly for the center grating is different from the two outer gratings, since it has the option to switch between a material and optical grating. It also does not require any longitudinal adjustability since this degree of freedom is covered by the outer gratings. Instead, it has one large transverse positioner (103 mm travel range), an additional vertical "wedge" positioner (63 mm travel range), and the same small transverse, vertical, yaw, and roll positioners as the other assemblies. The high-load vertical positioner can lift the entire assembly to allow LUMI to work with highly parabolic beams. This is necessary for high-mass particles in a horizontal setup in order to stay below the maximal allowed $m \times v$ product for a TLI or KDTLI scheme. The cylindrical lens is connected to the large transverse positioner and the grating mirror to both the large and small transverse positioners, which allows the focus to be adjusted in-vacuum.
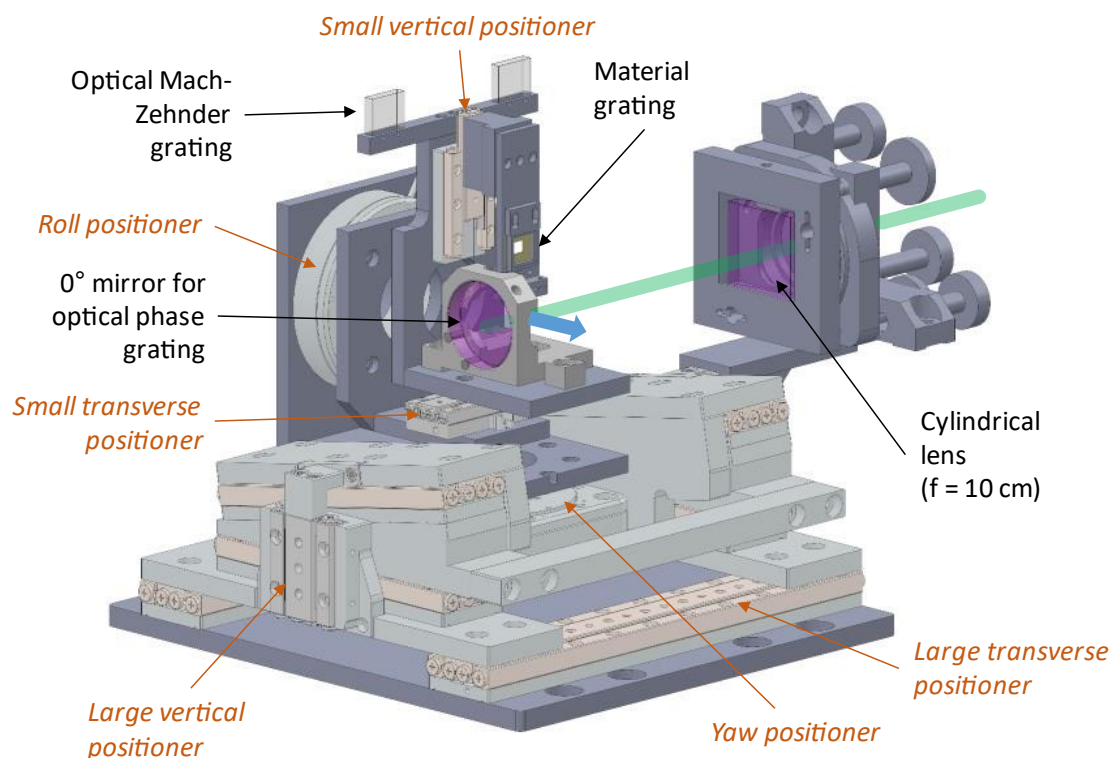
Figure 20: *The center grating assembly. It has the same motional degrees of freedom as the outer gratings, with the exception that the longitudinal stage is replaced with a second, larger range vertical positioner. The longitudinal degree of freedom is satisfied by the outer gratings, and a large vertical range is useful for the second grating to make use of highly parabolic flight paths of the molecules. The blue arrow indicates the beam, shown grazing the mirror where the standing light wave is formed from the cylindrically focused and back-reflected laser beam, shown in green. The material grating is shown vertically withdrawn from the beamline.*

To use the optical grating the material grating is withdrawn from the beam and the laser is vertically adjusted to maximize overlap with the molecular beam. This is done by inserting a block with two crossing orthogonal apertures: one allows the molecular beam to pass, and the other, at the same height, provides a visual reference for the height of the laser. Good overlap

can be obtained by maximizing the molecular flux through the first aperture and then adjusting the laser height to match. This procedure needs to be repeated on a regular basis, since the molecular beam height changes based on the source position and beam velocity. A refined procedure involves optimizing the interference visibility as a function of laser grating height, as described in Chapter 4.

The material gratings were initially clamped in place in the grating mounts, but unusual features in the Littrow reflection during the pre-alignment procedure led us to instead glue them into place to avoid mechanical stress and potential warping of the free-standing gratings. This was done with Torr Seal, a low-outgassing UHV-compatible epoxy.

The experiment is operated primarily via LabVIEW with data analysis performed in MATLAB. A master LabVIEW program controls the interference experiments, and is partly automated, in particular for the fine-alignment procedure and to enable day-long scans which were conducted as a proof-of-principle for dark matter searches with molecule interferometry as discussed in Chapter 4.

| *Grating*	Period [nm]	Open fraction (266 nm)	Open fraction (support structure)
1st grating	266.2	0.43	0.69
2nd grating (material)	266.2	0.41	0.77
2nd grating (optical)	266.1	--	--
3rd grating	266.2	0.43	0.81

Table 1: *Parameters of the material gratings used in the experiments in this thesis. The first grating was exchanged after heavy coating during the initial alignment, and only the current grating parameters are given. The second material grating was typically used only for atomic beams or supersonic molecular beams. All material gratings have a thickness of 160 ± 10 nm. The slight period mismatch between the material and optical gratings is compensated by yawing the material gratings with respect to normal to reduce their effective periods.*

3.3 Vibrational isolation

As discussed in Chapter 2, the long baseline of LUMI makes vibration isolation a key concern. In particular, it needs to be robust to beams of different longitudinal velocities as well as changing environmental noise sources[4]. Several designs were considered and tested, and ultimately a damped pendulum design was employed. The 140 kg interferometer bar which supports the gratings is made of Invar for thermal and mechanical stability. It is suspended via steel wires inside the vacuum chamber and damped with magnetic eddy brakes. The bar is supported from below by the pendulum, and the supporting mount contains alternating layers

---

[4] An extension to the neighboring chemistry faculty building was under construction during the end of the thesis work. Luckily, planned construction on a nearby underground train line was delayed and did not impact the experiments.

of steel stacks, metal springs, and Teflon balls for additional isolation. The key elements of the passive vibrational isolation system are illustrated in Figure 21.
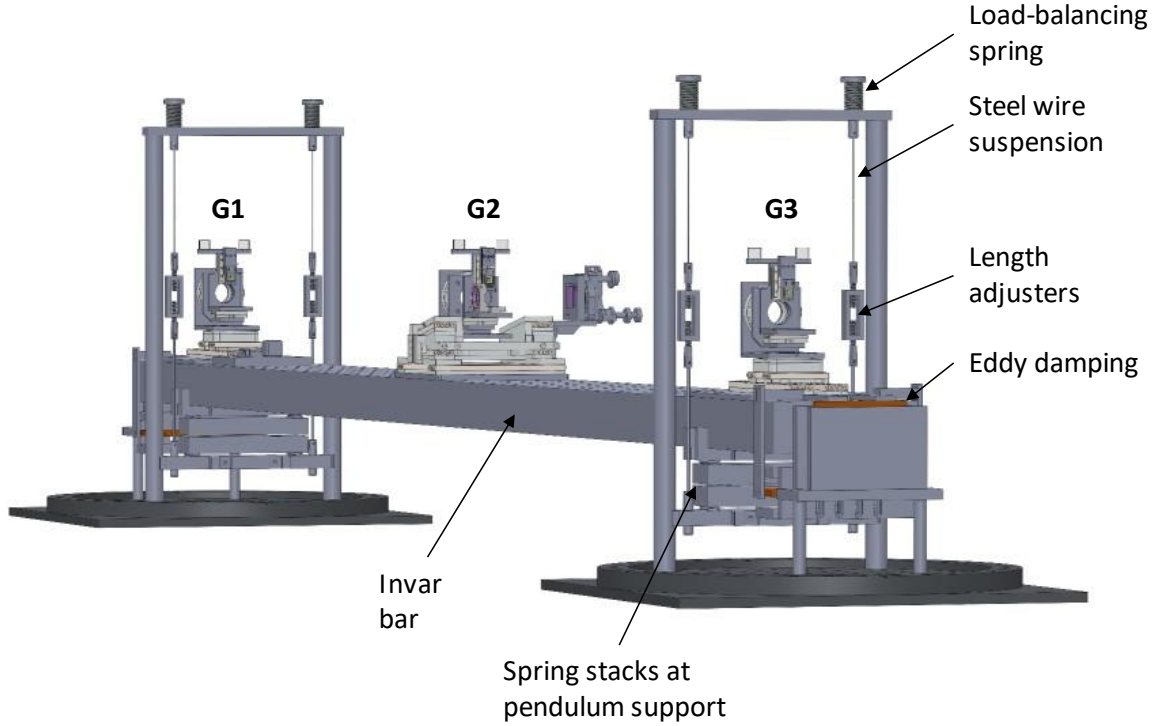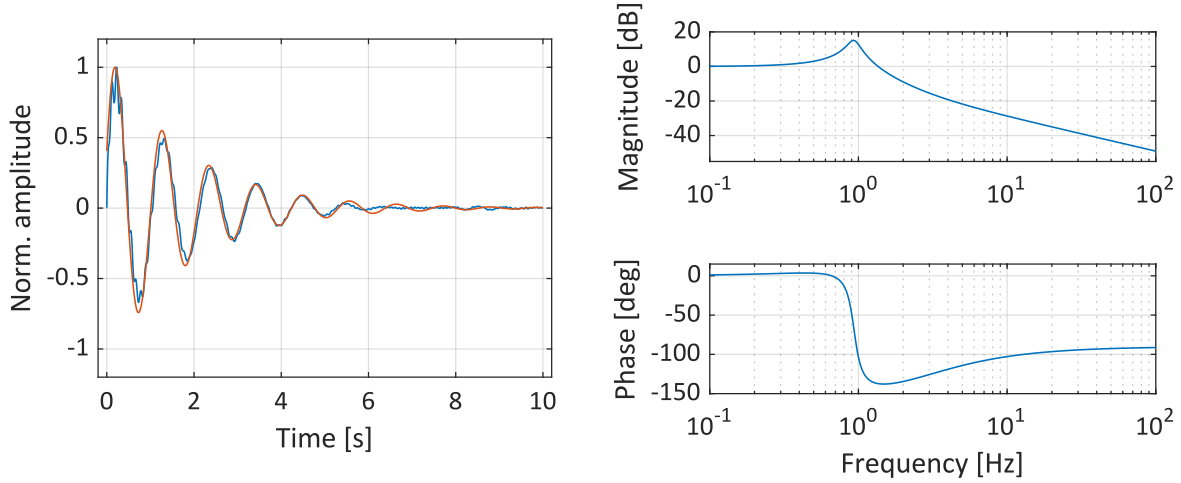

Figure 21: *The suspension system of the interferometer bar. Steel wires with 1.6 mm diameter support the interferometer bar from below, with two wires on either side. Each wire is intersected by a clamping block that can be screwed to adjust the height and tilt of the bar. The wires are connected to a support structure below the bar which consists of alternating steel blocks, metal springs, and Teflon balls for further isolation. The interferometer is only in contact with the vacuum chamber via the wires. Damping is provided by copper blocks mounted to the bar which pass between rows of permanent magnets mounted to the floor of the vacuum chamber. Eddy currents in the copper induced by the relative motion through the magnetic field provide the damping force.*

Although there are several coupled components in the system, the behavior can be described reasonably well by a single damped pendulum with a moving support. The transfer function of such a system is given by the ratio of the Laplace transforms of the output to the input,

$$H(s) = \frac{\mathcal{L}(output)}{\mathcal{L}(input)} = \frac{4\zeta s + \omega_0^2}{s^2 + 2\zeta\omega_0 s + \omega_0^2} \tag{68}$$

for the complex variable s, where $\omega_0 = \sqrt{g/l}$ and ζ is the damping ratio which is inversely proportional to the pendulum mass. The appearance of the damping term in the numerator (usually absent in the case of a viscously air-damped pendulum) is due to the eddy damping mechanism, which enters the equations of motion differently than for a pendulum damped by air resistance. The length of the pendulum can be approximated by the distance from the pivot point to the center of the mass, which is near the center of the Invar bar. The calculated effective length of 28 cm determines the natural frequency $f_0 = 0.9$ Hz, which was confirmed by an

impulse response test in which the pendulum was excited and the ring-down frequency measured with a Michelson interferometer, as shown in Figure 22. The impulse test can also be used to estimate the damping ratio ζ, and the frequency response of the estimated transfer function is given by the Bode plot in Figure 22. The strong suppression in the frequency range above 1 Hz is visible, demonstrating the motivation for the pendulum suspension system. Additionally, the optical table supporting the setup can be pumped, providing additional damping that was particularly effective at low frequencies near the natural frequency of the pendulum.

Figure 22: *Measured impulse response and calculated frequency response of the LUMI suspension system.* ***Left:*** *Transverse displacement of the interferometer bar after pushing the vacuum chamber (and indirectly the pendulum support point), with data in blue and the result of an estimated transfer function in red. The frequency of the oscillations matches that expected for a pendulum of length 28 cm.* ***Right:*** *Bode plot showing the magnitude and phase of the frequency response of the transfer function in Equation 68 with the fitted damping factor.*

Three distinct measurement devices were used to characterize the vibrational characteristics of the setup: accelerometers, a compact Michelson interferometer measuring grating displacements, and an optical Mach-Zehnder interferometer with gratings which are rigidly connected to the mounts of the interferometer gratings. Four high-precision tilt-meters (Applied Geomechanics model 1172) used for tracking the tilt of the optical table and interferometer bar were also employed as vibration sensors but provided comparatively low-quality data due to their poor bandwidth and natural frequency near 1 Hz. The use of independent sensors with different operational mechanisms provided clearer insights into the behavior of the system than relying on a single sensor type alone, allowing us to measure across a wide frequency band and to differentiate common-mode grating motion from independent grating motion.

3.3.1 Accelerometers

Two shear accelerometers were used during the vibration characterization of LUMI. A low-outgassing tri-axial unit (PCB 356M98) mounted on the interferometer bar for use under vacuum, and a uni-axial unit (PCB 393B12) mounted to the optical table outside the vacuum

chamber. The accelerometers have sensitivities of 1 V/g and 10 V/g respectively and were used with low-noise signal conditioners.

Power spectral densities collected for the transverse axis inside and outside the vacuum chamber are shown in Figure 23, with both a floating and non-floating optical table. Although the in-vacuum sensor has a higher noise floor, several key observations can be made. First, floating the optical table has clear benefits at low frequencies, most notably on the table sensor, but also in the reduction of the peaks at 9 and 11 Hz on the interferometer bar. Second, while the turbo pump frequencies at 820 Hz and their harmonics are clearly visible on the table sensors, they are almost entirely suppressed on the interferometer bar, which can be attributed to the high-frequency isolation provided by the pendulum. At low (<50 Hz) frequencies, the noise floor of the sensors mostly dominates the spectrum, although besides for the peaks at 9 and 11 Hz, there is no frequency component above the 10 nm threshold on the bar that can be resolved. However, as low frequencies are more of a concern at LUMI than at previous experiments, this was studied in more detail by the two other sensors types.
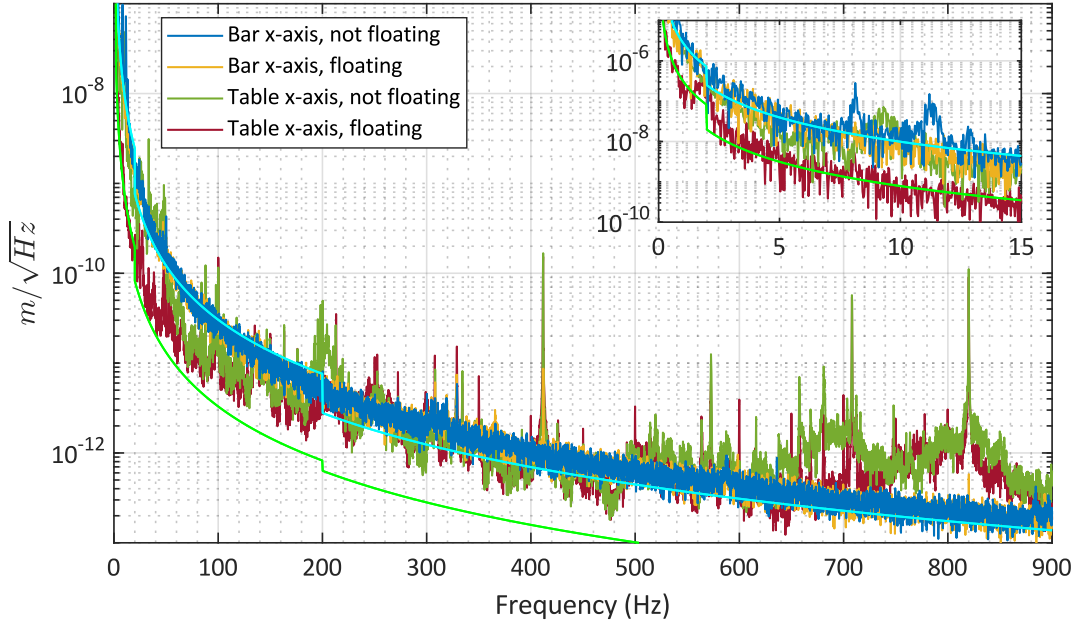
Figure 23: *Square root of the power spectral density of the two accelerometers for the transverse x-axis, with a pumped and un-pumped optical table. The inset shows the low-frequency data. The solid green and cyan curves are the specified noise floors of the uni-axial and tri-axial accelerometers respectively. Peaks at 9 and 11 Hz are visible on the bar only when the table is un-pumped. Higher frequency peaks such as turbo pumps are clearly resolved on the table and significantly reduced inside the chamber. The main plot is smoothed with a 10-bin running average to help identify the various curves, while the low-frequency data is left unsmoothed.*
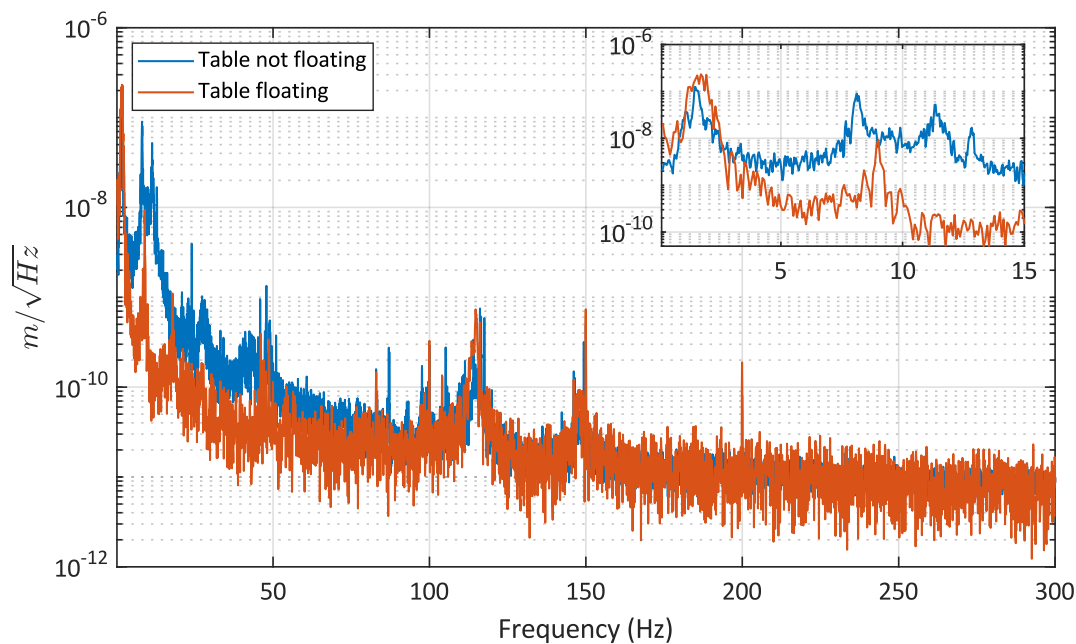
3.3.2 Optical Michelson interferometer

A compact commercial Michelson interferometer (SmarAct PicoScale) was used to measure grating displacements. It works by reflecting an infrared beam from a target surface and

recombining it with a reference beam in a beam splitter integrated on the unit head, yielding displacement information with 1 pm resolution. In our setup, silicon chips attached to the side of the grating mounts serve as the target surfaces.

Such a sensor is convenient since, unlike the accelerometers, it directly yields displacement information. However, it has two drawbacks in our setup. First, since the sensor head is mounted rigidly to the table it is difficult to discriminate table vibrations from motion of the grating mount. Second, operating through a vacuum viewport and at long distances (about 25 cm) led to a weak and sometimes unstable signal.

Sample data obtained with the PicoScale sensor for the first grating, with both a floating and non-floating table is shown in Figure 24. The displacement noise floor at low frequencies was a significant improvement over the in-vacuum accelerometer, and largely corroborated the accelerometer measurements with the only new significant peak observed at about 1.6 Hz. This can be attributed to noise transmitted to the sensor head itself, since extensive testing proved this peak to also be visible on the optical table and can thus not be attributed exclusively to motion of the gratings themselves.


Figure 24: *The spectrum from the commercial PicoScale Michelson interferometer reflected from a reflective section of the mount of the first grating. There is a clear difference when the optical table is floating vs. not floating, seen in both the full spectrum and the low-frequency data (inset). Because the measurement was referenced to the table, it is likely that the improvement is largely due to suppressed vibrations on the table itself rather than on the suspended interferometer bar, as suggested by the accelerometer data. All data is left unsmoothed.*

3.3.3 Optical Mach-Zehnder

An optical Mach-Zehnder was built with a frequency stabilized He-Ne laser (Melles Griot 25-STP-912) and three blazed transmission gratings (80 lines per mm, 25% intensity into the 0th

and $\pm 1^{st}$ orders respectively) mounted rigidly to the interferometer grating mounts, similar to the design employed by Reference [95], and as shown schematically in Figure 25. This sensor was particularly useful for measuring independent grating vibrations, since it is insensitive to common-mode vibrations, which can be seen by setting $v \to \infty$ in Equation 23 and Equation 25.
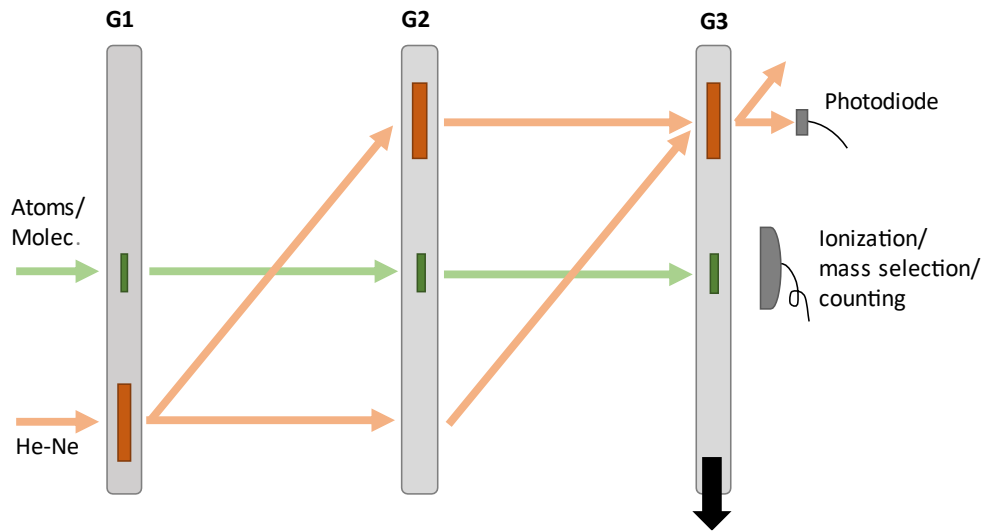

Figure 25: *Top-down view of the optical Mach-Zehnder in parallel with the molecule interferometer. The grey rectangles indicate the grating mounts, which support both the Mach-Zehnder 12.5 µm period gratings, shown in orange, and the matter-wave 266 nm period gratings, shown in green.*

A vibration spectrum from the custom-built Mach-Zehnder is shown in Figure 26, for both a floating and non-floating optical table. Disregarding the electronic 50 Hz peak and its harmonics, the next largest peaks of potential concern are the sub-2 Hz peak also visible with the Picoscale sensor and a peak at 86 Hz that was not as significant in either of the other sensor measurements. While this peak was initially attributed to a resonance specific to the Mach-Zehnder geometry, testing the response of C_{60} interference with a speaker and frequency generator showed a distinct visibility loss at this frequency, indicating that it is indeed an eigenfrequency of the interferometer.

Scanning the third grating transversely produces sinusoidal intensity fringes with the period of the Mach-Zehnder gratings, as shown in Figure 27. The SmarAct motor's slip-stick mechanism is clearly visible and leads to a slight effective miscalibration for closed loop motions between slip positions. Since the period in a TLI/KDTLI is determined by the grating periods, which are known on the sub-nanometer level, the transverse position could be recalibrated to the expected periodicity for measurements where the absolute period is important, such as in electric and magnetic deflection. Scanning over multiple slip positions during a matter-wave interference measurement confirmed the expected 266 nm periodicity, in an analogous way as the 12.5 µm Mach Zehnder period is reproduced over several slip positions as shown in Figure 27.
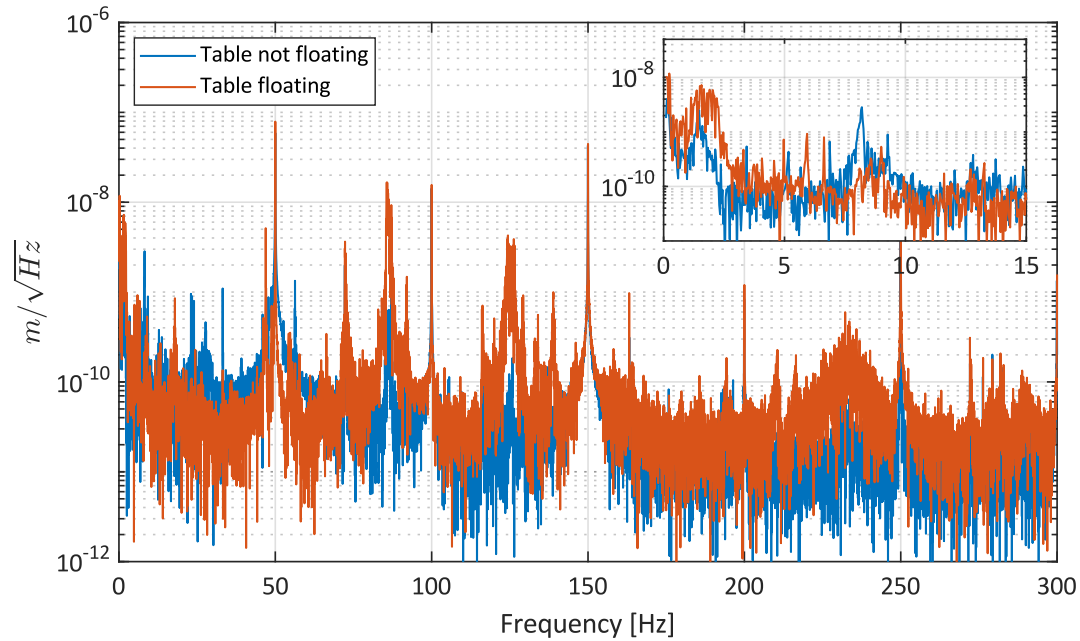
Figure 26: *Square root of a power spectral density of the optical Mach-Zehnder mounted in parallel with the LUMI grating mounts. This sensor is mostly sensitive to independent motion of the grating mounts rather than common-mode motion. Electronic noise at 50 Hz and its harmonics contaminates the spectrum, but if this is neglected the only new feature is the peak at 86 Hz, which was later shown to be a real eigenfrequency of the system. All data is left unsmoothed.*
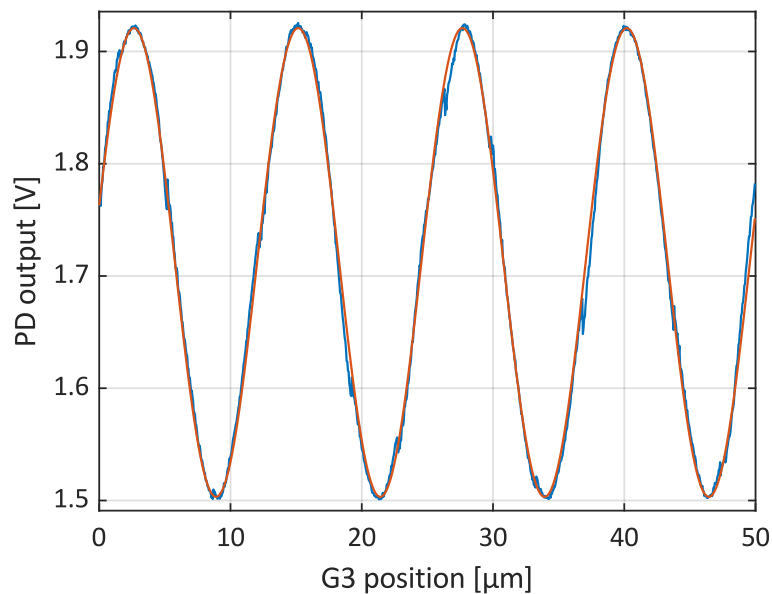

Figure 27: *Photodiode signal (blue) and sine fit (red) of the optical Mach-Zehnder produced by transversely scanning the third grating in closed loop steps of 50 nm. The "spikes" in the blue signal that occur every few µm are due to the SmarAct motor's slip-stick mechanism. While the encoder position is correct over several periods (the fit period of the sine is the expected 12.5 µm), a slight miscalibration is observed between slip positions where it appears that the same closed loop motion catches up to the fitted sine curve. This is also visible in TLI/KDTLI*

interference data as a motor-dependent discrepancy of about 10 nm from a 266 nm periodicity, which could be recalibrated to the known grating periods.

3.4 Beam sources

One of the largest experimental hurdles in molecule interference experiments is the preparation of a sufficiently intense neutral beam in vacuum. This necessitates the use of various beam sources tuned to the needs of the experiment, of which several were developed and tested in-house. Some examples of beam sources used at LUMI are illustrated in Figure 28.
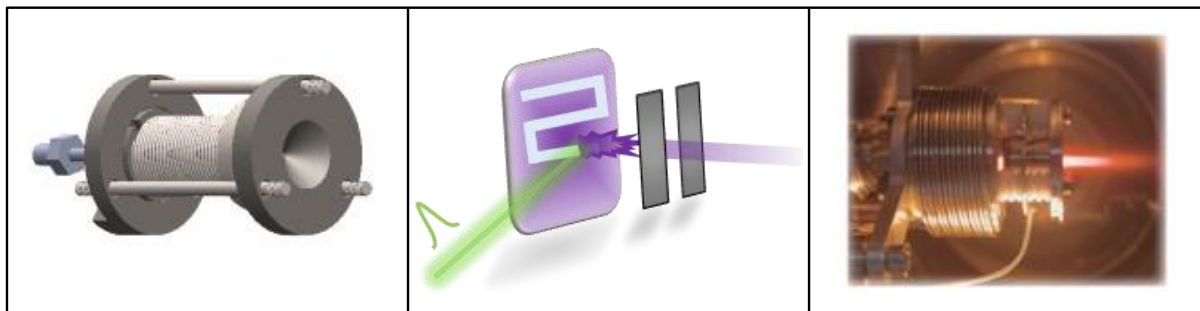
*Figure 28: Various sources used in the LUMI experiment. **Left panel:** This Knudsen cell, or oven, can be heated to 1000 K, contains a gas feedthrough and a 200 µm circular aperture, enabling us to work with continuous supersonic fullerene beams. The basic design is common to most ovens used at LUMI, in which a capsule containing the molecules is wrapped with resistive heating wire and the temperature is measured via a thermocouple element in the oven body. **Middle panel:** Illustration of a nanosecond pulsed laser desorption scheme as used for the high-mass oligoporphyrin experiments described in Chapter 4. Molecules are coated on a glass slide that is scanned in a raster pattern to continually expose fresh molecules to the desorption laser. **Right panel:** Image of an Even-Lavie valve, similar to the one used in LUMI, emitting a beam of excited neon (image by U. Even, Creative Commons Attribution License). Such valves are used to create pulsed supersonic beams.*

3.4.1 Thermal sources

The simplest approach to create a beam of atoms or thermally stable molecules is to sublimate them in a Knudsen cell, or oven. This is just a heated container with a small orifice to allow particles to escape effusively with their angular distribution given by a cosine of the emergence angle. The velocity distribution for particles with mass m at a temperature T is then given by a modified Maxwell-Boltzmann distribution

$$\rho(v) \propto \left(\frac{m}{kT}\right)^{\frac{3}{2}} v^3 \exp\left[-\frac{mv^2}{kT}\right] \tag{69}$$

where the additional factor of v arises since the probability for the particle to escape through the orifice is proportional to its forward velocity. The broad velocity spread can be reduced by various means as discussed later in this chapter, but it is usually not problematic due to the wide de Broglie wavelength acceptance range of the KDTLI scheme. A thermal source was used for most experiments with fullerenes, alkaline-earth atoms, and functionalized tripeptides.

A modified oven for cesium was built and tested already during the initial alignment of the interferometer, and was used for calibration of the electric deflectometer as well as the anti-Helmholtz coils, as described in Chapter 5. The oven is a steel canister wrapped in heating wire that was loaded with cesium in an argon environment. In place of a circular or rectangular aperture in the oven cap as in the more conventional ovens used at LUMI, a hypodermic needle with an inner diameter of 340 µm was implemented to provide a more collimated flux and more efficient usage of the cesium. Initial difficulties with clogging were solved by heating the nozzle to a significantly higher temperature than the oven body, and under the right parameters the source provided an intense, stable, and long-lived signal.

3.4.2 Supersonic sources

It is sometimes beneficial to work with supersonic beams to decrease the velocity spread compared to thermal beams and/or to reduce the interaction time of the molecules in a fixed external field. This was the case for the magnetic deflection experiments with small hydrocarbons described in Chapter 5. For this purpose, we used a heated Even-Lavie valve which creates 20-30 µs long supersonic pulses of molecules carried by a seed gas at repetition rates up to 1 kHz. Such a source was used in combination with a skimmer to aid in beam formation and provide additional differential pumping. The choice of seed gas in combination with its backing pressure determines the beam velocity, where for noble gases with no velocity slip one can expect a velocity boost of $v = 1.6 v_{MB}$, where v_{MB} is the most probable thermal velocity of the gas. The temperature of the expanding beam will typically be lower than the nozzle temperature by an amount dependent on the Mach number, the ratio of the beam velocity to the local speed of sound [96]. The heated valve, which was modified to additionally heat the sample container [97], allows us to work with molecules with low vapor pressures.

A continuous supersonic oven was also built for similar experiments with fullerenes to circumvent the temperature limit of the Even-Lavie valve (E.L-7-4-2015-HRR) [98] which was limited to 575 K due to internal Kapton insulation and sealings. The continuous seeded source was based on a conventional oven, with the modifications of a gas feedthrough and a small pinhole orifice. The disadvantage of such a source is the high gas load on the first pumping stage in the source chamber, although it was manageable with a sufficiently small source orifice and two differential pumping stages. Characterization data for this beam source is shown in Chapter 5.

3.4.3 Laser desorption

For large organic molecules, thermal evaporation is typically not a viable option due to competing fragmentation processes. Nanosecond to femtosecond pulsed laser desorption from a molecule-coated surface can then be a preferable option since it has been shown to be a softer desorption mechanism for organic molecules [99,100]. Nanosecond laser desorption was employed for the high-mass oligoporhpyrin experiments, with more details of the scheme given in Chapter 4. Such a desorption scheme is similar to matrix-assisted laser desorption/ionization

(MALDI), although at LUMI the molecules were desorbed without a matrix, and we are generally only interested in the neutral, rather than charged, desorbed molecules.

3.5 Detection schemes

As with the beam sources, the detection scheme is frequently modified to suit the particle used in a particular experiment. In all of the detection schemes employed so far at LUMI, the particles are ionized and accelerated onto a high-voltage dynode which emits a shower of secondary electrons that an electron multiplier (Detech 402A-H) converts into a measurable pulse. Mass selection is typically necessary to avoid a detector dark rate, since the ionization process will often produce ions uncorrelated with the beam. This dark rate can be due to the ionization of background gases like nitrogen or water vapor, or it can be produced by the ionization mechanism itself, such as outgassing of alkalis and alkaline-earth atoms from a Langmuir-Taylor detector. Mass selection is always required when the beam is not pure, which is often the case when working with fragile biomolecules which tend to fragment during volatilization. When working with pure beams and low-dark-count ionization schemes, mass selection is not necessary at all, for example when working with fullerenes thermally ionized in an optical cavity.

However, the ionization mechanism and the mass selection mechanism, if employed, must be adapted to the experiment. The following sections describe various mass selection mechanisms as well as alternative ionization schemes that were used at LUMI when electron bombardment proved insufficient. Discussion of other detection schemes planned for future experiments are discussed in Chapter 6.

3.5.1 Mass selection

For mass selection of the beam in LUMI we employ a quadrupole mass spectrometer (QMS). In a QMS, ions are sent between four parallel metal poles, with each opposing pair supplied equal but opposite radiofrequency (RF) and constant voltage (DC) offsets. The dynamics of the ions in such a system are described by the Mathieu differential equation, the solution of which shows that only ions of a given m/z ratio undergo stable oscillations between the four poles while the rest are ejected from the beam. The mass resolution of a QMS is a function of the chosen ratio of the DC to RF fields, the RF frequency, and the geometry of the poles. High resolution typically comes at the cost of reduced transmission through the filter, and for many experiments it is sufficient to work with low resolution when working with pure beams where the main purpose of the QMS is to filter out low-mass particles which would otherwise contribute to the dark rate.

The workhorse detection scheme at LUMI employs an Extrel MAX-4000HT QMS with ionization provided by electron bombardment and ion counting with a dynode-Channeltron assembly. In place of the built-in 5 kV dynode power supply we use a Bertan high voltage supply capable of providing up to 10 kV to the dynode, which gives an improved conversion efficiency when working with high mass particles. With the standard 19 mm diameter

quadrupole rods and 440 kHz RF frequency, this scheme is suitable for masses up to 4000 u. Such a commercial device offers high resolution, and electron impact ionization is a rather universal, if inefficient, ionization mechanism.

For the high-mass interference experiments described in Chapter 4, a different quadrupole was necessary, since even upon substitution of the 19 mm poles with 9.5 mm poles, the Extrel QMS system cannot resolve masses beyond 16,000 u. To detect higher masses, a quadrupole mass filter (QMF) from Oxford Applied Research (QMF200) was fitted with an electron impact ionization stage and ion guiding lenses from an older Extrel QMS. A shielded dynode-electron multiplier assembly was added behind the quadrupole for ion counting. This custom-assembled detector was interfaced with a custom LabVIEW program which directly controlled the DC and RF fields applied to the poles, with the latter tunable in frequency from 3 to 100 kHz.

Finally, for source tests a time-of-flight (TOF) mass spectrometer was sometimes also used, but until now has not been connected to the LUMI experiment. The mass selection mechanism relies on a high post-acceleration voltage (16 kV in the system used) to sort the ions by time, with the lighter ions arriving at the end of the drift length faster than the heavier ions. Unlike a QMS which is tuned to a particular mass, each measurement in the TOF mass spectrometer yields a mass spectrum, in which the resolution is mostly determined by the post-acceleration voltage. The TOF mass spectrometer is a pulsed detection scheme with the electronics supporting a repetition rate of 70 kHz, though in practice the duty cycle is limited by the ionization laser, typically a fluorine excimer laser with a maximum repetition rate of 250 Hz.

3.5.2 Langmuir-Taylor ionization

For experiments with alkali and alkaline-earth elements such as cesium, barium, and strontium, Langmuir-Taylor or "hot-wire" surface ionization was used instead of electron bombardment due to its higher ionization efficiency. When an atom lands on a metal surface with a high work function, it is likely to donate an electron, and, if the surface is sufficiently hot, rapidly desorb as an ion. The ionization probability in the case when the atoms thermally equilibrate with the surface is determined by the Saha-Langmuir equation, which gives the rate of ions s^+ and neutrals s^0 leaving the surface [101] as

$$\frac{s^+}{s^0} \propto e^{\left(\frac{\Phi - I}{kT}\right)},$$
(70)

where Φ is the work function of the metal surface, I is the atom's ionization energy, and T is the surface temperature.

The atoms adsorb to the metal surface for a residence time τ before flying off as ions [102], given by

$$\tau = \tau_0 \exp\left(\frac{E_{ads}}{k_B T}\right)$$
(71)

where E_{ads} is the adsorption energy and the pre-factor τ_0 can range from 10^{-17} to 10^{-13} seconds depending on the mobility of the ions on the metal surface. This yields residence times which can range from microseconds to seconds depending on the atomic species, wire properties, and temperature.

After initial tests with tungsten and iridium wires, Langmuir-Taylor ionization was eventually incorporated at LUMI with a resistively heated rhenium wire supported inside an electrostatic lens placed several centimeters in front of the quadrupole entrance lens. Rhenium is well-suited since its work function of 4.72 eV [103] yields a high ionization efficiency. This setup was used for the cesium measurements as well as the magnetic deflection measurements with barium and strontium described in Chapter 5.

The residence time of alkaline-earth elements on hot rhenium surfaces is particularly long [102], and can introduce a significant systematic error into time-of-flight measurements. The origin of the long residence time of alkaline-earth elements may be due to their increased reactivity with the surface after losing one valence electron. Several techniques were tested to compensate this effect. There was some limited success in reducing the residence time by applying ultraviolet light to the hot-wire surface, motivated by the light-induced atomic desorption technique used by the Bose-Einstein condensate (BEC) community for increasing the background alkali vapor pressure and the number of trapped atoms [104]. However, we found that the most effective approach was heating the wire to sufficiently high temperatures such that the residence time had a negligible impact on the time-of-flight spectra. This was confirmed by showing the convergence of the velocity spectra as a function of wire temperature, as demonstrated in Figure 29 for barium and strontium atoms.
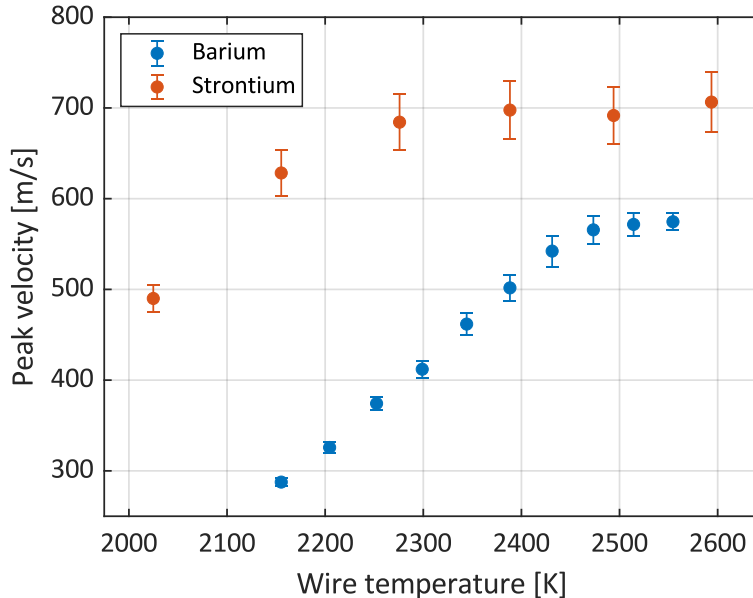

Figure 29: *Convergence of the measured peak velocities as a function of the rhenium wire current for barium (blue) and strontium (red). Temperature is calculated from the wire current using Equation 72 and error bars are from 68% confidence intervals of the velocity calibration. Figure adapted from Reference [89].*

Knowing the resistivity $\rho(T)$ and emissivity $\epsilon(T)$ of the wire allows one to determine the temperature from the current by equating the dissipated electrical power per unit length to the radiated power per unit length,

$$\frac{\rho(T)I^2}{\pi r(T)^2} = \epsilon(T)\sigma T^4 2\pi r(T), \tag{72}$$

in which σ is the Stefan-Boltzmann constant and $r(T)$ the wire radius, with the temperature dependence arising due to thermal expansion. Temperatures determined using this equation roughly agreed with optical pyrometer measurements, which had significant uncertainty due to the wire filling only a small portion of the field of view. Wire temperatures in excess of 2500 K were used for the time-of-flight measurements with barium and strontium, corresponding to residence times of order 100 µs or less according to Equation 71. These high temperatures were another motivation for choosing rhenium with its melting point of 3459 K; several earlier tests with iridium wires failed when the wire melted.
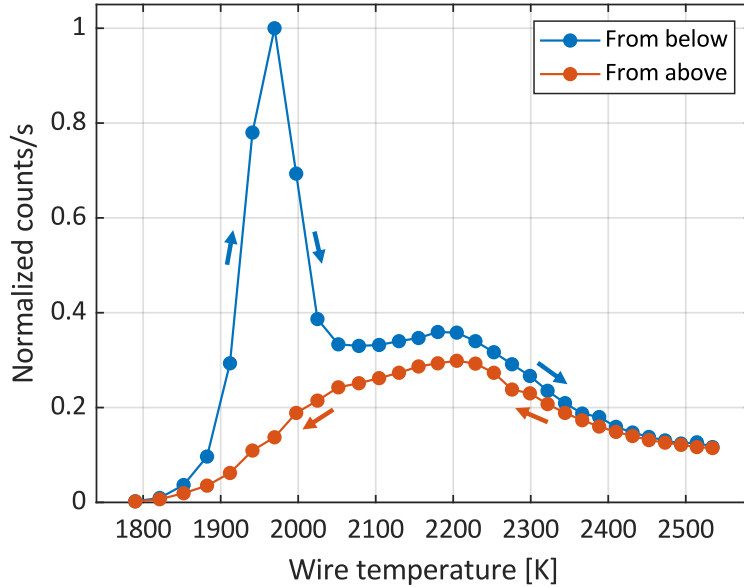
Figure 30: *Hysteresis of barium flux on a rhenium wire as a function of temperature. Temperature is calculated from the wire current using Equation 72. An older setup in which the wire was suspended inside the ionization region of the QMS was used for these measurements.*

Alkaline-earth elements also exhibited a hysteresis in the beam flux as a function of wire current, as shown in Figure 30. When the flux was measured as a function of increasing wire current, a strong peak appeared at about 1950 K, which was absent when the flux was collected as a function of decreasing current. An interpretation consistent with this behavior is that at low temperatures the wire became coated in atoms at a higher rate than they are desorbed, leading to a rapid increase in signal when temperatures are reached that are sufficient to desorb both the accumulated layer and the beam itself. A positive bias applied to the wire may affect the onset of this feature, as well as the residence time, by repelling the positive ions from the surface

[105]. The temperature dependence of the surface ionization mechanism is also strongly dependent on the surface chemistry, in particular the formation of oxides on the wire surface [102].

The flux also displayed high-amplitude spikes that were seemingly uncorrelated with the typical outgassing of low-mass alkalis at high temperatures. They increased in frequency at high temperatures, which introduced noise into the time-of-flight measurements. Interference measurements were performed at wire temperatures below 2100 K both to avoid the frequent spikes and to gain in signal.

### 3.5.3 Thermal ionization in an optical cavity

An optical cavity for thermal ionization of fullerenes was used during the initial alignment stage and the polarizability measurements described in Chapter 5. Thermal ionization in this scheme was more efficient than electron impact ionization, with the additional benefit that the small cavity beam waist functioned as a vertical delimiter, which helped to reduce the velocity spread of the detected beam. Several versions of the cavity were designed and tested. An early aluminum version was mounted directly on the Extrel QMS, while later steel and then Invar versions contained ion optics to directly guide the ions onto a dynode-Channeltron assembly without mass selection. The Invar version was the one used for the initial alignment of the interferometer with C_{60} and the fullerene deflection experiments. No mass selection was necessary in these experiments due to the purity of the fullerene source material and the negligible dark count rate with such a scheme.
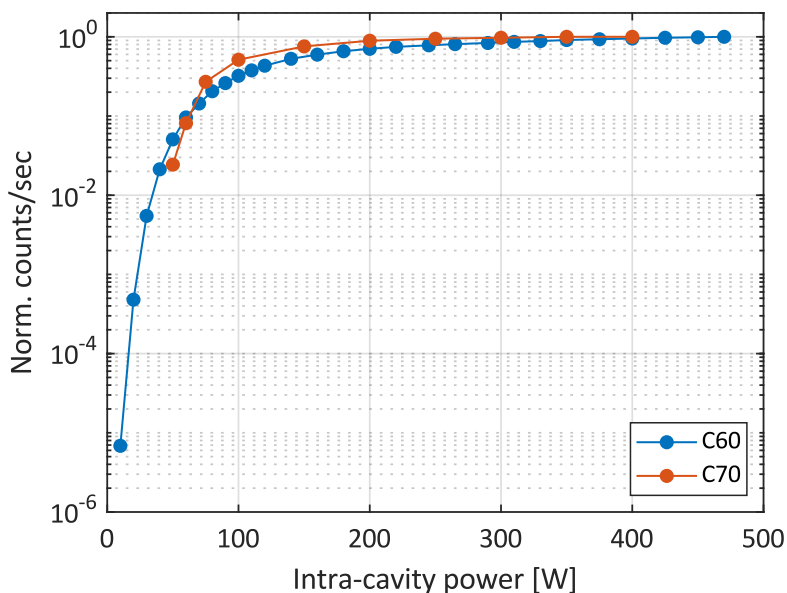
Figure 31: *Ion counts as a function of intra-cavity power for C_{60} and C_{70}, showing that saturation is achieved for both at the typical operational power beyond 250 W. Saturation is desirable since small fluctuations in intra-cavity power then have less effect on the count rate during interference measurements. Stable operation was possible above 200 W intra-cavity power, yielding saturated counts for both fullerene types.*

Cavity locking was achieved with a side-of-fringe lock implemented in LabVIEW, which could provide feedback on the millisecond time scale, sufficient to maintain a stable lock once high-frequency vibrations from the laser chiller were passively suppressed. The Invar cavity had a cavity length of 5.5 mm and 99.9% reflective mirrors with a radius of curvature $R = 100$ mm, yielding a cavity beam waist of approximately 55 µm. The ionization process was saturated for both C_{60} and C_{70} beyond 200 W of intra-cavity power, as shown in Figure 31. At low powers, the counts are expected to follow a power law dependence of $P^{5.6-5.8}$ [106,107], which is consistent with the observed dependence for both C_{60} and C_{70}.

The early setup with mass selection also afforded an interesting opportunity to investigate fragmentation processes in fullerenes due to thermal ionization. Figure 32 shows the fragmentation of C_{70} as a function of intra-cavity power. The coefficient of the observed power law dependence increases for smaller fragments, perhaps indicating higher order fragmentation processes, in which fragments then fragment again, leading to a loss channel for the parent peaks and a higher rate of increase for the daughter fragments.
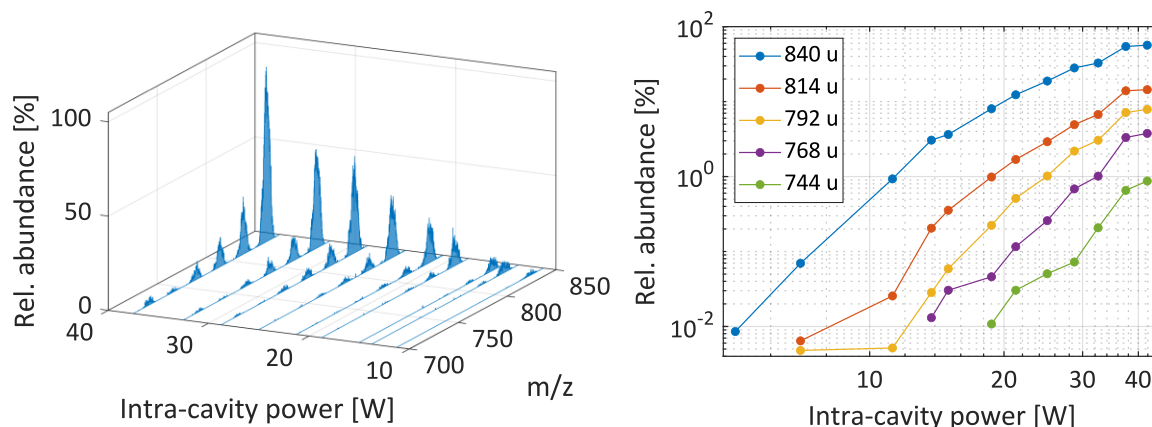
Figure 32: *Analysis of C_{70} fragmentation during the thermal ionization process.* **Left:** *Fragment birth as a function of intra-cavity power for C_{70}.* **Right:** *Log-log plot of counts vs. intra-cavity power showing the increasing rate of fragment production as a function of fragment number.*

3.6 Grating alignment

The various alignment requirements for a TLI have been derived in several publications [37,53,54]. The same conditions hold here, although some values change due to the increased baseline of $L = 0.981$ m compared with previous setups. The angle definitions and coordinate system used throughout are shown in Figure 17, and the alignment conditions for LUMI are summarized in Table 2.

3.6.1 Inter-grating separation and pitch alignment

The required equality of the longitudinal grating separation can be approximated as $\Delta L < L/N$, where N is the number of illuminated grating slits. Assuming a typical beam width of 1 mm yields $\Delta L < 260$ µm.

The longitudinal separation requirement also plays a role in the pitch and yaw alignment requirements. Since a pitch angle φ leads to a change in longitudinal distance over the height h of the molecular beam, simple geometric considerations lead one to the requirement that $\Delta\varphi < 2L/hN$. Even assuming a beam as high as the material grating itself (3 mm) leads to the lenient requirement $\Delta\vartheta < 170$ mrad, or $\Delta\vartheta < 520$ mrad for a 1 mm high beam. The longer baseline compared to previous experiments relaxes both the absolute longitudinal and pitch alignment criteria.

While the absolute requirement for the longitudinal grating separation may not seem stringent, it requires a relative accuracy on the order of 10^{-4}, and it emerged during the final alignment procedure that it was in fact the most misaligned parameter.

3.6.2 Period equality

The periods of the gratings should be well matched, with $\Delta d/d \ll 1/2N$ the condition required to avoid half a period shift over N slits. This requires a period matching between the gratings better than 0.4 Å for a 1 mm wide beam. As shown in Table 1 the material gratings satisfy this condition, and their periods can be matched with that of the optical grating by introducing a small yaw offset ϕ to reduce their effective period by $d_{eff} = d \cos\Delta\phi$.

3.6.3 Yaw alignment

A yaw misalignment has three distinct effects relevant for interference: an effective ΔL across the beam width, a slit width change, and a grating period change from the perspective of the molecular beam. The first two effects impose only very lenient alignment requirements corresponding to 520 mrad and 70 mrad respectively for a beam width of 1 mm, as derived explicitly in Reference [54]. Consideration of the period change $d_{eff} = d \cos\Delta\phi$ leads to the condition $\Delta\phi < 1/\sqrt{N}$, which requires a relative grating yaw alignment within 16 mrad, still a rather lenient criterion. This condition assumes yaw angles near normal from the perspective of the beam, which is satisfied in the LUMI setup.

There is a stricter requirement for an optical grating since one must ensure that the mirror surface is sufficiently parallel to the beam to avoid molecules passing both nodes and antinodes of the standing light wave, which would lead to phase averaging. This leads to the condition $\Delta\phi < \operatorname{atan}(d/2b)$, with b the width of the standing light wave in the longitudinal direction. At the focus of the 10 cm cylindrical lens $b \approx 50\,\mu\text{m}$, such that the molecular beam must be aligned to within 3 mrad of the mirror surface.

3.6.4 Roll alignment

The strictest alignment criteria at LUMI is the relative roll of the three gratings, which is due to two underlying effects. The first and smaller effect is the effective period increase $d_{eff} = d/\cos\Delta\theta$ across the beam caused by a roll offset $\Delta\theta$, giving $\Delta\theta < 1/\sqrt{N}$, following

the same reasoning as the effective period change due to a yaw offset. As with yaw, this yields a 16 mrad requirement for a 1 mm wide beam.

The tighter criterion is due to a height-dependent phase shift as a function of the roll angle. The visibility reduction caused by rolling the first and third grating with respect to the second grating can be estimated as $V/V_0 = sinc(2\pi h_1 \Delta\theta_1/d)sinc(2\pi h_3 \Delta\theta_3/d)$ for a beam height h_i at the ith grating. For a constant beam height of 1 mm the relative roll angles must satisfy the condition $\Delta\theta_{1,3} < 0.08$ mrad to avoid a 50% loss of visibility. In a more general treatment the geometry of the setup and positions of any velocity-selection delimiters can be used to determine the beam height at the gratings [53].

Additionally, the presence of gravity will favor an absolute common roll angle nearly parallel to gravity to avoid averaging over the velocity classes in the beam which will all accumulate a different gravitational phase shift. However, when the Coriolis force is also considered, a slight common roll offset with respect to gravity is in fact optimal, as described in Chapter 2.

Alignment parameter	Material gratings	Optical grating
Pitch	520 mrad	520 mrad
Yaw	16 mrad	3 mrad
Roll w.r.t G2	0.08 mrad	--
Longitudinal spacing	260 μm	260 μm
Period equality	0.4 Å	0.4 Å

Table 2: *Summary of the grating alignment requirements at LUMI for a beam width of 1 mm, beam height of 1 mm, and inter-grating separation of 0.98 m. The roll with respect to G2 assumes a misalignment of only one grating.*

3.6.5   Alignment procedure

Alignment of the gratings was done in several stages[5]. An initial geometric alignment was performed on all relevant degrees of freedom before the vacuum chamber was closed and evacuated to allow straightforward access to the gratings. The final alignment was performed under vacuum with a molecular beam of C_{60} by systematically scanning the parameter space of the gratings and optimizing the interference visibility. This is regularly readjusted to account for small drifts as well as to adjust the velocity-dependent optimal roll angle to compensate the Coriolis effect.

The longitudinal separation of the gratings was first measured with a tape measure, and later repeated with higher accuracy by means of a rail-mounted alignment laser which could be moved along the setup and could localize the relative longitudinal position of each grating to within 1 mm over the two-meter long interferometer. The pitch alignment criterion is very

---

[5] The alignment of LUMI was performed together with Dr. Stefan Gerlich.

lenient, and an initial alignment to a gravity-aligned reference laser was sufficient without further adjustment. Since this angle was the only one not motorized, the adjustment was done manually by inserting Teflon spacers below the motor assemblies and adjusting the tightness of the mounting screws.

Pre-alignment of the material grating yaws was done by overlapping the back-reflections of the gratings with a reference laser sent along the beam path. This ensures a relative yaw of the material gratings to better than 0.5 mrad with respect to the beam normal. The yaw of each material grating is then adjusted by $\mathrm{acos}(d_{opt}/d_{mat})$ to satisfy the period-equality condition. The final alignment was confirmed by optimizing interference visibility as the yaw parameter space was systematically scanned, with an example of this procedure shown in Figure 33.
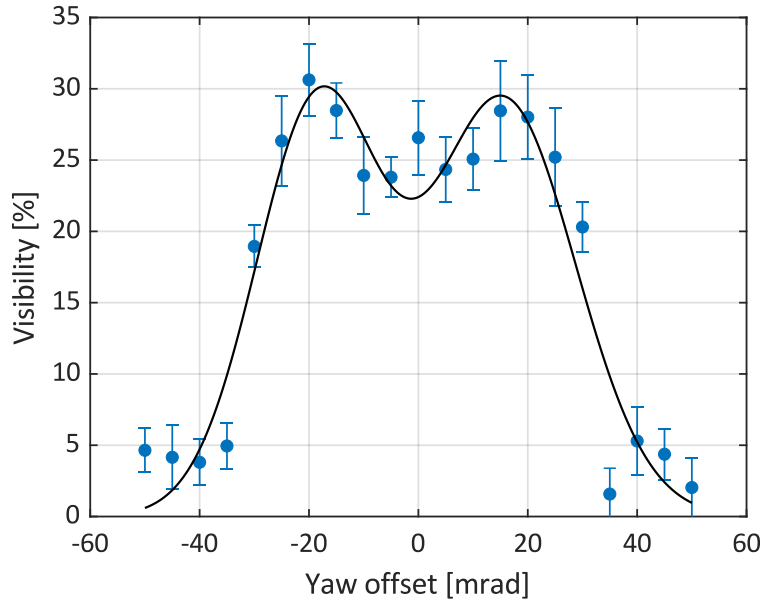
Figure 33: Yaw scan of the third grating. The black line is a double Gaussian fit, with the two maxima corresponding to the two choices of yaw angle ϕ such that the effective period of the material gratings d_{mat} matches the optical grating period d_{opt}, as given by $d_{mat} \cos \Delta\phi = d_{opt}$. Since the first grating was kept fixed during this scan there is additionally an envelope due to the relative yaw misalignment of the first and third gratings. The zero-point of the yaw axis is approximately at the normal position to the molecular beam, and error bars correspond to 68% confidence intervals of the fitted sine amplitudes.

Alignment of the yaw of the optical second grating to the beam, the second most critical alignment criterion after roll, was done only after evacuating the chamber with the aid of a molecular beam. The mirror was inserted about halfway into the beam and then rocked back and forth to find the angle of maximum flux to ensure that the molecular beam and the standing light wave are parallel, with a typical accuracy of about 0.2 mrad. Once the optimal angle is determined, the mirror is retracted such that the molecular beam passes about 200-300 μm from the mirror surface, near the focus of the cylindrical lens. This procedure must be repeated if the yaw of the molecular beam changes significantly, due, for example, to a modified detector position when working with no horizontal beam delimiters.

The pre-alignment of the roll angles was done by aligning each grating to gravity using a reference laser beam that was pre-aligned to gravity with an optical level accurate to better than 1 mrad (D-626 Davidson Optronics). The optical grating was aligned by simply overlapping the mirror back reflection with the reference beam, since the mirror surface defines the node of the standing light wave and hence the grating. The material gratings, on the other hand, face the molecular beam and a simple back-reflection would therefore only give information about the pitch angle. We therefore aligned the reference beam to the first order Littrow diffraction, in which the angle of the incoming beam is equal to the angle of the first diffraction order in the case of normal incidence, $\theta_L = \mathrm{asin}(\lambda/2d)$. This technique works when the laser wavelength λ is less than twice the grating period, as for the blue (405 nm) laser used for this purpose. The final roll alignment is then obtained by optimizing interference visibility, as illustrated by the contour plot in Figure 34. As the most sensitive alignment parameter, the rolls are regularly re-optimized via an automated routine, especially after exchanging the beam source.
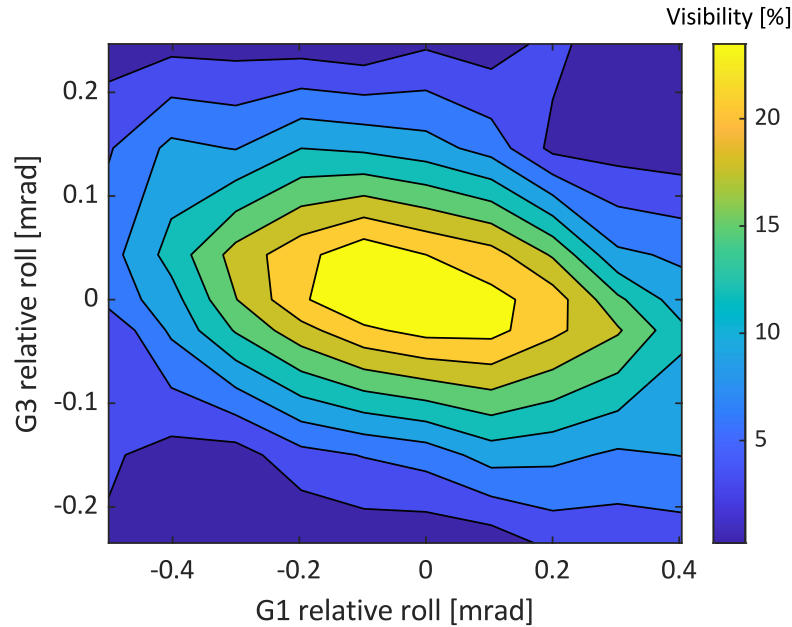
Figure 34: *Typical roll alignment data showing the small region of high contrast as a function of the roll of the first and third gratings (G1 and G3 respectively). Such fine-alignment scans are typically done with limited vertical collimation such that the relative roll alignment is more critical. The larger range for the first grating is due to the smaller height of the beam at this position, before the velocity spread causes the beam to spread in the vertical direction. The zero-points of the roll axes are arbitrary.*

Since the interferometer is mounted on a pendulum, it is critical to track the roll angle of the bar, especially when the optical table is floating. This is done with the four tilt sensors described in the discussion of vibrational isolation, with two orthogonal sensors on the interferometer bar and two on the optical table. This provides real-time feedback of the common roll and pitch of the table and interferometer bar. During early interference experiments the table was typically floated on bottled nitrogen, which avoided the instabilities of a compressor. However, the floating table made the interferometer sensitive to small drifts and perturbations,

triggered, for example, by the flowboxes above the table being switched on or off or the lab door being opened. In practice, the interferometer was typically able to operate with full interference visibility without floating the optical table, which made the system significantly more stable.

3.7 Velocity measurement and selection schemes

For interference and metrology experiments it is often important to know the velocity distribution of the atomic or molecular beam and sometimes also to narrow the spread of velocities to avoid phase averaging. As with the choice of beam source and detection scheme, the choice of velocity measurement and selection technique varies with the experimental requirements and on whether the source is continuous or pulsed. The various schemes employed so far at LUMI are outlined below.

3.7.1 Mechanical pseudo-random chopping

The time-of-flight measurement technique used most frequently at LUMI is known as cross-correlation chopping, which is done by mechanically modulating the beam with a pseudo-random sequence. The pseudo-random sequence has a special autocorrelation property such that the time-of-flight distribution can be obtained via cross-correlation of the sequence with the measured signal. The advantage of this technique is that 50% transmission of the beam can be maintained without loss of resolution [108] when compared to the much lower efficiency of conventional single-bin chopping. The technique was first implemented with thermal neutron sources [109] and its utility in this context was also shown in the previous KDTLI experiment [110].

The measured signal s can be written as a discrete convolution of the time-of-flight distribution g with the chopper sequence a over k time steps,

$$s_i = \sum_{k=0}^{N-1} a_{i-k} g_k \,. \tag{73}$$

To solve for the time-of-flight distribution thus requires convoluting the signal with the inverse of the chopper sequence. Due to the correlation property of pseudo-random sequences of length N,

$$\sum_{i=0}^{N-1} a_i a_{i+k} = \frac{N+1}{4} \left(1 + \delta_{k,0}\right), \tag{74}$$

one can deconvolute the signal via cross-correlation with the chopper sequence itself [108]

$$g_i \propto \sum_{k=0}^{N-1} a_{k-i} s_k + const. \tag{75}$$

This cross-correlation is conveniently performed in Fourier space.

Experimentally, the modulation is achieved with a steel chopper disk (12 cm outer diameter) which was laser cut[6] with a pseudo-random sequence of 255 bins and 64 openings as generated by the algorithm in Reference [111]. The chopper disk is rotated with a brushless DC vacuum compatible motor with analog Hall sensors (Faulhaber Series 1628) and controlled with a proprietary position and speed controller. The chopper sequence is detected by an optical switch placed about 180° out of phase with the position of the molecular beam, and the beam signal is collected with a fast counting card (FAST ComTec P7882) with 10 µs time bins. The chopper sequence from the optical switch is collected both with a DAQ and the fast card, to ensure the temporal overlap of the chopper signal and the beam signal necessary for the cross-correlation. The chopper assembly is installed in the differential pumping stage immediately before the interferometer chamber to avoid a high molecular flux from contaminating the motor. A picture of the assembly is shown in Figure 35.
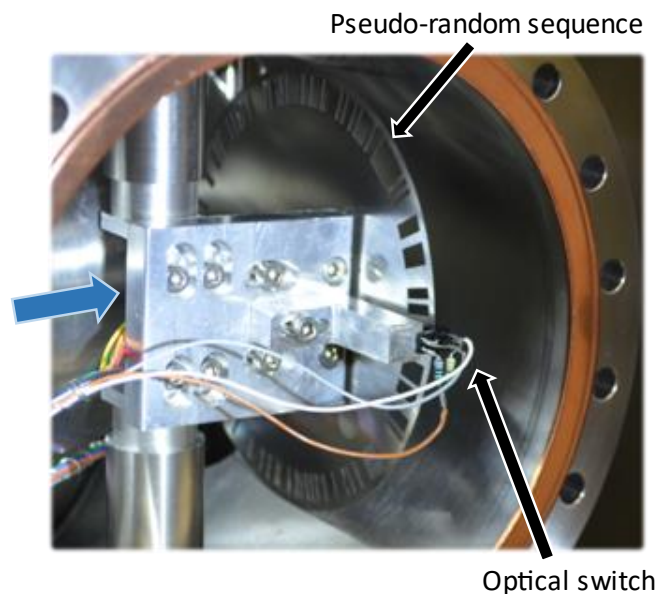

Figure 35: The chopper assembly installed in the differential pumping chamber, showing the positions of the optical switch and the particle beam, which are about 180° out of phase with respect to each other.

Determining the $t = 0$ point of a time-of-flight measurement requires us to know the angle between the position on the chopper where the beam passes and the position where the optical switch encodes the sequence, since this inserts an artificial delay between the measured signal and the measured sequence. A calibration routine to determine this angle is run each time the source position is changed, as described in Figure 36.

---

[6] Dr. Ronny Barnea at Tel Aviv University performed the laser cutting of the chopper disk as well as several of the vertical and horizontal delimiting slit plates used in the interferometer.
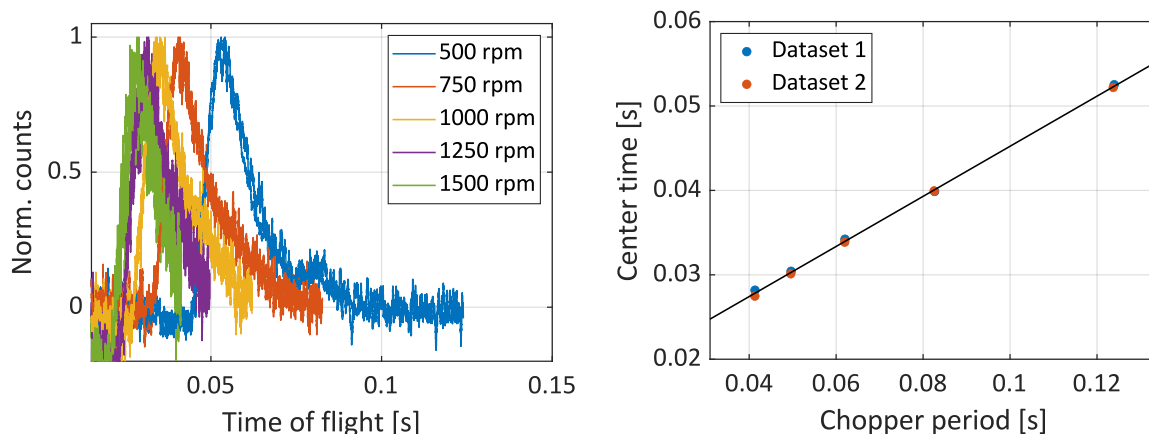
Figure 36: *Example of the velocity calibration routine with a C_{60} beam.* **Left:** *Time-of-flight distributions are collected at five different chopper rotational speeds with two sequential datasets overlaid. The relative angular offset between the position of the atomic beam and the optical switch on the chopper must be accounted for by a calibration factor which determines the start points of the time-of-flight measurements. If this factor is chosen correctly, the velocity spectra should overlap for all chopper speeds, while an incorrect value causes the spectra to be separated in time. A value of 0.2 is chosen for this figure to exaggerate the effect.* **Right:** *The dependence of the peak of the time-of-flight distributions on the chopper rotational period. The extracted slope of the linear fit (solid black line) gives the correction to the arbitrarily chosen calibration factor. In this example a slope of 0.297 yields a calibration factor of 0.497, where a value of 0.5 would correspond to an exact 180° angular offset between the beam and optical switch.*

3.7.2 Gravitational velocity selection

Sufficiently slow beams ($\lesssim 200$ m/s) can be velocity-selected with the aid of vertical delimiters due to the parabolic flight paths of the molecules under the influence of gravity. Such a technique can yield velocity spreads below 5% of the mean velocity, but with a significant tradeoff between flux and selectivity. Vertical delimiters have the additional benefit of limiting the height of the beam traversing the gratings, thus relaxing the roll angle alignment criterion. While the velocity can be selected gravitationally, the empirical velocity is always determined by a time-of-flight measurement with the pseudo-random chopper, as described above.

At LUMI, beam delimiters were implemented as stainless steel plates with rectangular apertures of heights ranging from 0.1 to 1 mm mounted on linear translation stages, such that the desired aperture size can be inserted into the beam or the delimiter plate withdrawn entirely. Two vertical delimiter plates were initially installed, with one in front of the second grating and the other after the third grating. A third delimiter plate was later installed in front of the first grating to limit the damaging coating caused by high flux. Additionally, two horizontal delimiter plates were sometimes employed to limit the beam width, especially during the initial alignment phase, with one before the first grating and the second directly before the third grating. The delimiters used at LUMI and their longitudinal separations are shown in Figure 37.
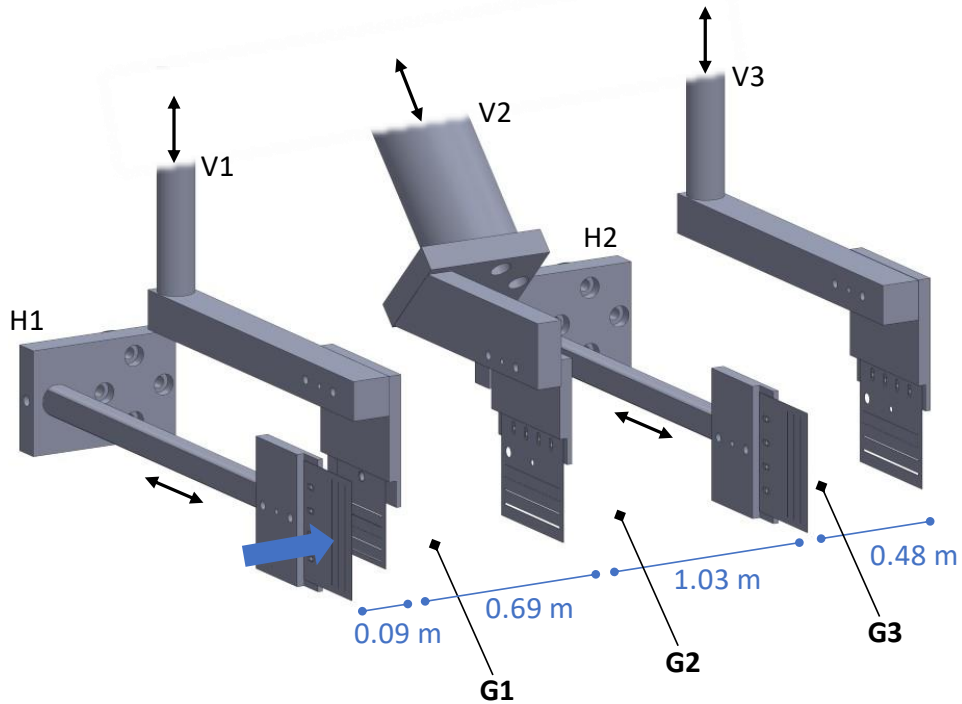
Figure 37: *The five beam delimiters used at LUMI. H1 and H2 are the horizontal delimiters to reduce the beam width, while V1, V2, and V3 are the vertical delimiters used to reduce the beam height and gravitationally select velocities. The blue arrow indicates the molecular beam while the black arrows show the axes of the linear translation stages used to move the delimiters in and out of the beam. H1 and V1 help to control the flux incident on the first grating, thus extending its operational lifetime. The distances between the delimiters are supplied, with the distance between V1 and G1 of 0.11 m (and 0.98 m between each grating).*

3.7.3   Time-resolved interference measurements

The high transmission of the pseudo-random chopping technique enables time-resolved interference scans, in which a time-of-flight measurement is taken at each transverse position step of the third grating. Such measurements enable the extraction of the phase of the interference fringes as a function of velocity. This is a useful feature for deflection experiments, since it yields deflection information about each velocity class contained in the beam rather than an averaged value. It was also useful for characterizing the compensation of the Coriolis force in the interferometer and can potentially be used for gravity or rotation measurements.

Such a measurement technique provides the advantages of good velocity selection without a flux trade-off, since the entire velocity distribution can be used rather than discarding a vast majority as with the gravitational velocity selection scheme. The effective velocity resolution is mainly limited by the inherent resolution of the chopper, given by $\Delta t/t \approx 1/N f t_{flight}$, with f the chopper rotation frequency and $N = 255$ the number of chopper bins. However, while the entire velocity distribution is used, the flux per velocity class is still small, thus requiring long integration times to collect enough counts across the velocity spectrum. The technique is

therefore only compatible with intense, stable beam sources, and requires a high level of phase stability of the interferometer.

3.7.4 Direct time-of-flight with pulsed beams

For pulsed beams with a well-defined trigger, such as those produced by an Even-Lavie valve, the time-of-flight distribution can be measured directly with the fast counting card by triggering both the valve and the counter card with a TTL signal produced by an external delay/pulse generator (Berkeley Nucleonics Model 575). A small internal delay of about 70 µs between the TTL trigger pulse and the gas flow must be considered to avoid a systematic error. Testing showed good agreement between velocity spectra obtained by the pseudo-random chopper and the direct time-of-flight measurement.

When working with such a source we often gate the signal, the effect of which is illustrated in Figure 38. This is done by inserting a switch in the QMS signal line which is modulated by another TTL pulse with a fixed delay from the trigger pulse. By shifting the width and delay of this pulse with respect to the trigger, different portions of the velocity spectrum can be selected. Gating has the additional advantage of significantly reducing the dark rate, since the signal is not collected during the time between pulses. This is a significant advantage since the dark rate of the QMS with electron impact ionization is not negligible in the mass range of the small hydrocarbons for which this technique is typically used.
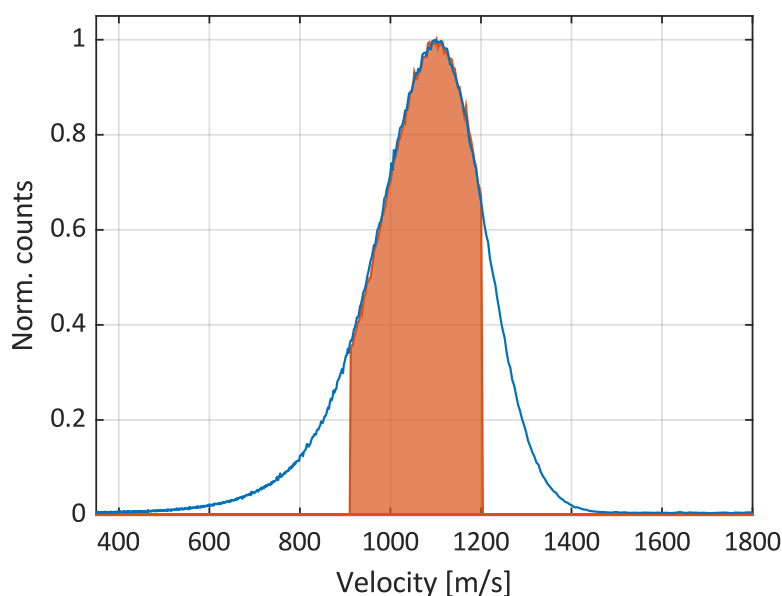

Figure 38: *Direct time-of-flight spectrum as measured from the heated Even-Lavie valve. This spectrum is for anthracene seeded by helium with low backing pressure (<1 bar) to obtain significant velocity slip, which was desirable for several experiments. The blue curve is the complete spectrum, while the red curve shows the effect of gating the signal to obtain lower dark counts and a narrower velocity spread.*

3.8 Coriolis compensation

The rotation of the Earth poses a challenge for an experiment like LUMI, since, like gravity, it creates a velocity-dependent phase shift that will blur the interference pattern of a non-monochromatic beam, as described in Chapter 2. There are several experimental approaches to avoid Coriolis dephasing. One can reduce the detrimental velocity averaging by working with nearly monochromatic beams or performing time-of-flight resolved interference, or one can actively compensate the Coriolis shift via counter-rotation of the gratings. The first two options are generally not practical for normal operation, since the first requires the ability to velocity select to a few percent of the mean velocity (possible with slow beams at the cost of significant flux reduction) and the second requires very stable and long-lived beam sources which are not always available, particularly for larger, more fragile molecules. We initially explored active compensation via motorized counter-rotation with the outer two gratings, which required significant timing requirements and introduced vibrations. We instead employ a passive compensation scheme which requires no moving components, which works by introducing a gravitational phase shift that cancels the velocity dependence of the Coriolis phase shift to first order. The theoretical description of the compensation technique is discussed in Chapter 2.

The technique was characterized by performing time-resolved interference scans for a series of common roll angles of the three gratings. The optimal roll angle in the absence of the Coriolis effect is aligned to gravity, such that the velocity-dependent gravitational phase shift is minimized. For a long-baseline interferometer like LUMI, especially when working with slow beams, such an alignment is no longer optimal. This is clearly seen in Figure 39, which shows time-resolved interference scans of C_{60} for a range of common roll angles, with time on the y-axis and transverse position on the x-axis. The rightmost image in the figure is the case of a common roll aligned nearly with gravity, which yields a strongly reduced visibility when averaged over the velocity distribution present in the beam (i.e., a vertical integration of the plot). The center image, on the other hand, shows the optimally aligned case where a small roll offset of about 1 mrad makes the combined gravitational and Coriolis phase nearly velocity independent, thus maintaining high visibility even when averaged over the velocity distribution [59].
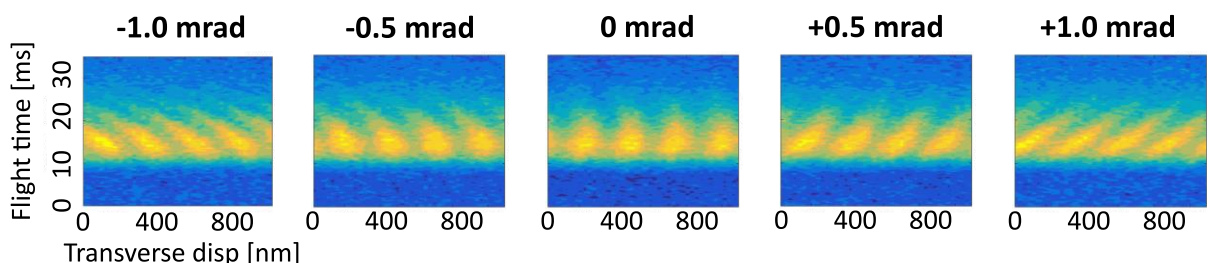

Figure 39: *From left to right, time-resolved interference scans of C_{60} with common roll angles with respect to the optimally-aligned roll offset of -1.0 mrad, -0.5 mrad, 0.0 mrad, +0.5 mrad, and +1.0 mrad respectively. The center image corresponds to near-optimal compensation, since an integration over the velocity distribution does not result in significant loss of visibility,*

as it would for the other cases. The rightmost image corresponds to a common roll nearly aligned with gravity.

3.9 Longitudinal Talbot carpet

The large motorized travel range of the gratings' longitudinal separation gives us the capability to directly observe Talbot carpets by symmetrically moving the outer two gratings and monitoring the flux as the third grating is scanned transversely at each longitudinal position step. An example of a molecular Talbot carpet is shown in Figure 40 for C_{60} with a mean velocity of 190 m/s, a spread of 8%, and a phase grating power of 8.5 W. The curvature in the carpet is not surprising on the nanometer level for a total travel range of centimeters, and it compares well with the theoretical expectation shown in Figure 13, which was calculated for a C_{60} beam with the same velocity distribution.
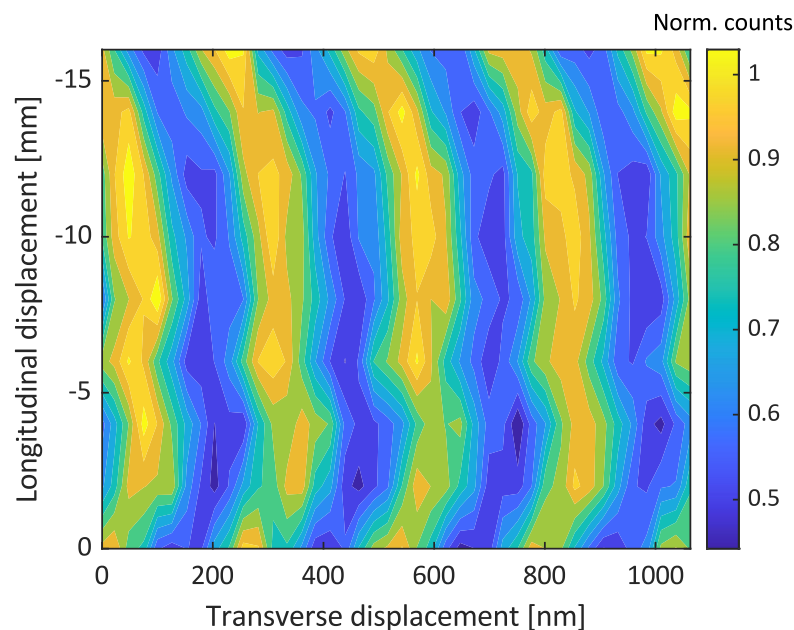
Figure 40: *Experimental Talbot carpet of C_{60} as the first and third grating are moved symmetrically inward in equal steps of 2 mm and a transverse scan of the third grating performed at each longitudinal position. The 266 nm spatial modulation in the beam over a symmetric longitudinal range of more than 15 mm is clearly visible. The data has been cropped to exclude portions at further longitudinal positions where the transverse drift became more extreme.*

4 High-mass interference and fundamental physics

This chapter discusses the experiments which set the current mass record of quantum interference, and the resulting limits that have been set on alternative quantum theories. The key results presented here have been published in Reference [32]. A brief overview of the universal nature of the experiment and implications for weak equivalence principle tests are also discussed.

4.1 Molecular structure

One of the biggest technical challenges in our experiments lies in producing intact neutral beams with velocities suitable for interference. The high-mass interferometry experiments described here were enabled by functionalized oligoporphyrins suitable for volatilization[7]. The details of the synthesis are beyond the scope of this thesis (see Reference [32] and its Supplemental Information for details), but the molecular structure and the motivation behind it are described here.

It has been observed that the addition of perfluoroalkyl chains to oligoporphyrin cores helps in the formation of stable molecular beams [112]. Such functionalization reduces the polarizability to mass ratio of the molecules, which helps in the formation of thermal beams, while at the same time adding significant mass to the molecule. In the earlier work [112], various functionalized oligoporphyrins were tested with nanosecond pulsed laser desorption and detected after a short distance with a time-of-flight mass spectrometer (TOF). Similar molecules were used in the current work, with their structure shown in Figure 41. A continuous or quasi-continuous beam is best suited to LUMI, and the beam must be intense given the source to detector distance of approximately 3.5 m. The beam source and detection scheme thus had to be adapted accordingly.

4.2 Beam source and detection

The oligoporphyrins were first tested in a conventional oven, but these thermal tests showed that the molecules suffered severe fragmentation, as shown in Figure 42. The mass spectra indicate that the central bond of the tetra-porphyrin system breaks, and the molecule loses its perfluoroalkyl chains. The fragmentation in the thermal source motivated us to instead adapt a nanosecond laser desorption scheme, which had been shown to work for similar molecular structures over shorter distances [112].

---

[7] Molecule design, synthesis, and characterization were performed by Patrick Zwick and Prof. Marcel Mayor at the Department of Chemistry, University of Basel.
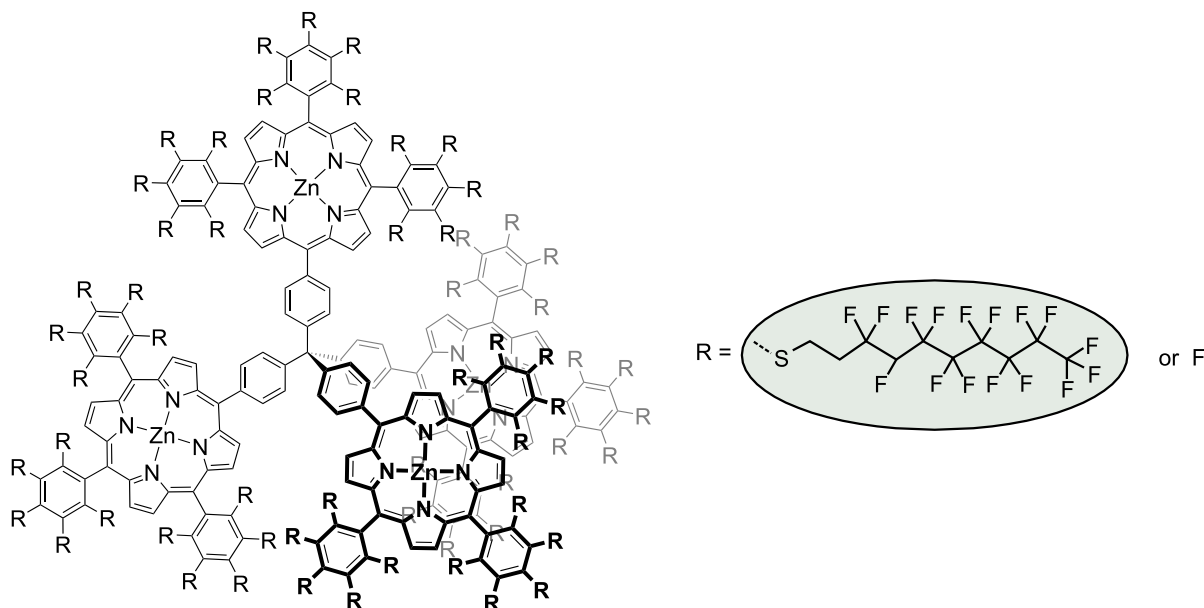
Figure 41: *Chemical structure of the oligoporphyrins synthesized for the high-mass interference experiments. Up to 60 perfluoroalkyl chains R, shown on the right, can be attached to the zinc-coordinated tetraporphyrin core; single fluorine atoms take the place of any absent chains. The most abundant molecules in the library contained about 50 chains, with some spread due to both the synthesis and desorption of the molecules.*
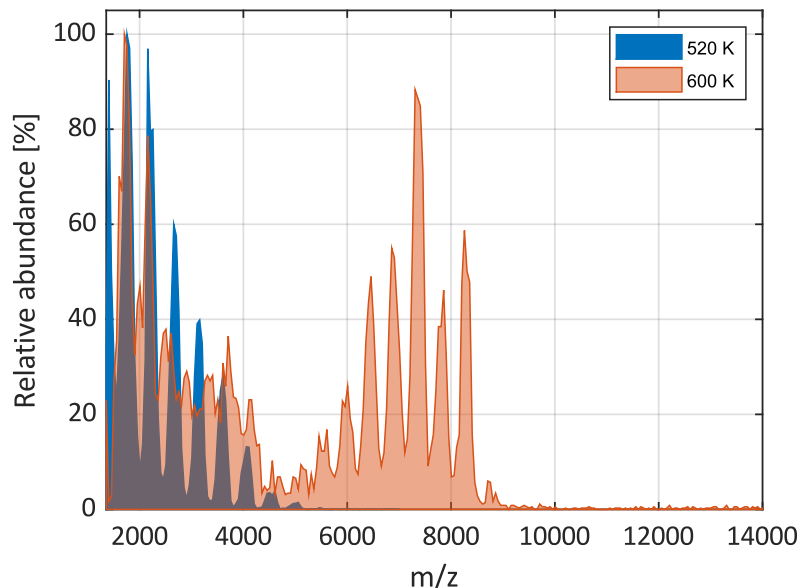
Figure 42: *Fragmentation of the oligoporphyrins in a thermal source. Mass spectra at two different source temperatures are shown, showing fragments up to about 8,000 u at high temperatures, but no significant intact signal. The observed peak separations of 450 ± 13 u are consistent with the loss of single perfluoroalkyl chains during the heating, which would correspond to a separation of 460 u. The high peak around 7,000 u could correspond to ¼ of the oligoporphyrin containing 50 chains, later shown to be the most abundant in the library after desorption. This implies that both fragmentation of the central bond connecting the four porphyrins along with the detachment of side chains play a role during thermal sublimation of these molecules.*

A pulsed nanosecond laser (Edgewave IS120-4L) was modified to output 532 nm alongside the standard doubled 266 nm output, since tests showed that the desorption was more efficient in this wavelength regime. A 50×50 mm^2 glass slide was thickly drip-coated with the molecules dissolved in Fluorinert FC-72, dried, and mounted in vacuum on a magnetic stage that could be translated in two dimensions via two stepper motors, as pictured in Figure 43 and described in Reference [113]. The laser was focused from behind onto a fixed position in the source chamber, and the slide was then scanned over this position in a raster pattern. The count collection was gated such that counts were only collected during travel in one direction, to avoid an effective shift of the source position upon the change in direction.
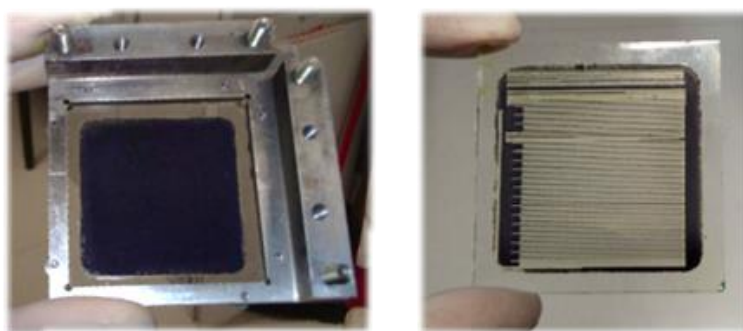

*Figure 43: Before and after pictures of the desorption slide. **Left:** Freshly coated glass slide in its mount before installation in the source chamber. **Right:** A slide after desorption, showing the raster pattern imprinted into the molecular layer as the slide is scanned in two dimensions. The laser spot is kept fixed and is focused onto the slide from behind and nearly normal to the surface, to minimize the desorption area. A pulse energy of about 1.8 mJ with a 1 kHz repetition rate was used; at higher energies thermal heating of the molecular layer would lead to discoloration of regions outside the laser beam diameter.*

A laser desorption source is particularly convenient for working with molecules that are of a limited supply (about 900 mg of the final product was available for optimization and interference tests), since it can be instantly turned off and one can easily monitor the amount of material remaining on the slide. This is to be compared with a conventional thermal source which will continue to heat the sample after the current is shut off, and which has no optical access, making it sometimes difficult to determine if the material has completely sublimated or another issue is causing a loss of flux. The challenge of working with this nanosecond desorption source is that there are more parameters to optimize than just temperature, such as the molecular coating thickness and homogeneity, as well as the desorption laser pulse strength, repetition rate, and focus.

As described in Chapter 3, the standard QMS detection scheme is not suitable for molecules beyond 16,000 u, which motivated the adaptation of a high-mass quadrupole mass filter for use as a detector. This custom high-mass QMS was used in a low-resolution mode to maximize counts, so it acted more as a high-pass filter than a mass selector in these experiments. The filter was calibrated at low mass, but a precise calibration was not critical due to the purity of the synthesized library. The mass of the molecules that survived the volatilization scheme was cross-checked with high-resolution MALDI/TOF spectra of material which was desorbed and

recollected in the LUMI experiment. This showed that there was some degree of fragmentation, but that the bulk of the desorbed material corresponded well to the pure product. Since the entire high-mass library rather than a single mass contributed to the interference patterns, the calculated visibilities were weighted according to the high-resolution mass spectrum shown in Figure 44.
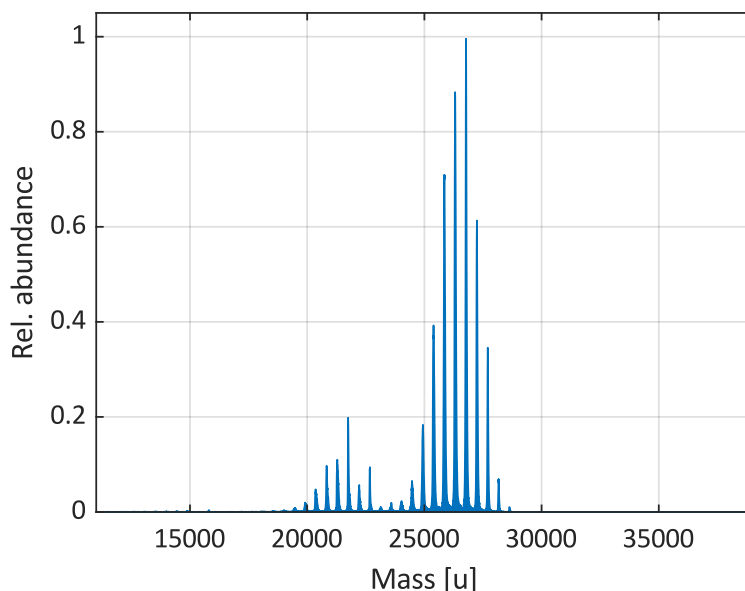

Figure 44: *Matrix-free laser desorption spectrum of the oligoporphyrin library as measured by Patrick Zwick from the University of Basel using a Bruker Daltonics solariX. The most abundant number of chain substitutions is 50, with molecules containing up to 55 chains visible. The relative weights of this distribution are used in the interference visibility calculation.*

4.3 Experimental protocol

The laser desorption technique, while successful in bringing the oligoporphyrins intact into the gas phase, yielded an unstable flux of molecules. We believe this was mainly due to inhomogeneity in the thickness and density of the molecular coating on the glass slide, and to a lesser extent some instability of the linear motors scanning the sample plate. The flux instability was compensated by using a reference scheme in which the 532 nm laser providing the second grating was mechanically pulsed, using a chopper built from a hard drive actuator to enable rapid switching. The grating laser was chopped at 2 Hz with a 50% duty cycle, and post-correlating the counts with the chopper sequence allowed us to separately bin the laser-on and laser-off collection periods. True interference effects are apparent by showing no modulation in the laser-off bins and the expected modulation in the laser-on bins, while signal modulation caused by source or detector variations will be visible in both bins. A small dead-time of typically 25 ms (calibrated with a photodiode placed behind the chopper) was introduced in the analysis to avoid any counts collected as the mechanical chopper was traversing the laser beam, during which the laser still partially illuminates the molecular beam.

The referencing scheme was shown to be highly robust to signal instability, as confirmed by intentionally modulating the signal strength during interference scans of fullerenes. Figure 45

shows the rejection of common-mode signal noise and the successful extraction of the C_{60} interference signal. Additionally, the laser-off bins give an estimate of the noise floor of the measurement, since any visibility obtained in the laser-off bins can only be a fitting artifact. In the high-mass interference experiments the noise floor was 6% due to the relatively poor signal to noise ratio, but well below the 30% visibilities observed near the optimal laser powers.
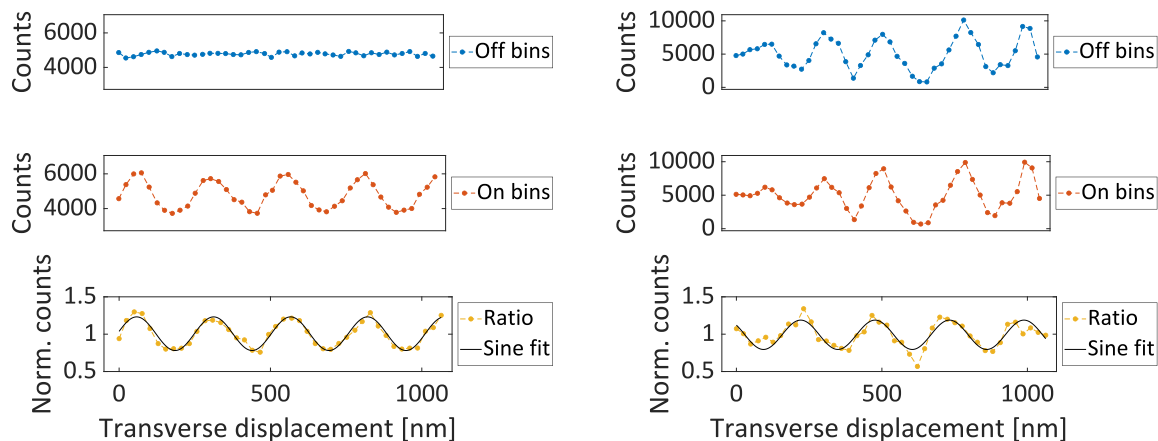
Figure 45: *Reference scheme demonstrated with C_{60}.* **Left column:** *Normal interference signal, where the laser-off bins (top) show no modulation, the laser-on bins show strong 266 nm modulation, and the ratio of the two (bottom) maintains the high visibility.* **Right column:** *A "worst-case" scenario where the signal is strongly modulated near the expected interference frequency by varying the multiplier voltage during the interference scan. This artificial modulation is captured in both the laser-off bins and the laser on bins, but taking the ratio removes the common-mode variation and reveals the real interference signal with the expected visibility.*

4.4 Results

In the following sections the main results of the high-mass oligoporphyrin experiments are described, as well as the benchmarking of the system with C_{60}. The main experimental protocol we use to unambiguously demonstrate quantum interference is a power scan, in which interference scans are performed as a function of the optical grating power. This allows us to directly compare the observations with the quantum and classical expectations, giving a value for fidelity which can be used for estimating macroscopicity and bounds on CSL parameter space.

4.4.1 Benchmarking with C_{60}

To benchmark the expected performance of the interferometer, tests were made with C_{60} immediately before and after the high-mass experiments. This allowed us to cross-check the grating alignment, the effective beam waist of the grating laser, the vertical overlap of the molecular beam with the optical phase grating, and the degree of Coriolis compensation. It was not practical to do these tests with the high-mass oligoporphyrins themselves due to both the sparseness of the sample and the comparatively poor signal-to-noise available compared with a fullerene beam.

These measurements uncovered a systematic vertical offset between the center of the optical grating and the molecular beam of about 140 µm. This was measured by setting the laser power to a value below the maximum visibility setting, and then measuring the visibility as a function of laser grating height. The visibility should be highest at the position of best overlap with the molecular beam since this position yields a higher effective laser power for the molecules. The data in Figure 46 illustrates this procedure, indicating a vertical offset of approximately 140 µm, which is representative of the typical offset since the vertical positioning of the laser is systematically done the same way, as described in Chapter 3.
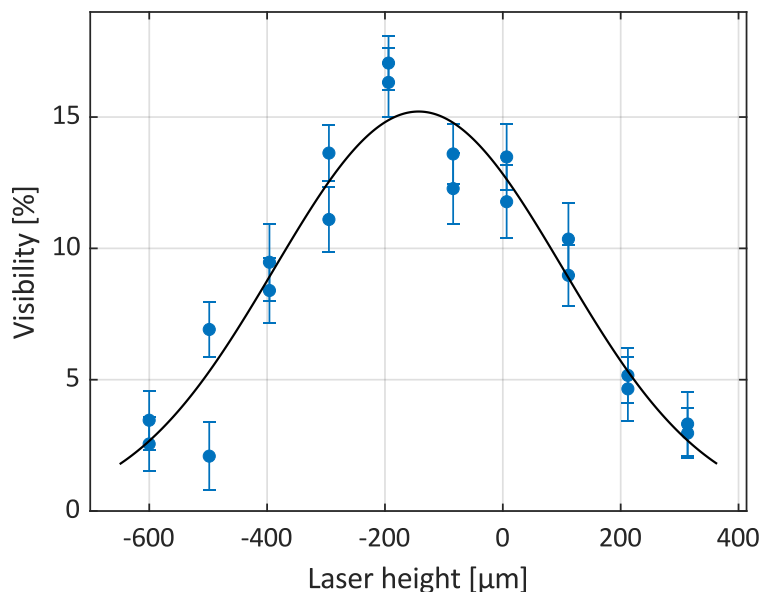

Figure 46: Visibility dependence on the optical grating height for C_{60}. Error bars correspond to 68% confidence intervals of the fitted sine amplitudes, and the black line is a Gaussian fit to the means, yielding an offset of 143 µm. The power was set to 4 W, on the left flank of the power curve, such that the best vertical overlap with the molecular beam yields the highest visibility. The low power is responsible for the moderate maximum visibility of 17%.

The maximum phase modulation ϕ_0 in the optical grating at a given input power as given in Equation 12 is thus slightly reduced in the high-mass experiments compared to the case of ideal vertical alignment. The reduced phase modulation is estimated by performing a power scan using the vertical position used in the high-mass experiments and extracting a beam waist w_y. The extracted beam waist value is slightly larger than the true beam waist as measured with a beam profiler, but, as expected, the discrepancy is reduced when the vertical position is set to maximally overlap with the molecular beam, as shown in Figure 47 by the shift of the visibility curve toward lower powers.

The degree of Coriolis compensation was determined by a series of time-resolved interference scans taken with C_{60} immediately following the high-mass measurements, using the technique illustrated in Chapter 3. Details on the other parameters entering the Talbot coefficient for the optical phase grating as given by Equation 10, such as the absorption cross section and optical polarizability of the molecules, can be found in the Methods section of Reference [32]. The polarizability was additionally weighted by the mass distribution as shown

in Figure 44, since molecules with different numbers of chain substitutions contribute differently to the polarizability. Using an optical polarizability of $4\pi\varepsilon_0 \times 108$ Å^3 for tetraphenylporphyrin at 532 nm [81,114] and the calculated value of $4\pi\varepsilon_0 \times 1321$ Å^3 for the oligoporphyrin with 52 chain substitutions, the polarizability as a function of substitutions s can be estimated as $4\pi\varepsilon_0 \times [4(108) + 17s]$ Å^3.
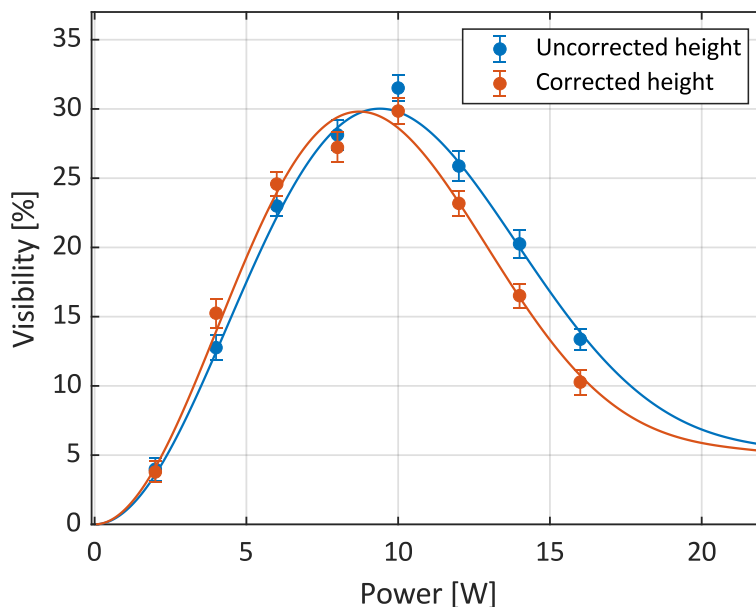

Figure 47: *Power scans at two different vertical positions of the optical grating. The blue curve corresponds to the typical, unadjusted height setting, while the red curve shifted to the left is a power scan with the small laser height adjustment as found in Figure 46. The shift of the peak to lower powers is expected since there is better overlap with the molecular beam in the adjusted setting, and thus the same phase modulation is achieved at lower power settings. Each point is the average visibility of two interference scans, with 68% confidence intervals of the fitted sine amplitudes.*

4.4.2 High-mass interference results

Several data runs were made with the oligoporphyrins at LUMI before the published results were achieved. Signal instability was initially the major confounding factor, at times even introducing periodic fluctuations that mimicked real interference results due to periodic sampling of the coating inhomogeneity. With the implementation of the referencing technique described above this issue was avoided, and the key experimental challenge lay in optimizing the beam conditions. Several incomplete or noisy datasets reproducibly showed high visibility interference at around 1 W before the optimal source settings were found.

Interference data as a function of optical grating power is shown in Figure 48, showing a maximum visibility of 30% at 1 W. The functional dependence on power is better illustrated in Figure 49, which shows the excellent agreement with quantum theory as modeled by Equation 7 using the second order Talbot coefficient for a KDTLI given by Equation 10. The classical expectation is also plotted, using the classical Talbot coefficient given in Equation 16, and is strongly ruled out by the data. This result is robust, in the sense that it would require a significant error in the various terms entering the visibility model for the results to be explained classically.

For example, the optical polarizability of the molecule would have to be smaller by a factor of nearly four for agreement with the classical prediction. The result is also largely determined by the most dominant mass in the distribution and good agreement with the quantum model is maintained even if the weights of the outer 50% of the mass library are set to zero.
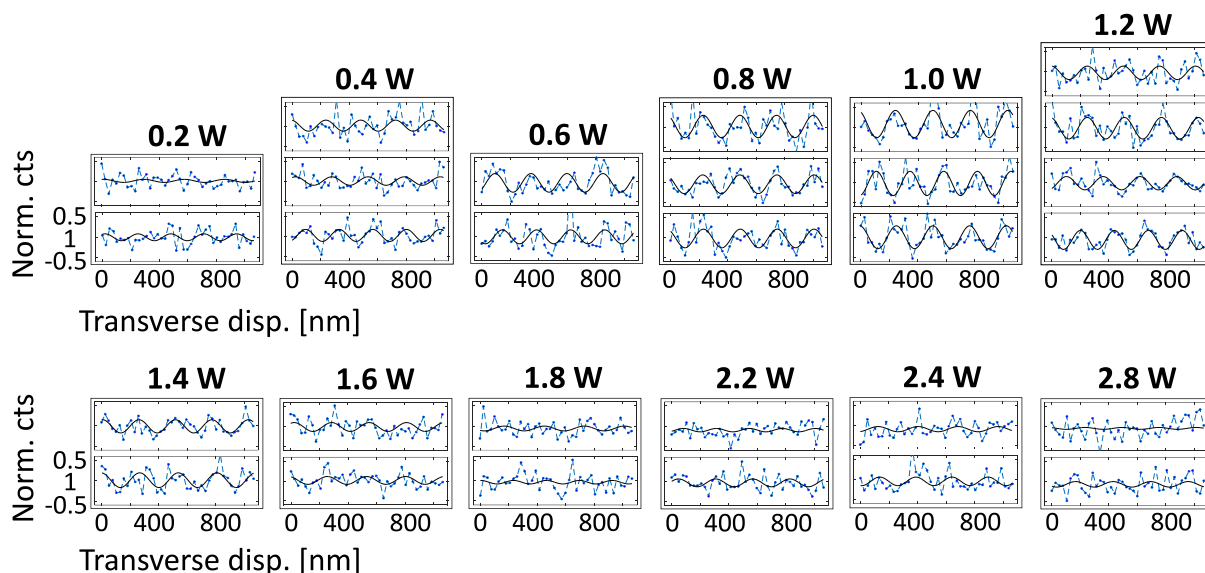
Figure 48: *High-mass interference data. Each column represents interference curves taken at a different power setting of the optical grating with sine fits given by the solid black lines. Several measurements were made at each power setting, all with the referencing scheme described in the text. Maximum visibility of 30 ± 3% is achieved at about 1 W, in excellent agreement with the theoretical prediction, and the reduced sine amplitudes away from 1 W powers can be observed. All plots have the same vertical and horizontal scales.*
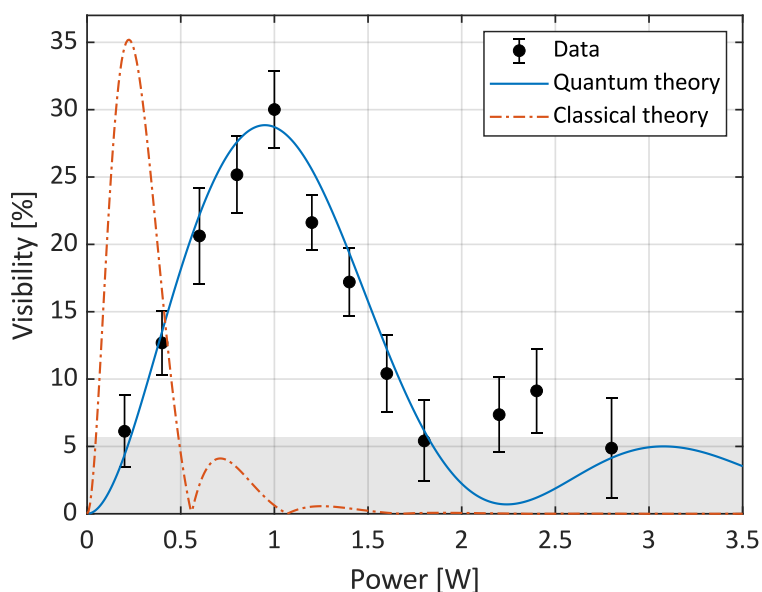

Figure 49: *Complete power scan of the high-mass oligoporphyrin library. Each data point corresponds to the mean amplitude of several interference curves at a given power as shown in Figure 48. There is excellent agreement with the quantum model (blue solid line) while the classical model (red dashed-dotted line) is strongly ruled out. The theory curves have no free*

parameters. The grey shaded region indicates the noise floor, as estimated from the laser-off bins of the referencing scheme. Data points near this region, such as the small anomalous peak beyond 2 W, are less trustworthy, since even with the second grating switched off the noise in the measurements could be fitted with sine curves of similar amplitude. Error bars correspond to 68% confidence intervals of the fitted sine amplitudes. Image adapted from Reference [32].

4.4.3 CSL bounds and macroscopicity

As discussed in Chapter 2, interference experiments with high mass particles are interesting from the perspective of placing bounds on alternative quantum models, in particular on the CSL class of collapse models. The bounds placed by the experiments described here are shown in green in Figure 50, along with bounds placed by other matter-wave experiments. The LUMI bounds are calculated by applying Equation 37, where V_{CSL}/V is set equal to the fidelity of the measurement, which is estimated as $93 \pm 6\%$ by fitting a scale factor to the quantum curve in Figure 49. The lower bound of 87% is used in the CSL bounds presented here as a conservative estimate.
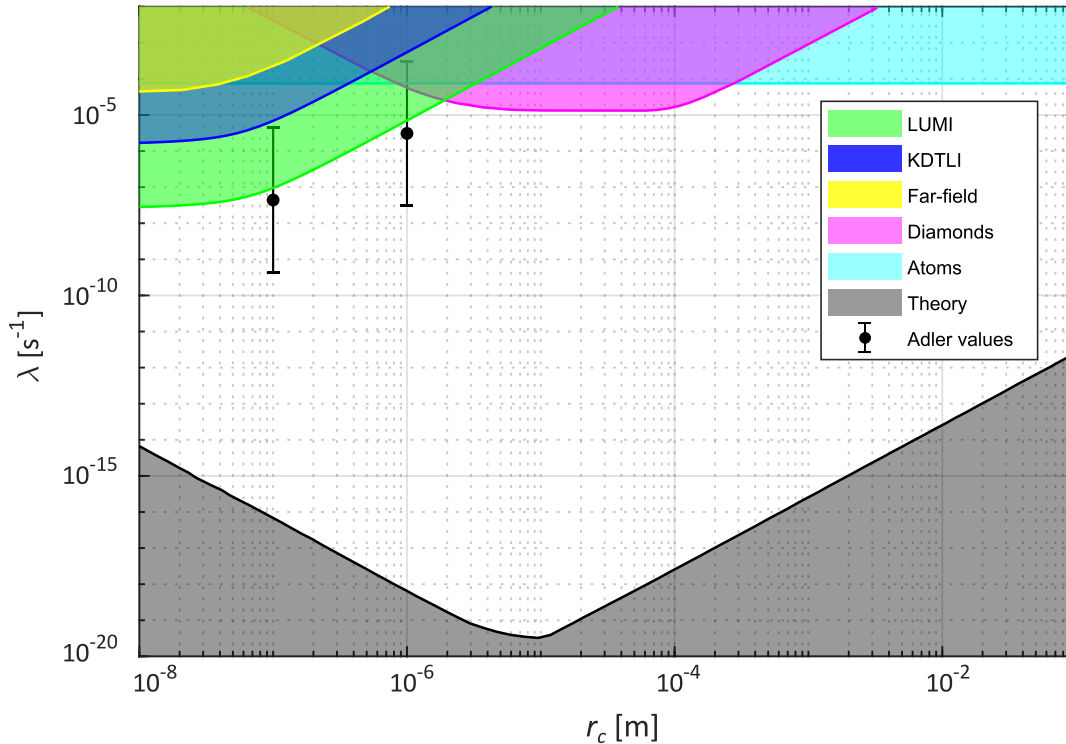
***Figure 50:** Bounds on the CSL parameter space from matter-wave experiments. Bounds for the entangled diamonds [115] and the atom interferometer fountain [6] are extracted from Reference [116] and the far-field interference bounds [117] and theory exclusion region at the bottom from Reference [70]. The KDTLI bounds from the previous mass record interference experiment [30] are calculated as described in the main text, and the LUMI bounds are from the results described in this chapter. The Adler values are a suggested parameter range from Reference [118].*

Additionally, the existence of a superposition state of a high-mass particle for an extended period of time leads to the highest published value of macroscopicity to date by the measure

defined in Reference [72] and given by Equation 38. The value of 14.1 represents a significant increase over the previous state-of-the-art values of about 12 for both atomic fountain interferometry [6] and the previous interferometric mass-record with 10,000 u particles [30]. As with the CSL bounds, a fidelity of 87% is used for the calculation of macroscopicity. A similar macroscopicity value for the experiment is found via Bayesian hypothesis falsification [73,119].

4.5 Universal nature of LUMI

Although not captured by measures such as macroscopicity, another intriguing aspect of the LUMI experiment is the wide range of particle types that can be interfered in the setup. Aside from the high-mass oligoporphyrins discussed here, LUMI was not used to merely demonstrate interference with a particular species; still, at the current tally, more than 12 different atomic and molecular species have been interfered at LUMI, as summarized in Table 3. Several tripeptide variants that yielded only noisy data have been excluded from the list, and only the oligoporphyrin corresponding to 50 attached perfluoroalkyl chains is included, since this was closest to the peak of the measured mass spectrum. If one considers the isotopic distributions of each of these species the list is in reality much longer, and in some cases isotopes were indeed studied independently and displayed isotope-dependent interference phenomena [89]. Besides the isotope distribution, the oligoporphyrin library alone contained up to 20 distinct molecules with varying numbers of attached chains. Additionally, the molecules are, with the exception of the atoms and the supersonically expanded small hydrocarbons, all highly excited, with many occupied rotational and vibrational states.

Name	Formula	Mass [u]
Strontium	Sr	88
Cesium	Cs	133
Barium	Ba	137
Adamantane	$C_{10}H_{16}$	136
Anthracene	$C_{14}H_{10}$	178
Coronene	$C_{24}H_{12}$	300
Tetraphenylporphyrin	$C_{44}H_{30}N_4$	615
Buckminsterfullerene	C_{60}	721
C_{70} fullerene	C_{70}	841
JSC159	C_5F_{11}-Ala-Trp-Ala-C_8F_{17}	1,115
JSC171	C_8F_{17}-Ala-Ala-Trp-C_8F_{17}	1,265
Functionalized oligoporphyrin	$C_{707}H_{260}F_{908}N_{16}S_{53}Zn_4$	26,809

Table 3: *A selection of the atoms and molecules that showed interference throughout this work in order of increasing mass. The given mass is always the isotopic average, and only representative molecules from the library of tripeptides and oligoporphyrins are shown.*

The different species were used for various purposes: fullerenes were initially used for aligning the interferometer and later in electric polarizability studies, cesium as a calibrant for the polarizability measurements and later for magnetic gradient measurements, and the tripeptides (functionalized Ala-Trp-Ala and Ala-Ala-Trp) were used in a polarizability study of structural isomers. The alkaline-earth elements barium and strontium were used for magnetic susceptibility measurements, as were the polycyclic aromatic hydrocarbons coronene, anthracene, and adamantane. Tetraphenylporphyrin interference was shown during preparation of the high-mass interference experiments, and the oligoporphyrin library was used in the high-mass experiments discussed above.

Testing the weak equivalence principle across a large mass and complexity scale is an interesting prospect that is accessible in such a universal interferometer. There are predictions that gravity may couple differently to different isospins [120], and the isotopic distribution of a given species as well as the large mass and complexity range already demonstrated to show interference at LUMI may provide an interesting testing ground. A similar idea was explored in Reference [121], in which a time-domain Talbot-Lau interferometer was used to test the equivalence principle with various isotopes of tetraphenylporphyrin. In this previous work, the measured free fall accelerations a of the different test masses yielded an Eötvös parameter

$$\eta = 2 \frac{a_1 - a_2}{a_1 + a_2} \tag{76}$$

of 0.01, far from the precision levels probed by torsion balances [122] or dedicated atom interferometry experiments [123]. Tests at LUMI using the time-resolved interference technique, as employed for the Coriolis compensation measurements [59], indicated that a similar Eötvös parameter could be achieved with fullerenes, but dedicated gravity measurements were not intensively pursued.

There are two primary challenges in using LUMI or a similar experiment for precision equivalence principle tests with massive molecules. First, generating a molecular flux sufficiently intense and stable for precision experiments is a challenge for molecules heavier and more complex than fullerenes. Second, the orientation of the gratings in LUMI is nearly parallel to gravity to minimize the velocity-dependent gravitational/Coriolis phase shift, which naturally makes LUMI in its current configuration less than optimal for gravity-related measurements.

4.6 Interferometric dark matter searches

There has been a recent surge of interest in applying matter-wave interferometry to cosmological questions. Potential dark energy interactions such as chameleon fields have recently been probed by atom interference experiments [124,125], while dark matter parameter space may be constrained using proposed long-baseline atom interferometers [126,127]. There are also ambitious proposals for applying high-mass interferometry to the search for dark matter [128,129] and in using long-baseline atom interferometers to detect gravitational waves in an unexplored frequency band [130,131].

Several proposals [132,133] aimed at the existing time-domain Talbot-Lau interferometer in Vienna take advantage of the interferometer's inherent high sensitivity to small momentum kicks to search for interaction with light dark matter. The arguments apply equally well to the LUMI experiment, which was not operating at the time of the proposals, and which is potentially well suited for such searches given its long-term stability and ability to interfere the highest masses to date.

The advantage of using high-mass particles to search for dark matter interactions lies in the expected coherent scattering enhancement of the scattering rate by the square of the number of nucleons in the test particle, similar to the amplification mechanism in collapse models as described in Chapter 2. This quadratic increase is expected when the superposed test particle is smaller than $\lambda_{dB}/2\pi$ of the dark matter particle, where the nucleons in the test particle can be considered to recoil together as in the Mössbauer effect. In other regimes one can expect partial or no scattering enhancement [132]. The use of decoherence as a detection mechanism offers a high sensitivity to processes with low momentum transfers, since to resolve a superposition with spatial extent Δx the momentum transferred only needs to be of order $1/\Delta x$. A high-mass interference experiment would be best suited to search for a dark matter particle with a mass below 100 MeV and a scattering cross section down to 10^{-22} cm^2 which interacts with matter via a new long-range interaction [133].

Optomechanical systems offer another platform for coherent quantum manipulation of massive systems, which one may also envision as a potential probe for dark matter. While such systems can be cooled to their vibrational ground states [134], the spatial extent of the superpositions achieved is typically limited to femtometers, much smaller than the extent of the system itself. This strongly limits their sensitivity when compared to the superposition extent achieved in interferometers like LUMI, which at 10^{-7} m is several orders of magnitude larger than the diameters of the interfering molecules themselves.

The main signature of interaction with dark matter particles would be a slight reduction in interference visibility, since a dark matter particle interacting with a superposed test particle via the hypothesized interaction should act as a soft form of collisional decoherence. The decoherence would vary periodically with the sidereal day as Earth moves through a dark matter wind, with the Earth itself shielding the interferometer from the dark matter flux as it rotates. A small fringe deflection may also be expected in some regimes. However, the resulting decoherence or deflection is expected to be small, and strongly dependent on the type of dark matter particle, the local shielding, and the mass of the interfering test particle.

A proof-of-principle test of the stability of LUMI over several days was done with C_{70}, in which four interference scans were performed nearly uninterrupted over the course of two days. The optical cavity described in Chapter 3 provided efficient detection which allowed us to keep the oven at a stable temperature throughout the measurement without depleting the sample. The KDTLI scheme was used for these measurements, and C_{70} was chosen over C_{60} since it saturates at lower intra-cavity power, thus allowing a more stable lock over the course of the measurements. To preserve the material gratings, they were automatically withdrawn from the beamline after a series of four interference scans which were repeated every 41 minutes. The

extracted visibility is plotted in Figure 51, showing a standard deviation of the mean of 0.2% over 46 hours.
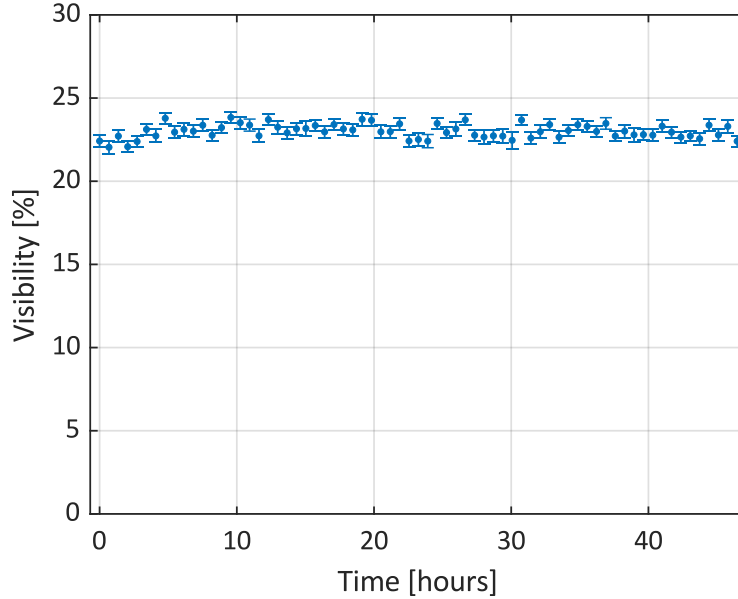
Figure 51: *Stability of C_{70} interference over 46 hours. Every 41 minutes for two days the material gratings were lowered into the beamline and four consecutive interference scans were made. Each point is the average visibility of the four scans with 68% confidence intervals of the fitted sine amplitudes.*

These measurements show that LUMI is indeed a stable instrument, although the stability was tested in an optimistic scenario. For the high masses necessary to place significant bounds on the dark matter parameter space, it will likely be significantly more challenging to produce the intense, stable, and long-lived flux and efficient detection that are relatively straightforward with a molecule like C_{70}.

Another legitimate concern is that the presence of anomalous decoherence is not definitive evidence of a dark matter particle. While it would be suggestive of cosmic origin if the decoherence rate varied with the sidereal day, it would be experimentally challenging to differentiate a sidereal period from the four minute longer solar day. Careful monitoring of the environmental conditions of the setup would be required to rule out slight day-to-night variations in laboratory conditions which may contribute to a periodically varying decoherence rate. Additionally, interferometers or interferometer arrays with variable orientations, at varying altitudes, and with variable levels of shielding could provide more suggestive evidence of a cosmic origin if a signal were to be detected.

5 Quantum-assisted metrology

This chapter discusses three types of metrology experiments performed at LUMI: electric deflection in an $(\boldsymbol{E} \cdot \nabla)E_x$ field, magnetic deflection in a $(\boldsymbol{B} \cdot \nabla)B_x$ field, and contrast revivals in a ∇B_x field. From these experiments, values for the static electric polarizability, magnetic susceptibility, and permanent magnetic moment can be extracted, respectively. The theoretical framework for these measurements has been laid out in Chapter 2.

The main advantage in using matter-wave interferometry to probe atomic and molecular properties lies in the spatial resolution gained via monitoring the interference fringes, which makes the technique orders of magnitude more sensitive than classical beam deflection. To illustrate this, let us conservatively assume a 10 nm resolution limit Δx_{min} in the fringe deflection, which would make LUMI sensitive to forces as small as

$$F_{min} = m\Delta x_{min} \frac{v^2}{L^2}, \tag{77}$$

which can be derived by inserting a constant acceleration into Equation 17. For strontium, the lightest atom used at LUMI to date, at 700 m/s, this gives $F_{min} \approx 10^{-27}$ N. This assumes a force acting along the entire length of the interferometer, while in the metrology experiments here it is only applied over a smaller region. Still, in the magnetic deflection measurements a force as small as 10^{-26} N is directly measured via fringe deflection [89]. The ability to use a large range of species in LUMI is another attractive feature for metrology experiments. It enables both calibration with atomic species for improved precision measurements with molecules and opens the door to the study of a larger range of properties.

Results that are the subject of publications [89,91,135] will be treated only briefly, with an emphasis on unpublished details and preliminary data. The coordinate system used for interference measurements in this section is the one defined in Figure 17 rather than the one in Figure 9, leading to a sign reversal of the x-axis with respect to previous interference data in this thesis, for consistency with published results.

5.1 Electric deflection

The main results of the electric deflection studies have been published in Reference [91,135], and the theoretical framework provided in Chapter 2. The electrode used for these experiments in LUMI is the same device described in detail in Reference [54], whose key feature is a highly uniform $(\boldsymbol{E} \cdot \nabla)E_x$ field. The voltage was supplied by a high voltage power supply (Stanford Research Systems model PS350), and deflection scans were done by switching between a low reference voltage (typically 250 V) and a higher deflection voltage at each transverse position of an interference scan to minimize the effect of any phase drift over the course of the scan.
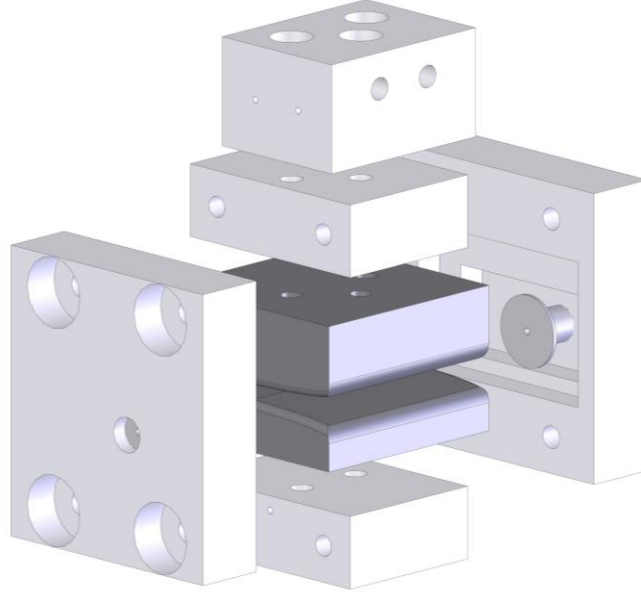
Figure 52: Exploded view of the electrode in LUMI, originally designed for and used in the previous KDTLI experiment. White parts are ceramic, and the curved metallic surfaces provide the fields. Small grounded metallic inserts at the entrance and exit prevent charge buildup on the ceramic components from affecting the performance.

5.1.1 Cesium calibration

The universality of LUMI allows for atomic calibration of metrology devices for improved molecular measurements. In the case of static polarizability, alkali atoms are excellent candidates, since it is straightforward to form thermal beams with them and their polarizabilities have been accurately measured [136]. Additionally, they are simply and efficiently detected with Langmuir-Taylor ionization due to their low ionization energies.

The oven used for cesium as well as the rhenium hot-wire detection are described in Chapter 3. Unlike with the alkaline-earth elements used in the magnetic measurements, the residence time delay on the wire surface was not an issue for cesium, since the associated times are typically orders of magnitude shorter than for the alkaline-earths [102].

Due to the high speed and low polarizability of the cesium, the all-material TLI scheme was preferable to a KDTLI for these experiments. The beam was deflected in the electrode with voltages up to 3500 V, and a time-resolved interference scan was taken for each deflection voltage. Using the known polarizability of cesium and the observed deflection of each velocity class, an overall calibration factor for the deflection, as given by Equation 64, can be empirically determined. The measured calibration factor K' is defined as

$$K' = KK_E = \left(LL_1 - \frac{L_1^2}{2} - L_1L_2 \right)K_E, \tag{78}$$

where K is the geometric factor from Equation 59 and K_E is the electrode factor from Equation 63. Note the slight redefinition of K' without the factor of $2\pi/d$ as compared to Reference [91]. We extract $K' = d/2\pi \times (500.42 \pm 0.18)$ m^{-2}, which allows one to also estimate $K_E \approx d/2\pi \times$ 15,300 m^{-4}, with $d = 266.1$ nm.

5.1.2 Fullerenes

The cesium-calibrated system was then used for electric deflection of fullerenes. The efficiency of the cavity-enhanced thermal ionization coupled with the cesium calibration reduced both statistical and systematic errors compared to previous measurements [88,137,138]. The KDTLI scheme was used due to the higher visibilities available with a phase grating when working with the slower and highly polarizable fullerenes. The slightly different inter-grating spacing used for the KDTLI and the TLI, as illustrated in Figure 53, must be considered in the analysis of the deflection, since the geometry of the setup enters through the calibration factor K which is not identical in the two schemes. Defining $L_{KDTLI} = L$ and $L_{TLI} = L + \Delta z$, the difference in the overall calibration factor K' can be written

$$K'_{KDTLI} = K'_{TLI} \frac{L - \frac{L_1}{2} - L_2}{L - \frac{L_1}{2} - L_2 + 2\Delta z}.$$

(79)

Given the KDTLI lengths $L = 0.98$ m, $L_1 = 0.04$ m, $L_2 = 0.15$ m, the calibration factor for deflection measurements in the KDTLI mode is therefore adjusted slightly downward from the measured TLI value by $K'_{KDTLI} = 0.995 K'_{TLI}$. This small correction is the main dependence of the extracted deflection on the geometry of the setup, which illustrates the advantage of the cesium calibration technique, since the lengths have significantly larger error bars than the polarizability of cesium.
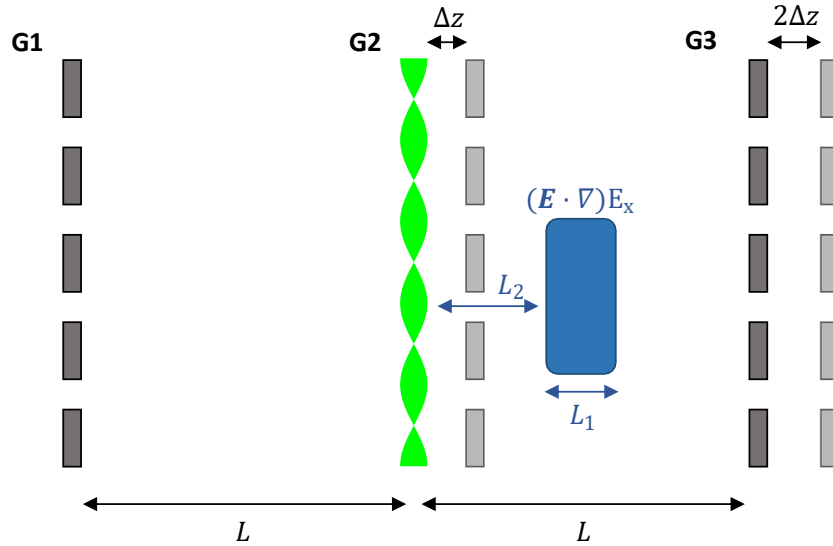
Figure 53: *Geometry difference of the TLI and KDTLI schemes. The first grating is in the same position, while the optical phase grating of the KDTLI is positioned slightly in front of the material second grating of the TLI (grayed out). The third material grating is thus moved back by twice this offset compared to its KDTLI position in order to keep the inter-grating separation G1-G2 equal to G2-G3.*

Several mean velocities were gravitationally selected to allow us to estimate the statistical uncertainty. The deflection dataset for C_{60} is shown in Figure 54, with fits to Equation 61 yielding the polarizability for each velocity class. The resulting mean polarizability values are

$\alpha_{C60} = 4\pi\varepsilon_0 \times (87.4 \pm 0.4 \pm 2.5) \text{ Å}^3$ and $\alpha_{C70} = 4\pi\varepsilon_0 \times (106.4 \pm 0.2 \pm 1.1) \text{ Å}^3$ with the first error statistical and the second systematic. These numbers are in good agreement with previous values, in particular with those obtained via a similar interferometric method [88].
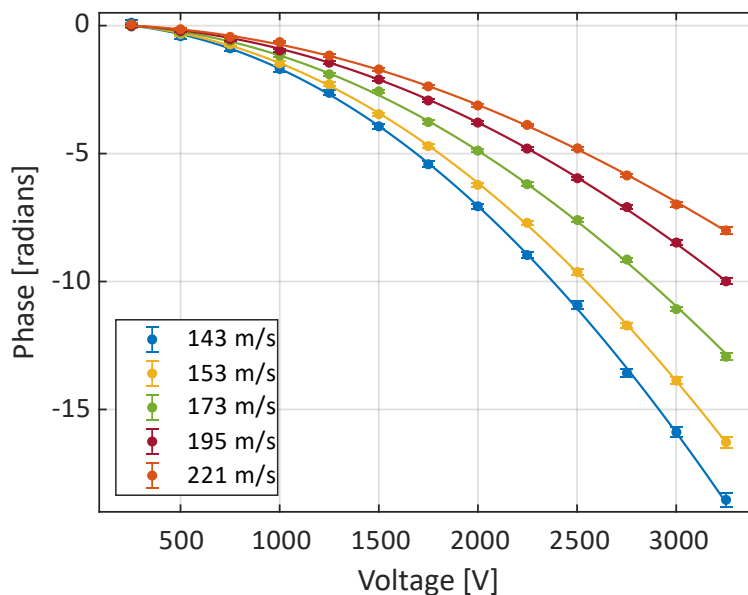
Figure 54: *Deflection of C_{60} as a function of voltage for various mean velocities with 68% confidence intervals of the fitted phases, albeit barely visible on this scale. Solid lines are best fits of the polarizability, taking the velocity distribution into account. Figure adapted from Reference [91].*
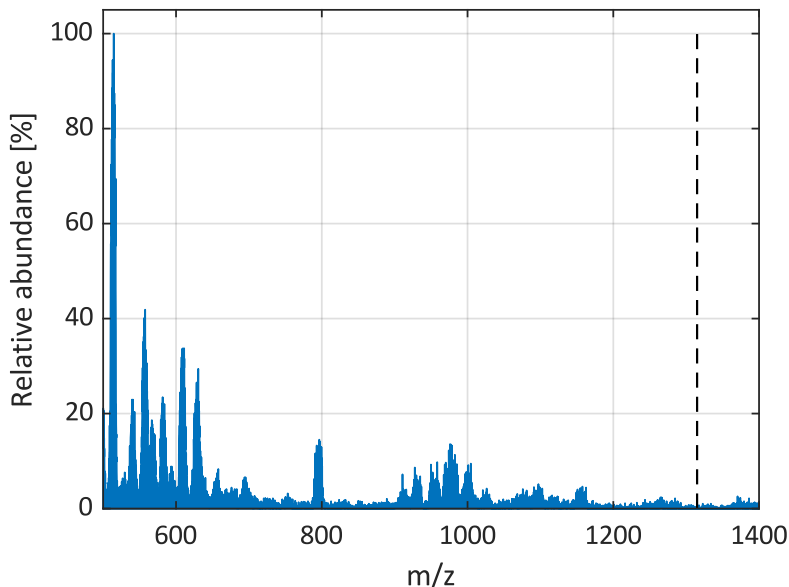
5.1.3 Tripeptides

Collaborators at the University of Basel[8] synthesized sequence isomers of various tripeptides with protective perfluoroalkyl chains of various lengths. The motivation behind working with these molecules at LUMI is twofold. First, demonstrating quantum interference with peptides is an interesting prospect in itself due to the biological nature of these molecules [139]. Second, the hope was to distinguish the sequence isomers by interferometric-assisted electric polarizability measurements, similar to the classical beam deflection measurements of peptides in Reference [140], but with the improved resolution available at LUMI.

A long series of tests, beginning at the KDTLI predecessor to LUMI [110], showed that the experiments were more challenging than anticipated. In particular, the molecules suffered from severe fragmentation in thermal sources, limiting both the absolute flux available and the lifetime and stability of the signal available for interference experiments. A summary of the beam test results is given in Table 4. The thermal beam signal typically lasted for less than an hour, although fragments that appeared at lower temperatures during the heating period could be used to align the laser grating, allowing us to preserve material. A sample mass spectrum showing the large amount of thermal fragmentation is shown in Figure 55.

---

[8]Dr. Jonas Schätti and Dr. Valentin Köhler, Department of Chemistry, University of Basel

Name	Sequence	Interference	Deflection	Beam
JSC159	C_8F_{17}-**Ala**-**Trp**-**Ala**- C_5F_{11}	Yes	$4\pi\varepsilon_0 \times 325$ Å^3	Thermal
JSC171	C_8F_{17}-**Ala**-**Ala**-**Tp**-C_8F_{17}	Yes	$4\pi\varepsilon_0 \times 270$ Å^3	Thermal
JSC172	C_8F_{17}-**Ala**-**Trp**-**Ala**-C_8F_{17}	Yes	Noisy	Thermal
JSC173	C_8F_{17}-**Trp**-**Ala**-**Ala**-C_8F_{17}	--	--	Weak signal (thermal)
JSC531A	C_5F_{11}-**Trp**-**Gly**-**Lys**-C_5F_{11}	--	--	No intact signal (thermal)
JSC531B	C_5F_{11}-**Trp**-**Lys**-(C_5F_{11})-**Gly**	--	--	No signal (laser desorption)
JSC532 short	C_4F_9-**Trp**-**Gly**-**Lys**-C_4F_9	--	--	No intact signal (thermal)
JSC532 long	C_8F_{17}-**Trp**-**Gly**-**Lys**-C_8F_{17}	--	--	No intact signal (thermal)
JSC549_1	C_4F_9-**Pro**-**Ala**-**Trp**-C_4F_9	--	--	Thermal
JSC549_2	C_8F_{17}-**Pro**-**Ala**-**Trp**-C_8F_{17}	Yes	Noisy	Thermal
JSC549_3	C_8F_{17}-**Trp**-**Pro**-**Ala**-C_8F_{17}	--	--	Weak signal (thermal)
JSC549_4	C_8F_{17}-**Tyr**-**Gly**-**Trp**-C_8F_{17}	--	--	No intact signal (thermal)
JSC549_5	C_8F_{17}-**Tyr**-**Trp**-**Gly**-C_8F_{17}	--	--	Weak signal (thermal)

Table 4: *Summary of the various tripeptides synthesized in Basel and tested at LUMI. Three groups of isomers with varying amino acids and perfluoroalkyl chain lengths. All contain tryptophan, as this was previously shown to be beneficial for efficient photoionization. Details on the synthesis and structure of the first four molecules can be found in Reference [141] and the others in [135]. The first compound also showed interference with 8% visibility in the KDTLI predecessor to the LUMI experiment.*

Figure 55: *Example of tripeptide thermal fragmentation. Mass spectrum of C_8F_{17}-Trp-Pro-Ala-C_8F_{17} showing the large amount of fragmentation with a thermal source at 530 K. The expected intact mass of 1315 u is indicated by vertical dashed line.*

Successful interference experiments were made with four different tripeptides, although only a few compounds were sufficiently stable for electric deflection experiments. The measured quantity in these experiments is the electric susceptibility χ_{el} as given by Equation 65, the dynamic dipole moments of such molecules may play a role [50,51,142]. In particular, we could compare the susceptibilities of Alanine-Trpyptophan-Alanine (Ala-Trp-Ala), labeled *JSC159* and *JSC171* in Table 4. The measured susceptibilities of the two Ala-Trp-Ala sequences (not strictly isomers since *JSC159* contained asymmetric chain lengths) are given in Table 4. The susceptibilities where not significantly different given the large error bars on this measurement due to the poor signal to noise ratio [135], although with an improved signal to noise ratio the technique should allow us to differentiate sequence isomers of peptides [140].

5.2 Magnetic deflection

Nearly analogous experiments to the electric deflection studies can be performed with magnetic fields to probe magnetic susceptibility. By applying a $(\boldsymbol{B} \cdot \nabla)B_x$ field, the interference fringes of a particle with no permanent magnetic moment are deflected according to its magnetic susceptibility, which is typically a diamagnetic repulsion toward regions of smaller magnetic field in the absence of a strong Van Vleck paramagnetic term.

The presence of a permanent magnetic moment, even on the order of a nuclear magneton, reduces the visibility in a $(\boldsymbol{B} \cdot \nabla)B_x$ field unless the moment is aligned to the field. Interestingly, this provides a route toward efficient sorting of nuclear isotopes in a beam without the need to ionize them. In the case of planar molecules, there is also a small alignment effect in the field due to rotational magnetic moments, which, combined with the anisotropic susceptibility tensor, complicates the interpretation of the measured deflection.

The magnetic deflection experiments are particularly demanding due to the requirement for excellent phase stability over the course of the measurement. In the electric deflection measurements each point of an interference curve was referenced with a low-field measurement, while here the reference measurement could only be made by manually withdrawing the permanent deflection magnet from the beam, a procedure which for practical reasons could not be done at each position step. Instead, the reference scan was made only after complete interference scans made with the magnet, making the measured deflection susceptible to phase drifts that may occur during the time the magnet is being inserted or withdrawn. While a constant drift can be compensated in post-analysis, we found that under stable conditions the drift was negligible over the time intervals concerned. Care also had to be taken to avoid mechanical shocks to the interferometer chamber when inserting or withdrawing the deflection magnet. The reproducibility of the phase shift was experimentally confirmed by repeating the deflection measurement several times, with the reference and deflected phase returning to the same values on each run.

The main results of the atomic magnetic deflection experiments have been published in Reference [89] while magnetic studies of molecules are still ongoing and are discussed below.
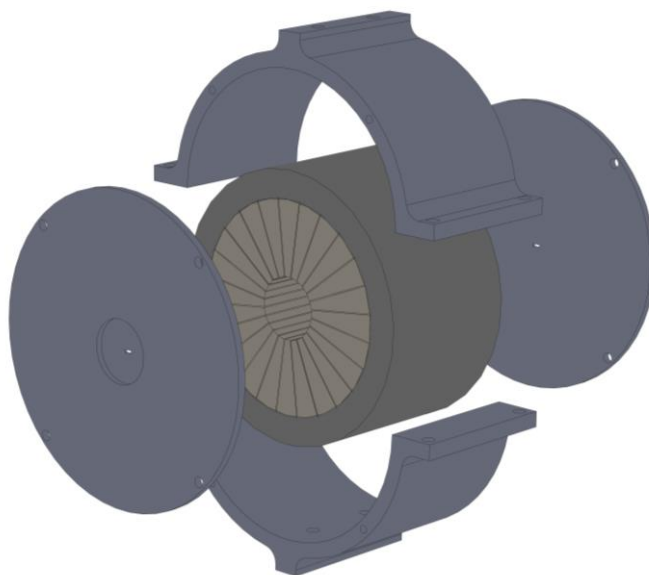
Figure 56: *Exploded view of the permanent deflection magnet, its casing, and the alignment apertures. It is mounted on a vertical translation stage allowing it to be withdrawn or inserted into the beamline as needed.*

5.2.1 Magnetic deflection of alkaline-earth elements

As with the electric deflection, atoms provide a useful benchmark for metrology experiments since they are easier to work with both experimentally and theoretically. In this case, alkaline-earth elements are ideal candidates since they are closed-shell and thus have no magnetic moment associated with an unpaired electron spin nor do they exhibit Van Vleck paramagnetism. Additionally, they can be efficiently ionized with the same Langmuir-Taylor detector already employed for the cesium electric deflection measurements. As already

discussed in Chapter 3, care must be taken to avoid long residence times of the atoms on the wire surface from spoiling velocity measurements.

The phase shift between interference fringes collected without the magnet compared to with the magnet inserted are shown in Figure 57 for both barium and strontium. The all-material TLI scheme was used due to the high beam velocities and low polarizabilities of the atoms. The extracted diamagnetic susceptibilities are $\chi_{Ba} = (-5.8 \pm 0.2 \pm 0.4) \times 10^{-9}$ m^3/kg and $\chi_{Sr} = (-7.0 \times 10^{-9} \pm 0.3 \pm 0.7) \times 10^{-9}$ m^3/kg for barium and strontium respectively, in excellent agreement with theoretical predictions[9]. The velocity-dependent visibility function of a TLI was required for weighting the various velocity classes in order to calculate the susceptibilities from the measured phase shifts. This was calculated using a retarded C$_4$ potential to model the interaction with the grating walls [37], using the literature values for the polarizability of barium and strontium [144].
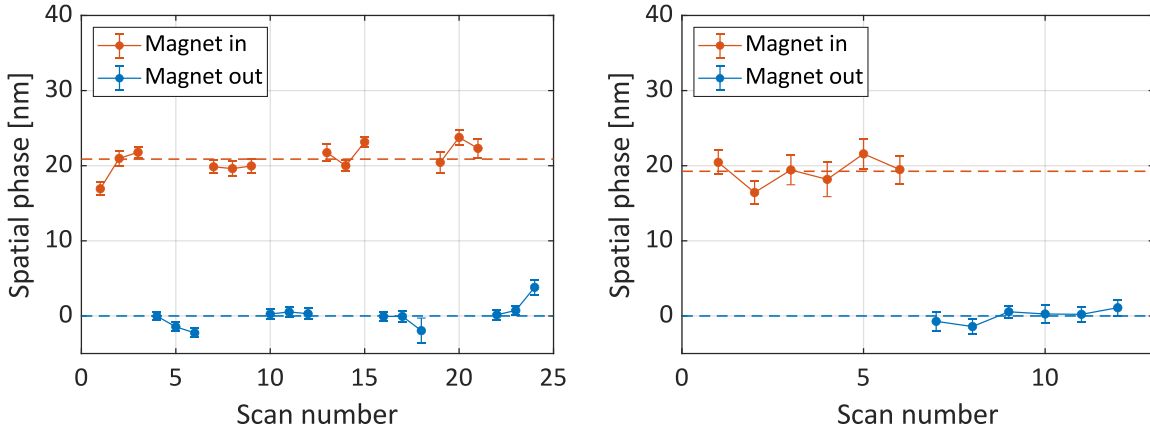
Figure 57: *Phase shifts of the barium and strontium interference fringes upon insertion of the deflection magnet with 68% confidence intervals of the fitted phases.* ***Left:*** *Extracted phases of barium interference, without the magnet inserted into the atomic beam (blue, bottom), and with the magnet inserted (red, top). The connected dots indicate the order of measurements: three measurements with the magnet in, then three with the magnet out, and repeated three times. This confirms the reproducibility of the phase shift upon insertion and withdrawal of the magnet. Dashed lines indicate the mean spatial phase relative to the magnet withdrawn case.* ***Right:*** *As on the left, but for strontium. This data was collected in two runs, i.e., six consecutive measurements with the magnet inserted followed by six consecutive measurements with it withdrawn. Figure adapted from Reference [89].*

The technique is intended to measure induced magnetic moments, while a permanent magnetic moment even on the order of a nuclear magneton completely dephases the interference fringes. This effect can be used as a means for sorting neutral isotopes, as demonstrated for strontium in Figure 58.

---

[9] As described in Reference [89], the theoretical values for the magnetic susceptibility of barium and strontium were calculated by density functional theory in Gaussian 16 [143], employing magnetic field dependent gauge-independent atomic orbitals.
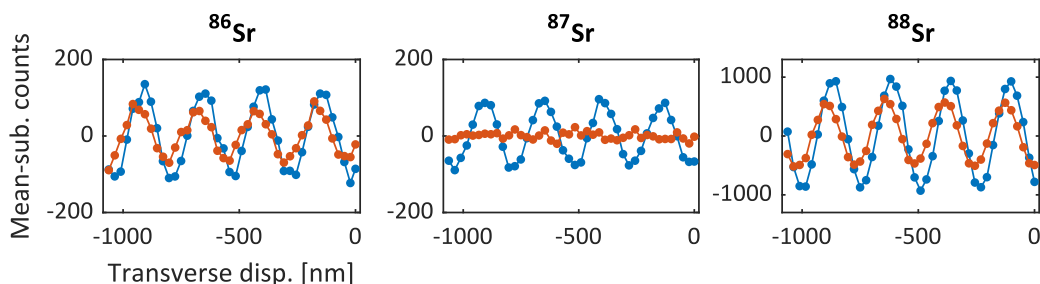
Figure 58: *Isotope-dependent interference of strontium. Nine consecutive interference scans were averaged to produce this data, with blue dots showing the reference visibilities without the magnet, and red dots with the magnet inserted in the beam. The visibility of ^{87}Sr is reduced due to the presence of a nuclear magnetic moment, while the diamagnetic deflection of the even isotopes is visible as a slight shift of the fringes to the left. With the magnet inserted, one can enhance the proportion of even isotopes in the transmitted beam by positioning the third grating at a maximum of the even isotopes' sine curve, and vice versa at the minimum.*

5.2.2 Magnetic deflection of molecules

Molecules often offer richer physics than atoms due to the large number of vibrational and rotational states available to couple with external fields. In the context of magnetism, the nature of the chemical bonding also plays a role, for example in aromatic and anti-aromatic systems. Aromaticity is often found in flat, ring-based structures such as anthracene ($C_{14}H_{10}$), which results in a highly asymmetric susceptibility tensor, with the out-of-plane component typically much larger than the in-plane components due to induced ring currents as illustrated in Figure 59. In fact, the anisotropy of magnetic susceptibility

$$\Delta \chi = \chi_{33} - \frac{1}{2}(\chi_{11} + \chi_{22}) \tag{80}$$

is sometimes used as a criterion of aromaticity [145].
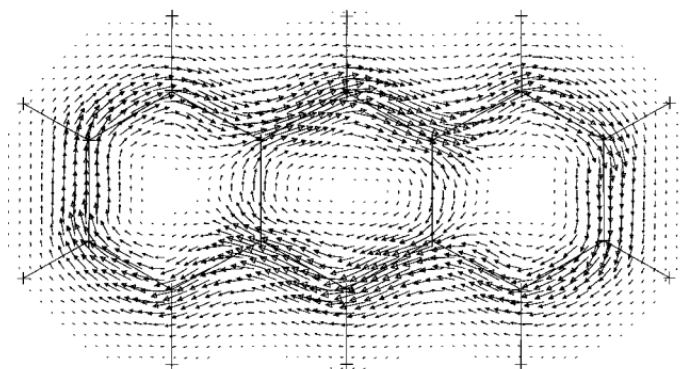
Figure 59: *Direction and magnitude of induced π-current above an anthracene molecule due to a magnetic field pointing out of the page. The out-of-plane induced field is 3-4 times larger than the in-plane components [146] due to induced ring currents, which causes the molecule to feel a torque in a magnetic field even in the absence of a permanent magnetic moment. Image taken with permission from Reference [146].*

Magnetic deflection of molecules at LUMI is more experimentally challenging than the analogous experiments with atomic beams. Since the magnetic field strength is fixed by the permanent magnet, the only way to control the magnitude of the deflection without moving the longitudinal position of the magnet is by varying the beam velocity. Deflections below 50 nm are preferred to maintain high interference visibility, which corresponds to beam velocities faster than thermal given the susceptibilities of the molecules being considered. A heated Even-Lavie valve was used to create supersonic beams, as described in Chapter 3, which provides higher beam velocities while also offering some degree of velocity tunability. The velocity can be controllably reduced by reducing the backing pressure of the seed gas, thereby reducing the number of collisions and introducing a velocity slip compared to a high-pressure supersonic expansion. The choice of seed gas naturally also effects the beam velocity, with heavier noble gases leading to slower beams.
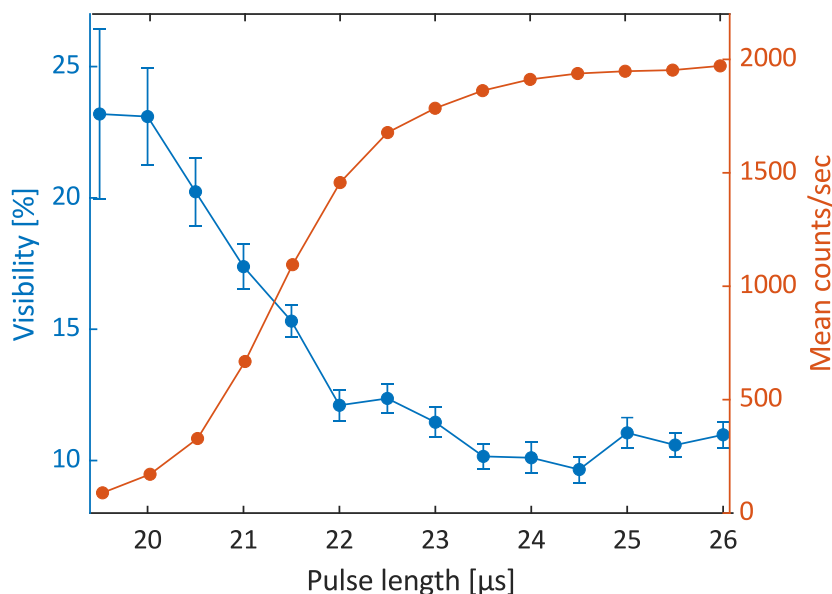
Figure 60: *Visibility loss of anthracene and mean count rate as a function of gas pulse length. This effect was apparent for several of the molecular species tested with the Even-Lavie valve and made magnetic measurements challenging since it required a significant tradeoff between beam flux and interference visibility, which are both further reduced upon insertion of the deflection magnet. Visibility values are shown with 68% confidence intervals of the fitted sine amplitudes.*

The gas load associated with this source creates a strong visibility dependence on the source parameters such as backing pressure, pulse length, and repetition rate, as shown in Figure 60 for anthracene. The source pressure in the chamber housing the valve, before two differential pumping stages separating it from the interferometer chamber, was typically between 3×10^{-6} and 3×10^{-5} mbar for these measurements and was linearly correlated with the pulse length. Somewhat mysteriously, the strong visibility dependence persists despite the pressure in the interferometer chamber being mostly unaffected due to the differential pumping stage separating it from the source chamber. We speculate that the cause is collisional decoherence due to the colinear seed gas pulse scattering from the material gratings or delimiter slits in the

interferometer. Maintaining high visibility therefore required us to work in a parameter regime with low flux, which made magnetic deflection measurements challenging given the further flux and visibility reduction upon insertion of the magnet.

In deflection experiments we are typically only sensitive to the isotropic susceptibility defined by Equation 50, even in the case of an anisotropic susceptibility tensor, because the molecules tumble freely through the magnetic field region, averaging over the tensor components. However, if the molecule has a preferred orientation as it traverses the deflection magnet, the measured susceptibility can be different from the isotropic value since the susceptibility tensor is not sampled uniformly. There are three distinct effects that may play a role in aligning molecules like anthracene during magnetic deflection experiments at LUMI.

First, it has been shown that in supersonic expansions planar molecules will be oriented such that they are preferentially flying like "frisbees" with their broad-side perpendicular to the direction of travel, due to collisions with the seed gas during the expansion. Alignment[10] in supersonic expansions was first shown in beams of alkali dimers [148] and later with benzene [149]. However, the effect is also strongly velocity dependent, with the faster molecules in the beam seeing a much higher degree of alignment than the slower ones [150]. The Even-Lavie valve used at LUMI to create pulsed supersonic beams was typically operated with low backing pressure to avoid decoherence, so this alignment effect is likely minimal in the presence of few collisions.

The second alignment effect which may play a role in these experiments is the torque due to a small rotational magnetic moment of the molecule. The origin of this moment can be easily derived for a rotating homonuclear diamagnetic diatomic molecule, in which the rotation of the nuclei leads to a magnetic moment proportional to the rotational angular momentum $\boldsymbol{J}$

$$\boldsymbol{\mu}_{rot}^{nuc} = \frac{Z\mu_N}{A\hbar}\boldsymbol{J} \tag{81}$$

with Z the atomic number and A the mass number [86]. The total rotational moment will be even smaller, since this nuclear component is partially compensated by an induced electron current, leaving a residual moment with a magnitude typically of order or smaller than a nuclear magneton [151]. In a molecule like anthracene, with its moment of inertia tensor largest in the out-of-plane-axis, rotations will primarily be excited around this axis at the low rotational temperatures of order 10 K which are produced in the pulsed supersonic beam. This leads to a rotational moment also around the out-of-plane axis, giving a torque $\boldsymbol{\tau} = \boldsymbol{\mu} \times \boldsymbol{B}$ that will serve to orient the molecule with the field. Although the magnitude of the moment is extremely small, it has already been demonstrated that a moment of order μ_N is sufficient to completely wash out interference visibility in the deflection magnet. For molecules with symmetric susceptibility tensors, this rotational moment will reduce the interference visibility since the resulting torque will not orient the molecule in any preferred direction. The resulting deflection from the magnet

---

[10] In this thesis the term "alignment" is used to describe both parallel and anti-parallel orientation with an external field, consistent with previous convention [147].

will then be distributed equally in both directions, leading to a washing out of the interference pattern as in the case of a non-zero nuclear or electronic spin.

Finally, there is also a torque due to the anisotropic susceptibility tensor of anthracene. A diagonal isotropic susceptibility tensor with $\chi_{11} = \chi_{22} = \chi_{33}$ leads to an induced moment proportional to $\boldsymbol{B}$ that does not experience a torque in a magnetic field, since $\boldsymbol{\tau} \propto \boldsymbol{B} \times \boldsymbol{B} = 0$. An anisotropic susceptibility tensor, on the other hand, yields a moment that does not point along $\boldsymbol{B}$, and thus experiences a torque in a magnetic field. In anthracene, $\chi_{11} \approx \chi_{22} \equiv \chi_{\parallel}$ and $\chi_{33} \approx 3.7\chi_{\parallel}$ (see Reference [146] and footnote[11]), the magnitude of the maximal torque is roughly proportional to the susceptibility anistropy $\Delta\chi$. Order-of-magnitude estimates indicate that this torque will be of a similar magnitude to the torque from the rotational magnetic moment discussed above.

A more quantitative estimate of the alignment due to these various effects would require more precise information about the rotational temperature of the anthracene molecules and the degree of alignment due to the supersonic expansion itself.
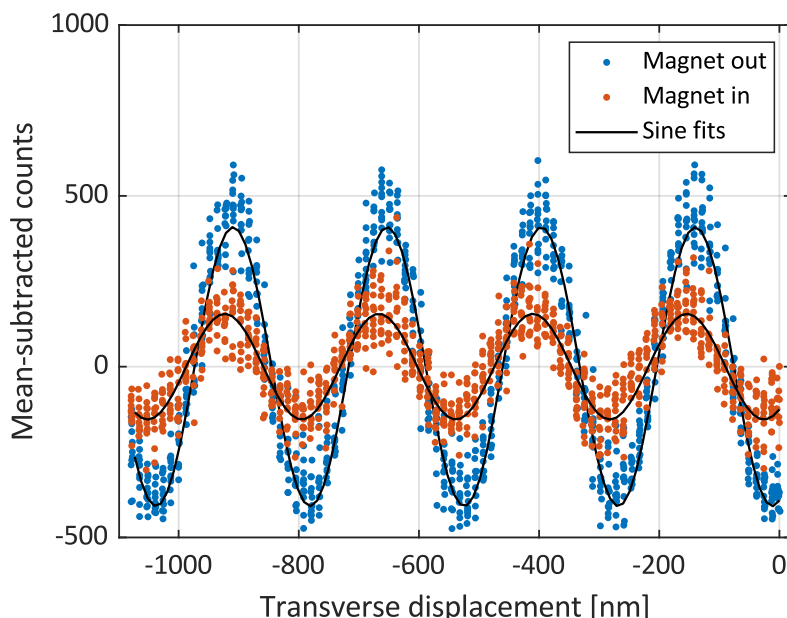
Figure 61: Magnetic deflection of anthracene. The data shown are 24 superimposed interference scans which were collected in four series of six scans, alternating between magnet inserted and magnet withdrawn, to confirm reproducibility in the phase shifts. A mean deflection of 14.5 nm is visible, along with a significant reduction in contrast upon insertion of the magnet. The extracted susceptibility is about 40% higher than the expected isotropic value, likely due to a combination of the three molecular alignment effects outlined above.

Deflection data for anthracene seeded with helium in the Even-Lavie valve is shown in Figure 61. Achieving a phase stable deflection measurement required a significant amount of source optimization, in particular to avoid the decoherence effect illustrated in Figure 60. The molecule sample was heated to 475 K, with a pulse length of 25.5 µs and repetition rate of 100 Hz. The collected signal was gated, as described in Chapter 3, with a peak velocity of 1105 m/s as shown in Figure 38. The mean deflection from this dataset is 14.5 ± 1.5 nm and yields a diamagnetic susceptibility of -1.33 × 10^{-9} m^3/kg, about 40% higher than the isotropic

susceptibility[11]. The calculation of susceptibility from the experimental deflection follows the same procedure as for barium and strontium, with a slightly modified TLI visibility function calculated using $4\pi\varepsilon_0 \times 26$ Å^3 for the polarizability of anthracene [152].

To better understand the anthracene results, a series of experiments were conducted with fullerenes and adamantane, since their symmetry (icosahedral and tetrahedral respectively) should almost entirely preclude the three alignment effects that may play a role for anthracene. However, velocity averaging in combination with strong visibility loss due to the high percentage of ^{13}C isotopes, washes out the interference visibility for thermal fullerenes after traversing the deflection magnet. The presence of ^{13}C isotopes, and thereby a non-zero nuclear spin, leads to a visibility reduction just like for ^{87}Sr in Figure 58. Additionally, the presence of rotational magnetic moments, which tend to align the anthracene molecules and enhance the measured susceptibility, instead cause a visibility reduction for symmetric molecules, as discussed above.

Potential solutions to this visibility loss include isotope selection in the QMS, time-resolved interference measurements, or improved velocity selection, but they all come with the cost of a large loss of flux. Increasing the beam velocity, however, would largely solve the velocity averaging issue without the corresponding loss in flux. Since the heated Even-Lavie valve used for anthracene could not tolerate the high temperature required for C_{60} sublimation, a continuous supersonic oven was designed and tested at LUMI. The oven itself is the one pictured in Figure 28, and the oven characteristics as a function of flow rate are shown in Figure **62**. Unfortunately, although the beam velocities obtained with the continuous supersonic oven were optimal for magnetic deflection with C_{60}, no combination of source parameters yielded a sufficiently high flux and visibility for phase stable deflection experiments.

Adamantane ($C_{10}H_{16}$) was then tested as an alternative to C_{60}, with the advantage of containing a smaller percentage of ^{13}C and thus less visibility reduction due to nuclear magnetic moments. Adamantane also sublimates in the temperature range available in the heated Even-Lavie valve and could be tested under very similar conditions as anthracene. Neon was used as the seed gas to provide a beam velocity well-suited to the expected susceptibility. As with the fullerenes, finding source conditions that yield phase-stable deflection proved challenging. Preliminary measurements which display a slight phase drift give a susceptibility value close to the expected isotropic value[12], which indicates that the enhanced measured anthracene

---

[11] Unlike barium and strontium which experience Pauli paramagnetism in bulk, it is expected that isolated anthracene should have the same susceptibility as its bulk counterpart. This was computationally confirmed by comparing the experimental value of -9.5×10^{-9} m^3/kg [103] to the theoretical ground state value of -9.2×10^{-9} m^3/kg. The theoretical value was calculated using density functional theory by Dr. Armin Shayeghi on the Vienna Scientific Cluster using the same methodology as in Reference [89], and yields an out-of-plane component 3.7 times the mean in-plane components. Ten geometries extracted from timesteps of an ab initio molecular dynamics simulation at 500 K yielded a mean susceptibility that agrees to within 1% of the ground state value (with a standard deviation of 1%), indicating that the finite temperature in the experiments can be safely neglected.

[12] The susceptibility of adamantane was calculated by Dr. Armin Shayeghi following the methodology in Reference [89], yielding a ground state value of -9.2×10^{-9} m^3/kg, with no significant difference between the diagonal tensor components.

susceptibility is indeed related to a rotational alignment in the magnet due to its planar, aromatic nature. This work is ongoing.
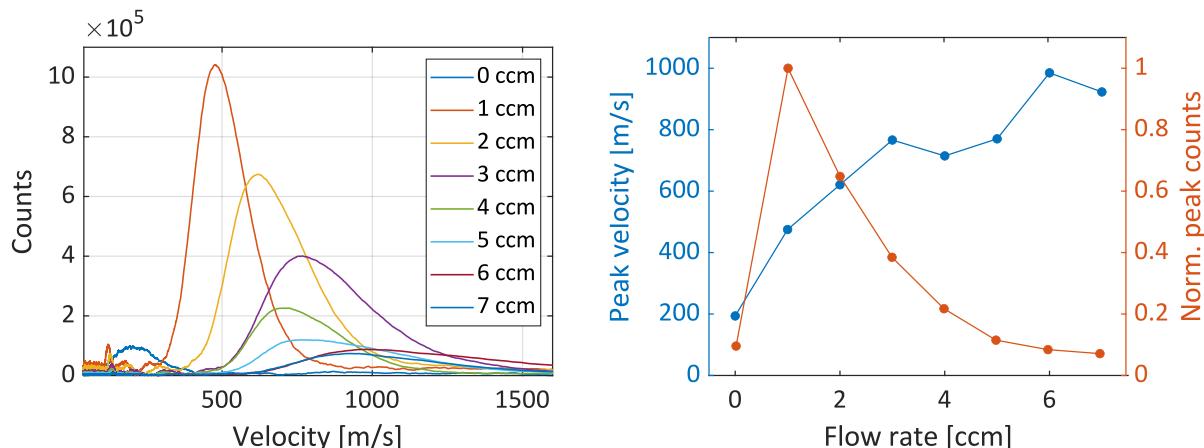

Figure 62: *Continuous seeded supersonic oven characteristics as tested with C_{60}.* **Left:** *velocity distribution as a function of argon flow rate.* **Right:** *Peak velocity (blue) and normalized peak counts (red) as a function of flow rate, showing a strong maximum at about 1 ccm, likely because at higher flow rates the corresponding source pressure, which reached 1.1×10^{-3} mbar at 7 ccm, was too poor for molecular beam formation.*

5.3 Anti-Helmholtz contrast revivals

The permanent deflection magnet allows us to study the induced magnetic moments of both atoms and molecules but is limited in several respects. First, the magnet's lack of tunability means that only binary measurements can be made, i.e. field on or field off, and the delay between the two measurements requires a high level of phase stability. While tuning the beam velocity in principle provides a means to tune the deflection, phase averaging at low velocities (large deflections) limits us to a small operational window of velocities for a given particle susceptibility. Second, as with the electric deflection measurements, permanent moments spoil the interference visibility. Finally, the closed design of the permanent magnet means there is poor optical access in the region of highest fields, which makes some experiments difficult, such as investigating the magnetic response of photo-switching in molecules.

To extend the magnetic metrology capabilities in LUMI, we implemented anti-Helmholtz coils in the setup[13]. These provide a ∇B_x field rather than a $(\boldsymbol{B} \cdot \nabla)B_x$ field, which yields a constant force on a permanent moment rather than an induced magnetic moment. As described in Chapter 2, tuning the coil current should lead to a dephasing and then rephasing of the interference visibility, with the functional form dependent on the level structure of the atom or molecule. The coils are illustrated in Figure 63.

---

[13] The design and characterization of the anti-Helmholtz coils was done together with Sebastian Pedalino.
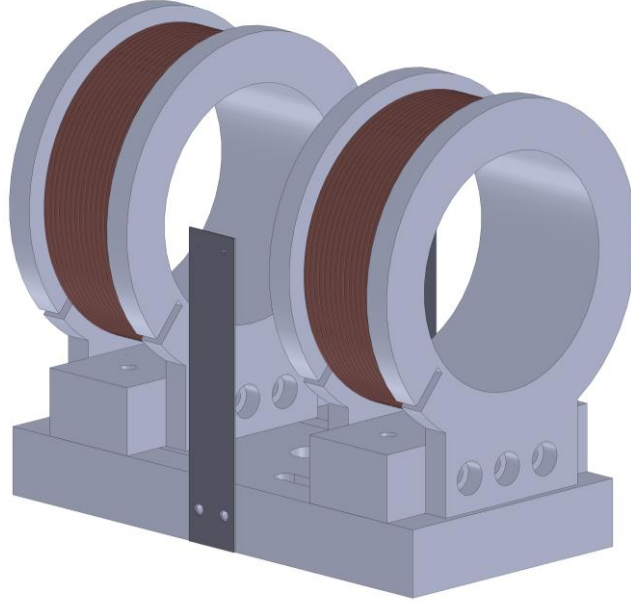
Figure 63: *The geometry of the anti-Helmholtz coils installed in LUMI which provide a constant transverse force on a permanent magnetic moment. The beam position is defined by two pinholes on the dark rectangular plates before and after the coils. The fields were characterized with a Hall probe before installation in LUMI.*

5.3.1 Cesium calibration

As with the electric deflection, cesium atoms are a convenient calibrant for the anti-Helmholtz coils due to the ease of creating and detecting a cesium beam as well as its simple electronic structure. With a nuclear spin $I = 7/2$ and a single s-shell outer electron, there are a total of 16 hyperfine states whose semi-classical trajectories must be considered, corresponding to 7 states from $F = 3$ and 9 states from $F = 4$ [153], as shown in the low-field regime of the energy splitting diagram Figure 64.
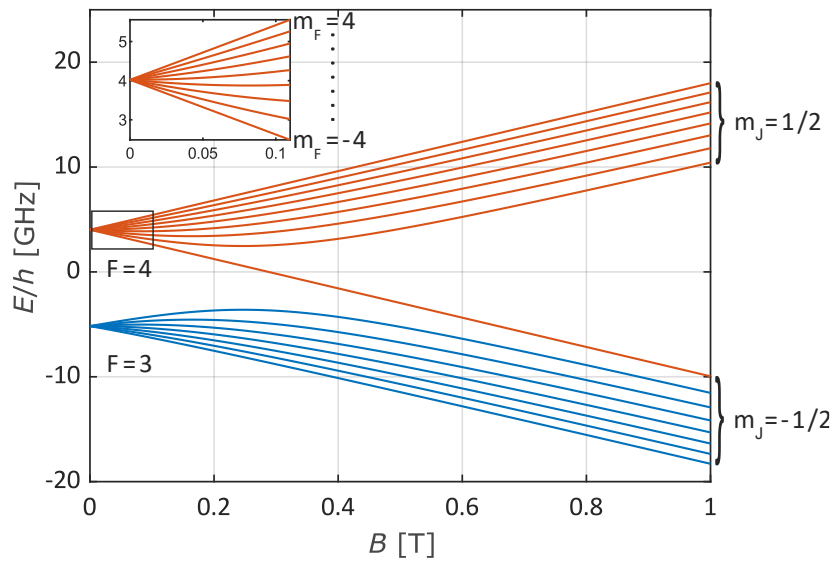
Figure 64: *Energy splitting as a function of applied magnetic field for $6^2S_{1/2}$ cesium, according to the Breit-Rabi formula. The anti-Helmholtz coils used in LUMI operate in the low-field regime*

98

where the energy splitting is linear in m_F, as displayed by the zoomed-in region for the $F = 4$ states. In the strong-field regime the levels are grouped according to m_J rather than F, in the so-called Paschen-Back effect.

A preliminary test of the anti-Helmholtz coils with cesium is shown in Figure 65. Interpretation of these results is complicated by the fringe fields of the permanent magnet used for the deflection experiments. Even when maximally withdrawn from the beamline, the fringe magnetic gradients resulted in significant visibility reduction of cesium interference. The effect could be largely mitigated by rotating the magnet by 90° such that the residual gradient was along the beam rather than transverse to it, but to eliminate any uncertainty regarding residual gradient the permanent magnet will be removed from the chamber entirely for a final calibration.
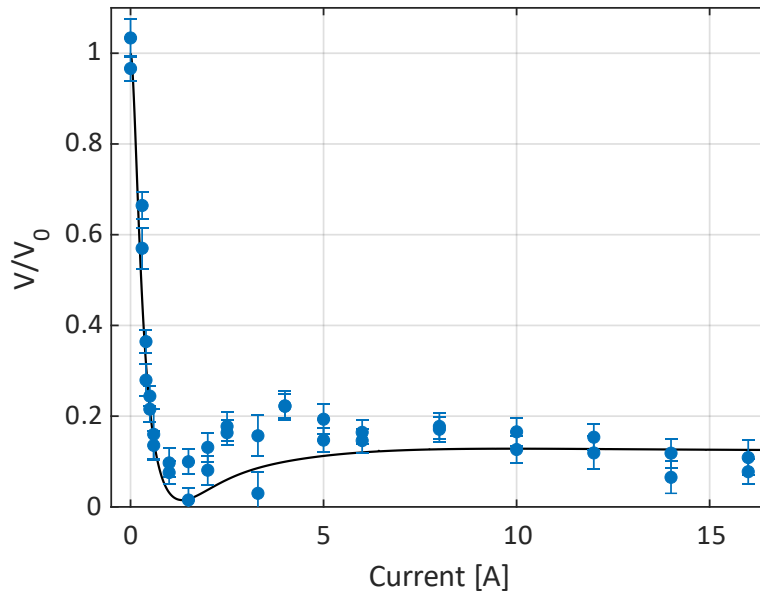
Figure 65: *Initial measurement with the anti-Helmholtz coils with a cesium beam. The theory and data asymptote to 1/8 of the initial visibility since only the two $m_{F=3,4} = 0$ sublevels out of the 16 hyperfine levels are not strongly deflected in high gradients and continue to contribute to the visibility. A drop in visibilities at high currents may be explained by thermal outgassing of the Kapton wire insulation contributing to collisional decoherence. At 20 A the pressure in the interferometer chamber rose by over an order of magnitude to the high 10^{-7} mbar range, and the local pressure in the vicinity of the coils may be significantly worse. Two scans at each current setting are shown, with 68% confidence intervals of the fitted sine amplitudes.*

5.3.2 Triplet state measurements (planned)

We plan to take advantage of the tunability and optical access of the coil design with excitation and photo-switching experiments in which a laser intersects the molecular beam as it traverses the coils, causing a conformational or electronic change that influences the molecules' magnetic response. To avoid a loss of interference visibility from the absorption of a photon transverse to the beam, the excitation light will cross the beam vertically with the use of a retroreflecting mirror. Fullerenes provide a convenient test system since they are efficiently excited to the

triplet state via inter-system crossing upon absorption of green or UV light. Similar experiments are being considered to investigate a proxy system for the radical pair mechanism that may be responsible for the impressive magnetic navigational sense of birds [154].

6 Future directions

This chapter outlines ongoing and planned work at the LUMI experiment, particularly in extending the interferometry mass record to particles with masses in excess of 100,000 u. Two schemes for metal cluster interferometry are described as well as the current status of an upgrade to the LUMI experiment.

6.1 Metal cluster interferometry

The use of metal clusters is a promising avenue toward scaling the current interferometer scheme to higher-mass particles. The reason for this optimism is due to the availability of several options to create intense neutral beams of metal clusters with masses ranging from 10^5 - 10^6 u. For example, magnetron sputtering sources yielding high fluxes of massive clusters are commercially available for use in nanocluster deposition systems. Metal cluster interferometry will also allow us to probe material properties as the clusters transition toward bulk properties with increasing atom number.

Sufficiently massive metal clusters are compatible with continuous optical depletion gratings as the grating mechanism in an upgraded version of LUMI. Clusters passing the standing wave antinodes would be ionized and removed from the beam to form a transmission grating, similar to the mechanism used for the pulsed gratings in the time-domain Talbot-Lau interferometer in Vienna [44]. Optical gratings are particularly appealing for high-mass interferometry because material gratings would become rapidly coated if subjected to the flux of a metal cluster source, as demonstrated in Figure 66.
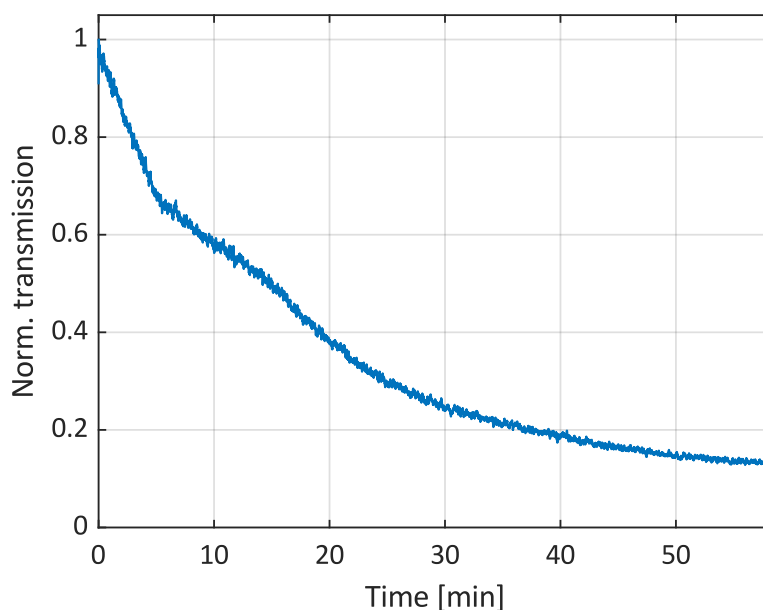
Figure 66: *The drop in transmission for a material grating placed 1 m in front of the cluster source for about an hour. The grating had similar specifications as the material gratings in LUMI, and the clusters were tantalum with a mass centered at about 9000 u. Although the absolute flux may not be exactly representative of the flux used in interference experiments,*

the rapid transmission drop still indicates an incompatibility of material gratings with the unfiltered output of metal cluster sources.

To determine the laser wavelength required to form depletion gratings for a given metal cluster type and mass, one needs to estimate the cluster ionization energy. A classical approach using the electron image charge potential [155] shows the ionization energy I approaching the bulk work function Φ for a cluster with N atoms,

$$I(N) \approx \Phi + \alpha e \left(\frac{4\pi\rho N_A}{3MN}\right)^{\frac{1}{3}} \times 10^{-9}. \tag{82}$$

Here, α is an empirical parameter, e the electron charge, ρ the mass density, M the molar mass, and N_A the Avogadro number. Although a semi-classical treatment shows that α is not strictly constant, experimental data shows that $\alpha \approx 3/8$ provides a good estimate for I, particularly for clusters with radii larger than 0.5 nm [156].

The calculated ionization energies for two different cluster materials, cesium and hafnium, are shown in Figure 67 for a range of cluster sizes. Cesium, with its particularly low bulk work function, would be suitable with depletion gratings formed with 532 nm light, while hafnium, along with a few other elements, would work with 266 nm depletion gratings. Details of the two different interferometer schemes are discussed in the following sections.
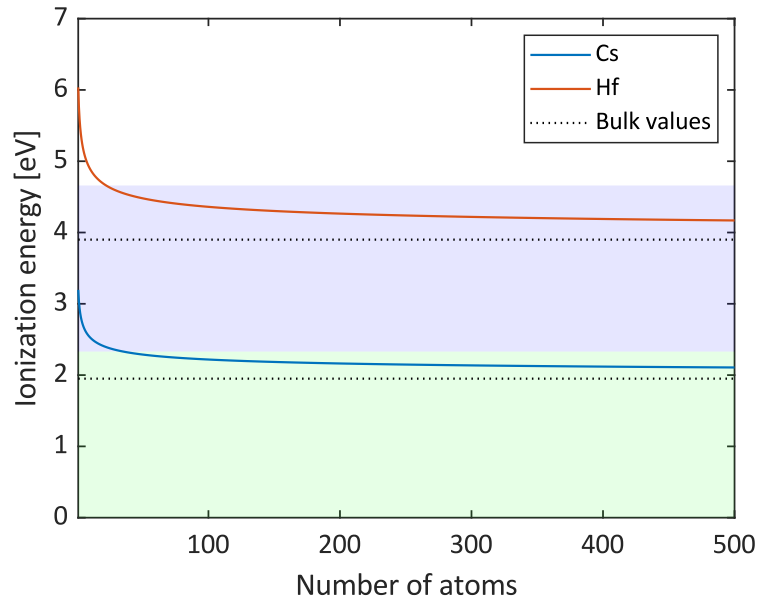
Figure 67: *Ionization energy and cross sections as a function of atom number for cesium (blue) and hafnium (red) metal clusters. Dotted lines indicate the bulk work functions for the respective elements. The lower green shaded region gives the energy range where green (532 nm) photons are sufficient for ionization, while this region together with the upper blue region give the energy range ionizable by blue (266 nm) photons.*

To estimate the efficiency of the depletion gratings one also needs to know the absorption cross section σ_{abs} of the clusters. This can be estimated by modeling the clusters as sub-wavelength spheres [157], giving

$$\sigma_{abs}(\lambda, N) = \frac{18\pi V \epsilon_2(\lambda)}{\lambda[(\epsilon_1(\lambda) + 2)^2 + \epsilon_2(\lambda)^2]} \tag{83}$$

where ϵ_1 and ϵ_2 are the real and imaginary parts of the relative permittivity respectively and V the volume of the cluster which implicitly contains the number of atoms N. There is additionally a dependence of the permittivity on cluster size [158], which becomes less significant for large clusters and is neglected for the moment. The number of absorbed photons is then given by

$$N_{abs} = \frac{P\lambda}{hc} \frac{\sigma_{abs}}{A} T \tag{84}$$

where A is the cross-sectional area of the laser beam and T is the flight time of the cluster through the beam. The estimated absorption cross sections and number of absorbed photons for cesium and hafnium clusters, using literature values for the permittivity, are shown in Figure **68**. The number of absorbed photons should be larger than one for efficient optical depletion gratings, which is easily achievable with cesium at 532 nm, and still possible for sufficiently massive hafnium clusters at 266 nm with experimentally available UV power.
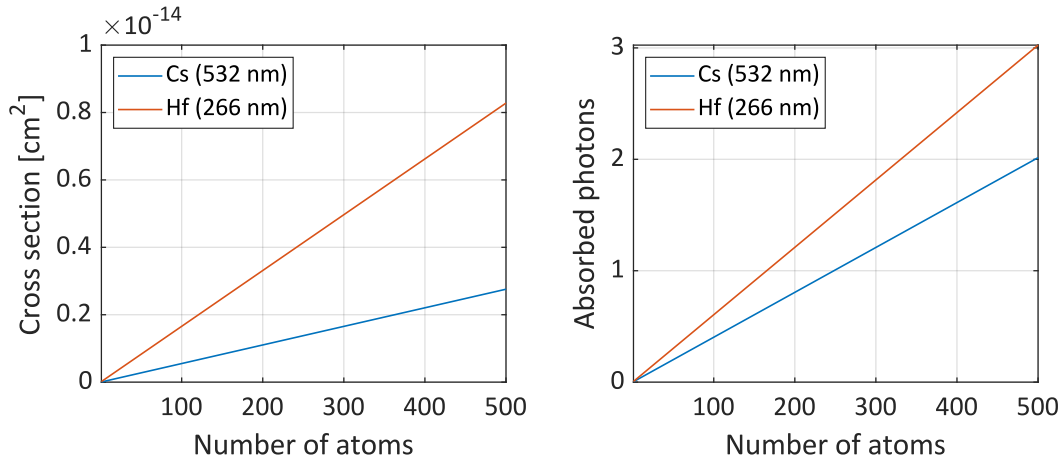
*Figure 68: Absorption properties of cesium and hafnium clusters. **Left:** Cross sections for cesium (blue) and hafnium (red). **Right:** Number of absorbed photons for cesium (blue) and hafnium (red), for a laser power of 0.3 W, beam waist of 0.7 mm, and beam velocity of 100 m/s.*

6.1.1 532 nm optical gratings with cesium clusters

By choosing a metal with a work function below 2.3 eV, continuous 532 nm standing light waves can be used to form optical depletion gratings, which is particularly appealing due to the accessibility of high-power 532 nm lasers. A closer look at the work functions of the elements quickly leads one to the conclusion that such a scheme would work best with cesium clusters, since cesium has a bulk work function of 1.95 eV [103]. While the work function of rubidium and sodium are both near 2.3 eV, Equation 82 shows that the cluster ionization energy will be larger, and therefore less efficient optical depletion gratings could be achieved with such clusters.

However, cesium brings with it several technical challenges. A conventional magnetron sputtering source cannot be directly employed for pure cesium clusters, since cesium melts just

above room temperature. Previous work has demonstrated the production of high-mass cesium clusters by means of thermal sublimation into an aggregation cell [159] and even pure vapor expansion [160]. Early tests[14] with a thermal source in a liquid nitrogen-cooled argon-seeded aggregation tube showed the production of high-mass clusters, albeit at the cost of a very high rate of material usage, with a gram of cesium completely used up within half an hour. The requirement for large quantities of such a volatile element is a significant downside to a cesium cluster interferometer. Additionally, an interferometer formed with three green optical depletion gratings would no longer be universal, since cesium is the only practical choice for such a scheme. For these reasons, focus has instead been placed on the use of UV optical depletion gratings, as discussed in the following section.

6.1.2 266 nm optical gratings with low-work-function clusters

An alternative to green depletion gratings is to frequency double the 532 nm light to produce high power continuous 266 nm gratings. This UV scheme is preferable for several reasons. First, there is a much longer list of elements with work functions below 4.7 eV, allowing us to choose more convenient elements than cesium. Elements can be chosen which are best suited to the needs of the interferometer scheme: compatibility with magnetron sputtering, low volatility and toxicity, high atomic masses, and non-magnetic. The second fundamental advantage of UV gratings is that the period of the standing light wave in such a scheme is 133 nm, and, as shown in Figure 5, a factor of four higher mass is accessible for a given inter-grating separation and beam velocity. Finally, UV gratings would be suitable not only for metal clusters but also for a range of organic molecules, potentially with photo-depletion tags for increased ionization efficiency. A reliable beam source of massive organic molecules is frequently an experimental bottleneck, and work into this topic is ongoing in Vienna.

Hafnium, with a standard atomic weight of 178.5 u and a bulk work function of 3.9 eV [103], is a good candidate for metal cluster interferometry with UV gratings. There are several other candidates, each with technical advantages and drawbacks, but hafnium provides a good starting point for testing the beam techniques that will be required for the LUMI upgrade.

6.2 LUMI upgrade

The experimental upgrade required for high-mass metal cluster interferometry at LUMI is discussed in more detail and the current status of the project is given.

### 6.2.1 Experimental details

The modified experimental setup is shown schematically in Figure 69. The cluster source assembly will contain up to two quadrupoles, with one to preselect the cluster masses and the other to transversely cool and longitudinally slow the cluster beam. Mass selection before the

---

[14] Cluster tests were performed together with Sebastian Pedalino and Dr. Philipp Geyer.

interferometer is desirable to avoid contamination of the interferometer chamber and to allow for the possibility of surface detection instead of transmission through a third grating. Surface detection, in which the clusters are collected on a slide in place of the final grating and analyzed with optical or electron microscopy [43,117], is particularly appealing for high-mass interferometry experiments due to its inherently high detection efficiency [75]. A second quadrupole will serve as an ion guide (RF fields only) and will be flooded with a buffer gas cooled with a pulse tube cryocooler to reduce the longitudinal beam velocity. Slowing the beam is necessary such that the Talbot length stays within the one meter grating separation, since the typical un-slowed velocities from a magnetron sputter source are in excess of 200 m/s [97]. Interference with clusters beyond 10^5 u would require beam velocities below 100 m/s, which should be readily achievable with buffer gas cooling.
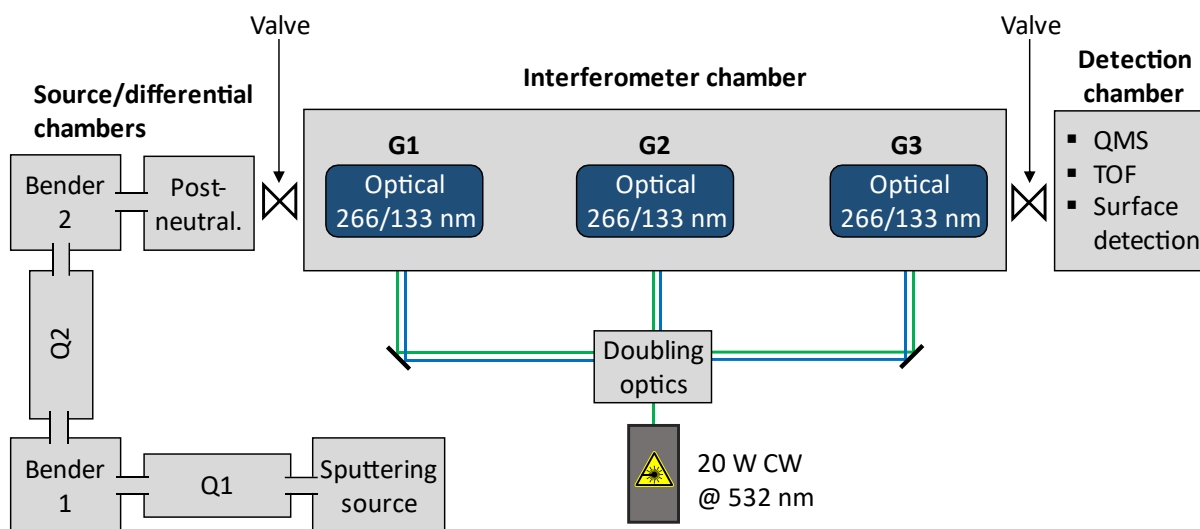
Figure 69: *Schematic overview of the planned LUMI upgrade. The original gratings and metrology tools will remain in place but are not shown for clarity. The source is comprised of the sputtering cluster source, up to two quadrupoles Q1 and Q2, two 90° benders, and a post-neutralization stage. The actual layout on the optical table will differ, with the first quadrupole and cluster source on the opposite side of the first bender. Several differential pumping regions are required due to the high gas flow both from the seeded magnetron sputtering source and the buffer gas cooling. The interferometer gratings will be optical depletion gratings formed by standing light waves of 532 or 266 nm light. There are several detection options, including a high-mass QMS, TOF, or surface detection.*

Up to 3 W of continuous UV power will be available using two Spectra-Physics Wavetrains, a cavity enhanced frequency doubler which converts 532 nm light into 266 nm light with up to 30% efficiency. A Coherent Verdi V20 and/or V18 will supply the 532 nm pump light for the Wavetrains. The total UV power will be divided among the three gratings, and potentially a post-neutralization and ionization beam as well, leaving about 600 mW per beam, not accounting for optics losses. The optical layout is significantly more involved than for the current version of LUMI, with up to five beamlines of high-power 532 nm and/or 266 nm. The current LUMI scheme, with two material gratings and an interchangeable central grating, will remain in place, with the central mirror and lens replaced with doubly coated 266/532 nm optics. In-house testing of UV cavities has shown that special mirror coatings are required to

achieve stable high-power UV reflection in UHV conditions. The design is intended to be as modular as possible, allowing in-vacuum switching between the material TLI, the mixed material-optical KDTLI, the 532 nm depletion TLI, and the 266 nm depletion TLI.

6.2.2 High-mass challenges

The slow velocities required for this interference scheme tightens the criteria already made stringent by the long baseline, namely the sensitivity to vibrations, the Coriolis effect, and thermal and collisional decoherence. The Coriolis dephasing should still be well-compensated at 100 m/s with the current scheme (see Figure 10), and thermal decoherence should likewise not play a role since the clusters will be internally cold after production in the liquid nitrogen-cooled baffle and the buffer gas cooling. Common-mode grating vibrations become more important with the longer flight time but should still not be critical at their current levels. The effect of collisional decoherence can be estimated using Equation 34 and using the London dispersion formula for the C_6 coefficient [161], similar to the treatment in Reference [61] which uses the Slater-Kirkwood approximation to calculate the same quantity for large hydrocarbons. This estimate shows that the pressure of the interferometer chamber when opened to the source should be improved to low 10^{-9} mbar to maintain 95% of maximal visibility. The interferometer chamber has a typical base pressure near this level, but the gas load of the cluster source will need to be carefully managed to avoid degrading the vacuum in the interferometer. Improving the base pressure of the interferometer chamber with another bakeout or increased pumping capacity may be necessary.

For significantly slower beams, figure-eight schemes can also be considered for improved Coriolis compensation, and the substitution of the third grating with a spatially resolving detector would also significantly boost the interferometer performance [75].

6.2.3 Current status

The LUMI upgrade is already underway. Initial tests with hafnium have shown the production of clusters beyond 10^6 u, and some depletion of the neutral beam with 266 nm light. Most of the components for the new cluster source are in-house or have been purchased, including the two quadrupoles, their electronics, a cryo-cooler for the buffer gas cooling (Sumitomo custom model similar to SRP-082B-F70H), optics, and additional vacuum chambers for the source. A more compact magnetron sputtering source (Oxford Applied Research NC200U-B) than the one currently being used for testing[15] will be used in the LUMI upgrade. Modifications to the grating mounts will be required, in particular for the first and third grating, to accommodate a cylindrical lens and mirror. The second grating mount can remain with minimal modifications.

A significant amount of work remains to complete the upgrade. This includes the assembly, testing, and characterization of the new cluster source and the demonstration of mass selection, slowing, and post-neutralization of the cluster beam. The grating mount modifications and the

---

[15] Built by Prof. Bernd von Issendorff, University of Freiburg.

optics setup for the optical gratings need to be finalized and implemented. A new detector will also need to be installed and calibrated, with three options shown in Figure 69. The experimental control software will also need to be adapted, and a new protocol for the pre-alignment of optical gratings will be required.

As described throughout this thesis, the current LUMI experiment has already demonstrated exciting results, including setting the current mass record of matter-wave interference. We expect the upgraded LUMI experiment to break this record, thereby validating quantum mechanics in a previously unexplored regime.

Bibliography

[1] A. D. Cronin, J. Schmiedmayer, and D. E. Pritchard, *Optics and interferometry with atoms and molecules*, Rev. Mod. Phys. **81**, 1051 (2009).

[2] J. B. Fixler, G. T. Foster, J. M. McGuirk, and M. A. Kasevich, *Atom interferometer measurement of the newtonian constant of gravity*, Science **315**, 74 (2007).

[3] R. Bouchendira, P. Cladé, S. Guellati-Khélifa, F. Nez, and F. Biraben, *New Determination of the Fine Structure Constant and Test of the Quantum Electrodynamics*, Phys. Rev. Lett. **106**, 080801 (2011).

[4] G. Rosi, F. Sorrentino, L. Cacciapuoti, M. Prevedelli, and G. M. Tino, *Precision measurement of the Newtonian gravitational constant using cold atoms*, Nature **510**, 518 (2014).

[5] M. Arndt, O. Nairz, J. Voss-Andreae, C. Keller, G. van der Zouw, and A. Zeilinger, *Wave-particle duality of C60 molecules*, Nature **401**, 680 (1999).

[6] T. Kovachy, P. Asenbaum, C. Overstreet, C. A. Donnelly, S. M. Dickerson, A. Sugarbaker, J. M. Hogan, and M. A. Kasevich, *Quantum superposition at the half-metre scale*, Nature **528**, 530 (2015).

[7] T. L. Gustavson, P. Bouyer, and M. A. Kasevich, *Precision Rotation Measurements with an Atom Interferometer Gyroscope*, Phys. Rev. Lett. **78**, 2046 (1997).

[8] M. J. Snadden, J. M. McGuirk, P. Bouyer, K. G. Haritos, and M. A. Kasevich, *Measurement of the Earth's Gravity Gradient with an Atom Interferometer-Based Gravity Gradiometer*, Phys. Rev. Lett. **81**, 971 (1998).

[9] A. Peters, K. Yeow-Chung, and S. Chu, *Measurement of Gravitational Acceleration by Dropping Atoms*, Nature **400**, 849 (1999).

[10] J. K. Stockton, K. Takase, and M. A. Kasevich, *Absolute Geodetic Rotation Measurement Using Atom Interferometry*, Phys. Rev. Lett. **107**, 133001 (2011).

[11] N. F. Ramsey, *A Molecular Beam Resonance Method with Separated Oscillating Fields*, Phys. Rev. **78**, 695 (1950).

[12] L. de Broglie, *Waves and Quanta*, Nature **112**, 540 (1923).

[13] G. P. Thomson, *The Diffraction of Cathode Rays by Thin Films of Platinum*, Nature **120**, 802 (1927).

[14] C. D. L. H. Germer, *The Scattering of Electrons by a Single Crystal of Nickel* Nature **119**, 558 (1927).

[15] I. Estermann and O. Stern, *Beugung von Molekularstrahlen*, Z. Phys. **61**, 95 (1930).

[16] H. Maier-Leibnitz and T. Springer, *Ein Interferometer für langsame Neutronen*, Z. Phys. **167**, 386 (1962).

[17] H. Rauch, W. Treimer, and U. Bonse, *Test of a Single Crystal Neutron Interferometer*, Phys. Rev.A **47**, 369 (1974).

[18] R. Colella, A. W. Overhauser, and S. A. Werner, *Observation of Gravitationally Induced Quantum Interference* Phys. Rev. Lett. **34**, 1472 (1975).

[19] S. A. Werner, J. L. Staudenmann, and R. Colella, *Effect of Earth's Rotation on the Quantum Mechanical Phase of the Neutron*, Phys. Rev. Lett. **42**, 1103 (1979).

[20] H. Rauch, A. Zeilinger, G. Badurek, A. Wilfing, Bauspie\ss, W., and U. Bonse, *Verification of Coherent Spinor Rotation of Fermions*, Phys. Lett. A **54**, 425 (1975).

[21] S. A. Werner, R. Colella, A. W. Overhauser, and C. F. Eagen, *Observation of the Phase Shift of a Neutron Due to Precession in a Magnetic Field*, Phys. Rev. Lett. **35**, 1953 (1975).

[22] M. K. S. Chu, *Measurement of the Gravitational Acceleration of an Atom with a Light-Pulse Atom Interferometer*, Appl. Phys. B **54**, 321 (1992).

[23] A. Peters, K. Y. Chung, and S. Chu, *High-precision gravity measurements using atom interferometry*, Metrologia **38**, 25 (2001).

[24] F. Riehle, T. Kisters, A. Witte, J. Helmcke, and C. J. Borde, *Optical Ramsey Spectroscopy in a Rotating Frame: Sagnac Effect in a Matter-Wave Interferometer*, Phys. Rev. Lett. **67**, 177 (1991).

[25] I. Dutta, D. Savoie, B. Fang, B. Venon, C. L. Garrido Alzar, R. Geiger, and A. Landragin, *Continuous Cold-Atom Inertial Sensor with 1 nrad/sec Rotation Stability*, Phys. Rev. Lett. **116**, 183003 (2016).

[26] E. Krüger, W. Nistler, and W. Weirauch, *Determination of the fine-structure constant by a precise measurement ofh/mn*, Metrologia **32**, 117 (1995).

[27] D. Weiss, B. Young, and S. Chu, *Precision measurement of the photon recoil of an atom using atomic interferometry*, Phys. Rev. Lett. **70**, 2706 (1993).

[28] C. Ekstrom, J. Schmiedmayer, M. Chapman, T. Hammond, and D. Pritchard, *Measurement of the electric polarizability of sodium with an atom interferometer*, Phys. Rev. A **51**, 3883 (1995).

[29] J. R. Friedman, V. Patel, W. Chen, S. K. Tolpygo, and J. E. Lukens, *Quantum superposition of distinct macroscopic states*, Nature **406**, 43 (2000).

[30] S. Eibenberger, S. Gerlich, M. Arndt, M. Mayor, and J. Tüxen, *Matter-wave interference of particles selected from a molecular library with masses exceeding 10 000 amu*, Phys. Chem. Chem. Phys. **15**, 14696 (2013).

[31] J. F. Clauser and S. Li, *Talbot-von Lau atom interferometry with cold slow potassium*, Phys. Rev. A **49**, R2213 (1994).

[32] Y. Y. Fein, P. Geyer, P. Zwick, F. Kiałka, S. Pedalino, M. Mayor, S. Gerlich, and M. Arndt, *Quantum superposition of molecules beyond 25 kDa*, Nat. Phys. **15**, 1242 (2019).

[33] A. W. Lohmann, D. Mendlovic, and G. Shabtay, *Talbot (1836), Montgomery (1967), Lau (1948) and Wolf (1955) on periodicity in optics*, Pure Appl. Opt. **7**, 1121 (1998).

[34] K. Patorski, in *Progress in Optics XXVII* edited by E. Wolf (Elsevier Science Publishers Amsterdam, 1989), pp. 1.

[35] E. Lau, *Beugungserscheinungen an Doppelrastern*, Ann. Phys. **6**, 417 (1948).

[36] J. Jahns and A. W. Lohmann, *The Lau Effect (a Diffraction Experiment with Incoherent Illumination)*, Opt. Comm. **28** (1979).

[37] S. Nimmrichter and K. Hornberger, *Theory of near-field matter-wave interference beyond the eikonal approximation*, Phys. Rev. A **78**, 023612 (2008).

[38] M. S. Chapman, C. R. Ekstrom, T. D. Hammond, J. Schmiedmayer, B. E. Tannian, S. Wehinger, and D. E. Pritchard, *Near-Field Imaging of Atom Diffraction Gratings: The Atomic Talbot Effect*, Phys. Rev. A **51**, R14 (1995).

[39] B. J. McMorran and A. D. Cronin, *An electron Talbot interferometer*, New J. Phys. **11**, 033021 (2009).

[40] L. Deng, E. W. Hagley, J. Denschlag, J. E. Simsarian, M. Edwards, C. W. Clark, K. Helmerson, S. L. Rolston, and W. D. Phillips, *Temporal, Matter-Wave-Dispersion Talbot Effect*, Phys. Rev. Lett. **83**, 5407 (1999).

[41] S. B. Cahn, A. Kumarakrishnan, U. Shim, T. Sleator, P. R. Berman, and B. Dubetsky, *Time-Domain de Broglie Wave Interferometry*, Phys. Rev. Lett. **79**, 784 (1997).

[42] B. Brezger, L. Hackermüller, S. Uttenthaler, J. Petschinka, M. Arndt, and A. Zeilinger, *Matter-Wave Interferometer for Large Molecules*, Phys. Rev. Lett. **88**, 100404 (2002).

[43] T. Juffmann, S. Truppe, P. Geyer, A. G. Major, S. Deachapunya, H. Ulbricht, and M. Arndt, *Wave and Particle in Molecular Interference Lithography*, Phys. Rev. Lett. **103** (2009).

[44] P. Haslinger, N. Dörre, P. Geyer, J. Rodewald, S. Nimmrichter, and M. Arndt, *A universal matter-wave interferometer with optical ionization gratings in the time domain*, Nat. Phys. **9**, 144 (2013).

[45] S. Gerlich *et al.*, *A Kapitza-Dirac-Talbot-Lau interferometer for highly polarizable molecules*, Nat. Phys. **3**, 711 (2007).

[46] P. L. Kapitza and P. A. M. Dirac, *The Reflection of Electrons from Standing Light Waves*, Proc. Camb. Philos. Soc. **29**, 297 (1933).

[47] P. E. Moskowitz, P. L. Gould, S. R. Atlas, and D. E. Pritchard, *Diffraction of an Atomic Beam by Standing-Wave Radiation*, Phys. Rev. Lett. **51**, 370 (1983).

[48] S. Gerlich, S. Eibenberger, M. Tomandl, S. Nimmrichter, K. Hornberger, P. Fagan, J. Tüxen, M. Mayor, and M. Arndt, *Quantum interference of large organic molecules*, Nat. Commun. **2**, 263 (2011).

[49] J. Tüxen, S. Gerlich, S. Eibenberger, M. Arndt, and M. Mayor, *Quantum interference distinguishes between constitutional isomers*, Chem. Commun. **46**, 4145 (2010).

[50] L. Mairhofer, S. Eibenberger, J. P. Cotter, M. Romirer, A. Shayeghi, and M. Arndt, *Quantum-Assisted Metrology of Neutral Vitamins in the Gas Phase*, Angew. Chem. Int. Ed. **56**, 10947 (2017).

[51] M. Gring *et al.*, *Influence of conformational molecular dynamics on matter wave interferometry*, Phys. Rev. A **81**, 031604(R) (2010).

[52] S. Eibenberger, X. Cheng, J. P. Cotter, and M. Arndt, *Absolute absorption cross sections from photon recoil in a matter-wave interferometer*, Phys. Rev. Lett. **112**, 250402 (2014).

[53] K. Hornberger, S. Gerlich, H. Ulbricht, L. Hackermüller, S. Nimmrichter, I. Goldt, O. Boltalina, and M. Arndt, *Theory and experimental verification of Kapitza-Dirac-Talbot-Lau interferometry*, New J. Phys. **11**, 043032 (2009).

[54] S. Gerlich, *Interferometry and Metrology with Macromolecules*, PhD thesis, University of Vienna, 2011.

[55] K. Hornberger, J. E. Sipe, and M. Arndt, *Theory of decoherence in a matter wave Talbot-Lau interferometer*, Phys. Rev. A **70**, 53608 (2004).

[56] S. Nimmrichter, *Macroscopic Matter Wave Interferometry* (Springer, Vienna, 2014), Springer Thesis.

[57] S. Y. Buhmann, *Dispersion Forces I: Macroscopic Quantum Electrodynamics* (Springer, Heidelberg, 2012), Vol. 1, Springer Tracts in Modern Physics, 247.

[58] A. Stibor, K. Hornberger, L. Hackermüller, A. Zeilinger, and M. Arndt, *Talbot-Lau interferometry with fullerenes: Sensitivity to inertial forces and vibrational dephasing*, Laser Physics **15**, 10 (2005).

[59] Y. Y. Fein, F. Kiałka, P. Geyer, S. Gerlich, and M. Arndt, *Coriolis compensation via gravity in a matter-wave interferometer*, New J. Phys. **22**, 033013 (2020).

[60] L. Hackermüller, K. Hornberger, B. Brezger, A. Zeilinger, and M. Arndt, *Decoherence of matter waves by thermal emission of radiation*, Nature **427**, 711 (2004).

[61] K. Hornberger, S. Uttenthaler, B. Brezger, L. Hackermüller, M. Arndt, and A. Zeilinger, *Collisional Decoherence Observed in Matter Wave Interferometry*, Phys. Rev. Lett. **90**, 160401 (2003).

[62] M. Born and E. Wolf, *Principles of Optics* (Pergamon Press, 1993).

[63] G. C. Ghirardi, A. Rimini, and T. Weber, *Unified dynamics for microscopic and macroscopic systems*, Phys. Rev. D **34**, 470 (1986).

[64] A. Bassi, K. Lochan, S. Satin, T. P. Singh, and H. Ulbricht, *Models of wave-function collapse, underlying theories, and experimental tests*, Rev. Mod. Phys. **85**, 471 (2013).

[65] P. Pearle, *Combining Stochastic Dynamical State-Vector Reduction with Spontaneous Localization*, Phys. Rev. A **39**, 2277 (1989).

[66] G. C. Ghirardi, P. Pearle, and A. Rimini, *Markov Processes in Hilbert Space and Continuous Spontaneous Localization of Systems of Identical Particles*, Phys. Rev. A **42**, 78 (1990).

[67] P. Pearle and E. Squires, *Bound state excitation, nucleon decay experiments and models of wave function collapse*, Phys. Rev. Lett. **73**, 1 (1994).

[68] S. Nimmrichter, K. Hornberger, P. Haslinger, and M. Arndt, *Testing spontaneous localization theories with matter-wave interferometry*, Phys. Rev. A **83**, 043621 (2011).

[69] S. Gerlich, Y. Y. Fein, and M. Arndt, in *Do wave functions jump? Perspectives on the work of GC Ghirardi*, edited by V. Allori *et al.* (Springer International Publishing, 2020).

[70] M. Toroš, G. Gasbarri, and A. Bassi, *Colored and dissipative continuous spontaneous localization model and bounds from matter-wave interferometry*, Physics Letters A, 3921 (2017).

[71] F. Fröwis, P. Sekatski, W. Dür, N. Gisin, and N. Sangouard, *Macroscopic quantum states: Measures, fragility, and implementations*, Rev. Mod. Phys. **90** (2018).

[72] S. Nimmrichter and K. Hornberger, *Macroscopicity of Mechanical Quantum Superposition States*, Phys. Rev. Lett. **110**, 160403 (2013).

[73] B. Schrinski, S. Nimmrichter, B. A. Stickler, and K. Hornberger, *Macroscopicity of quantum mechanical superposition tests via hypothesis falsification*, Phys. Rev. A **100**, 032111 (2019).

[74] V. Xu, M. Jaffe, C. D. Panda, S. L. Kristensen, L. W. Clark, and H. Müller, *Probing gravity by holding atoms for 20 seconds*, Science **366**, 745 (2019).

[75] F. Kiałka, B. A. Stickler, K. Hornberger, Y. Y. Fein, P. Geyer, L. Mairhofer, S. Gerlich, and M. Arndt, *Concepts for long-baseline high-mass matter-wave interferometry*, Phys. Scr. **94**, 034001 (2019).

[76] J. H. Denschlag, J. E. Simsarian, H. Häffner, C. McKenzie, A. Browaeys, D. Cho, K. Helmerson, S. L. Rolston, and W. D. Phillips, *A Bose-Einstein condensate in an optical lattice*, J. Phys. B **35**, 3095 (2002).

[77] A. Tonomura, N. Osakabe, T. Matsuda, T. Kawasaki, J. Endo, S. Yano, and H. Yamada, *Evidence for Aharonov-Bohm effect with magnetic field completely shielded from electron wave*, Phys. Rev. Lett. **56**, 792 (1986).

[78] B. E. Allman, A. Cimmino, A. G. Klein, G. I. Opat, H. Kaiser, and S. A. Werner, *Scalar Aharonov-Bohm experiment with neutrons*, Phys. Rev. Lett. **68**, 2409 (1992).

[79] A. Cimmino, G. I. Opat, A. G. Klein, H. Kaiser, S. A. Werner, M. Arif, and R. Clothier, *Observation of the topological Aharonov-Casher phase shift by neutron interferometry*, Phys. Rev. Lett. **63**, 380 (1989).

[80] L. Hackermüller, K. Hornberger, S. Gerlich, M. Gring, H. Ulbricht, and M. Arndt, *Optical polarizabilities of large molecules measured in near-field interferometry*, App. Phys. B **89**, 469 (2007).

[81] S. Eibenberger, S. Gerlich, M. Arndt, J. Tüxen, and M. Mayor, *Electric moments in molecule interferometry*, New J. Phys. **13**, 043033 (2011).

[82] J. H. V. Vleck, *The theory of electric and magnetic susceptibilities* (Oxford University Press London, 1965).

[83] P. W. Atkins and R. Friedman, *Molecular Quantum Mechanics* (Oxford University Press Oxford, 2005), 4th Ed. edn.

[84] F. Hagelberg, *Magnetism in Carbon Nanostructures* (Cambridge University Press, Cambridge, 2017).

[85] U. Rohrmann and R. Schafer, *Stern-Gerlach experiments on Mn@Sn12: identification of a paramagnetic superatom and vibrationally induced spin orientation*, Phys. Rev. Lett. **111**, 133401 (2013).

[86] W. Demtröder, *Molecular Physics* (Wiley VCH Weinheim, 2005).

[87] L. Mairhofer, S. Eibenberger, A. Shayeghi, and M. Arndt, *A Quantum Ruler for Magnetic Deflectometry*, Entropy **20**, 516 (2018).

[88] M. Berninger, A. Stefanov, S. Deachapunya, and M. Arndt, *Polarizability measurements of a molecule via a near-field matter-wave interferometer*, Phys. Rev. A **76**, 013607 (2007).

[89] Y. Y. Fein, A. Shayeghi, L. Mairhofer, F. Kiałka, P. Rieser, P. Geyer, S. Gerlich, and M. Arndt, *Quantum-Assisted Measurement of Atomic Diamagnetism*, Phys. Rev. X **10**, 011014 (2020).

[90] S. Eibenberger, *Quantun Interference Experiments with Complex Organic Molecules*, PhD thesis, University of Vienna, 2015.

[91] Y. Y. Fein, P. Geyer, F. Kiałka, S. Gerlich, and M. Arndt, *Improved accuracy fullerene polarizability measurements in a long-baseline matter-wave interferometer*, Phys. Rev. Research **1**, 033158 (2019).

[92] M. Berninger, *Molecule Metrology with Matter Waves*, Master thesis, University of Vienna, 2006.

[93] W. Gerlach and O. Stern, *Der experimentelle Nachweis des magnetischen Moments des Silberatoms*, Z. Phys. **8**, 110 (1922).

[94] T. A. Savas, S. N. Shah, M. L. Schattenburg, J. M. Carter, and H. I. Smith, *Achromatic Interferometric Lithography for 100-Nm-Period Gratings and Grids*, J. Vac. Sci. Technol. **B 13**, 2732 (1995).

[95] D. W. Keith, C. R. Ekstrom, Q. A. Turchette, and D. E. Pritchard, *An Interferometer for Atoms*, Phys. Rev. Lett. **66**, 2693 (1991).

[96] M. Marksteiner, G. Kiesewetter, L. Hackermüller, H. Ulbricht, and M. Arndt, *Cold Beams of Biomolecules for Quantum Optics*, Acta Physica Hungarica A) Heavy Ion Physics **26**, 87 (2006).

[97] P. Geyer, *Matter wave interferometry with complex nanoparticles*, PhD thesis, University of Vienna, 2016.

[98] U. Even, *The Even-Lavie valve as a source for high intensity supersonic beam*, EPJ Tech. Instrum. **2** (2015).

[99] M. Marksteiner, P. Haslinger, M. Sclafani, H. Ulbricht, and M. Arndt, *UV and VUV Ionization of Organic Molecules, Clusters, and Complexes*, J. Phys. Chem. A **113**, 9952 (2009).

[100] J. Schätti *et al.*, *Pushing the mass limit for intact launch and photoionization of large neutral biopolymers*, Commun. Chem. **1**, 93 (2018).

[101] É. I. A. Zandberg and N. I. Ionov, *Surface Ionization* (Israel Program for Scientific Translations, 1971).

[102] F. Stienkemeier, M. Wewer, F. Meier, and H. O. Lutz, *Langmuir–Taylor surface ionization of alkali (Li, Na, K) and alkaline earth (Ca, Sr, Ba) atoms attached to helium droplets*, Rev. Sci. Instrum. **71**, 3480 (2000).

[103] D. R. Lide, *CRC Handbook of Chemistry and Physics* (CRC Press, New York, 2004), 84 edn., p.^pp. 4-130.

[104] C. Klempt, T. van Zoest, T. Henninger, O. Topic, E. Rasel, W. Ertmer, and J. Arlt, *Ultraviolet light-induced atom desorption for large rubidium and potassium magneto-optical traps*, Phys. Rev. A **73**, 013410 (2006).

[105] M. Kaack and D. Fick, *Determination of the work functions of Pt(111) and Ir(111) beyond 1100 K surface temperature*, Surf. Sci. **342**, 111 (1995).

[106] D. Ding, J. Huang, R. Compton, C. Klots, and R. Haufler, *cw laser ionization of C60 and C70*, Phys. Rev. Lett. **73**, 1084 (1994).

[107] O. Nairz, M. Arndt, and A. Zeilinger, *Experimental challenges in fullerene interferometry*, J. Mod. Opt. **47**, 2811 (2000).

[108] L. K. Verheij and P. Zeppenfeld, *Are the time resolutions for the conventional and the pseudorandom methods for time-of-flight analysis different?*, Rev. Sci. Instrum. **58**, 2138 (1987).

[109] K. Sköld, *A mechanical correlation chopper for thermal neutron spectroscopy*, Nucl. Instrum. Meth. **63**, 114 (1968).

[110] L. Mairhofer, *Quantum-interference assisted Metrology with Complex Biomolecules*, PhD thesis, University of Vienna, 2017.

[111] D. D. Koleske and S. J. Sibener, *Generation of pseudorandom sequences for use in cross-correlation modulation*, Rev. Sci. Instrum. **63**, 3852 (1992).

[112] U. Sezer, P. Schmid, L. Felix, M. Mayor, and M. Arndt, *Stability of high-mass molecular libraries: the role of the oligoporphyrin core*, J. Mass Spectrom. **50**, 235 (2015).

[113] J. Rodewald, *Experiments with a pulsed Talbot Lau matter-wave interferometer*, PhD thesis, University of Vienna, 2017.

[114] S. Deachapunya, A. Stefanov, M. Berninger, H. Ulbricht, E. Reiger, N. L. Doltsinis, and M. Arndt, *Thermal and electrical properties of porphyrin derivatives and their relevance for molecule interferometry*, J Chem Phys **126**, 164304 (2007).

[115] K. C. Lee *et al.*, *Entangling Macroscopic Diamonds at Room Temperature*, Science **334**, 1253 (2011).

[116] M. Carlesso and A. Bassi, in *Fourteenth Marcel Grossmann Meeting - MG14* 2018), p. E12.

[117] T. Juffmann, A. Milic, M. Müllneritsch, P. Asenbaum, A. Tsukernik, J. Tüxen, M. Mayor, O. Cheshnovsky, and M. Arndt, *Real-time single-molecule imaging of quantum interference* Nature Nanotechn. **7**, 297 (2012).

[118] S. L. Adler, *Lower and upper bounds on CSL parameters from latent image formation and IGM heating*, J. Phys. A: Math. Theor. **40**, 2935 (2007).

[119] B. Schrinski, *Assessing the macroscopicity of quantum mechanical superposition tests via hypothesis falsification*, PhD thesis, University of Duisburg-Essen, 2019.

[120] M. A. Hohensee and H. Müller, *Precision tests of general relativity with matter waves*, J. Mod. Opt. **58**, 2021 (2011).

[121] J. Rodewald, N. Dörre, A. Grimaldi, P. Geyer, L. Felix, M. Mayor, A. Shayeghi, and M. Arndt, *Isotope-selective high-order interferometry with large organic molecules in free fall*, New J. Phys. **20** 033016 (2018).

[122] T. A. Wagner, S. Schlamminger, J. H. Gundlach, and E. G. Adelberger, *Torsion-balance tests of the weak equivalence principle*, Classical Quant. Grav. **29**, 184002 (2012).

[123] G. Tino and M. Kasevich, *Atom Interferometry* (IOS, Varenna, 2014), Vol. 188, Proceedings of the International School of Physics "Enrico Fermi".

[124] P. Hamilton, M. Jaffe, P. Haslinger, Q. Simmons, H. Müller, and J. T. Khoury, *Atom-interferometry constraints on dark energy*, Science **349**, 849 (2015).

[125] A. D. Rider, D. C. Moore, C. P. Blakemore, M. Louis, M. Lu, and G. Gratta, *Search for Screened Interactions Associated with Dark Energy below the 100 μm Length Scale*, Phys. Rev. Lett. **117**, 101101 (2016).

[126] L. Badurina *et al.*, arXiv:1911.11755v2.

[127] J. Coleman, arXiv:1812.00482v1.

[128] R. Kaltenbaek, G. Hechenblaikner, N. Kiesel, O. Romero-Isart, K. C. Schwab, U. Johann, and M. Aspelmeyer, *Macroscopic quantum resonators (MAQRO)*, Exp. Astron. **34**, 123 (2012).

[129] J. Bateman, I. McHardy, A. Merle, T. R. Morris, and H. Ulbricht, *On the Existence of Low-Mass Dark Matter and its Direct Detection*, Sci. Rep. **5**, 8058 (2015).

[130] S. Dimopoulos, P. Graham, J. Hogan, M. Kasevich, and S. Rajendran, *Atomic gravitational wave interferometric sensor*, Phys. Rev. D **78** (2008).

[131] B. Canuel *et al.*, *Exploring gravity with the MIGA large scale atom interferometer*, Sci. Rep. **8**, 14064 (2018).

[132] C. J. Riedel, *Direct detection of classically undetectable dark matter through quantum decoherence*, Phys. Rev. D **88** (2013).

[133] C. J. Riedel and I. Yavin, *Decoherence as a way to measure extremely soft collisions with dark matter*, Phys. Rev. D **96**, 023007 (2017).

[134] M. Aspelmeyer, T. J. Kippenberg, and F. Marquardt, *Cavity optomechanics*, Rev. Mod. Phys. **86**, 1391 (2014).

[135] J. Schaetti, V. Köhler, M. Mayor, Y. Y. Fein, P. Geyer, L. Mairhofer, S. Gerlich, and M. Arndt, *Matter-wave interference and deflection of tripeptides decorated with fluorinated alkyl chains* J. Mass Spectrom. (accepted, 2020).

[136] M. D. Gregoire, I. Hromada, W. F. Holmgren, R. Trubko, and A. D. Cronin, *Measurements of the ground-state polarizabilities of Cs, Rb, and K using atom interferometry*, Phys. Rev. A **92** (2015).

[137] R. Antoine, P. Dugourd, D. Rayane, E. Benichou, M. Broyer, F. Chandezon, and C. Guet, *Direct measurement of the electric polarizability of isolated C60 molecules*, J. Chem. Phys. **110**, 9771 (1999).

[138] I. Compagnon, R. Antoine, M. Broyer, P. Dugourd, J. Lermé, and D. Rayane, *Electric polarizability of isolatedC70molecules*, Phys. Rev. A **64** (2001).

[139] A. Shayeghi, P. Rieser, G. Richter, U. Sezer, J. H. Rodewald, P. Geyer, T. Martinez, and M. Arndt, *Matter-wave interference of a native polypeptide*, Nat. Commun. (accepted, 2020).

[140] R. Antoine *et al.*, *Application of Molecular Beam Deflection Time-of-Flight Mass Spectrometry to Peptide Analysis*, Anal. Chem. **75**, 5512 (2003).

[141] J. Schätti, U. Sezer, S. Pedalino, J. P. Cotter, M. Arndt, M. Mayor, and V. Köhler, *Tailoring the volatility and stability of oligopeptides*, J Mass Spectrom **52**, 550 (2017).

[142] R. Antoine *et al.*, *Electric dipole moments and conformations of isolated peptides*, Eur. Phys. J. D. **20**, 583 (2002).

[143] M. J. Frisch *et al.*, Gaussian 16 Rev. C.01, 2016.

[144] H. L. Schwartz, T. M. Miller, and B. Bederson, *Measurement of the Static Electric Dipole Polarizabilities of Barium and Strontium*, Phys. Rev. A **10**, 1924 (1974).

[145] J. A. N. F. Gomes and R. B. Mallion, *Aromaticity and Ring Currents*, Chem. Rev. **101**, 1349 (2001).

[146] A. Ligabue, U. Pincelli, P. Lazzeretti, and R. Zanasi, *Current Density Maps, Magnetizability, and Nuclear Magnetic Shielding Tensors for Anthracene, Phenanthrene, and Triphenylene*, J. Am. Chem. Soc. **121**, 5513 (1999).

[147] B. Friedrich, D. P. Pullman, and D. R. Herschbach, *Alignment and Orientation of Rotationally Cool Molecules*, J. Phys. Chem. **95**, 8118 (1991).

[148] M. P. Sinha, C. D. Caldwell, and R. N. Zare, *Alignment of Molecules in Gaseous Transport: Alkali Dimers in Supersonic Nozzle Beams*, J. Chem. Phys. **61**, 491 (1974).

[149] F. Pirani, D. Cappelletti, M. Bartolomei, V. Aquilanti, M. Scotoni, M. Vescovi, D. Ascenzi, and D. Bassi, *Orientation of Benzene in Supersonic Expansions, Probed by IR-Laser Absorption and by Molecular Beam Scattering*, Phys. Rev. Lett. **86**, 5035 (2001).

[150] V. Aquilanti, D. Ascenzi, D. Cappelletti, and F. Pirani, *Rotational Alignment in Supersonic Seeded Beams of Molecular Oxygen*, J. Phys. Chem. **99**, 13620 (1995).

[151] N. F. Ramsey, *The Rotational Magnetic Moments of H_2, D_2, and HD Molecules. The Rotational Radiofrequency Spectra of H_2, D_2, and D in Magnetic Fields*, Phys. Rev. **58**, 226 (1940).

[152] M. Huzak and M. S. Deleuze, *Benchmark theoretical study of the electric polarizabilities of naphthalene, anthracene, and tetracene*, J. Chem. Phys. **138**, 024319 (2013).

[153] D. Steck, (Los Alamos National Laboratory, Los Alamos 2003), pp. 1.

[154] W. Wiltschko and R. Wiltschko, *Magnetic orientation and magnetoreception in birds and other animals*, J. Comp. Physiol. A: Neuroethol. Sens. Neural Behav. Physiol. **191**, 675 (2005).

[155] D. M. Wood, *Classical Size Dependence of the Work Function of Small Metallic Spheres*, Phys. Rev. Lett. **46**, 749 (1981).

[156] K. H. Meiwes-Broer, *Work functions of metal clusters*, Hyperfine Interactions **89**, 263 (1994).

[157] J. A. Creighton and D. G. Eadon, *Ultraviolet–visible absorption spectra of the colloidal metallic elements*, Journal of the Chemical Society, Faraday Transactions **87**, 3881 (1991).

[158] U. Kreibig and M. Vollmer, *Optical Properties of Metal Clusters* (Springer, Berlin, 1995).

[159] H. G. Limberger and T. P. Martin, *Photoionization spectra of cesium and cesium oxide clusters*, J. Chem. Phys. **90**, 2979 (1989).

[160] J. Gspann, *Large clusters of cesium from pure vapor expansions*, Z. Phys. D: At., mol. clusters **20**, 421 (1991).

[161] K. Bonin and V. Kresin, *Electric-Dipole Polarizabilities of Atoms, Molecules and Clusters* (World Scientific, 1997).

Acknowledgements

To begin with I must extend my gratitude to my supervisor Markus Arndt. His continuous support and confidence in my abilities, as well as his near-constant accessibility and rapid feedback, are deeply appreciated. A good scientist is not necessarily a good mentor, and I am lucky to have found both in Markus.

There are many people who have been involved with the LUMI experiment from its conception to its current stage. I acknowledge (alphabetically) the help of Maximme Debiossac, Stefan Gerlich, Philipp Geyer, Filip Kiałka, Lukas Mairhofer, Themistoklis Parousis, and Sebastian Pedalino, as well as Armin Shayeghi for assistance with molecular simulations. I would also like to thank our collaborators in Basel, Patrick Zwick, Jonas Schätti, Valentin Köhler, and Marcel Mayor for the chemical synthesis and characterization of molecules, as well as the workshop employees at the University of Vienna for their time fabricating various components for the experiment.

I would be amiss not to individually thank the two postdocs I have had the pleasure to work with the most over the past years, Stefan Gerlich and Philipp Geyer. Without Stefan's guidance and Philipp's technical skills the experiment could never have produced results. I would also like to thank Stefan for his help and patience in proofreading papers and this thesis.

A doctorate is more than just the time spent in the lab or writing papers, and I am grateful for the community and friends I have made during my time here. For weekend mountain adventures, after-work drinks, and entertaining lunchtime conversations, I thank everyone in the Arndt group.

Finally, I would like to thank my family for their constant support and love. My father inspired my love of physics at a young age and my mother believed in me as only a mother can. My older siblings Miriam and Dovid have been sources of inspiration, and my sister, Devora, has been my connection to home even when it is oceans away.

List of publications

- Filip Kiałka, Benjamin Stickler, Klaus Hornberger, <u>Yaakov Y. Fein</u>, Philipp Geyer, Lukas Mairhofer, Stefan Gerlich, and Markus Arndt
  Concepts for long-baseline high-mass matter-wave interferometry
  Physica Scripta **94**, 034001 (2019)

- <u>Yaakov Y. Fein</u>, Philipp Geyer, Patrick Zwick, Filip Kiałka, Sebastian Pedalino, Marcel Mayor, Stefan Gerlich, and Markus Arndt
  Quantum superposition of molecules beyond 25 kDa
  Nature Physics **15**, 1242 (2019)

- <u>Yaakov Y. Fein</u>, Philipp Geyer, Filip Kiałka, Stefan Gerlich, and Markus Arndt
  Improved accuracy fullerene polarizability measurements in a long-baseline matter-wave interferometer
  Physical Review Research **1**, 033158 (2019)

- <u>Yaakov Y. Fein</u>, Armin Shayeghi, Lukas Mairhofer, Filip Kiałka, Philipp Rieser, Philipp Geyer, Stefan Gerlich, and Markus Arndt
  Quantum-Assisted Measurement of Atomic Diamagnetism
  Physical Review X **10**, 011014 (2020)

- <u>Yaakov Y. Fein</u>, Filip Kiałka, Philipp Geyer, Stefan Gerlich, and Markus Arndt
  Coriolis compensation via gravity in a matter-wave interferometer
  New Journal of Physics **22**, 033013 (2020)

- Stefan Gerlich, <u>Yaakov Y. Fein</u>, and Markus Arndt
  Interferometric tests of wave-function collapse
  "Do wave functions jump? Perspectives on the work of GC Ghirardi", Springer, (**accepted**, 2020)

- Jonas Schätti, Valentin Köhler, Marcel Mayor, <u>Yaakov Y. Fein</u>, Philipp Geyer, Lukas Mairhofer, Stefan Gerlich, and Markus Arndt
  Matter-wave interference and deflection of tripeptides decorated with fluorinated alkyl chains
  Journal of Mass Spectrometry (**accepted**, 2020)

Reprints of selected publications

A selection of publications resulting from this thesis is reprinted with the permission of the respective journals:

Quantum superposition of molecules beyond 25 kDa

Yaakov Y. Fein [1], Philipp Geyer[1], Patrick Zwick[2], Filip Kiałka[1], Sebastian Pedalino[1], Marcel Mayor[2,3,4], Stefan Gerlich[1] and Markus Arndt [1]*

Matter-wave interference experiments provide a direct confirmation of the quantum superposition principle, a hallmark of quantum theory, and thereby constrain possible modifications to quantum mechanics[1]. By increasing the mass of the interfering particles and the macroscopicity of the superposition[2], more stringent bounds can be placed on modified quantum theories such as objective collapse models[3]. Here, we report interference of a molecular library of functionalized oligoporphyrins[4] with masses beyond 25,000 Da and consisting of up to 2,000 atoms, by far the heaviest objects shown to exhibit matter-wave interference to date. We demonstrate quantum superposition of these massive particles by measuring interference fringes in a new 2-m-long Talbot–Lau interferometer that permits access to a wide range of particle masses with a large variety of internal states. The molecules in our study have de Broglie wavelengths down to 53 fm, five orders of magnitude smaller than the diameter of the molecules themselves. Our results show excellent agreement with quantum theory and cannot be explained classically. The interference fringes reach more than 90% of the expected visibility and the resulting macroscopicity value of 14.1 represents an order of magnitude increase over previous experiments[2].

In recent years there has been a growing experimental effort to create highly macroscopic quantum states in a range of systems, including superconducting quantum interference devices[5], Bose–Einstein condensates (BECs)[6], optomechanical systems[7] and matter-wave interferometers[8,9]. Such systems probe the universality of quantum mechanics by showing that their dynamics cannot be understood without quantum theory.

To demonstrate the wave nature of a new class of massive particles we built the Long-Baseline Universal Matter-Wave Interferometer (LUMI), a three-grating Talbot–Lau interferometer with a baseline of 2 m, the longest macromolecular interferometer to date. LUMI can be operated with either three mechanical gratings or two mechanical grating and one optical grating. The latter scheme, which is the one used in these experiments, is known as a Kapitza–Dirac–Talbot–Lau interferometer (KDTLI)[10], and relies on diffraction at a thin optical grating via the optical dipole force[11]. The essential physics is similar in both schemes: the first grating acts as an array of narrow collimation slits to prepare a coherent illumination of the second grating, resulting in a near-field self-imaging phenomenon known as the Talbot–Lau effect. A third grating further downstream is transversely scanned to detect the presence of the interference fringes, which are collected by an integrating detector.

In the case of a KDTLI, coherent self-imaging of a monochromatic molecular beam occurs when the gratings are spaced by half-integer multiples of the Talbot length, $L_{\mathrm{T}} = d^2/\lambda_{\mathrm{dB}}$. Here, d is the grating period (266 nm) and $\lambda_{\mathrm{dB}} = h/mv$ is the de Broglie wavelength, with m and v being the molecular mass and velocity. Observing coherent imaging with large masses therefore requires a long interferometer baseline and/or a small longitudinal beam velocity. The 2 m length of LUMI thus allows us to access de Broglie wavelengths as small as 35 fm with readily available molecular beam techniques. It should also be noted that the Talbot condition does not have to be exactly satisfied to maintain high interference visibility in the KDTLI scheme, nor does the molecular beam require a high degree of initial spatial coherence[12].

A schematic of the experiment is shown in Fig. 1. A molecular beam is formed by pulsed laser desorption from a coated glass slide. The beam is collimated by slits (500 μm horizontal, 400 μm vertical) and modulated by a chopper disc with a pseudorandom sequence of openings for time-of-flight (TOF) measurements[13]. The molecules we use are tailored derivatives of oligo-tetraphenylporphyrins enriched by a library of up to 60 fluoroalkylsulfanyl chains[4] (see Methods for details). A differential pumping stage separates the source chamber from the interferometer chamber, which houses the three gratings and their translation and rotation stages. After traversing the interferometer, the molecules are ionized by electron impact, mass-selected in a quadrupole and counted. Interference fringes are then detected by shifting the final mechanical grating transversely in small steps while monitoring the transmitted molecular flux.

The long baseline of LUMI renders it sensitive to global external forces, such as gravity and rotation, smaller than 10^{-26} N. The intrinsic sensitivity of molecular interferometry has shown its utility in measuring properties such as polarizabilities, dipole moments and absorption cross-sections[14–17], but the enhanced sensitivity of LUMI also introduces challenges. In particular, vibration isolation, compensation of the Coriolis effect, and beam intensity and stability become significant hurdles.

The interferometer is built on a 160 kg Invar bar for high thermal and mechanical stability. It is suspended by a pendulum and damped with magnetic eddy-current brakes for vibration isolation. The stability of the interferometer was thoroughly characterized using accelerometers and optical interferometers, as discussed in the Methods.

The effect of the Earth's rotation plays a significant role in our experiment, since the Coriolis force is velocity-dependent and our molecular beam contains a broad spread of velocities. Given the

[1]Faculty of Physics, University of Vienna, Vienna, Austria. [2]Department of Chemistry, University of Basel, Basel, Switzerland. [3]Karlsruhe Institute of Technology, Institute of Nanotechnology, Karlsruhe, Germany. [4]Lehn Institute of Functional Materials, School of Chemistry, Sun Yat-Sen University, Guangzhou, China. *e-mail: markus.arndt@univie.ac.at
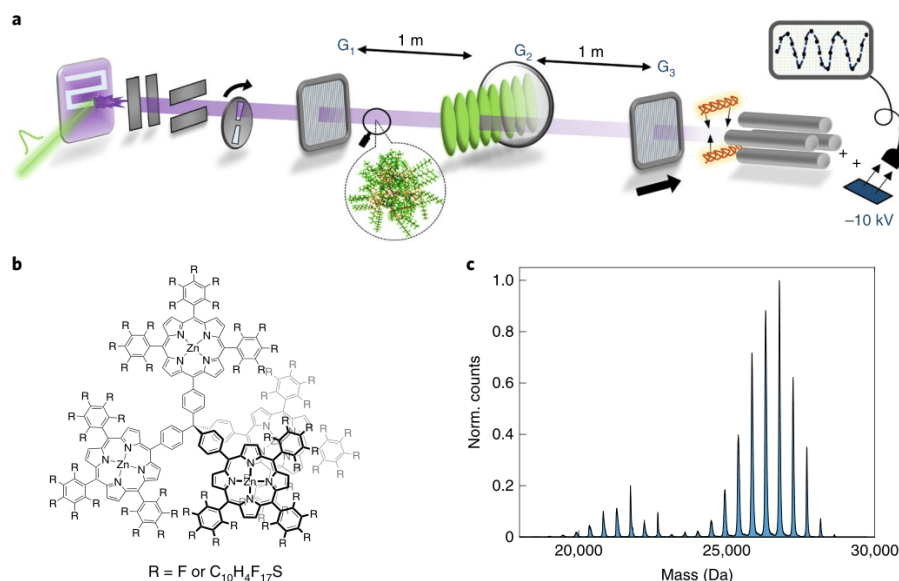
Fig. 1 | Experimental schematic and molecule details. a, The molecular beam is created via nanosecond laser desorption (532 nm, 1 kHz, $I \approx 1 \times 10^8$ W cm^{-2}), followed by collimation and TOF encoding via a pseudo-random chopper. The beam then enters the interferometer chamber, passing two SiN gratings G$_1$ and G$_3$ (266 nm period, 43% open fraction, 160 nm thick) and the optical grating G$_2$ ($\lambda = 532$ nm, vertical beam waist 690 μm), spaced by $L = 0.98$ m. The third grating shifts transversely across the molecular beam to detect the presence of quantum interference fringes that manifest as a molecular density pattern of period d. The molecules are then ionized by electron impact and are mass-selected and counted in a customized quadrupole mass spectrometer that can resolve masses beyond 1 MDa. **b,** The molecules in this study consist of a tetraphenylmethane core with four zinc-coordinated porphyrin branches. Each branch contains up to 15 fluoroalkylsulfanyl chains. **c,** The MALDI-TOF spectrum of the molecular library after matrix-free desorption. The mass resolution in LUMI during interference experiments was lower to maximize transmission, as discussed in the Methods.

Earth's angular velocity Ω_E, each velocity class is transversely shifted by an amount proportional to $\Omega_E L^2/v$, resulting in blurred interference fringes. Owing to the 1 m grating separation L, the Coriolis shift is significant compared to the grating period. We compensate this shift with the velocity-dependent phase shift caused by gravity. The gravitational shift is proportional to $g \sin(\theta) L^2/v^2$, where θ is a common roll of the grating bars relative to gravity. Time-resolved measurements of fullerene interference confirm that the Coriolis effect was more than 95% compensated for the parameters of the interference measurements described here (see Methods for details).

An intense neutral beam of intact molecules is a prerequisite for our experiments, but soft neutral volatilization and post-ionization of complex molecules is an outstanding technical challenge. While matrix-assisted laser desorption and electrospray ionization are useful tools for molecular analysis, the charged beams they produce are incompatible with the stringent dephasing requirements of interferometry. Continuous effusive thermal beams, on the other hand, suffer from thermal fragmentation for masses beyond a few kilodaltons. This can be overcome via fluoroalkyl-functionalization of the molecules, which adds mass, reduces the polarizability-to-mass ratio and increases volatility[4].

Here we use matrix-free nanosecond pulsed laser desorption of a tailor-made library of functionalized oligoporphyrins (see Fig. 1 and Methods). The molecules are coated on a glass slide that is continuously translated to expose a fresh molecular layer to the high-repetition-rate desorption laser beam. Instability of the molecular flux, probably due to inhomogeneity of the molecular coating, is compensated by mechanically chopping the optical grating during an interference scan. The data are then divided into laser-on and laser-off bins, where the laser-off bins constitute control measurements in which interference cannot occur. This technique is highly robust to the varying source intensity, as discussed in the Methods.

We verify the quantum nature of the observed fringes by measuring their sinusoidal visibility as a function of the diffraction laser power. This enables us to rule out classical phase-space trajectories as the mechanism behind the observed fringes. The theoretical expectation of such a measurement is calculated by propagating the Wigner function through the interferometer, yielding the sinusoidal visibility V of the interference curves

$$V = 2 \left| \operatorname{sinc}(\pi f_1) \operatorname{sinc}(\pi f_3) B_{qm,cl}\left(\frac{L}{L_T}\right) \right| \qquad (1)$$

The exact form of the Talbot coefficients $B_{qm,cl}$ can be found in the literature[12]. The effect of the first and third mechanical gratings are described by the sinc terms, which depend on the respective grating open fractions of the mechanical gratings, $f_{1,3}$. The optical grating is described by the B coefficients, which can be modelled using the complete quantum mechanical treatment (B_{qm}) or using classical dynamics (B_{cl}) in which classical phase-space trajectories can also create sinusoidal fringes under certain conditions. The B coefficients contain the combined effects of photon absorption and phase modulation of the matter wave and depend on the laser power of the optical grating. The different dependence of B_{qm} and B_{cl} on laser power allows us to clearly differentiate quantum from classical dynamics.

Figure 2 shows a typical interference scan, as well as the observed visibilities of such scans as a function of laser power along with the classical and quantum predictions. A number of parameters enter the calculation of visibility, including the molecules' polarizability and absorption cross-section, as well as the open fractions of the mechanical gratings (see Methods). We also take into account the experimental Gaussian velocity distribution ($v_o = 261 \pm 9$ m s^{-1}, $\sigma = 52 \pm 7$ m s^{-1}) and the mass distribution of the molecular library.
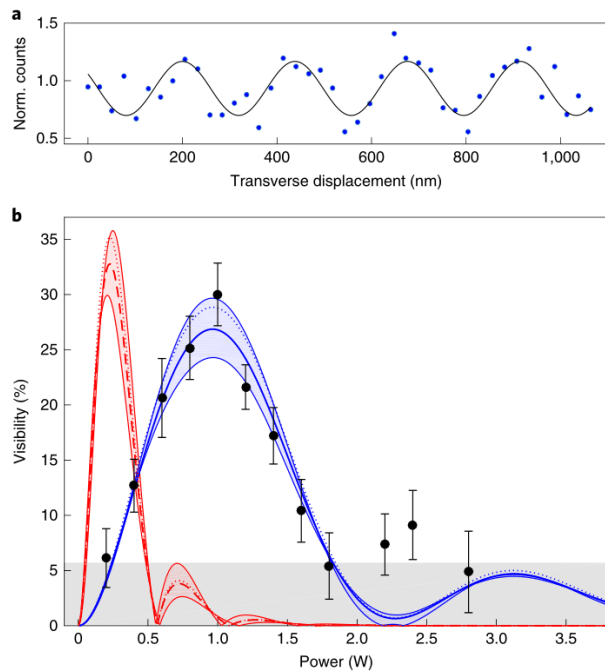
Fig. 2 | Interference data. a, Counts as a function of the transverse position of the third grating with a sine-fit (solid black line) yielding a visibility of $25 \pm 3\%$. The optical grating power was 1.2 W for this single scan. Counts are dark-rate-corrected and normalized to the control measurements. **b**, Visibility as a function of diffraction laser power. The solid blue line indicates the quantum mechanical model and the dashed red line is a classical model, both scaled vertically by a factor of 0.93. The shaded areas on the curves represent uncertainty in the model parameters, and the dotted lines indicate unscaled theory curves. Each data point includes two or more individual sine curves, and error bars are 68% confidence intervals of the sine fit amplitudes added in quadrature. The grey shaded area is the noise floor of the measurements.

The latter plays a role because during typical operation the quadrupole in LUMI transmits the entire mass library shown in Fig. 1, as discussed in the Methods.

The measurement uncertainty of the velocity distribution yields a spread in the calculated visibility for a given power, which is represented by the shaded area of the theory curves. The data show good agreement with the quantum prediction, yielding up to 30% visibility in a power range where negligible visibility is expected from purely classical dynamics. We thus find that classical dynamics are strongly ruled out. A vertical scale factor for the theory curves of 0.93 gives the best agreement with the data, which may be attributed to slight grating misalignment due to grating drift and residual visibility loss due to the Coriolis effect and the effective open fractions of the mechanical gratings (see Methods). The last two effects are estimated to each contribute less than 5% visibility reduction, but combined with a roll misalignment of order $100\,\mu\mathrm{rad}$ around the longitudinal axis could readily explain the observed 7% visibility reduction. Estimates show that collisional and thermal decoherence do not yet play a major role in reducing the observed visibility, given a typical vacuum pressure of $2\times10^{-8}\,\mathrm{mbar}$ and molecular temperatures below $1,000\,\mathrm{K}$ (ref. [18]).

Our experiment tests quantum mechanics in a new regime and it is interesting to put this into a wider perspective. Various measures of macroscopicity have been proposed as a means of comparing matter-wave interference experiments[19,20]. Here we use the macroscopicity measure μ introduced by Nimmrichter and Hornberger in 2013[2], which quantifies the extent to which minimal nonlinear modifications to quantum mechanics are ruled out by a given experiment. The macroscopicity value of our superposition by this measure is given by

$$\mu = \log_{10}\left(\frac{1}{\ln(\eta)}\left(\frac{m}{m_\mathrm{e}}\right)^2\frac{\tau}{1\,\mathrm{s}}\right) = 14.1 \qquad (2)$$

with the coherence time $\tau = 7.5\,\mathrm{ms}$ and m_e being the electron mass. We have used the lower bound of the fitted scale factor (0.93 ± 0.06) as the fidelity η, and 26,777 Da for the mass m, the most abundant mass in the molecular library. This value of μ represents an order of magnitude improvement over previous interferometric experiments, as shown by the circled red diamond in Fig. 3.
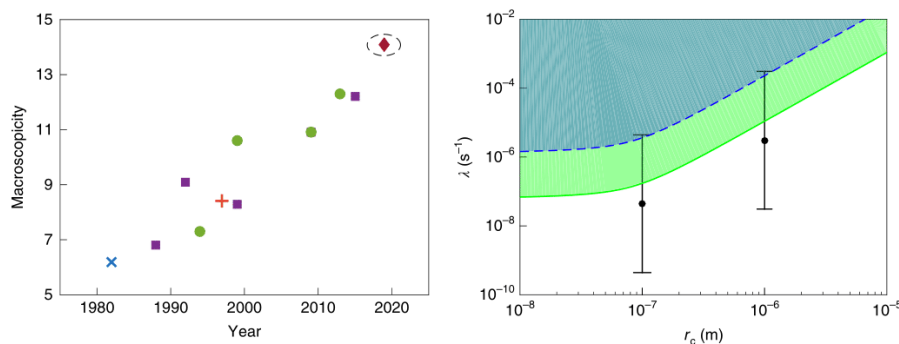
Fig. 3 | Macroscopicity and CSL bounds. a, Selected macroscopicity values of matter-wave interference experiments as a function of year of publication[2,8,9]. The circled red diamond is for our current work, and the other symbols are for experiments with atoms (purple squares), neutrons (blue cross), BECs (red plus) and molecules (green circles). **b**, Bounds on the CSL model for the relevant parameters of correlation length r_c and rate λ, assuming a 50% reduction in visibility is ruled out in the shaded regions. The upper bound (blue, dashed) is the previous interferometric bound in this region of parameter space[31], and the green lower bound is from the current experiment. Note that the bound is an approximation that breaks down for $r_\mathrm{c} < r_\mathrm{molec}$ (ref. [23]); that is, outside the range displayed here. The error bars correspond to values proposed by Adler[21].

As an example of a modified quantum theory, we consider the well-studied continuous spontaneous localization (CSL) model[3]. CSL adds a stochastic nonlinear term to the Schrödinger equation that effectively destroys macroscopic superpositions over time. The rate λ and the correlation length r_c determine the frequency and length scale of the wavefunction collapse. By experimentally demonstrating macroscopic superposition states, we exclude regions of the CSL parameter space. In Fig. 3 we show the bounds we place on CSL with the current experiments. The interference experiments presented here begin to significantly restrict the CSL parameters proposed by Adler[21]. Although stronger bounds are imposed by non-interferometric methods that exclude spontaneous heating effects[22], interferometric bounds are more robust to a wider range of modified collapse models, such as CSL with coloured noise and dissipation[23]. The next generation of matter-wave experiments that will push the mass by an order of magnitude[24] will directly test the remainder of the Adler values and become competitive with non-interferometric bounds.

The delocalized molecules in our experiment are each roughly the mass of the green fluorescent protein[25] (27 kDa) or a small BEC, while exceeding the temperature of a BEC by more than nine orders of magnitude. High-contrast quantum interference persists despite the thousands of excited vibrational levels and billions of structural and conformational isomers present in the molecular beam. This is because we probe the centre-of-mass motion, and can thus discount internal degrees of freedom as long as the internal temperature is kept at a level where thermal radiation does not provide which-path information[18]. With advances in beam sources for biomolecules and metal clusters[26,27], techniques to cool the particles below 80 K (refs. [28,29]), and refined grating[26] and imaging technologies[30], our experiment is scalable and will push matter-wave interference and macroscopicity tests by another order of magnitude[24].

Online content

Any methods, additional references, Nature Research reporting summaries, source data, statements of code and data availability and associated accession codes are available at https://doi.org/10.1038/s41567-019-0663-9.

References

1. Arndt, M. & Hornberger, K. Testing the limits of quantum mechanical superpositions. *Nat. Phys.* **10**, 271–277 (2014).
2. Nimmrichter, S. & Hornberger, K. Macroscopicity of mechanical quantum superposition states. *Phys. Rev. Lett.* **110**, 160403 (2013).
3. Bassi, A., Lochan, K., Satin, S., Singh, T. P. & Ulbricht, H. Models of wave-function collapse, underlying theories, and experimental tests. *Rev. Mod. Phys.* **85**, 471–527 (2013).
4. Sezer, U., Schmid, P., Felix, L., Mayor, M. & Arndt, M. Stability of high-mass molecular libraries: the role of the oligoporphyrin core. *J. Mass Spectrom.* **50**, 235–239 (2015).
5. Friedman, J. R., Patel, V., Chen, W., Tolpygo, S. K. & Lukens, J. E. Quantum superposition of distinct macroscopic states. *Nature* **406**, 43–46 (2000).
6. Andrews, M. R. et al. Observation of interference between two Bose condensates. *Science* **275**, 637–641 (1997).
7. Marinković, I. et al. Optomechanical Bell test. *Phys. Rev. Lett.* **121**, 220404 (2018).
8. Kovachy, T. et al. Quantum superposition at the half-metre scale. *Nature* **528**, 530–533 (2015).
9. Eibenberger, S., Gerlich, S., Arndt, M., Mayor, M. & Tüxen, J. Matter-wave interference of particles selected from a molecular library with masses exceeding 10,000 amu. *Phys. Chem. Chem. Phys.* **15**, 14696–14700 (2013).
10. Gerlich, S. et al. A Kapitza–Dirac–Talbot–Lau interferometer for highly polarizable molecules. *Nat. Phys.* **3**, 711–715 (2007).
11. Nairz, O., Brezger, B., Arndt, M. & Zeilinger, A. Diffraction of complex molecules by structures made of light. *Phys. Rev. Lett.* **87**, 160401 (2001).
12. Hornberger, K. et al. Theory and experimental verification of Kapitza–Dirac–Talbot–Lau interferometry. *New J. Phys.* **11**, 043032 (2009).
13. Koleske, D. D. & Sibener, S. J. Generation of pseudorandom sequences for use in cross-correlation modulation. *Rev. Sci. Instrum.* **63**, 3852–3855 (1992).
14. Hackermüller, L. et al. Optical polarizabilities of large molecules measured in near-field interferometry. *Appl. Phys. B* **89**, 469–473 (2007).
15. Mairhofer, L. et al. Quantum-assisted metrology of neutral vitamins in the gas phase. *Angew. Chem. Int. Ed.* **56**, 10947–10951 (2017).
16. Eibenberger, S., Cheng, X., Cotter, J. P. & Arndt, M. Absolute absorption cross sections from photon recoil in a matter-wave interferometer. *Phys. Rev. Lett.* **112**, 250402 (2014).
17. Eibenberger, S., Gerlich, S., Arndt, M., Tüxen, J. & Mayor, M. Electric moments in molecule interferometry. *New J. Phys.* **13**, 043033 (2011).
18. Hornberger, K., Sipe, J. E. & Arndt, M. Theory of decoherence in a matter wave Talbot–Lau interferometer. *Phys. Rev. A* **70**, 053608 (2004).
19. Fröwis, F., Sekatski, P., Dür, W., Gisin, N. & Sangouard, N. Macroscopic quantum states: measures, fragility, and implementations. *Rev. Mod. Phys.* **90**, 025004 (2018).
20. Schrinski, B., Nimmrichter, S., Stickler, B. A. & Hornberger, K. Macroscopicity of quantum mechanical superposition tests via hypothesis falsification. Preprint at https://arXiv.org/abs/1902.11092v1 (2019).
21. Adler, S. L. Lower and upper bounds on CSL parameters from latent image formation and IGM heating. *J. Phys. A* **40**, 2935–2957 (2007).
22. Carlesso, M., Bassi, A., Falferi, P. & Vinante, A. Experimental bounds on collapse models from gravitational wave detectors. *Phys. Rev. D* **94**, 124036 (2016).
23. Toroš, M., Gasbarri, G. & Bassi, A. Colored and dissipative continuous spontaneous localization model and bounds from matter-wave interferometry. *Phys. Lett. A* **381**, 3921–3927 (2017).
24. Kiałka, F. et al. Concepts for long-baseline high-mass matter-wave interferometry. *Phys. Scr.* **94**, 034001 (2019).
25. Chalfie, M. GFP: lighting up life. *Proc. Natl Acad. Sci. USA* **106**, 10073–10080 (2009).
26. Debiossac, M. et al. Tailored photocleavable peptides: fragmentation and neutralization pathways in high vacuum. *Phys. Chem. Chem. Phys.* **20**, 11412–11417 (2018).
27. Haberland, H., Karrais, M. & Mall, M. A new type of cluster and cluster ion source. *Z. Phys. D* **20**, 413–415 (1991).
28. Hutzler, N. R., Lu, H. I. & Doyle, J. M. The buffer gas beam: an intense, cold, and slow source for atoms and molecules. *Chem. Rev.* **112**, 4803–4827 (2012).
29. Barry, J. F. & DeMille, D. Low-temperature physics: a chilling effect for molecules. *Nature* **491**, 539–540 (2012).
30. Piliarik, M. & Sandoghdar, V. Direct optical sensing of single unlabelled proteins and super-resolution imaging of their binding sites. *Nat. Commun.* **5**, 4495 (2014).
31. Nimmrichter, S., Hornberger, K., Haslinger, P. & Arndt, M. Testing spontaneous localization theories with matter-wave interferometry. *Phys. Rev. A* **83**, 043621 (2011).

Author contributions

M.A. conceived the experiment. Y.Y.F., S.G. and P.G. designed and constructed the experiment. P.Z. and M.M. synthesized the molecules used in the experiment. Y.Y.F, S.G., S.P. and P.G. carried out the experiments described here. Y.Y.F., F.K. and S.G. analysed the data, and Y.Y.F., S.G. and M.A. prepared the manuscript.

Competing interests

The authors declare no competing interests.

Additional information

Supplementary information is available for this paper at https://doi.org/10.1038/s41567-019-0663-9.

Reprints and permissions information is available at www.nature.com/reprints.

Correspondence and requests for materials should be addressed to M.A.

Peer review information *Nature Physics* thanks Stephen Adler and the other, anonymous, reviewer(s) for their contribution to the peer review of this work.

Publisher's note Springer Nature remains neutral with regard to jurisdictional claims in published maps and institutional affiliations.

LETTERS

Methods

Molecule synthesis and characterization. The molecules used in the interference experiments are members of a library based on a tetrahedral arrangement of four zinc-coordinated porphyrins around a tetraphenylmethane core. The target library of perfluorothioalkyl-substituted porphyrin tetramers was synthesized in two steps as illustrated in Supplementary Fig. 1. A fourfold Suzuki–Miyaura cross-coupling reaction of [5-bromo-10,15,20-tris(perfluorophenyl)porphyrinato] zinc(II) (ref. [32]) and (methanetetrayltetrakis(benzene-4,1-diyl))tetraboronic acid[33] in a four-to-one ratio yielded the tetrameric porphyrin intermediate with an 87% yield. Treatment of a mixture of this compound and dry Cs_2CO_3 in dry and degassed N,N-dimethylformamide with commercially available $1H,1H,2H,2H$-perfluorodecanethiol gave access to the target library. The resulting library was characterized using matrix-assisted-laser desorption/ionization (MALDI) and TOF mass spectrometry, as shown in Fig. 1. See Supplementary Information for further synthesis details.

Beam formation and detection. The fragility and high mass of the oligoporphyrin library necessitated a specialized source and detector for compatibility with LUMI. The molecules were dissolved in Fluorinert FC-72, coated on a 50×50 mm² glass slide and then desorbed in high vacuum using sub-10 ns, 532 nm laser pulses at a 1 kHz repetition rate. The pulse energy was measured as 1.8 mJ and focused to about 0.15 mm². The coated plate was scanned in a raster pattern, but counts were always collected in the same direction of travel.

After traversing the interferometer, the molecules were ionized by electron impact ionization at 35 eV, focused by electrostatic lenses through a quadrupole mass filter (QMF200, Oxford Applied Research) and accelerated to a conversion dynode held at −10 kV to ground. The resulting electrons were counted by a continuous secondary electron multiplier (Detech 402 A-H). This system can detect molecules beyond 25 kDa with 2% mass resolution. In practice, the resolution was reduced to $\Delta m/m = 30\%$ to increase the transmission of the mass filter. This resolution transmitted the entire mass library shown in Fig. 1, which was reflected in the theory visibility curves of Fig. 2.

The centre of the transmitted mass distribution shifts to lower masses as the resolution of the quadrupole mass filter is decreased (by decreasing the ratio of d.c. to radiofrequency voltage at a fixed radiofrequency), such that the maximal counts were detected below 25 kDa for the 30% resolution used in the experiments. We verified that the detected molecules represent the expected high-mass molecular library in two ways. First, we collected mass spectra as a function of resolution, which shows that the true distribution is shifted to higher mass as the resolution is improved (Supplementary Fig. 2). Second, we compared MALDI-TOF spectra of the original synthesized molecules with desorbed and recollected material (Supplementary Fig. 3) to confirm that the masses of the detected library of molecules remained largely the same after volatilization in the LUMI laser desorption source. The secondary mass peak visible at 15 kDa at higher resolutions of the LUMI mass spectrometer is probably due to electron-impact-induced fragmentation, as shown in Supplementary Fig. 2.

Parameters of the visibility calculation. The visibility calculation in equation (1) is key to interpreting the data in Fig. 2 and to our claim that the quantum model is confirmed while the classical one is ruled out. The Talbot coefficients, $B_{qm,cl}$, depend on the accumulated phase of the matter wave in the optical grating and the number of absorbed photons. These depend on the molecular absorption σ_{abs} and optical polarizability at the grating wavelength $\alpha_{532\,nm}$, as well as on the molecular beam velocity and the laser beam waist. Furthermore, the sinc functions contain a dependence on the open fractions (the ratio of the grating opening width to the period) of the first and third gratings. Below we discuss the measurement/estimation of each of these parameters.

The molecular velocity distribution is measured by modulating the beam in a pseudo-random sequence with a customized chopper disc and then deconvolving the measured TOF signal with that same sequence as measured by a photodiode[13]. The uncertainty is estimated by the standard deviation of seven velocity measurements taken over the course of the experiments.

The optical grating beam waist is measured using a beam profiler (Coherent BeamMaster) and is cross-checked by calibrating the set-up with C_{60}. Since the C_{60} optical polarizability and absorption cross-section at 532 nm are well known, the only free parameter in the visibility is the laser beam waist. This calibration revealed a slightly larger $1/e^2$ beam waist than the profilometry (690 μm versus 570 μm), which is consistent with the assumption that the effective power of the optical grating is less than the value we measure outside the vacuum chamber. We attribute this to two effects: a measured systematic offset of about 200 μm in the vertical positioning of the optical grating with respect to the molecular beam (which accounts for nearly half of the beam waist discrepancy), along with some power loss due to in-vacuum optics.

The absorption cross-section of the molecule at 532 nm is estimated as $\sigma_{abs} = 1.6 \times 10^{-20}$ m². This was determined by scaling the UV/visible spectrum of the oligoporphyrins in solution to agree with four times the zinc tetraphenylporphyrin value[34] at the Soret band, as shown in Supplementary Fig. 4. The UV/VIS spectrum of the oligoporphyrins in solution was compared to a spectrum of dry material to confirm that there was no significant solvent-induced line shift.

The optical polarizability at 532 nm can be estimated by summing the contributions of the static polarizability of the four porphyrin branches with their respective fluoroalkylsulfanyl chains. The static polarizability was calculated in Gaussian16 for several conformations, yielding an average of $\alpha = 4\pi\varepsilon_0 \times 1,321 \pm 18$ ų. The static and optical polarizabilities should be in reasonable agreement since the UV/VIS spectrum confirms that the molecule is not near a resonance at 532 nm.

The final open parameters in the visibility are the open fractions of the mechanical gratings. The geometric open fraction of the mechanical gratings was measured as 43% after their fabrication. However, this value can be effectively reduced in two ways: first, by coating the first grating with molecules; and second, via van der Waals interactions that deflect molecules near the grating walls out of the beam[35]. By again comparing to C_{60} reference measurements and taking into account the relative polarizability-to-mass ratios, the visibility of the functionalized oligoporphyrins should still reach about 95% of the theoretical contrast expected for a purely geometric open fraction[24,36]. Due to the smallness of the effect and uncertainty in the model parameters, this 5% factor is not included in the scaling of the visibility, although its inclusion would boost the fidelity η and the macroscopicity value.

Coriolis compensation. Compensation of the Coriolis effect is critical to obtaining high-visibility interference fringes in LUMI. By tilting the gratings, we introduce a gravitational deflection that opposes the Coriolis shift

$$\frac{g\sin(\theta_{roll})L^2}{v_p^2} \approx -\frac{2\Omega_E L^2}{v_p}$$

where L is the interferometer length and Ω_E is the angular velocity of the Earth at the position of the interferometer. Choosing the appropriate roll angle θ_{roll} allows us to compensate at a desired velocity, v_p.

The level of Coriolis compensation can be determined experimentally by taking a time-resolved measurement of the interference pattern and extracting the phase as a function of velocity. The system was calibrated with C_{60} immediately after the series of experiments with the functionalized oligoporphyrins. A small uncertainty remains due to a realignment of the gratings on the level of 300 μrad that was necessary for the C_{60} calibration, but we estimate greater than 95% compensation during the interference experiments with the high-mass particles. As with the effective open-fraction estimate, we do not include this small factor in the scaling of the data in Fig. 2 in an effort to keep the fidelity estimate conservative.

Vibrational isolation. Vibrations present another concern for long-baseline interferometry. We consider three grating motions: independent, common and torsional. Independent, or phase-uncorrelated motion of the gratings, should not exceed an amplitude of 5 nm at all frequencies to retain 98% of full interference visibility. Common-mode motion of the gratings is less critical; a sinusoidal motion of 10 nm amplitude at 50 Hz still allows for 97% visibility. Torsional motion around the centre grating has similar bounds as common-mode motion. The formulae used are adapted from those in Stibor et al.[37], and all numbers are calculated for the empirical velocity distribution of the oligoporphyrins.

Experimentally we took care to mechanically isolate and characterize our system. The interferometer is suspended inside the vacuum chamber on a 28 cm pendulum with magnetic eddy current brakes to provide damping. Metal springs are used both at the pendulum pivot point and at the support points of the interferometer bar. The vibrational spectrum of the system was characterized using accelerometers inside and outside the vacuum chamber (PCB 356M98 and 393B12 respectively), Michelson interferometers (SmarAct PicoScale) reflecting off the grating mounts, and an optical Mach–Zehnder interferometer mounted in parallel with the gratings. The last of these was particularly useful for characterizing independent motion of the gratings. The observed vibrational levels were sufficient for full interference visibility, which was experimentally confirmed by obtaining full visibility in the set-up with fullerenes.

Reference measurement procedure. The instability of the source occasionally modulated the count rate with periodic fluctuations correlated to the scanning motion of the plate rather than real interference effects. This motivated us to introduce a mechanical chopper to modulate the diffraction laser at 2 Hz, such that over the typical integration time of 10 s per scan position, there were 5 s with laser exposure and 5 s without. By properly binning the counts, any source-related count modulation is readily compensated, as shown in Supplementary Fig. 5.

Data availability

The data that support the plots within this paper and other findings of this study are available from the corresponding author on request.

References

32. Frost, J. R. et al. H oxygenation catalyzed by a supramolecular ruthenium complex. *Angew. Chem. Int. Ed.* **54**, 691–695 (2015).

LETTERS

33. Fournier, J.-H., Maris, T., Wuest, J. D., Guo, W. & Galoppini, E. Molecular tectonics. Use of the hydrogen bonding of boronic acids to direct supramolecular construction. *J. Am. Chem. Soc.* **125**, 1002–1006 (2003).

34. Dixon, J. M., Taniguchi, M. & Lindsey, J. S. PhotochemCAD 2. A refined program with accompanying spectral databases for photochemical calculations. *Photochem. Photobiol.* **81**, 212–213 (2005).

35. Juffmann, T., Nimmrichter, S., Arndt, M., Gleiter, H. & Hornberger, K. New prospects for de Broglie interferometry. *Found. Phys.* **42**, 98–110 (2010).

36. Nimmrichter, S. & Hornberger, K. Theory of Talbot–Lau interference beyond the eikonal approximation. *Phys. Rev. A* **78**, 023612 (2008).

37. Stibor, A., Hornberger, K., Hackermüller, L., Zeilinger, A. & Arndt, M. Talbot–Lau interferometry with fullerenes: sensitivity to inertial forces and vibrational dephasing. *Laser Phys.* **15**, 10–17 (2005).

126

Improved accuracy fullerene polarizability measurements in a long-baseline matter-wave interferometer

Yaakov Y. Fein [ORCID], Philipp Geyer, Filip Kiałka, Stefan Gerlich, and Markus Arndt [ORCID][*]

Faculty of Physics, University of Vienna, Boltzmanngasse 5, A-1090 Vienna, Austria

We present electric deflection results for the fullerenes C_{60} and C_{70} obtained with a long-baseline matter-wave interferometer. The second grating of the interferometer is interchangeable between a material grating for fast atom beams and an optical phase grating for polarizable molecules. This allows us to use cesium as a calibration particle and thus measure molecular susceptibilities with improved systematic uncertainty. The static polarizabilities of C_{60} and C_{70} are measured as $4\pi\varepsilon_0 \times 87.4 \pm 0.4 \pm 2.5$ Å^3 and $4\pi\varepsilon_0 \times 106.4 \pm 0.2 \pm 1.1$ Å^3, respectively, in excellent agreement with previous deflection experiments, but with improved uncertainties.

I. INTRODUCTION

Electric deflectometry has been a hallmark of atomic and molecular beam research since the early work of Scheffer and Stark [1]. It has been employed in atomic [2], molecular [3–5], and cluster physics [6–8], as well as in the study of molecular dynamics [9] and in understanding the transition from atomic to bulk properties in clusters [10].

Matter-wave-assisted deflectometry is a natural extension of this technique, in which one measures the deflection of interference fringes rather than the deflection of an entire beam profile. Modern molecular interferometers [11–13] can resolve nanometer-scale fringe shifts, which provides orders of magnitude better resolution than classical beam deflectometry.

Several proof-of-principle experiments have demonstrated the technique by measuring the scalar static polarizability of fullerenes [14] as well as the dynamic susceptibilities of functionalized azobenzenes [15] and native vitamins [16]. The technique has also been used to identify the presence of electric dipole moments [17] and to distinguish molecular fragmentation pathways [18] and structural conformers [19].

Taking full advantage of the technique requires a good knowledge of the geometry of the deflection electrode as well as the various drift lengths of the experiment. An alternative approach, used here, is to calibrate the setup with an alkali atom, the polarizabilities of which have been accurately measured using far-field Mach-Zehnder interferometry [20–22].

Here, we use Talbot-Lau near-field interferometry [23,24], which is better suited to the typically low coherence of molecular beams than far-field techniques. We distinguish between two schemes, the Talbot-Lau interferometer (TLI)

with three equally spaced material gratings [25], and the Kapitza-Dirac-Talbot-Lau interferometer (KDTLI) in which the second grating is an optical phase grating [11].

The TLI scheme is well suited for fast particles with low polarizability, such as atoms, while the KDTLI scheme is best suited for slow and highly polarizable molecules. The measurements presented here were made in the Long-Baseline Universal Matter-Wave Interferometer (LUMI), which can alternate between the TLI and KDTLI schemes with nanometer-precise ultrahigh-vacuum compatible motors. Moreover, the 1-m grating separation provides a force sensitivity on the order of 10^{-26} N. The universality of the interferometer allows for a direct comparison of atoms with molecules in the same apparatus.

We demonstrate the capabilities of LUMI by measuring the static scalar polarizability of the fullerenes C_{60} and C_{70} after calibration with cesium. The atomic calibration together with improved detection techniques allowed us to make both statistical and systematic uncertainty improvements compared to previous fullerene values [4,14,26,27]. These polarizability values are of interest due to the range of theoretical models which give conflicting polarizability predictions [28,29].

II. EXPERIMENTAL DESIGN

In a Talbot-Lau interferometer such as LUMI (see Fig. 1), the first grating prepares transverse coherence in the beam by acting as an array of point sources. Under partially coherent illumination, the second grating is self-imaged, imprinting revivals of the grating structure in the beam density. A third grating is placed at the position of one of these revivals and is transversely scanned to reveal a periodic modulation of the transmitted flux.

We use silicon nitride nanomechanical gratings with periods of $d = 266$ nm for the first and third gratings, while the second is interchangeable between another material grating and an optical phase grating formed by a retroreflected 532-nm laser [11,25]. The all-material TLI scheme was used for the cesium calibration, while the mixed material-optical KDTLI scheme was used for the fullerene measurements.
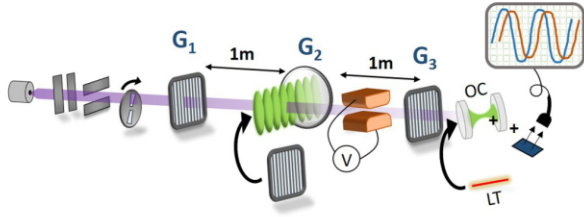
---

*markus.arndt@univie.ac.at

FIG. 1. Experimental setup, from left to right: the thermal source, beam collimators, chopper, and the three gratings (G$_1$–G$_3$). G$_2$ is interchangeable between a mechanical and an optical phase grating, and the electrode is between G$_2$ and G$_3$. The fullerenes are detected by thermal ionization in an optical cavity (OC) while the cesium atoms are counted after Langmuir-Taylor surface ionization (LT) and quadrupole mass selection (not shown).

We deflect the interference fringes with a specially designed electrode in which the value of $(\mathbf{E} \cdot \nabla)E_x$ is constant to within 1% over the traversed region [15]. An electric dipole moment is induced and experiences a constant force which yields a transverse phase shift of the fringes proportional to the static polarizability α_{stat},

$$\Delta\phi = \alpha_{\text{stat}} \frac{KV^2}{mv^2}, \qquad (1)$$

for a particle of mass m, velocity v, and with an applied voltage V. The constant K depends on the length and longitudinal position of the electrode as well as the geometry of the electrode surface. For a force perfectly constant within the electrode and zero elsewhere, $K = \frac{2\pi}{d}(L_1^2/2 - L_1L_2 - L_1L)K_E$, where K_E is the electrode geometry factor, L the intergrating spacing (0.98 m), L_1 the distance from the second grating to the front edge of the electrode (0.15 m), and L_2 the electrode length (0.04 m).

The fringe patterns with amplitudes A must be integrated over the velocity distribution $\rho(v)$ of the beam, giving the averaged pattern

$$\overline{A}\cos\left(kx + \overline{\Delta\phi}\right) = \int_0^\infty dv\rho A\cos\left(kx + \Delta\phi\right), \qquad (2)$$

where x is the direction transverse to the grating bars, $k = 2\pi/d$, and overbars denote velocity-averaged values. The averaged phase shift $\overline{\Delta\phi}$ which we measure is

$$\overline{\Delta\phi} = \arg\left[\int_0^\infty dv\rho A\exp\left(i\Delta\phi\right)\right], \qquad (3)$$

where the velocity dependence of the amplitudes A follows from the visibility function of the interferometer [30,31]. The velocity averaging reduces the fringe visibility for large deflections and finite velocity spreads.

III. RESULTS

A. Cesium calibration

We perform electric deflection of cesium to empirically determine the constant K in Eq. (1), using the literature value for the polarizability of cesium, $\alpha_{\text{Cs}} = 4\pi\varepsilon_0 \times 59.39 \pm$
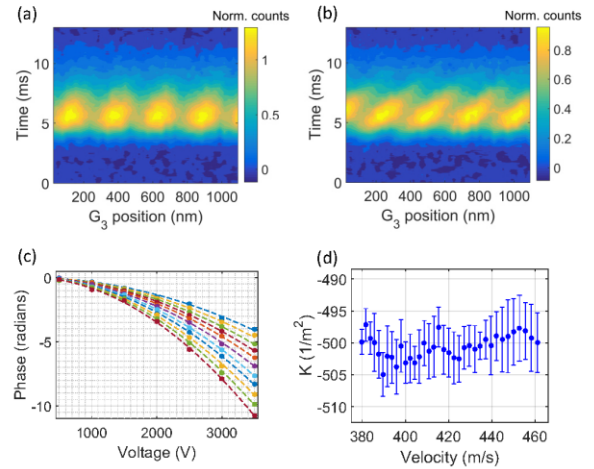

FIG. 2. (a) Time-resolved interference scan taken at the reference electrode voltage of 250 V. (b) As (a) but for 2500 V. (c) Cesium deflection curves for velocities ranging from 380 to 640 m/s, extracted from time-resolved data as shown in (a) and (b). (d) A selection of the curves in (c) is used to determine the mean calibration factor. Every fourth point is shown for clarity. Error bars are 68% confidence intervals of the fitted phase values.

0.03 ± 0.09 Å^3 [22], with the first error statistical and the second systematic.

Cesium was evaporated at 530 K and detected via Langmuir-Taylor surface ionization from a hot rhenium wire followed by quadrupole mass selection. For cesium we use the TLI scheme which gives visibilities up to 18% despite the dispersive van der Waals phase shift introduced at the second material grating [11,32,33]. The combination of high flux and efficient detection permitted the extraction of accurate phase data despite the moderate fringe visibility.

To estimate the statistical error of the calibration constant we compare the values of K extracted for a range of beam velocities. A time-of-flight measurement was made at each position step of G$_3$, yielding contour plots as shown in Fig. 2. This method allows for the extraction of many individual interference scans at a broad range of velocities by taking line cuts at different times. Time-resolved interference measurements were taken for deflection voltages ranging from 500 to 3500 V, with each position of the scan referenced to 250 V to remove the effect of slow phase drifts. Short-term stability of the interferometer was measured to be better than 0.03 nm/s.

The time of flight is measured by modulating the beam with a pseudorandom chopper and deconvoluting the time-resolved signal using the measured chopper sequence [34]. The velocity distribution at a given central velocity is approximated as a Gaussian with a full width at half maximum equal to the inherent resolution of the chopper, $\Delta t/t \approx 1/(fNt_{\text{flight}})$, where f is the chopper rotation frequency and $N = 255$ is the number of chopper bins. The extracted phase shifts in Fig. 2 for various velocities show the expected dependence on voltage.

Fitting Eq. (3) to the deflection data then yields the product $K\alpha_{\text{Cs}}$, which gives K upon insertion of the literature value of

α_{Cs}. The extracted values of K are shown in Fig. 2(d), and an error-weighted average yields $K = 500.42 \pm 0.18\,\mathrm{m}^{-2}$, where the uncertainty is the standard error of the values. The velocity dependence of the fringe amplitudes A can be neglected here due to the small range of velocities contained in each deflection scan. From this value of K the electrode calibration factor K_E can also be estimated as $1.53 \times 10^4\,\mathrm{m}^{-3}$.

With this empirical value of the calibration factor K, we can now extract the polarizability of other particles in the same setup.

B. Fullerene measurements

A thermal fullerene beam (C_{60}: 843 K; C_{70}: 880 K) was produced from a ceramic oven, and velocities were gravitationally selected with the aid of several vertical delimiters (down to 100 μm aperture height). The lower beam velocity compared to cesium made the velocity selection more effective, allowing us to directly tune the velocity distribution without the need for time-resolved interference measurements. The molecules were detected via thermal ionization [35,36] in a 532-nm optical cavity providing up to 300 W of intracavity power in a beam waist of 50 μm. The ions were then directly counted with an electron multiplier. Mass selection was unnecessary due to the purity of the samples (C_{60} 98%, C_{70} >99%) and the negligible dark count rate with thermal ionization. The isotopic distribution of the fullerenes is accounted for by using the molar mass in the calculation of the polarizability. The cavity-enhanced thermal ionization scheme was particularly beneficial since it is more efficient than the electron impact and also acts as a vertical delimiter, thus reducing the velocity spread of the detected beam.

Given the low-beam velocity and high polarizability of the fullerenes we employ the KDTLI scheme, thus avoiding dephasing due to van der Waals interactions at the second grating. Interference visibilities of 35% and 24% could be obtained for C_{60} and C_{70}, respectively.

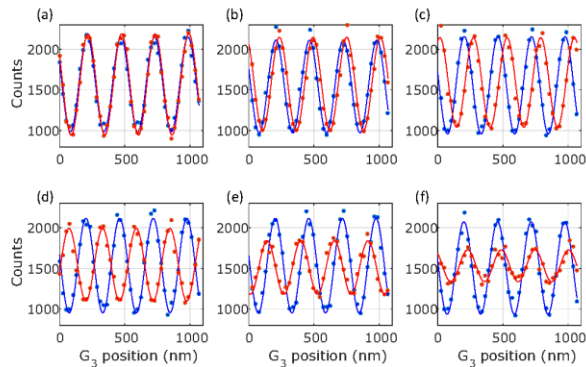Interference scans were collected for electrode voltages of 250–3250 V for a range of selected beam velocities, as

FIG. 3. (a)–(f) Deflection data for C_{60} with sine fits for increasing deflection voltages from 500 to 3000 V in steps of 500 V. Red curves are with the deflection voltage applied, blue with a fixed 250 V reference voltage. The mean velocity for these measurements was 221 m/s. The fringe deflection and visibility loss due to velocity averaging are clearly visible.
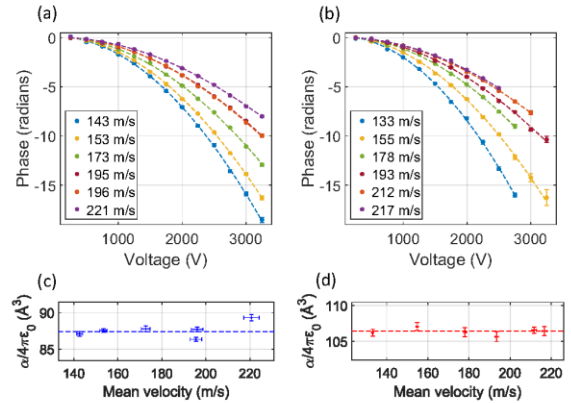
FIG. 4. (a) C_{60} deflection curves for a range of mean velocities. (b) C_{70} deflection curves. (c) C_{60} extracted polarizability values for the various velocities with error bars corresponding to 68% confidence intervals of the fitted phases and the mean velocity. (d) As (c), but for C_{70}. The smaller horizontal error bars are because more data were taken for the velocity calibration during the C_{70} data run.

illustrated in Fig. 3, with the complete deflection data shown in Fig. 4. Velocity measurements were taken six times both before and after each deflection measurement of a given velocity class. A reference measurement at 250 V was taken at each position step to compensate for any phase drifts. The power of the 532-nm laser creating the standing light wave was adjusted for each velocity class, and ranged from 4.4 to 9.3 W.

Inserting the geometry constant K obtained from the cesium measurements into Eq. (3) gives the mean polarizability values $4\pi\varepsilon_0 \times 87.4 \pm 0.4 \pm 2.5\,\text{Å}^3$ and $4\pi\varepsilon_0 \times 106.4 \pm 0.2 \pm 1.1\,\text{Å}^3$ for C_{60} and C_{70}, respectively. The first uncertainty (statistical) is estimated from the standard error of the extracted polarizabilities for different velocity classes as shown in Figs. 4(c) and 4(d). The second uncertainty (systematic) is dominated by the uncertainty of the velocity measurement calibration and a smaller contribution due to the sample impurity. The velocity dependence of the fringe amplitudes A is taken into account in Eq. (3) by using the visibility function in Ref. [31]. A small correction has been applied to account for the slightly different longitudinal position of the optical grating used here and the material grating used for the cesium calibration. Our measured polarizability values are in excellent agreement with previous results, which range from $4\pi\varepsilon_0 \times 76.5\,\text{Å}^3$ to $4\pi\varepsilon_0 \times 88.9\,\text{Å}^3$ for C_{60} and from $4\pi\varepsilon_0 \times 101.9\,\text{Å}^3$ to $4\pi\varepsilon_0 \times 108.5\,\text{Å}^3$ for C_{70} [4,14,26,27].

IV. SUMMARY

The LUMI experiment permits the direct comparison of atoms and molecules across a wide range of masses and polarizabilities. This allowed us to calibrate the deflection setup with cesium and then measure the static dipole polarizability of the fullerenes C_{60} and C_{70}, with a systematic uncertainty two times better for C_{60} and more than five times better for C_{70}.

[1] H. Scheffers and J. Stark, Phys. Z. **35**, 625 (1934).

[2] L. Ma, J. Indergaard, B. Zhang, I. Larkin, R. Moro, and W. A. de Heer, Phys. Rev. A **91**, 010501(R) (2015).

[3] R. Antoine, I. Compagnon, D. Rayane, M. Broyer, P. Dugourd, G. Breaux, F. C. Hagemeister, D. Pippen, R. R. Hudgins, and M. F. Jarrold, Eur. Phys. J. D **20**, 583 (2002).

[4] R. Antoine, P. Dugourd, D. Rayane, E. Benichou, M. Broyer, F. Chandezon, and C. Guet, J. Chem. Phys. **110**, 9771 (1999).

[5] R. Moro, R. Rabinovitch, C. Xia, and V. Kresin, Phys. Rev. Lett. **97**, 123401 (2006).

[6] S. Schäfer and R. Schäfer, Phys. Rev. B **77**, 205211 (2008).

[7] S. Schäfer, S. Heiles, J. Becker, and R. Schäfer, J. Chem. Phys. **129**, 044304 (2008).

[8] W. D. Knight, K. Clemenger, W. A. de Heer, and W. A. Saunders, Phys. Rev. B **31**, 2539 (1985).

[9] D. Rayane, R. Antoine, P. Dugourd, E. Benichou, A. R. Allouche, M. Aubert-Frécon, and M. Broyer, Phys. Rev. Lett. **84**, 1962 (2000).

[10] J. Bowlan, A. Liang, and W. A. de Heer, Phys. Rev. Lett. **106**, 043401 (2011).

[11] S. Gerlich *et al.*, Nat. Phys. **3**, 711 (2007).

[12] P. Haslinger, N. Dörre, P. Geyer, J. Rodewald, S. Nimmrichter, and M. Arndt, Nat. Phys. **9**, 144 (2013).

[13] Y. Y. Fein, P. Geyer, P. Zwick, F. Kiałka, S. Pedalino, M. Mayor, S. Gerlich, and M. Arndt, Nat. Phys. (2019), doi: 10.1038/s41567-019-0663-9.

[14] M. Berninger, A. Stefanov, S. Deachapunya, and M. Arndt, Phys. Rev. A **76**, 013607 (2007).

[15] M. Gring *et al.*, Phys. Rev. A **81**, 031604(R) (2010).

[16] L. Mairhofer, S. Eibenberger, J. P. Cotter, M. Romirer, A. Shayeghi, and M. Arndt, Angew. Chem., Int. Ed. **56**, 10947 (2017).

[17] S. Eibenberger, S. Gerlich, M. Arndt, J. Tüxen, and M. Mayor, New J. Phys. **13**, 043033 (2011).

[18] S. Gerlich, M. Gring, H. Ulbricht, K. Hornberger, J. Tüxen, M. Mayor, and M. Arndt, Angew. Chem., Int. Ed. **47**, 6195 (2008).

[19] J. Tüxen, S. Gerlich, S. Eibenberger, M. Arndt, and M. Mayor, Chem. Commun. **46**, 4145 (2010).

[20] A. Miffre, M. Jacquey, M. Büchner, G. Trenec, and J. Vigue, Phys. Rev. A **73**, 011603(R) (2006).

[21] W. F. Holmgren, M. C. Revelle, V. P. A. Lonij, and A. D. Cronin, Phys. Rev. A **81**, 053607 (2010).

[22] M. D. Gregoire, I. Hromada, W. F. Holmgren, R. Trubko, and A. D. Cronin, Phys. Rev. A **92**, 052513 (2015).

[23] J. F. Clauser and S. Li, Phys. Rev. A **49**, R2213 (1994).

[24] B. Brezger, M. Arndt, and A. Zeilinger, J. Opt. B **5**, S82 (2003).

[25] B. Brezger, L. Hackermüller, S. Uttenthaler, J. Petschinka, M. Arndt, and A. Zeilinger, Phys. Rev. Lett. **88**, 100404 (2002).

[26] I. Compagnon, R. Antoine, M. Broyer, P. Dugourd, J. Lermé, and D. Rayane, Phys. Rev. A **64**, 025201 (2001).

[27] A. Ballard, K. Bonin, and J. Louderback, J. Chem. Phys. **113**, 5732 (2000).

[28] K. Bonin and V. Kresin, *Electric-Dipole Polarizabilities of Atoms, Molecules and Clusters* (World Scientific, Singapore, 1997).

[29] D. S. Sabirov, RSC Adv. **4**, 44996 (2014).

[30] S. Nimmrichter and K. Hornberger, Phys. Rev. A **78**, 023612 (2008).

[31] K. Hornberger, S. Gerlich, H. Ulbricht, L. Hackermüller, S. Nimmrichter, I. Goldt, O. Boltalina, and M. Arndt, New J. Phys. **11**, 043032 (2009).

[32] R. E. Grisenti, W. Schöllkopf, J. P. Toennies, G. C. Hegerfeldt, and T. Köhler, Phys. Rev. Lett. **83**, 1755 (1999).

[33] C. Brand *et al.*, Nat. Nanotechnol. **10**, 845 (2015).

[34] D. D. Koleske and S. J. Sibener, Rev. Sci. Instrum. **63**, 3852 (1992).

[35] D. Ding, J. Huang, R. N. Compton, C. E. Klots, and R. E. Haufler, Phys. Rev. Lett. **73**, 1084 (1994).

[36] O. Nairz, M. Arndt, and A. Zeilinger, J. Mod. Opt. **47**, 2811 (2000).

Quantum-Assisted Measurement of Atomic Diamagnetism

Yaakov Y. Fein, Armin Shayeghi, Lukas Mairhofer, Filip Kiałka, Philipp Rieser,
Philipp Geyer, Stefan Gerlich, and Markus Arndt[*]
Faculty of Physics, University of Vienna, Boltzmanngasse 5, A-1090 Vienna, Austria

We report the first measurement of ground-state diamagnetism of isolated neutral atoms in an atomic beam. We realize this measurement using magnetic deflection of fringes in a long-baseline matter-wave interferometer. The observed diamagnetic susceptibilities of $-5.8 \pm 0.2 \pm 0.4 \times 10^{-9}$ m^3/kg for barium and $-7.0 \pm 0.3 \pm 0.7 \times 10^{-9}$ m^3/kg for strontium are in good agreement with the theoretical values and correspond to a measured force on the order of 10^{-26} N. The high force sensitivity also allows us to observe the isotope dependence of the interference visibility due to the nuclear permanent magnetic moment, thereby demonstrating a new method for neutral isotope selection. The universality of the technique allows the magnetism of a wide range of atoms and molecules to be studied in the gas phase.

Subject Areas: Atomic and Molecular Physics,
Magnetism

I. INTRODUCTION

Diamagnetism is a fundamental effect in all atoms and molecules, but it is often dwarfed by larger paramagnetic contributions to the susceptibility [1]. In bulk materials, the net susceptibility of both paramagnetic and diamagnetic materials can be measured using a variety of established methods, such as the Gouy or Evans balance, NMR shifts, and SQUID-based measurements.

Paramagnetism has also been observed on the single-particle level, as has been exploited in the famous Stern-Gerlach experiment [2], the Rabi resonance method [3], and routinely in atom cooling and trapping experiments [4]. Modern beam deflection methods are also sensitive to the paramagnetism of small clusters and molecules [5–10].

Single-particle diamagnetism, however, is typically much harder to measure due to the smallness of the effect. For high-vapor-pressure materials such as the noble gases and a few simple hydrocarbons, the diamagnetic susceptibility has been measured using gas balance techniques [11–13]. Diamagnetic susceptibilities of highly excited Rydberg states have also been reported for a range of metal atoms including barium [14,15], which is possible due to the scaling of the effect with the electron orbit radius.

Measurements on isolated particles are important because bulk magnetic properties can differ significantly

from those of the constituent atoms or molecules. For example, the closed-shell alkaline-earth elements barium and strontium are paramagnetic in bulk due to Pauli paramagnetism but are predicted to be diamagnetic when isolated. While the bulk paramagnetic susceptibilities have been measured [16], the ground-state atomic susceptibilities of barium and strontium have not been experimentally accessible until now. The measurement of neutral strontium may be of particular interest to the atomic-clock community, which typically relies on a calculated diamagnetic correction to the nuclear g-factor [17].

Here, we report on a new technique to measure single-particle magnetic susceptibilities via fringe deflection in a matter-wave interferometer [18]. We use the Long-baseline Universal Matter-wave Interferometer (LUMI) [19], a three-grating near-field interferometer that can accept a wide range of atoms and molecules.

Various realizations of matter-wave interferometers have been employed with a range of atomic and molecular species in tests of fundamental physics and precision sensing [20]. Interferometers have also been used to measure electronic and optical properties of atoms and molecules [21–25], and here we extend this concept to atomic diamagnetism. The magnetic susceptibility manifests as a shift of the interference fringes due to the repulsive force on a small magnetic moment induced in a tailored magnetic field. The fringes can be monitored with nanometer resolution, which is what lends the technique its high sensitivity.

A permanent paramagnetic moment, on the other hand, is deflected in different directions, dependent on the projection of the magnetic moment onto the magnetic field axis. Averaging over an ensemble of atoms thus reduces the

---

[*]markus.arndt@univie.ac.at

interference visibility. We show the sensitivity of the experiment to a nonzero nuclear spin by comparing the interference visibilities of different isotopes.

Alkaline-earth and alkaline-earth-like elements have attracted significant interest in recent years for their potential use in precision measurements. Several strontium interferometers have been demonstrated [26–29], along with a range of other elements [30–33], with envisioned applications including gravimetry, gravitational wave sensing, and equivalence principle tests. The insensitivity to magnetic fields is one of the key benefits of working with such atoms. In the gravity gradiometer demonstrated in Ref. [29], the extremely low sensitivity of strontium to magnetic field gradients was demonstrated, although the sensitivity of this particular experiment was about 3 times too low to observe the diamagnetic contribution. In the current work, we measure this small diamagnetic term for strontium as well as for barium, which shares many of the appealing aspects for precision measurements.

II. EXPERIMENTAL SETUP

We demonstrate the technique with barium and strontium since they both form thermal atomic beams, have vanishing electron magnetic moments, and have several stable isotopes. A thermal atomic beam is formed in a ceramic oven held at 1000–1300 K. The atoms then traverse the three-grating interferometer (see Fig. 1) and a specially designed deflection magnet that can be moved in and out of the atomic beam with a vertical translation stage.

The LUMI deflectometry experiments rely on the Talbot-Lau effect in the scheme illustrated in Fig. 1. The Talbot-Lau effect [34,35] is a near-field self-imaging phenomenon first demonstrated with atoms [36] and later
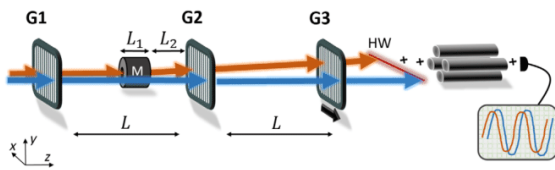

FIG. 1. The experimental setup showing the two modes of operation in our experiment. Blue arrows indicate the reference measurements, where atoms traverse the interferometer with the deflection magnet withdrawn from the beam; red arrows show the deflected paths of the atoms when the experiment is repeated with the beam passing through the magnet. The thermal barium beam enters from the left, passes the three gratings (*G*1, *G*2, *G*3) and the cylindrical deflection magnet (*M*), and is ionized by the hot rhenium wire (HW). The sinusoidal interference patterns are sampled by scanning *G*3 transversely. Here, *L* is the inter-grating separation (0.98 m), L_1 the length of the magnet (0.04 m), and L_2 the distance of the magnet edge from *G*2 (0.12 m).

with increasingly massive molecules [19,37]. The first grating *G*1 creates transverse coherence such that the second grating *G*2 is coherently self-imaged. This process produces a density pattern in the beam behind *G*2, which we sample by scanning a third grating *G*3 across the beam. We use the symmetric configuration in which each grating period is equal and the gratings are separated equidistantly. The modulation then has the grating period *d* and is strongest when the intergrating spacing *L* is approximately an integer multiple of the Talbot length, $L_T = d^2/\lambda_{\mathrm{dB}}$, with λ_{dB} the de Broglie wavelength. Typical values of L_T in the experiments presented here are of order one centimeter; hence, *L* is close to $100L_T$. The low collimation requirements of such a scheme permit higher throughput than a far-field interferometer with a similar baseline.

We use nanomechanical gratings with a period of 266 nm, which are compatible with the high beam velocities and relatively small polarizabilities of barium and strontium [38], where particle-grating interactions are weak. For slower and highly polarizable particles such as large molecules, *G*2 can be exchanged for an optical phase grating in the same experiment [19].

After traversing the interferometer, the atoms are ionized (see the Appendix for details), mass-selected by a quadrupole mass spectrometer (QMS), and counted with an electron multiplier.

III. DIAMAGNETIC DEFLECTION

For magnetic deflection experiments, we employ a retractable permanent deflection magnet positioned before the second grating. The magnet is a modified Halbach cylinder arrangement of 24 neodymium-iron-boron segments, each with a typical remanent magnetization of 1.29 T. It was designed to have a uniform $(\mathbf{B} \cdot \nabla)B_x$ field in a region near the cylinder axis [18]. Rectangular apertures at the entrance and exit of the magnet ensure that the atoms fly through a $2.00 \times 0.75 \ \mathrm{mm}^2$ region of the magnet chosen to be large enough to permit significant flux while still sampling a force field sufficiently homogeneous to avoid strong dephasing. The magnet was characterized with a Hall probe, showing a peak $(\mathbf{B} \cdot \nabla)B_x$ field of $59 \pm 5 \ \mathrm{T}^2/\mathrm{m}$, falling off near the magnet edges, as shown in Fig. 2. The force within the magnetic cylinder over the selected region is constant to 9%.

The magnetic field induces a dipole moment $\boldsymbol{\mu} = (\chi_m m)\mathbf{B}/\mu_0$, with χ_m the mass magnetic susceptibility and *m* the particle mass, which leads to a force

$$F_x = (\boldsymbol{\mu} \cdot \nabla)B_x = \frac{m(\mathbf{B} \cdot \nabla)B_x}{\mu_0}\chi_m. \qquad (1)$$

This force causes a transverse position and velocity shift of the atoms after traversing the magnet,
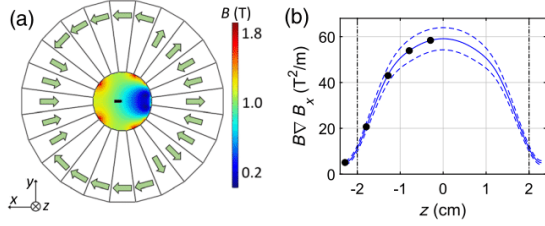
FIG. 2. (a) Pole arrangement of the 24 permanent magnet segments and simulated magnetic flux density map inside the hollow cylinder (16 mm inner diameter). The small black rectangle indicates the region traversed by the atoms. (b) The $(\mathbf{B} \cdot \nabla)B_x$ field over the traversed region as a function of longitudinal position as determined from Hall-probe measurements (black dots). The vertical black dashed lines indicate the extent of the magnet cylinder. The mirror symmetry of the magnet with respect to the $z = 0$ plane has been used to extrapolate the fields for the spline fit shown in blue, where the blue dashed lines correspond to 1 standard deviation of the measured values, indicating the uniformity of the force field.

$$\Delta x_{\mathrm{mag}} = \int_0^{L_1} \int_0^{z'} \frac{F_x(z')}{m v_z^2} \, dz' dz, \qquad \Delta v_x = \int_0^{L_1} \frac{F_x(z)}{m v_z} \, dz. \tag{2}$$

The integrals of $F_x(z)$ are obtained numerically using the z dependence shown in Fig. 2. In the reference frame of the atoms, the second and third gratings are shifted by $\Delta x_2 = -\Delta x_{\mathrm{mag}} - \Delta v_x L_2 / v_z$ and $\Delta x_3 = -\Delta x_2 - \Delta v_x L / v_z$, respectively. The phase shift of the interference pattern is then obtained by the formula [20,39] $\Delta \phi = k[\Delta x_1 - 2\Delta x_2 + \Delta x_3]$, where $\Delta x_1 = 0$ and $k = 2\pi/d$.

To account for the finite spread of velocities in the beam, one must average the interference pattern over the velocity distribution $\rho(v_z)$. The observed pattern $\overline{A} \cos(kx + \overline{\Delta\phi})$ is an incoherent sum of the contributions of different velocity classes,

$$\overline{A} \cos(kx + \overline{\Delta\phi}) = \int_0^\infty dv \rho A \cos(kx + \Delta\phi), \tag{3}$$

where A is the velocity-dependent fringe visibility. The velocity dependence of the amplitudes A is determined following the treatment in Ref. [40] for a retarded C4 potential. Its effect on the mean deflection is less than 5% for our parameters.

The velocity of the atomic beam was measured via cross-correlation with a pseudorandom chopper sequence and fitted to a skew normal distribution. Care was taken to account for the residence time of the atoms on the rhenium surface of the Langmuir-Taylor detector, as described in the Appendix, along with further details of the measured distributions.

Interference measurements were made with and without the $(\mathbf{B} \cdot \nabla)B_x$ field to determine the relative phase shift induced by the deflection magnet. This process was done by mechanically moving the magnet in and out of the atomic beam with a vertical translation stage. The experiment was repeated several times to ensure that the observed phase shift was reproducible, as shown in Fig. 3. For barium, three consecutive interference scans were recorded with and then without the magnet; this sequence was repeated 4 times, for a total of 24 measurements. For strontium, six consecutive measurements were taken with and then without the magnet, for a total of 12 measurements.

The barium deflection data were taken with the QMS in a low-resolution mode to maximize the count rate, in which the various barium isotopes were not distinguished. For strontium, the high-resolution mode was used throughout, and for these deflection measurements, we selected the most abundant isotope, ^{88}Sr. The mean observed visibility of the barium (strontium) interference fringes without the magnet was 11.6% (13.8%), slightly below the expected visibility after taking into account Casimir-Polder dephasing at the second grating [40]. The barium (strontium) visibility was reduced to 7.2% (8.5%) upon insertion of the magnet.

The mean deflection of the barium fringes in Fig. 3 is 20.9 ± 0.7 nm. Solving Eq. (3) for this deflection and
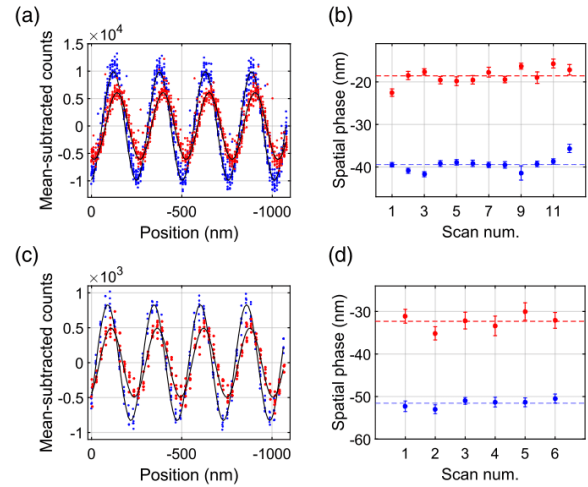
FIG. 3. (a) Barium interference patterns with (red) and without (blue) the deflection magnet, where solid curves are sine fits. Mean counts are subtracted to adjust for a small drop of the count rate during the measurement, and several outliers due to signal instabilities lie beyond the plotting region. A phase shift and contrast loss due to the magnet are both clearly visible. (b) The phase of each measurement, with dashed lines showing the mean values (red with magnet, blue without). Error bars are 1-σ confidence intervals of the phase. (c) Same as in panel (a), but for strontium. (d) Same as in panel (b), but for strontium.

finding the best-fit susceptibility yields $\chi_m(\text{Ba}) = -5.8 \pm 0.2 \pm 0.4 \times 10^{-9}$ m^3/kg. Since the induced magnetic moment $\boldsymbol{\mu} = (\chi_m m)\mathbf{H}$, the susceptibility per atom, $\chi_m m$, is $-1.33 \pm 0.05 \pm 0.09 \times 10^{-33}$ m^3. The first error is the statistical error due to the standard error of the observed deflection, while the second error is systematic and is dominated by the uncertainty in the velocity distribution and $(\mathbf{B} \cdot \nabla)B_x$ field.

In a similar manner, the observed strontium deflection of 19.3 ± 0.7 nm yields a diamagnetic susceptibility $\chi_m(\text{Sr}) = -7.0 \pm 0.3 \pm 0.7 \times 10^{-9}$ m^3/kg. The susceptibility per strontium atom is $-1.02 \pm 0.04 \pm 0.10 \times 10^{-33}$ m^3. To put this into context, the magnitude of the induced magnetic moment of a strontium atom in a 1-Tesla field is 4 orders of magnitude smaller than a single Bohr magneton.

We can compare the measured susceptibilities with values calculated using density functional theory with magnetic-field-dependent gauge-independent atomic orbitals (GIAOs) [41], as implemented in Gaussian16 [42]. We used the PBE0 exchange-correlation functional [43] and the def2-QZVPP basis set [44]. The method was benchmarked with xenon, which reproduced the measured value [13] to 2%. The isotropic susceptibilities were calculated as -6.17×10^{-9} m^3/kg for barium and -7.34×10^{-9} m^3/kg for strontium, in good agreement with the measured values. The ratio of the theoretical values, $\chi_m(\text{Sr})/\chi_m(\text{Ba}) = 1.19$, is in excellent agreement with the measured ratio of 1.19 ± 0.06, in which most of the systematic error cancels.

The experimental values are both 6% smaller than the theoretical values, suggestive of a small systematic error.

IV. ISOTOPE-SELECTIVE INTERFERENCE

Operating the QMS in a high-resolution mode allows us to perform interference measurements on each of the three most abundant isotopes of barium and strontium, with and without the deflection magnet. Figure 4 shows the complete loss of interference visibility for the odd-numbered isotopes in the presence of the $(\mathbf{B} \cdot \nabla)B_x$ field. Without the magnet, full interference visibility is recovered for each of the isotopes.

Unlike the even-numbered isotopes, ^{137}Ba and ^{87}Sr carry a permanent magnetic moment due to an unpaired nuclear spin, with $I = 3/2$ for ^{137}Ba and $I = 9/2$ for ^{87}Sr. The permanent magnetic moment of ground-state ^{137}Ba is given by $\mu_z = g\mu_N m_I/\hbar = 0.94\mu_N$ for the $m_I = 1/2$ component [45], with four possible spin projections. The effect of a ∇B_x field on ^{137}Ba is, in general, a reduction of the interference visibility. Assuming a transversely constant ∇B_x (peak value of 77 T/m) and treating the four Stern-Gerlach branches as a classical mixture of trajectories (since the different spin states cannot interfere), the reduced barium fringe amplitude is

$$\overline{A} = \frac{1}{2}\left| \int_0^\infty dv_z \rho A[\cos(\Delta\phi_p) + \cos(3\Delta\phi_p)]e^{i\Delta\phi} \right|. \quad (4)$$
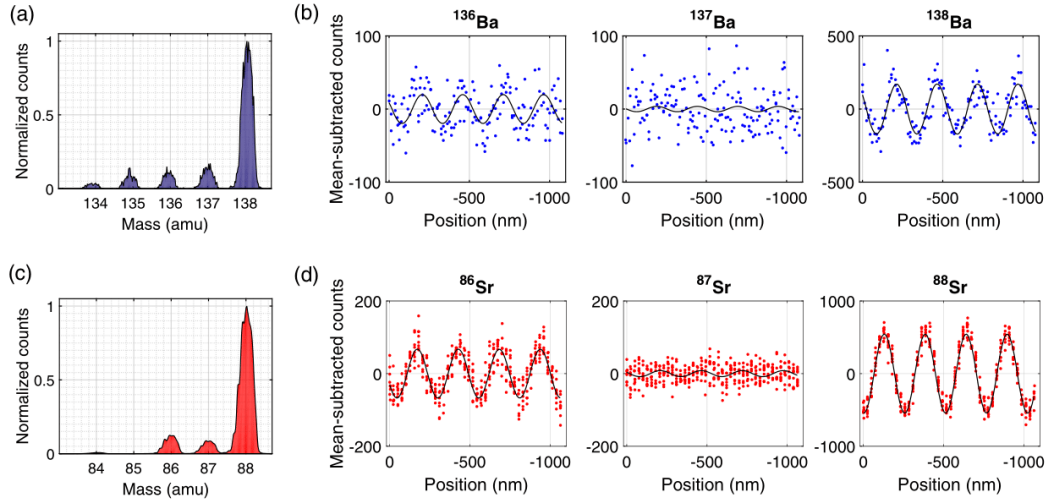
FIG. 4. (a) Measured isotope distribution of barium. Interference scans were performed with the QMS tuned to a particular isotope peak. (b) Interference of ^{136}Ba, ^{137}Ba, and ^{138}Ba, with the deflection magnet inserted. Solid curves indicate sine fits. Here, ^{137}Ba, with its unpaired nuclear spin, exhibits no contrast, while the even isotopes retain full contrast. (c) Measured isotope distribution of strontium. (d) Interference of ^{86}Sr, ^{87}Sr, and ^{88}Sr, with the deflection magnet inserted, showing even more clearly the loss of visibility for the odd-numbered isotope.

Here, $\Delta\phi_p$ is the paramagnetic shift of the $m_I = 1/2$ level, as obtained from Eq. (2) and the first part of Eq. (1) for a permanent magnetic moment $\boldsymbol{\mu}$. For generality, the diamagnetic shift $\Delta\phi$ has been included as well.

Equation (4) predicts a visibility loss greater than 85% for ^{137}Ba. This loss is a conservative estimate since in our magnet $(\mathbf{B} \cdot \nabla)\mathrm{B}_x$ is nearly constant and ∇B_x is not, resulting in additional spatial averaging. The observed loss of interference visibility is thus consistent with the presence of a permanent nuclear magnetic moment. Such an experiment can be operated without a QMS as a technique for neutral isotope selection, with the level of selectivity determined by the interference contrast.

V. CONCLUSION

The diamagnetic susceptibility of isolated barium and strontium atoms was measured via the shift of interference fringes in a long-baseline matter-wave interferometer. By mass-selecting the various isotopes, the presence of nuclear spin was observed through a loss of interference visibility for the odd-numbered isotopes with unpaired nuclear spins.

The universal nature of LUMI allows us to show interference with molecules as well as atoms. The addition of a constant gradient magnetic field in the setup will allow further studies of permanent magnetic moments, photo-isomerization effects, and triplet-state lifetimes in complex molecules. The technique can also be used to purify nuclear isotopes for applications in spectroscopy.

APPENDIX: EXPERIMENTAL DETAILS

Langmuir-Taylor surface ionization from a heated rhenium wire was used to ionize the atoms after the interferometer. Alkaline-earth elements such as barium and strontium can exhibit residence times up to several seconds before desorption from a hot metal surface. To prevent a systematic error in time-of-flight measurements and a corresponding error in susceptibilities, we collected the spectra at a wire current of 5.8 A for barium and 6.0 A for strontium, corresponding to wire temperatures of 2550 K and 2590 K, respectively [46]. At these temperatures, the residence times for barium and strontium are estimated as 120 μs and 2 μs, respectively [47,48], short enough to have a minimal impact on velocity measurements, as confirmed
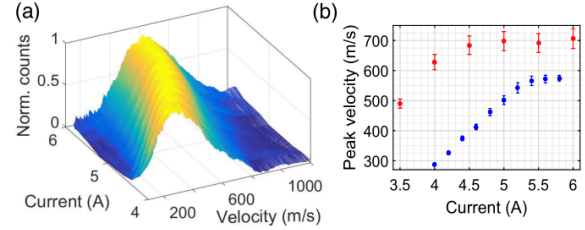

FIG. 5. (a) Velocity spectra as a function of hot-wire current for barium. (b) The convergence of the velocity spectra at high wire temperatures, seen by plotting the peak velocities of skew normal fits to the velocity data against the wire current. The blue marks show barium data; red marks are for strontium. Error bars are from 1-σ confidence intervals of the velocity calibration.

by the convergence shown in Fig. 5. A small correction for barium was applied by deconvoluting the velocity spectrum with an exponential delay corresponding to the 120 μs residence time.

Skew normal distributions were used for fitting the velocity distributions, defined according to the probability density function [49],

$$\frac{1}{\pi\sigma}\exp\left[\frac{(1-\xi)^2}{2\sigma^2}\right]\int_{-\infty}^{\alpha(x-\xi)/\sigma} dt \exp\left(\frac{-t^2}{2}\right), \quad (A1)$$

with ξ the location parameter, σ the scale parameter, and α the shape parameter that determines the skewness. For barium (strontium), fitting yields distributions with a location parameter of 444 m/s (473 m/s), a scale parameter of 284 m/s (372 m/s), and a shape parameter of 2.0 (2.7).

During interference measurements, a lower wire current of 3.5–3.6 A was used to mitigate signal instabilities that appeared at higher temperatures. We also maximized the atomic flux by working with a large velocity spread, thus avoiding the use of narrow velocity-selecting delimiters. The combination of a moderate wire temperature and high flux allowed us to achieve the most stable interference patterns.

[1] J. H. V. Vleck, *The Theory of Electric and Magnetic Susceptibilities* (Oxford University Press, London, 1965).

[2] W. Gerlach and O. Stern, *Der Experimentelle Nachweis des Magnetischen Moments des Silberatoms*, Z. Phys. **8,** 110 (1922).

[3] I. I. Rabi, S. Millman, P. Kusch, and J. R. Zacharias, *The Molecular Beam Resonance Method for Measuring Nuclear Magnetic Moments. The Magnetic Moments of $_3$Li^6, $_3$Li^7 and $_9$F^{19}*, Phys. Rev. **55,** 526 (1939).

[4] H. Metcalf and P. v. d. Straten, *Laser Cooling and Trapping* (Springer, New York, 1999).

[5] D. Cox, D. Trevor, R. Whetten, E. Rohlfing, and A. Kaldor, *Aluminum Clusters: Magnetic Properties,* J. Chem. Phys. **84**, 4651 (1986).

[6] U. Rohrmann and R. Schafer, *Stern-Gerlach Experiments on* $Mn@Sn_{12}$*: Identification of a Paramagnetic Superatom and Vibrationally Induced Spin Orientation,* Phys. Rev. Lett. **111**, 133401 (2013).

[7] U. Rohrmann, P. Schwerdtfeger, and R. Schafer, *Atomic Domain Magnetic Nanoalloys: Interplay between Molecular Structure and Temperature Dependent Magnetic and Dielectric Properties in Manganese Doped Tin Clusters,* Phys. Chem. Chem. Phys. **16**, 23952 (2014).

[8] M. B. Knickelbein, *Magnetic Moments of Small Bimetallic Clusters:* $Co_n Mn_m$, Phys. Rev. B **75**, 014401 (2007).

[9] M. B. Knickelbein, *Magnetic Ordering in Manganese Clusters,* Phys. Rev. B **70**, 014424 (2004).

[10] K. Miyajima, M. B. Knickelbein, and A. Nakajima, *Stern-Gerlach Study of Multidecker Lanthanide-Cyclooctatetraene Sandwich Clusters,* J. Phys. Chem. A **112**, 366 (2008).

[11] A. P. Wills and L. G. Hector, *The Magnetic Susceptibility of Oxygen, Hydrogen and Helium,* Phys. Rev. **23**, 209 (1924).

[12] G. G. Havens, *The Magnetic Susceptibilities of Some Common Gases,* Phys. Rev. **43**, 992 (1933).

[13] C. Barter, R. G. Meisenheimer, and D. P. Stevenson, *Diamagnetic Susceptibilities of Simple Hydrocarbons and Volatile Hydrides,* J. Phys. Chem. **64**, 1312 (1960).

[14] F. A. Jenkins and E. Segrè, *The Quadratic Zeeman Effect,* Phys. Rev. **55**, 52 (1939).

[15] R. J. Fonck, F. L. Roesler, D. H. Tracy, K. T. Lu, F. S. Tomkins, and W. R. S. Garton, *Atomic Diamagnetism and Diamagnetically Induced Configuration Mixing in Laser-Excited Barium,* Phys. Rev. Lett. **39**, 1513 (1977).

[16] D. R. Lide, *CRC Handbook of Chemistry and Physics,* 84th ed. (CRC Press, New York, 2004), pp. 4–130.

[17] M. M. Boyd, T. Zelevinsky, A. D. Ludlow, S. Blatt, T. Zanon-Willette, S. M. Foreman, and J. Ye, *Nuclear Spin Effects in Optical Lattice Clocks,* Phys. Rev. A **76**, 022510 (2007).

[18] L. Mairhofer, S. Eibenberger, A. Shayeghi, and M. Arndt, *A Quantum Ruler for Magnetic Deflectometry,* Entropy **20**, 516 (2018).

[19] Y. Y. Fein, P. Geyer, P. Zwick, F. Kiałka, S. Pedalino, M. Mayor, S. Gerlich, and M. Arndt, *Quantum Superposition of Molecules Beyond 25 kDa,* Nat. Phys. **15**, 1242 (2019).

[20] A. D. Cronin, J. Schmiedmayer, and D. E. Pritchard, *Optics and Interferometry with Atoms and Molecules,* Rev. Mod. Phys. **81**, 1051 (2009).

[21] W. Holmgren, M. Revelle, V. Lonij, and A. Cronin, *Absolute and Ratio Measurements of the Polarizability of Na, K, and Rb with an Atom Interferometer,* Phys. Rev. A **81**, 053607 (2010).

[22] L. Hackermüller, K. Hornberger, S. Gerlich, M. Gring, H. Ulbricht, and M. Arndt, *Optical Polarizabilities of Large Molecules Measured in Near-Field Interferometry,* Appl. Phys. B **89**, 469 (2007).

[23] S. Eibenberger, S. Gerlich, M. Arndt, J. Tüxen, and M. Mayor, *Electric Moments in Molecule Interferometry,* New J. Phys. **13**, 043033 (2011).

[24] S. Eibenberger, X. Cheng, J. P. Cotter, and M. Arndt, *Absolute Absorption Cross Sections from Photon Recoil in a Matter-Wave Interferometer,* Phys. Rev. Lett. **112**, 250402 (2014).

[25] L. Mairhofer, S. Eibenberger, J. P. Cotter, M. Romirer, A. Shayeghi, and M. Arndt, *Quantum-Assisted Metrology of Neutral Vitamins in the Gas Phase,* Angew. Chem. Int. Ed. **56**, 10947 (2017).

[26] T. Mazzoni, X. Zhang, R. Del Aguila, L. Salvi, N. Poli, and G. M. Tino, *Large-Momentum-Transfer Bragg Interferometer with Strontium Atoms,* Phys. Rev. A **92** (2015).

[27] L. Hu, N. Poli, L. Salvi, and G. M. Tino, *Atom Interferometry with the Sr Optical Clock Transition,* Phys. Rev. Lett. **119**, 263601 (2017).

[28] X. Zhang, R. P. del Aguila, T. Mazzoni, N. Poli, and G. M. Tino, *Trapped-Atom Interferometer with Ultracold Sr Atoms,* Phys. Rev. A **94**, 043608 (2016).

[29] R. P. del Aguila, T. Mazzoni, L. Hu, L. Salvi, G. M. Tino, and N. Poli, *Bragg Gravity-Gradiometer Using the* $^1S_0$–$^3P_1$ *Intercombination Transition of* ^{88}Sr, New J. Phys. **20**, 043002 (2018).

[30] J. Hartwig, S. Abend, C. Schubert, D. Schlippert, H. Ahlers, K. Posso-Trujillo, N. Gaaloul, W. Ertmer, and E. M. Rasel, *Testing the Universality of Free Fall with Rubidium and Ytterbium in a Very Large Baseline Atom Interferometer,* New J. Phys. **17**, 035011 (2015).

[31] M. G. Tarallo, T. Mazzoni, N. Poli, D. V. Sutyrin, X. Zhang, and G. M. Tino, *Test of Einstein Equivalence Principle for 0-Spin and Half-Integer-Spin Atoms: Search for Spin-Gravity Coupling Effects,* Phys. Rev. Lett. **113**, 023005 (2014).

[32] P. W. Graham, J. M. Hogan, M. A. Kasevich, and S. Rajendran, *New Method for Gravitational Wave Detection with Atomic Sensors,* Phys. Rev. Lett. **110**, 171102 (2013).

[33] A. O. Jamison, B. Plotkin-Swing, and S. Gupta, *Advances in Precision Contrast Interferometry with Yb Bose-Einstein Condensates,* Phys. Rev. A **90**, 063606 (2014).

[34] K. Patorski, in *Progress in Optics XXVII*, edited by E. Wolf (Elsevier Science Amsterdam, 1989), p. 1.

[35] K. Hornberger, S. Gerlich, P. Haslinger, S. Nimmrichter, and M. Arndt, *Colloquium: Quantum Interference of Clusters and Molecules,* Rev. Mod. Phys. **84**, 157 (2012).

[36] J. F. Clauser and S. Li, *Talbot-von Lau Atom Interferometry with Cold Slow Potassium,* Phys. Rev. A **49**, R2213 (1994).

[37] S. Eibenberger, S. Gerlich, M. Arndt, M. Mayor, and J. Tüxen, *Matter-Wave Interference of Particles Selected from a Molecular Library with Masses Exceeding 10 000 amu,* Phys. Chem. Chem. Phys. **15**, 14696 (2013).

[38] H. L. Schwartz, T. M. Miller, and B. Bederson, *Measurement of the Static Electric Dipole Polarizabilities of Barium and Strontium,* Phys. Rev. A **10**, 1924 (1974).

[39] M. K. Oberthaler, S. Bernet, E. M. Rasel, J. Schmiedmayer, and A. Zeilinger, *Inertial Sensing with Classical Atomic Beams,* Phys. Rev. A **54**, 3165 (1996).

[40] S. Nimmrichter and K. Hornberger, *Theory of Near-Field Interference Beyond the Eikonal Approximation,* Phys. Rev. A **78**, 023612 (2008).

[41] J. R. Cheeseman, G. W. Trucks, T. A. Keith, and M. J. Frisch, *A Comparison of Models for Calculating Nuclear*

Magnetic Resonance Shielding Tensors, J. Chem. Phys. **104**, 5497 (1996).

[42] M. J. Frisch *et al.*, Gaussian 16 Rev. C.01, 2016.

[43] C. Adamo and V. Barone, *Toward Reliable Density Functional Methods without Adjustable Parameters: The PBE0 Model*, J. Chem. Phys. **110**, 6158 (1999).

[44] F. Weigend and R. Ahlrichs, *Balanced Basis Sets of Split Valence, Triple Zeta Valence and Quadruple Zeta Valence Quality for H to Rn: Design and Assessment of Accuracy*, Phys. Chem. Chem. Phys. **7**, 3297 (2005).

[45] N. J. Stone, *Table of Nuclear Magnetic Dipole and Electric Quadrupole Moments*, At. Data Nucl. Data Tables **90**, 75 (2005).

[46] C. T. Sims, C. M. Craighead, R. I. Jaffe, D. N. Gideon, E. N. Wyler, F. C. Todd, D. M. Rosenbaum, E. M. Sherwood, and I. E. Campbell, *Investigations of Rhenium*, Report No. 54-371, 1954.

[47] M. D. Scheer and J. Fine, *Kinetics of Desorption. II. Cs^+ and Ba^+ from Rhenium*, J. Chem. Phys. **38**, 307 (1963).

[48] F. Stienkemeier, M. Wewer, F. Meier, and H. O. Lutz, *Langmuir–Taylor Surface Ionization of Alkali (Li, Na, K) and Alkaline Earth (Ca, Sr, Ba) Atoms Attached to Helium Droplets*, Rev. Sci. Instrum. **71**, 3480 (2000).

[49] A. Azzalini, *A Class of Distributions Which Includes the Normal Ones*, Scand. J. Stat. Theory Appl. **12**, 171 (1985).

137

New Journal of Physics

The open access journal at the forefront of physics

PAPER

CrossMark

Coriolis compensation via gravity in a matter-wave interferometer

Yaakov Y Fein [ID] , Filip Kiałka, Philipp Geyer, Stefan Gerlich and Markus Arndt [ID]

Faculty of Physics, University of Vienna, Vienna, Austria

E-mail: Markus.Arndt@univie.ac.at

Abstract

Matter-wave interferometry offers insights into fundamental physics and provides a precise tool for sensing. Improving the sensitivity of such experiments requires increasing the time particles spend in the interferometer, which can lead to dephasing in the presence of velocity-dependent phase shifts such as those produced by the Earth's rotation. Here we present a technique to passively compensate for the Coriolis effect using gravity, without the need for any moving components. We demonstrate the technique with fullerenes in a long-baseline molecule interferometer by measuring the gravitational and Coriolis phase shifts and obtaining the maximum visibility one would expect in the absence of the Coriolis effect.
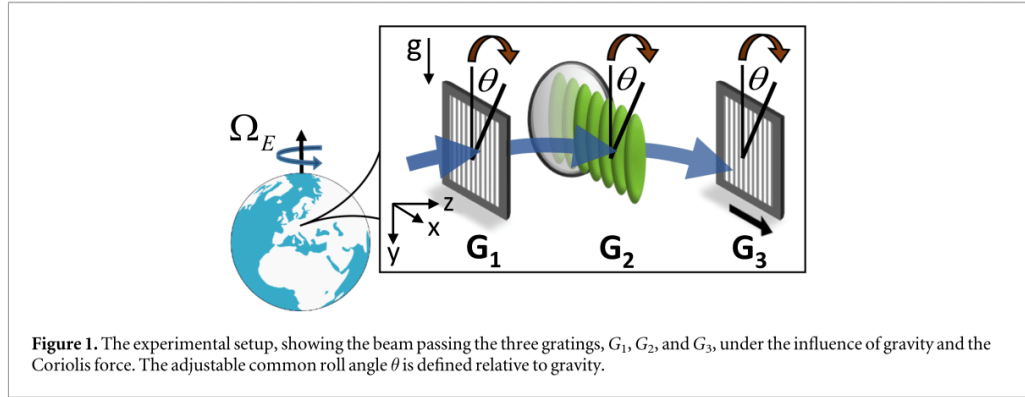
1. Introduction

Increasing the interrogation time in matter-wave interferometers is desirable for a range of applications, including the demonstration of macroscopic superpositions [1–3], inertial sensing [4–7], weak equivalence principle tests [8], and precision measurements of the fine-structure constant [9] and the gravitational constant [10]. Long interaction times can be achieved via particle slowing or trapping [11], moving to a free-fall environment [12–14], or increasing the interferometer baseline [3].

A major challenge facing ground-based interferometers is the Coriolis effect, which reduces the interference fringe visibility for slow non-monochromatic beams. Various approaches for compensating the Coriolis force or employing a Sagnac phase as compensation for another dispersive force have been proposed [15, 16] and employed [17–19], for example via mechanical actuation of the gratings. The Coriolis compensation scheme presented here requires no moving components which may induce vibrations nor velocity-resolved measurements which require increased integration times, making it particularly well-suited for long-baseline molecule interferometry.

Gravitational and Sagnac phases were first observed in a series of neutron interferometry experiments [20–22] and later in atom and electron interferometers [23, 24]. Here we use the gravitational phase induced by a tilt of our interferometer to compensate the phase due to the Earth's rotation. We demonstrate this compensation technique with the long-baseline universal matter-wave interferometer (LUMI), a two-meter long Talbot–Lau interferometer which is compatible with both supersonic atomic beams and slow molecular beams. Coriolis compensation is critical for reaching high interference visibilities in the LUMI experiment [3].

1.1. Theory

Talbot–Lau interferometers [3, 25–31] require at least two gratings. The first grating, G_1, prepares transverse coherence in the beam, while G_2 acts as the diffraction element. The grating structure of G_2 is imprinted into the density of the molecular beam in the near field behind the second grating. It is common to employ a third grating, G_3, as a transmission mask which is moved transversely to detect these fringes as a sinusoidal variation of the transmitted flux. We use a symmetric scheme, in which the gratings are spaced equidistantly by L and have equal periods d.

Figure 1. The experimental setup, showing the beam passing the three gratings, G_1, G_2, and G_3, under the influence of gravity and the Coriolis force. The adjustable common roll angle θ is defined relative to gravity.

The phase of the interference fringes after traversing such an interferometer subject to a constant transverse acceleration a is [32, 33]

$$\phi = \frac{2\pi}{d} a \frac{L^2}{v^2},$$ (1)

where v is the longitudinal beam velocity.

We define θ as the roll angle of the three gratings around the molecular axis, measured with respect to gravity (see figure 1). We consider $\theta \ll 1$, giving a transverse acceleration $a \approx 2\Omega v + g\theta$, where the first term is due to the Coriolis effect and the second due to gravity. We can therefore express the total phase as

$$\phi = \frac{2\pi}{d} \left[\frac{2\Omega L^2}{v} + \frac{g\theta L^2}{v^2} \right].$$ (2)

Here, $\Omega = \Omega_E \sin 48°$, where $\Omega_E > 0$ is the rotational frequency of Earth and $48°$ is the geographical latitude of our experiment. We neglect higher order effects such as the contribution of the centrifugal force or the vertical Coriolis shift due to the East–West velocity component.

Velocity-dependent phase shifts reduce the visibility of the interference pattern when averaged over the velocity distribution of the beam, which is typically broad in molecule interferometry. For a Gaussian velocity distribution $\rho(v)$ with center velocity v_0 and spread σ, the velocity-averaged fringe visibility A' becomes

$$A' = \left| \int_0^\infty \rho(v) A(v) e^{i\phi(v)} dv \right|.$$ (3)

We neglect the negative tail of the Gaussian distribution in the normalization, which is a good approximation for the velocities and spreads we consider. The velocity dependence of the visibility amplitudes A, assuming fixed grating open fractions, is given in [34].

We define the reduced visibility

$$R = \frac{A'}{\left| \int_0^\infty \rho(v) A(v) dv \right|}$$ (4)

as the ratio of the visibility in the presence of gravity and rotation to the visibility without any velocity-dependent phase shifts.

If we set $\theta = 0$ by aligning the gratings to gravity, only the Coriolis shift contributes in equation (2). In figure 2 the numerically integrated R demonstrates the strong visibility reduction caused by the Coriolis effect alone.

This can be compensated by choosing a grating roll θ such that the gravitational phase term makes ϕ nearly constant over the velocity range of interest. The roll angle which optimizes R is numerically determined for each velocity, with the improved visibility shown in figure 2.

Several approximations can be made to obtain analytic forms of the reduced visibility R and the optimal roll angle. First, we assume A to be constant over the velocity range of interest, such that $R = A'/A$.

For the $\theta = 0$ case we expand ϕ to first order around v_0, giving

$$R_{\mathrm{uncomp}} \approx \exp\left[-8\left(\frac{\pi}{d} \frac{\Omega \sigma L^2}{v_0{}^2} \right)^2 \right].$$ (5)

Figure 2. The reduced visibility R in LUMI for uncompensated (blue, lower curves) and compensated (red, upper curves) schemes. Solid lines are calculated numerically for a beam of C_{60} using equations (3) and (4), where R is maximized over θ at each velocity for the compensated case. Dashed lines are the approximate analytic expressions (5) and (7). The two pairs of lines for each scheme correspond to $\sigma/v = 0.1$ and 0.2, with the latter corresponding to the lower R values in each case.

For the compensated case we choose a roll angle θ_0 such that ϕ is constant to first order for $v = v_p$, giving

$$\theta_0 = -\frac{\Omega \ v_p}{g}. \tag{6}$$

Expanding ϕ to second order around v_0 and setting $v_0 = v_p$ to achieve maximal compensation at each velocity gives

$$R_{comp} \approx \left[1 + \left(\frac{4\pi\sigma^2\Omega L^2}{dv_0^3} \right)^2 \right]^{-\frac{1}{4}}. \tag{7}$$

Equations (5) and (7) are plotted as the dashed lines in figure 2 together with the numerically integrated values, showing reasonable agreement especially for small velocity spreads.
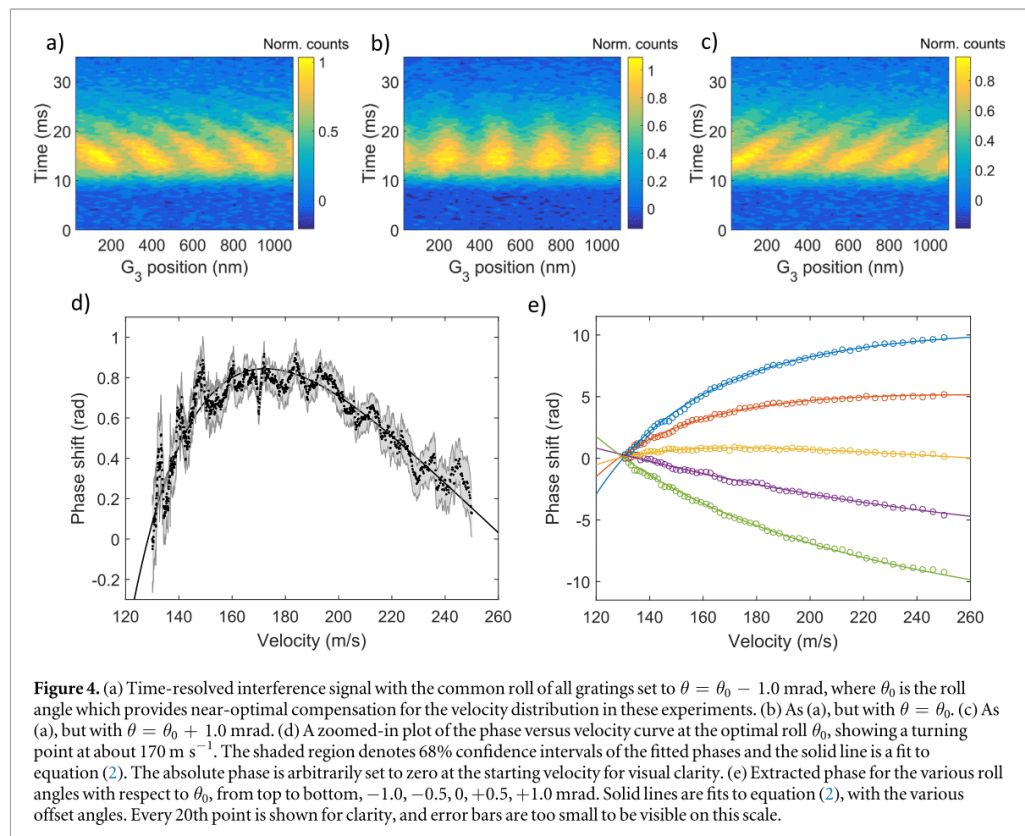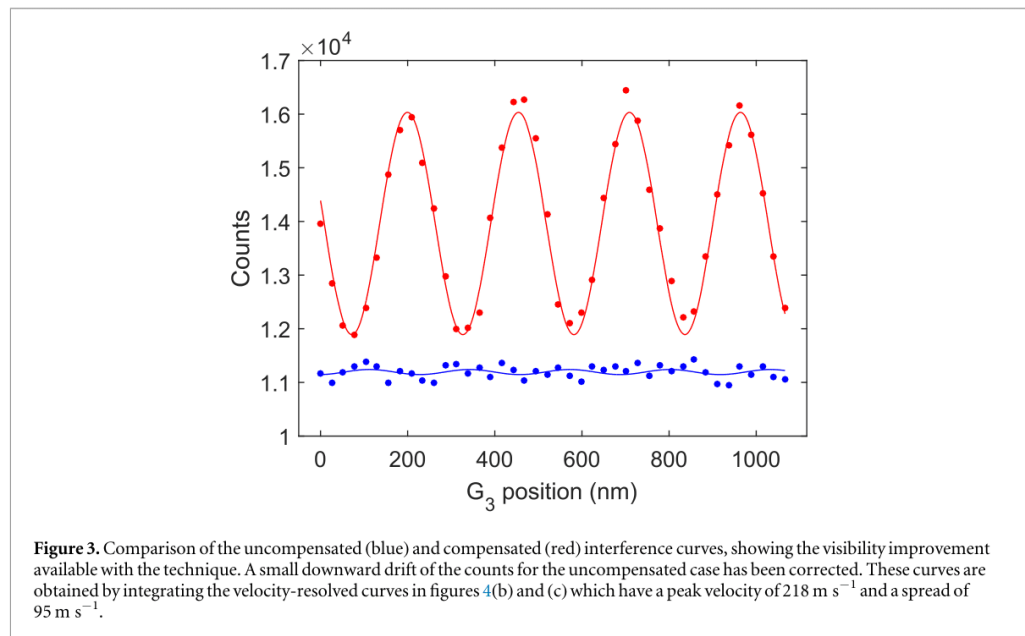
1.2. Experimental setup

In the LUMI experiment, the first and third gratings are silicon nitride nano-structures with period $d = 266$ nm, while the center grating is a phase grating formed by a back-reflected 532 nm laser. Such a mixed mechanical-optical grating scheme is advantageous for observing interference of slow beams of highly polarizable molecules [28]. C_{60} fullerenes were used for these measurements since they form a stable thermal beam and their optical polarizability at 532 nm is known [35]. Detection was via electron impact ionization followed by quadrupole mass selection and ion counting.

We studied the Coriolis compensation mechanism by measuring the relative contributions of gravity and the Coriolis force to the phase of the interference fringes as a function of velocity. This was done by modulating the beam with a periodic pseudo-random sequence [36] and cross-correlating the beam signal with the sequence to retrieve the time-of-flight distribution. The third grating was moved transversely and a time-of-flight measurement taken at each position step.

This procedure yields an intensity map of the flux as a function of both transverse grating position and time, such as those shown in figures 4(a)–(c). Each line-cut of the time axis contains a small spread of times determined by the resolution of the time-of-flight measurement. For typical parameters this spread is 3% full-width-at-half-maximum, small enough that velocity averaging over a given line-cut can be safely neglected in the data analysis.

2. Results

Coriolis compensation allows high interference visibility to be retained when interference data is integrated over all velocities in the beam. This is illustrated in figure 3, which shows the improvement in the integrated interference visibility when the gratings are rolled to $\theta \approx \theta_0$ as compared to the uncompensated case of $\theta \approx 0$. A

Figure 3. Comparison of the uncompensated (blue) and compensated (red) interference curves, showing the visibility improvement available with the technique. A small downward drift of the counts for the uncompensated case has been corrected. These curves are obtained by integrating the velocity-resolved curves in figures 4(b) and (c) which have a peak velocity of 218 m s^{-1} and a spread of 95 m s^{-1}.

Figure 4. (a) Time-resolved interference signal with the common roll of all gratings set to $\theta = \theta_0 - 1.0$ mrad, where θ_0 is the roll angle which provides near-optimal compensation for the velocity distribution in these experiments. (b) As (a), but with $\theta = \theta_0$. (c) As (a), but with $\theta = \theta_0 + 1.0$ mrad. (d) A zoomed-in plot of the phase versus velocity curve at the optimal roll θ_0, showing a turning point at about 170 m s^{-1}. The shaded region denotes 68% confidence intervals of the fitted phases and the solid line is a fit to equation (2). The absolute phase is arbitrarily set to zero at the starting velocity for visual clarity. (e) Extracted phase for the various roll angles with respect to θ_0, from top to bottom, $-1.0, -0.5, 0, +0.5, +1.0$ mrad. Solid lines are fits to equation (2), with the various offset angles. Every 20th point is shown for clarity, and error bars are too small to be visible on this scale.

visibility of 21% for an optical grating power of 7 W would be expected in the absence of the Coriolis effect, while 15% was achieved with compensation, despite a large velocity spread of 0.44 v_0. This reduced visibility R of 0.65 is in reasonable agreement with the predicted value of 0.73 for the given parameters. The lesser degree of experimental compensation compared with theory can likely be explained by a slight relative roll misalignment

to which the visibility is very sensitive when working with vertically extended beams [35], as were required for the large velocity spread.

To analyze the compensation systematically we performed a series of time-resolved interference scans as a function of θ. The roll was adjusted for the three gratings equally in order to maintain their relative alignment while introducing a gravitational phase shift.

A subset of these measurements is shown in figures 4(a)–(c), in which the gravitational phase shift, which dominates at large roll angles, is visible as a shearing of the contours. The power of the optical grating was held fixed at 7 W for these measurements.

To extract the phase shift as a function of velocity we take horizontal line-cuts of the time-resolved interference signal and fit a sine curve to each of these cuts. This is done first for the optimal-roll setting θ_0 shown in figure 4(b), with the extracted phases shown in figure 4(d). The value of θ_0 used here was determined by an optimization of the visibility as a function of roll, rather than calculating it via equation (6), since there was some uncertainty regarding the initial grating rolls with respect to gravity.

The turning point observed at about 170 m s^{-1} indicates optimal compensation near this velocity. It is also clear evidence that the observed phase shifts are not merely gravitational, as these would be monotonically increasing or decreasing with velocity. We fit equation (2) to the observed phase shifts with an additional constant offset and the roll θ as free parameters. The best-fit value of θ_0 is -0.96 mrad, which provides optimal Coriolis compensation at a velocity of 173 m s^{-1}, as estimated from equation (6).

The other roll settings of $\theta = \theta_0 \pm 0.5$ mrad and $\theta = \theta_0 \pm 1.0$ mrad can be similarly analyzed. The results are shown in figure 4(e). With θ_0 fixed, the only free parameter is the arbitrary constant phase offset. The fits show excellent agreement with the data.

Similar experiments can also be used to measure local gravity or perform equivalence principle tests if g in equation (2) is left as a free parameter.

3. Conclusion

A passive scheme to compensate for the velocity-dependent Coriolis force is demonstrated in a two-meter long Talbot–Lau molecule interferometer. The scheme uses a grating roll offset to give a gravitational phase shift which compensates the Coriolis shift in the velocity band of interest. The technique provides a simple and robust means to compensate for the Coriolis effect in matter-wave interferometers with non-monochromatic beams.

Acknowledgments

ORCID iDs

Yaakov Y Fein ● https://orcid.org/0000-0001-5737-7800
Markus Arndt ● https://orcid.org/0000-0002-9487-4985

References

[1] Eibenberger S, Gerlich S, Arndt M, Mayor M and Tüxen J 2013 *Phys. Chem. Chem. Phys.* **15** 14696
[2] Kovachy T, Asenbaum P, Overstreet C, Donnelly C A, Dickerson S M, Sugarbaker A, Hogan J M and Kasevich M A 2015 *Nature* **528** 530
[3] Fein Y Y, Geyer P, Zwick P, Kiałka F, Pedalino S, Mayor M, Gerlich S and Arndt M 2019 *Nat. Phys.* **15** 1242
[4] Peters A, Yeow-Chung K and Chu S 1999 *Nature* **400** 849
[5] Gustavson T L, Bouyer P and Kasevich M A 1997 *Phys. Rev. Lett.* **78** 2046
[6] Stockton J K, Takase K and Kasevich M A 2011 *Phys. Rev. Lett.* **107** 133001
[7] Snadden M J, McGuirk J M, Bouyer P, Haritos K G and Kasevich M A 1998 *Phys. Rev. Lett.* **81** 971
[8] Cronin A D, Schmiedmayer J and Pritchard D E 2009 *Rev. Mod. Phys.* **81** 1051
[9] Bouchendira R, Cladé P, Guellati-Khélifa S, Nez F and Biraben F 2011 *Phys. Rev. Lett.* **106** 080801
[10] Fixler J B, Foster G T, McGuirk J M and Kasevich M A 2007 *Science* **315** 74
[11] Cohen-Tannoudji C 1992 *Phys. Rep.* **219** 153
[12] Müntinga H *et al* 2013 *Phys. Rev. Lett.* **110** 093602
[13] Kaltenbaek R *et al* 2016 *EPJ Quantum Technol.* **3** 5
[14] Becker D *et al* 2018 *Nature* **562** 391
[15] Clauser J F 1988 *Physica* B+C **151** 262
[16] Jacquey M, Miffre A, Trénec G, Büchner M, Vigué J and Cronin A 2008 *Phys. Rev. A* **78** 013638
[17] Lan S-Y, Kuan P-C, Estey B, Haslinger P and Müller H 2012 *Phys. Rev. Lett.* **108** 090402

[18] Dickerson S M, Hogan J M, Sugarbaker A, Johnson D M S and Kasevich M A 2013 *Phys. Rev. Lett.* **111** 083001
[19] Roberts T D, Cronin A D, Tiberg M V and Pritchard D E 2004 *Phys. Rev. Lett.* **92** 060405
[20] Colella R, Overhauser A W and Werner S A 1975 *Phys. Rev. Lett.* **34** 1472
[21] Werner S A, Staudenmann J L and Colella R 1979 *Phys. Rev. Lett.* **42** 1103
[22] Staudenmann J L, Werner S A, Colella R and Overhauser A W 1980 *Phys. Rev. A* **21** 1419
[23] Riehle F, Kisters T, Witte A, Helmcke J and Borde C J 1991 *Phys. Rev. Lett.* **67** 177
[24] Hasselbach F and Nicklaus M 1993 *Phys. Rev. A* **48** 143
[25] Patorski K 1989 *Progress in Optics XXVII* ed E Wolf (Amsterdam: Elsevier) p 1
[26] Clauser J F and Li S 1994 *Phys. Rev. A* **49** R2213
[27] Brezger B, Hackermüller L, Uttenthaler S, Petschinka J, Arndt M and Zeilinger A 2002 *Phys. Rev. Lett.* **88** 100404
[28] Gerlich S *et al* 2007 *Nat. Phys.* **3** 711
[29] Haslinger P, Dörre N, Geyer P, Rodewald J, Nimmrichter S and Arndt M 2013 *Nat. Phys.* **9** 144
[30] Juffmann T, Truppe S, Geyer P, Major A G, Deachapunya S, Ulbricht H and Arndt M 2009 *Phys. Rev. Lett.* **103** 263601
[31] McMorran B J and Cronin A D 2009 *New J. Phys.* **11** 033021
[32] Oberthaler M K, Bernet S, Rasel E M, Schmiedmayer J and Zeilinger A 1996 *Phys. Rev. A* **54** 3165
[33] Schmiedmayer J, Chapman M S, Ekstrom C R, Hammond T D, Kokorowski D A, Lenef A, Rubenstein R A, Smith E T and Pritchard D E 1997 *Atom Interferometry* ed P R Berman (New York: Academic) p 1
[34] Nimmrichter S 2014 *Macroscopic Matter Wave Interferometry* (Berlin: Springer)
[35] Hornberger K, Gerlich S, Ulbricht H, Hackermüller L, Nimmrichter S, Goldt I, Boltalina O and Arndt M 2009 *New J. Phys.* **11** 043032
[36] Koleske D D and Sibener S J 1992 *Rev. Sci. Instrum.* **63** 3852

Curriculum Vitae

❖ Personal

Name   Yaakov Yisrael Fein

Place of birth   New York, USA

❖ Education

2016 – 2020   **Doctoral studies** in Physics, University of Vienna, supervised by Prof. Markus Arndt

2014 – 2015   **Master of Science** (with distinction) in Physics, University of Melbourne, supervised by Prof. Robert Scholten

2009 – 2013   **Bachelor of Arts** and **Master of Arts** in Physics (Summa Cum Laude), Queens College, City University of New York

❖ Scholarships and awards

2016 – 2020   Fellow of the Vienna Doctoral School of Physics

2015   Dr. Jean E. Laby Bursary (University of Melbourne)

2014   N.D. Goldsworthy Scholarship for Physics (University of Melbourne)

2014   International Postgraduate Coursework Award (University of Melbourne)

2012   Barry M. Goldwater Scholarship Honorable Mention

2011   Michael Craig-Scheckman Award for Undergraduate Research (Queens College)